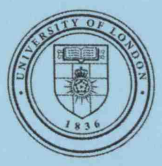

UNIVERSITY OF LONDON THESIS

Degree PhD Year 2007 Name of Author OWOYEMI, Olumuyiwa Ayodeji

CFD modelling of mono-component & binary gas-solid fluidized beds with application to industrial materials

Olumuyiwa Owoyemi
Department of Chemical Engineering
University College London

A thesis submitted for the degree of
Doctor of Philosophy in the University of London

July 2007

ProQuest LLC
789 East Eisenhower Parkway
P.O. Box 1346
Ann Arbor, MI 48106-1346

"Would that I were wiser! Would that I were wise from the very heart". "But I am asking the impossible. Therefore I do ask my pride to go always with my wisdom!" "And if my wisdom should some day forsake me :- alas! it loves to fly away!- may my pride fly with my folly!"

Friedrich Nietzsche (1844 - 1900)

I would like to dedicate this thesis to my loving parents . . .

Abstract

Fluidized bed technology is employed in a wide range of industrial applications, covering the pharmaceutical, food, chemical and petrochemical industries as well as the mining and power generation industries. However in most industrial applications of fluidization, the suspension consists of non-spherical particles of different diameters and sometimes-different densities. Computational Fluid Dynamics modelling has been recognized by several in academia and industry as an indepensible tool to study multiphase systems including fluidization. CFD models that describe gas solid flow systems can be formulated at different levels of mathematical detail. The use of the Eulerian-Eulerian approach has been considered as the highest possible level of continuum modelling where both the fluid and particle phase are treated as interpenetrating continua and mass and momentum conservation equations are solved for each phase. The Eulerian-Eulerian approach has been successfully used by many researchers for tackling problems relating to the modelling of gas-solid fluidized beds coupled with using the kinetic theory of granular flow for the description of the solid phase as derived from the kinetic theory of gases. However, most of the CFD investigations carried out to date have been limited to the study of the fluidization behaviour of mono-component gas-solid systems of modelling type materials (e.g. Ballotini).

The aim of this thesis is to address the computational modelling of mono-component and binary gas-solid fluidized beds with particular focus placed on industrial materials. This work, sponsored by Huntsman Tioxide, is concerned with the titanium refining industry where a bubbling fluidized bed is used for extracting titanium from naturally occurring ore. The refining process begins in a fluidized bed with the chlorination of titanium rich rutile ore which is composed of many constituents. Due to the size and density differences of all the feedstock components used in the process, there are industrial concerns about the

pervasiveness of *dead zones* within the fluidized bed as a result of feed stock segregation. Thus, the objective of the work is to develop a model capable of predicting the degree of mixing and segregation in the fluid bed system. To this end, the following powders, slag, natural and synthetic rutile, belonging to the Geldart Group B classification and used as feedstock in the Huntsman Tioxide chlorination process, were provided for the experimental and computational investigations in this project.

This work presents a new hydrodynamic model for the CFD simulations of the mono-component and binary industrial materials using a commercial code (CFX4.4). The modelling development allowed the assessment of suitable governing equations for the description of the internal stress relevant to the solid phase(s), the fluid-particle and particle-particle interphase exchange terms. For the mono-component systems, a new expression for the fluid-particle interaction term has been developed based on the fluid bed elasticity concept originally proposed by Wallis (1969). Consequently, the procedure followed to obtain a stability criterion was re-examined analytically and subsequently numerical simulations were performed to validate the ability of the model to predict the fluidization behavior of the materials investigated. As part of the development, a comparison was conducted between the model proposed in this thesis and the granular kinetic theory model in order to assess the impact of the collisional stresses on the numerical predictions.

The new modelling approach was subsequently extended to the modelling of binary systems using the *three fluid* approach, where a separate momentum equation is solved for the fluid and each solid phase. This part of the study also assessed the effect of the particle-particle drag force on the dynamics of the binary system by comparing three different closures available in literature and catering for this contribution against a reference test case where such contribution was not accounted for. Similar to the approach followed for the mono-component systems, a sensitivity analysis on the effect of the collisional stress on the simulations of the binary systems was also performed. Furthermore, a sensitivity analysis on grid and time step resolution was also carried out. Results of these analyses enabled the qualitative and quantitative numerical investigation into the mixing and segregation behaviour of

the binary mixture of the industrial materials provided for this project. In this investigation, three different average compositions, corresponding to the average mass fraction of jetsam particles of 0.25, 0.50, 0.75 in the bed were considered, so that the hydrodynamic behavior of three binary mixtures in all was studied.

In addition, a new fluid-particle interaction force closure for well mixed binary systems based on the two-fluid approach, where mixture continuity and momentum equations are employed in the description of the solid phases, was also derived and corresponding CFD simulations are carried out to assess the reliability of the derived mixture models.

Acknowledgements

I would like to thank Dr Paola Lettieri for her immense support and constant encouragement throughout this PhD project. Paola's stimulating supervision and enthusiasm has much to do with the fruition of this thesis.

I am also greatly indebted to Mr Roger Place, Mr Mike Westwood and Dr Stephen Sutcliffe for providing constructive technical criticism during the undertaking of this project. In particular, I am grateful for the many intellectually stimulating discussions with Roger concerning many areas of this work.

A special thank you to Professor Renzo Di Felice for his many useful insights and advice. I am especially thankful for his hospitality during my secondment at the *Dipartimento di Ingegneria Chimica e di Processo* - University of Genoa- Italy. My stay in Genoa remains one of the fondest memories of my PhD study.

To Luca Mazzei's persistent and carefully orchestrated intellectual challenges and discussions, this thesis owes more than I can adequately express. A special thanks also to Liban Yassin "Libs" whose encouragement and great friendship made my PhD life more enjoyable. Many thanks also to my dear friends and fellow PhD colleagues, Deji, John, Maxwell, Nnamso, Sarah, Cristina, Panos, Baudong and Toju with whom I shared the good and stressful times. To the memory of Mr Luca Cammarata, a person who had an immense cerebral capacity, this work and the writing of this thesis would have been an insurmountable task had he not introduced me to the world of computational modelling and LaTeX 2_ε.

Many thanks are also due to the staff of the computing and electronic systems office within the department of Chemical Engineering at UCL. In particular, Mr Martyn Vale and Mr Mark

Spurgeon for handling hardware and software problems in an expedient manner. Thanks also to members of the chemical engineering workshop for building my experimental rig.

A heartfelt thankyou to the administrative staff of the Chemical Engineering Departmental office at UCL. I am especially indebted to Pattie, who allowed me to use document processing facilities present in the departmental office.

To my friends who have provided me with a constant source encouragement outside my academic life; Gbenga, Biodun, Bobola, Hauwa and Chika thanks for being true friends through some of the most trying periods of my PhD and indeed my life. Many thanks also to friends at the Royal African Society who provided a much needed distraction from the pressures of PhD study. A very special thankyou to Femi Atinmo, who has been a source of constant encouragement and emotional support throughout my PhD. Thankyou for being patient with me.

Finally, I would like to thank my entire family; not only have they always given me love and support, but they have been a constant source of encouragement throughout my PhD. In this regard, a very special thanks to my father, who encouraged me to undertake this PhD study in the first place and provided important support and my mother, who encouraged me with her prayers and selfless support throughout my PhD.

I would like to acknowledge the financial support of the UK Engineering and Physical Science Research Council (EPSRC) and Huntsman Tioxide Ltd for providing funding for this project.

Contents

List of Figures

List of Tables

Chapter 1

General Introduction

Summary

An overview of different types of fluidization behaviour is given in this chapter. The computational modelling of fluidized beds is also discussed. The goal of this project is presented thereafter and the chapter concludes with an outline of the thesis.

1.1 Introduction to fluidization

The phenomenon of fluidization can be described as a random upward motion of stationary discrete particles in a vertical vessel caused by the upward flow of a fluid of lower density through the system, at a sufficiently high velocity. In other words the upward flow of fluid causes the particles to become buoyant and mobile. The weight of the particles is borne by the drag forces and the fluid pressure gradient, the bed is said to be *incipiently fluidized* or at *minimum fluidization* at this point. Further increase of the fluid velocity causes the discrete particles to expand and the void fraction to increase. In liquid-solid systems a further increase in flow rate above minimum fluidization results in a smooth, progressive expansion of the bed. A bed such as this is called a *homogeneously fluidized* bed.

In gas-solid systems, such beds are observed only under special conditions of fine-light particles with dense gas at high-pressure. For these systems, increasing the fluidizing gas velocity further causes the bed to expand so that the average distance between the particles will be

greater, or the excess fluid will pass through the bed in the form of bubbles, giving rise to a two-phase system. This type of bed is called a *bubbling fluidized bed.* The velocity at which the first bubble forms is called minimum bubbling velocity, u_{mb}. In gas solid systems, gas bubbles coalesce and grow as they rise. In a deep enough bed of small diameter they may eventually become large enough to spread across the vessel, this is called *slugging.* For fine particles the above change is observed as axial slugs whilst for coarse particles it is observed as flat slugs.

Turbulent fluidization is observed in a fluid bed when the velocity of the fluidizing gas exceeds the terminal velocity of the particle. Further increase in the gas velocity results in a lean phase fluidized bed with pneumatic transport. Figure 1.1 shows the various regimes of fluidization described above.

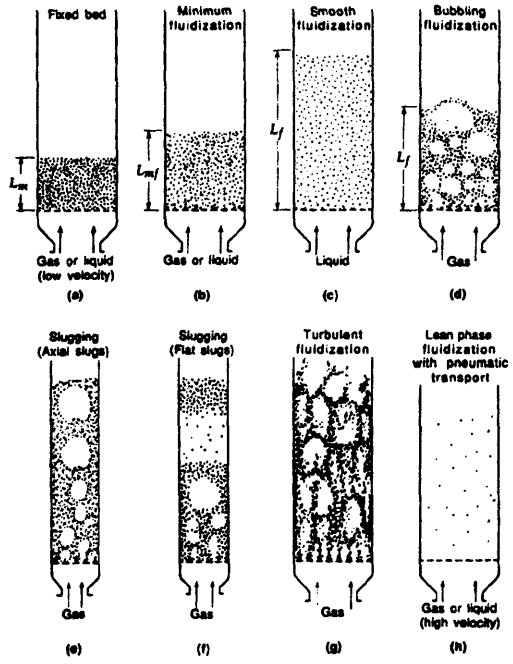

Figure 1.1: *Different regimes of fluidization (Kunii & Levenspiel, 1989)*

The mutual interaction between discrete particles and continuum gas provides an ideal environment for rapid heat and mass transfer, good mixing of solids and fast chemical reaction inside the fluidized bed. These features are very desirable for many industrial applications. Fluid beds are applied in processes where chemical reactions are the dominant mechanism

such as gas /gas reactions were the solid acts as a catalyst (*i.e.* in the catalytic cracking of oil); and also in gas/solid reactions were the solids are transformed (*i.e.* Extraction of titanium oxide from its ore). The good heat and mass transfer properties of fluid beds find application in processes where high degree of gas /particle and particle/particle contacting and mixing is required. Examples include solids drying (gas/particle), Coating of pharmaceuticals tablets (particle/particle). Some industrial applications of fluid beds are reported below in Table 1.1 and 1.2 (Lettieri, 2002).

Table 1.1: *Industrial uses of gas fluidized beds based on physical mechanism (Lettieri, 2002)*

Physical mechanism		
Heat and/or mass transfer between gas /particles	Heat and/or mass transfer between particles/particles	Heat and/or mass transfer between bed/surface
• Solids drying • Adsorption of solvents • Food freezing	• Granulation • Mixing of solids • Coating of pharmaceutical tablets	• Heat treatment of glasses, rubber, textile fibers

Table 1.2: *Industrial uses of gas fluidized beds based on chemical mechanism (Lettieri, 2002)*

Chemical mechanism	
Gas/gas reaction in which solids act as catalyst	Gas/gas reaction in which solids are transformed
• Oil cracking and reforming • Manufacture of ★ polyethylene ★ chlorinated hydrocarbons ★ acrylonitrile	• Coal combustion • Gasification • Incineration of liquid and solid waste • Titanium oxide manufacture • Catalyst regeneration

The behaviour of particulate solids in gas fluidized beds depends largely on a combination of their physical properties, such as their mean particle size and density, on which basis Geldart (1973) distinguished four groups and introduced the so-called Geldart classification of powders. Geldart (1973) came up with four recognizable kinds of particle behaviour by carefully observing the fluidization of all sorts and sizes of solids. The system of classification divides the fluidization behaviour according to the mean particle size, gas and particle densities. A, B, C and D indicates the four typical fluidization regimes, for materials fluidized with air at ambient conditions. Boundaries between these groups are proposed in the

form of a dimensional plot of $(\rho_p - \rho_g)$ versus d_p as shown in Figure 1.2. Group C particles

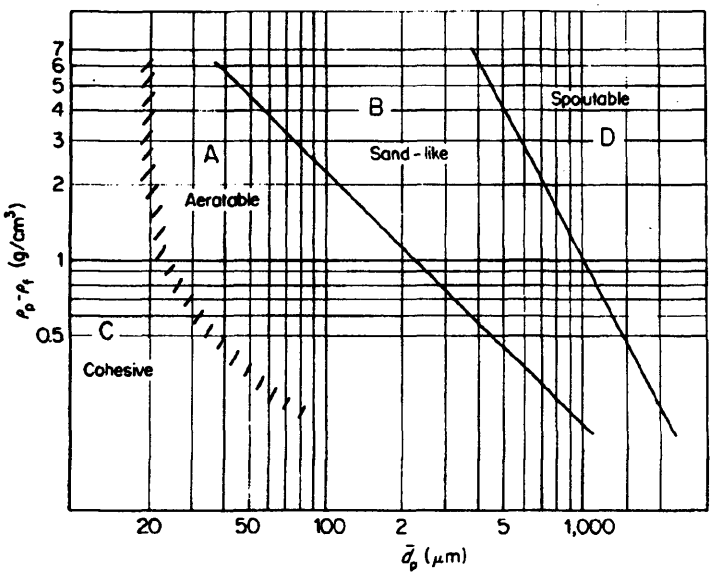

Figure 1.2: *Classification of powders according to their fluidization behaviour in air at ambient temperatures (Geldart, 1973)*

are classified as cohesive. Van der Waals attractive forces between such particles are larger than the forces exerted by gravity and fluid drag which results in the particles tend sticking together and consequently making fluidization difficult. The gas cannot readily separate particles and channelling occurs, giving in most cases poor mixing and heat transfer. Fluidization of Group C materials can be improved by the use of mechanical stirrers or vibrators, which break up the stable channels. Group A powders exhibit a stable region of homogenous expansion at velocities between u_{mf} and u_{mb} (with $u_{mb}/u_{mf} > 1$) are said to be "aeratable".

The powders that fall in the Group B region exhibit bubbling fluidization as soon as they are fluidized. In this case $u_{mf} = u_{mb}$ thus bubbles start to form in this type of powder only slightly above minimum fluidization velocity. The interparticle forces are considered to be negligible for these powders. Group D powders are typically large or dense particles. The distinction between this and the previous groups concerns the rise velocity of the bubbles, which is in general, less than the interstitial gas velocity. The gas velocity in the dense phase is high and solids mixing is relatively poor, consequently, back mixing of the dense phase is small (Geldart, 1986). The type of fluidization behaviour associated with the four Geldart Groups at ambient conditions is best summarized by Figure 1.3.

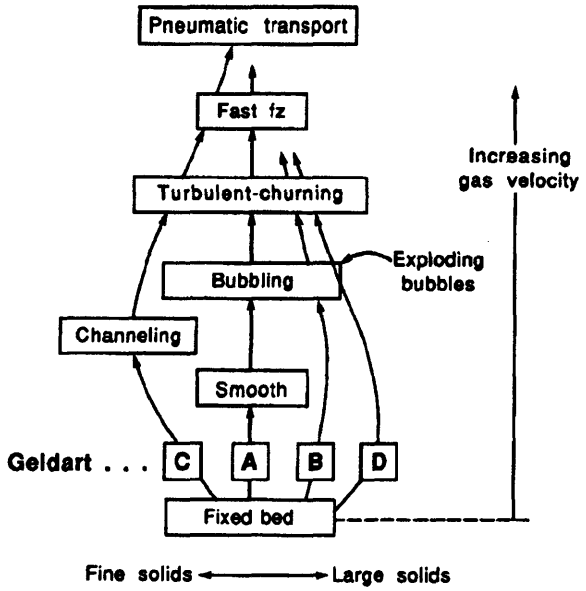

Figure 1.3: *Different types of fluidization behaviour exhibited by the various Geldart Classified powders (Kunii & Levenspiel, 1989)*

1.2 Computational modelling of fluidized beds

The early development of fluidized bed technology was characterized by the use of empirical correlations to understand observed physical phenomena, however the last 40 years has seen a shift in paradigm towards gaining a fundamental understanding of the mechanisms governing the highly complex solid fluid flow phenomena. As a result of this increased interest computational fluid dynamics software has increasingly become an indispensable tool used by scientists and engineers for studying multiphase systems including fluidization.

The numerical solution of the conservation equations for fluid flow is known as computational fluid dynamics (CFD). Since the 1980's, when it was first realized that it was possible to base quantitative design calculations regarding the fluidized beds on differential equations of continuity and momentum, the use of CFD has grown increasingly as a modelling tool to study multiphase systems including fluidization. CFD modelling tools now span a wide variety of industries ranging from the power generation, pharmaceutical to the titanium refining industry. In process industries for instance the use of CFD in single phase systems has led to reductions in the cost of product and process development activities (by reducing downtime), reduced the need for physical experimentation, shortened time to market, improved design

reliability and increased conversions and yields (Davidson, 2002).

CFD models used to predict gas-solid flows can be subdivided in two groups, Discrete particle models or Lagrangian-Eulerian Models and *two fluid models* or Eulerian-Eulerian models. The latter and former approaches vary in the level of mathematical detail used for their descriptions. Lagrangian models calculate the path of each discrete particle present in the spatial domain using Newton's second law of motion. The gas velocity rather than being specified at each point in the domain is replaced by its average, taken over a spatial domain large enough to contain many particles but still small compared to the whole region occupied by the mixture. The main drawback of this technique is the fact that only a small amount of discrete particles $\left(< 10^4\right)$ can be simulated due to the large computational memory requirements.

Eulerian-Eulerian models treat the particle and fluid phase as an interpenetrating continua. Computations using this approach can predict the behaviour of dense gas solid phase flows using more realistic fluid bed geometry. In the modelling of mono-component dense gas-solid flows, the granular kinetic theory is typically employed by many researchers to translate the behaviour of the many particles into one continuum (Gidaspow & Ettehadieh, 1983, Gidaspow, 1994). This approximation has however been proven to be inadequate in giving a fully theoretical description of the behaviour of particles in dense gas-solid flows (Jackson, 1997, Curtis & van Wachem, 2004). This has lead to the use of concepts borrowed from the field of soil mechanics as well as analogies drawn from the continuum theory of solid elasticity in providing a description adequate for the dense particulate phase (Savage, 1982, Johnson & Jackson, 1987, Foscolo & Gibilaro, 1987, Makkawi & Ocone, 2006).

The picture gets even more turbid when the Eulerian-Eulerian approach is applied to modelling of dense binary gas-solid systems. The problem of accounting for the behaviour of the solid phases becomes more intricate. Constitutive expressions for the interaction between the two solid phases have to be provided as well as suitable expressions for the behaviour of each solid phase. Some researchers have circumvented this issue by developing ingenious ways of reducing the complexity of the problem. One such way is modeling the *three phase* system

within the framework of a *two phase* system (van Wachem et al., 2001). This reduces the problem to a *two fluid* problem, however care has to be taken to use suitable expressions to account for the drag force exerted by the fluid on the *solid mixture* as well expressions for the behaviour of the mixed solid particles.

The differences in results predicted by Eulerian and Lagrangian simulations when compared with corresponding experimental results, for mono-component systems, are very small nowadays, this is due primarily to better constitutive models used in Eulerian models as well as better collision dynamics used in Lagrangian models. The same cannot be confidently said for the simulation of binary systems. Both modelling approaches suffer from different drawbacks, in the case of the Lagrangian approach, the sheer computational effort required to simulate realistic particle systems makes it an improbable choice for simulating large scale industrial dense beds. Eulerian simulations of large scale dense binary gas-solid systems on the other hand suffer from the time discrepancy in predicted macroscopic properties like mixing time and segregation rate. This is caused by differences between the actual physics and constitutive models used in the simulations. A number of reviews have been published covering the above mentioned issues associated with modelling gas-solid flows (see Kuipers & van Swaaji, 1997, van den Akker, 1997, Sundaresan, 2000, Arastoopour, 2001, Campbell, 2006).

1.2.1 Introduction to CFX 4.4

This work uses the CFX4 code of Ansys.Ltd (formerly AEA Technology). Typically the solution of fluid flow problem by means of a CFD approach involves the 3 following steps: Pre-processing, solving and post processing. These are briefly introduced below.

Step 1: Pre-processing:

The information necessary for problem specification, i.e. the geometry of the computational domain, the subdivision of the domain into a number of cells, the physical and chemical phenomena involved and the related model equations, the fluid

properties and finally the boundary conditions on the boundary cells is provided.

Step 2: Solving:

The numerical solution technique employed in most of the commercially available CFD codes, such as: CFX4, FLUENT, PHOENICS and STAR-CD CFD codes is the Finite Volume Method (FVM). The numerical algorithm is used herein and consists of the following steps

1. Integration of the problem equations over each of the computational cells
2. The conversion of the integral equation in a set of algebraic equations by means of a suitable discretization technique that consists in the substitution of the differential convection, diffusion and source terms into finite difference approximations.
3. An iterative solution method of the resulting algebraic equations

Step 3: Post-Processing:

Used to display and analyze the simulation results by means of graphics and data management and export.

1.3 Research objectives

The main focus of this research is on the computer modelling of the dense gas-solid hydrodynamics applied to the fluidization of binary mixtures. The project is sponsored in part by Huntsman Tioxide Ltd as well as from the EPSRC DTA. The development has been carried out using the Eulerian-Eulerian approach since it represents the largest length scale for modelling fluidized beds on an industrial scale.

The problem which is being addressed by this work concerns the titanium refining industry where a bubbling fluidized bed is used for extracting titanium from naturally occurring ore (see Figure 1.4). The refining process begins in a fluidized bed with the chlorination of titanium rich rutile ore (Natural and Synthetic rutile). Chlorine gas is bubbled through a bed

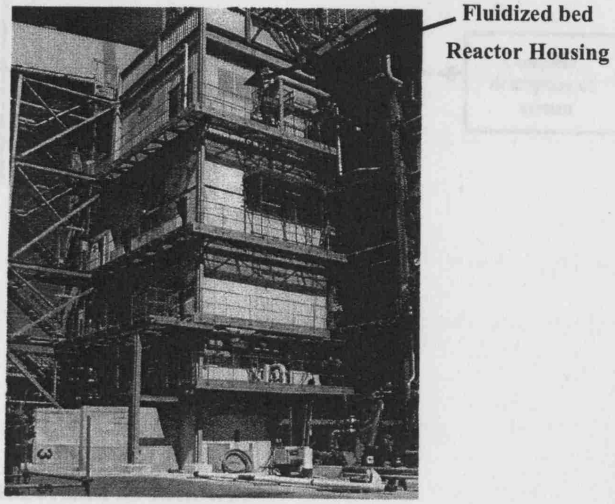

Figure 1.4: *Greatham FBR: An Example of an Industrial Fluidized Bed Reactor. Reproduced with kind permission from Huntsman Tioxide Ltd.*

of rutile particles, coke and slag at a high temperature $\left(\approx 900\,^{0}C\right)$, where they all react to form an intermediate species of titanium tetrachloride, as well as carbon dioxide and carbon monoxide gases.

$$TiO_2 + C + 2\,Cl_2 \xrightarrow{900^{\circ}C} TiCl_4 + CO + CO_2$$

Because of the size and density differences of all the reactants, the rutile particles are smaller than the slag and coke components, there are industrial concerns about the pervasiveness of *dead zones* within the fluidized bed which is caused by segregation of the feedstock. The eventual effect of the above is refractory lining erosion. Refractory erosion represents a significant cost of chlorinator operation, requiring the reactor to be shutdown every 12 months and the refractory replaced. It will thus be of great importance to gain a better understanding of the mixing and segregation phenomena at play within the system. The above step has been the objective of this PhD and represents the first step in understanding the entire scope of the industrial problem, which is represented in Figure 1.5. The materials which has been used in this investigation are slag, natural and synthetic rutile powders provided by Huntsman Tioxide Ltd. The materials all belong to the Geldart Group B classification. The main

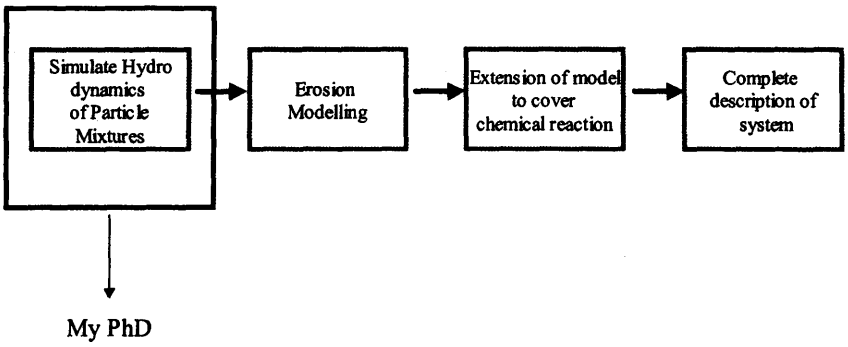

Figure 1.5: *PhD Project Overview*

goals of this work can be summarized as follows:

i Experimental characterization of the fluidization behaviour of the mono-component rutile powders and slag. CFD modelling of individual industrial powders using the Granular Kinetic Model (GKT). Validation of computational results with corresponding experimental observation.

ii Determine the suitable governing equations suitable for the modelling of binary systems and elucidate the true nature of the solid phase stress tensor in a binary system.

iii Develop an alternative modelling strategy for the solid stress tensor as well as develop a new constitutive equation for the fluid-particle interaction force applicable to binary and mono-component systems.

iv Validation of the new model for mono-component materials with results obtained from the GKT within CFX4.4 as well as experimental results to investigate the effect of collisional stresses.

v Sensitivity analysis of the closure models describing the *particle-particle drag* force required for the modelling of a binary system described as a *three fluid* system and compare the impact of each constitutive expression on simulations of an ideal binary mixture using modelling materials *i.e.* Ballotini. Validation of the results from simulations with experimental data

vi Validation of the new binary mixture model with experiments by carrying out

mixing and segregation simulations using the industrial materials provided for the project. Comparison of the model predictions with experimental results using the mixing index, coefficient of segregation, bubble dynamics, bed height and bed voidage.

vii Develop a constitutive expression for the drag force in a binary mixture within the frame work of a *two-fluid* mixture. Compare results with similar *three fluid* simulation

1.4 Thesis outline

Chapter 2 presents a literature review of the various approaches used for modelling gas fluidized beds. Chapter 3 focuses on the experimental methods as well as the analytical techniques used for the experimental investigation carried out in this thesis. Chapter 4 presents an outline of a model for the CFD simulation of binary gas-solid fluidized beds. The averaged equations of motion for the fluid and solid phases were derived by extending the two-fluid equations of change for identical spheres in a Newtonian fluid. Herein, the components that make up the internal stress relevant to each of the solid phases is elucidated. The chapter also outlines the development of a fluid-particle constitutive expression for binary mixtures. Chapter 5 and 6 present the results from the mono-component and binary mixture validation study conducted during this work. In Chapter 7, the main conclusions are summarized as well as a short description of the future work.

Chapter 2

Modelling Gas-Solid Fluidized Beds

Summary

An overview of different approaches available in the literature for the modelling of gas-solid fluidized beds is presented herein. The Eulerian-Eulerian approach which has been adopted in this thesis for the modelling dense mono-component and binary gas-solid systems is presented. The problem of closure of the equations of change for Eulerian-Eulerian systems is also discussed. This chapter concludes with an overview of the computational modelling of particle mixing and segregation in gas fluidized beds.

2.1 Modelling Approaches

CFD models that describe gas-solid flow systems can be formulated at different levels of mathematical detail. These levels of mathematical detail have been represented within the framework of a *multi-scale modelling concept* (van der Hoef et al., 2004) represented schematically in Figure 2.1. At the most fundamental level the motion of the whole system is determined by the Newtonian equations of motion for the translation and rotation of each particle and the Navier-Stokes and continuity equations, satisfied at every point of the interstitial

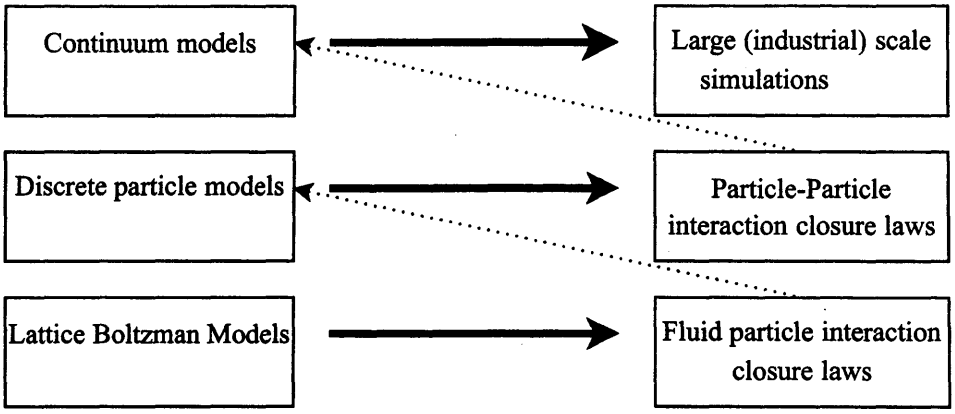

Figure 2.1: *Multi-scale modelling concept for fundamental hydrodynamic models of gas-fluidized beds (Hoomans et al., 1996).*

fluid. In this approach the gas flow field is modelled at a length scale much smaller than that of the solid phase (Jackson, 2001). The *Lattice-Boltzmann Model* (LBM) (Ladd, 1993, Succi, 2001) is the most commonly applied technique for computing gas solid interactions at this fundamental level. van der Hoef et al. (2004) used the LBM to compute the average drag force exerted by the gas phase for flows past spheres. They found that the current empirical drag correlations available in literature significantly underestimated the drag force in the laminar flow regime. Although characterizing the motion of the gas phase at a length scale smaller than the solid phase, it represents the most detailed mathematical description of gas solid interaction; the simulations are however only limited to a few particles (< 100). Thus, the sheer computational effort that would be involved in the modeling of a dense system such as that of fluidized bed would make this method an impractical approach for exploring fluidization problems of engineering interest.

Simulating the individual solid particles, whilst the gas phase is simulated on a length scale larger than that of the particle phase, commonly referred to as the *Lagrangian-Eulerian* approach represents the next level of mathematical detail. Here, the Newtonian equation of motion for each particle is solved separately taking into account direct collisions between particles when it is appropriate.

For describing the collisions of particles, two types of approaches are possible, the *hard-sphere* approach and the *soft-sphere* approach. In the *hard sphere* approach, particles in-

teract via binary, quasi-instantaneous collisions where contact occurs at a point. The velocities between particles emerging from collisions are calculated by considering the balance of both linear and angular momentum in the collision. This method of simulation was pioneered by Allen & Tildesley (1990). Since their publication many authors have found the hard sphere approach a useful tool in modelling the collision dynamics of granular systems. Hoomans et al. (1996) implemented the hard-sphere approach in their two dimensional model for a gas fluidized bed. It was the first time that the technique had been applied to a dense system such as that of a bubbling fluidized bed. Many authors have since published papers using this simulation strategy (Tsuji et al., 1987, Ouyang & Li, 1999, HL et al., 2005). Figure 2.2 shows a sample snapshot of a bubble at different times after injection calculated by a *hard sphere* Discrete Particle Model (DPM).

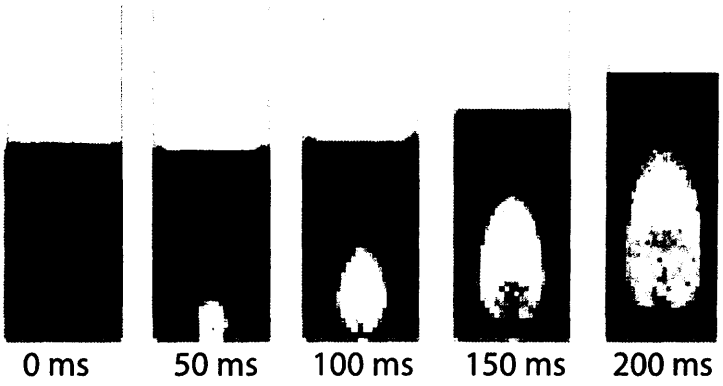

Figure 2.2: *Discrete Particle Model (DPM) simulation results for a single bubble in a mono-component fluidized bed using a hard sphere collision model*
Source: Reproduced from Bokkers et al. (2004)

The application of the soft sphere model for fluid beds was instead pioneered by Tsuji et al. (1993), who developed their approach on the basis of earlier work done by Cundall & Strack (1979). In the soft-sphere approach, particles are allowed to overlap slightly allowing contact forces to be calculated from the deformation history of the contact using a linear spring/dashpot model which is the most popular soft-sphere model for fluidization simulations. This has been used by Xu & Yu (1997), Dahl & Hrenya (2005), Pandit et al. (2005), Ye et al. (2005) to name just a few. Some authors have also presented hybrid simulation techniques, which feature the former and latter approaches to modelling discrete particle systems, and to study

the microscopic properties of fluidized beds, a recent example is the work by Kafui et al. (2002).

DPM models have also been applied for the simulation of segregation phenomena in binary gas fluidized beds. Hoomans (1999) simulated the segregation due to density differences in binary and ternary particle systems using *soft sphere* dynamics. In this case the number of particles used was in the region of 5000 particles. The results obtained showed good agreement with corresponding experimental results. Bokkers (2005) also carried out similar DPM simulations but increased the numbers of particles used to around 100, 000. Figure 2.3 shows a snapshot of experiments being compared with DPM simulations. In the DPM snapshot a small layer of small (blue) particles is formed at the top of the bed and the thickness increases as a function of time, this is in concurrence with the experimental snapshot. Discrete particle modelling is a valuable research tool to study the effect of different gas particle closures as well as the effect of particle-particle collisions on fluidization behaviour. The major drawback of the above studies is that the number of particles used is not representative of the typical number of particles encountered in most gas fluidized beds of practical interest. The fluidized bed used in this work for instance contains $\approx 4.7 \times 10^7$ particles. Thus, the restriction on the numbers of particles and the sheer computational effort required to model large scale fluidized beds makes this type of modelling approach impracticable in this work.

Simulating both phases as continuous and fully interpenetrating, a concept based on the two fluid model (TFM), is termed as the *Eulerian-Eulerian* approach. Many researchers have successfully carried out simulations of bubbling bed fluidization of mono-component systems Ding & Gidaspow (1990), for example compared qualitatively with experiments, simulations of the formation, growth, and bursting of bubbles of Geldart Group B particles in a jet bubbling fluidized bed. van Wachem et al. (1998) investigated the bubble behaviour of Geldart Group B particles in gas-fluidized beds at different superficial gas velocities and the resultant behaviour of the bubbles in different column diameters; they validated their work both qualitatively and quantitatively, by using semi-empirical correlations. Peirano et al. (2001) investigated the effect of the spatial computational domain on the simulated fluidized

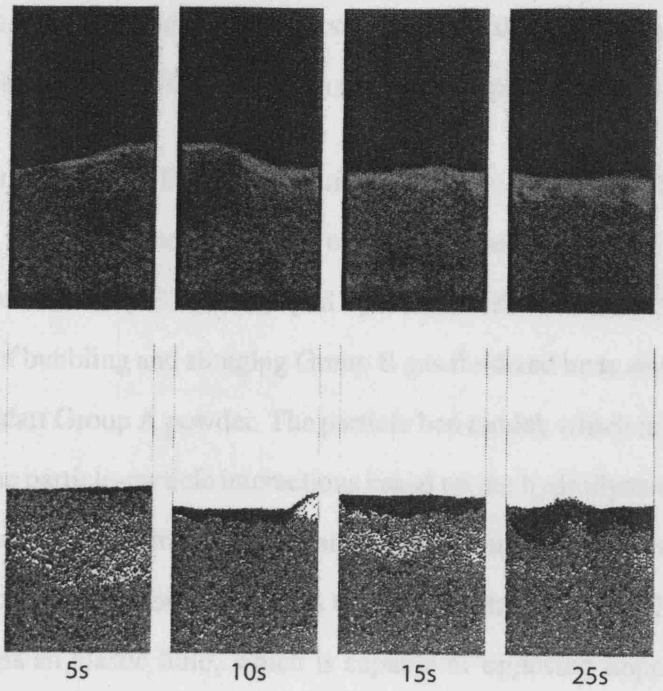

Figure 2.3: *An example of a comparison between a discrete particle simulation and experimental snapshots*
Source: Reproduced from Bokkers (2005)

bed dynamics. Pain et al. (2001) carried out 2D simulations on bubbling and slugging phenomena in gas fluidized beds. They also investigated the effect of an obstruction on the fluidization efficiency in gas fluidized beds.

Boemer et al. (1997) computed the distribution of time-averaged voidage and bubble formation at a jet within a bubbling bed. Gelderbloom et al. (2003) applied a multiphase CFD model to simulate the bubbling and collapsing behaviour of Geldart group A, group B and group C powders. In this case computed bubble sizes were validated by comparison with Davidson & Harrison (1963a) bubble size relation. Lettieri et al. (2004) used the Eulerian-Eulerian approach to simulate the transition from a bubbling to slugging gas fluidized bed of a Geldart Group B powder and used semi-empirical correlations to validate the prediction of the transition velocity and maximum slugging bed height obtained from the simulation. More recently the simulation of industrial mono-size powders has also been successfully tackled by Owoyemi et al. (2005). Results of 2D bubbling bed simulations of Geldart B industrial powders were validated with corresponding experimental data. All of the previously

mentioned authors have used the two fluid model approach that utilizes the Granular Kinetic Theory (GKT) (Gidaspow, 1994) description for the solid phase internal stress.

There are however, alternative Eulerian-Eulerian models based on the TFM that have been developed for the modelling and simulation of fluidized beds. Lettieri et al. (2003) have used the particle bed model (PBM) developed by Foscolo & Gibilaro (1984) to simulate in 2D the behaviour of bubbling and slugging Group B gas fluidized beds and the homogeneous expansion of a Geldart Group A powder. The particle bed model, which is semi theoretical in origin, describes the particle-particle interactions based on the hydrodynamic forces involved in the gas-solid flow (gravity, drag and buoyancy). In this model, direct collisions between particles are not a prerequisite for the particles to exchange momentum. The continuum solid phase is regarded as an elastic fluid, which is capable of opposing imposed deformations. A particle phase elasticity is derived and an additional force, the so called *particle phase elasticity force*, dependent on the solids volume fraction gradient is introduced in the solid phase momentum balance equation. Cammarata et al. (2003) investigated the consistency between two and three-dimensional simulations of a Geldart Group B material using the granular kinetic theory and the particle bed model. This study showed good qualitative and quantitative agreement between the two models. Simulation results on bed voidage and bubble diameter were reported and the latter were compared with empirical correlations.

The Eulerian-Eulerian computational modelling of binary systems, conversely, has not met with the same resounding success. The continuum modelling of binary mixtures is typically carried out using two approaches. The first is characterized by the use of separate momentum equations to cater for each particle species whilst the second makes use of the averaged mixture properties for the formulation of a mixture momentum equation coupled with the use of averaged constitutive relations. Each of the two modelling approaches described above has been applied separately to simulate particulate flow patterns within binary gas-fluidized beds. The first approach based on separate momentum equations has been employed by Gidaspow et al. (1985), Bell (2000), Gera et al. (2004), Copper & Coronella (2005). Their investigations, carried out using Geldart Group D particles, report good model predictions

however, with a limited set of experimental measurements. The second approach based on the mixture momentum balance has been employed by van Wachem et al. (2001) to predict the flow of a binary fluidized suspension of Geldart Group B particles. Results from their work showed good predictions with regard to bed expansion and minimum fluidization velocity. However, the relatively little research conducted in the field of computational fluid dynamics involving binary mixtures and more generally mixtures with a Particle Size Distribution (PSD) does not yet allow accurate theoretical predictions of the flow behaviour of such systems.

In what follows, an overview of the Eulerian-Eulerian modelling approach of mono component powders is given. This is then followed by a description of the Eulerian modelling strategies used for binary systems.

2.2 Eulerian-Eulerian modelling of mono-component systems

An initial step of this work involved looking at the mono-component behaviour of the industrial powders provided for this project with a view to understanding their fluidization behaviour. The equations of change for mono-component gas-solid flows advanced by Jackson (1997) were employed in this analysis. The equations are summarized in Table 2.2, the explanation of the symbols can be found in the nomenclature. A review of closure models employed as well as other closures available in literature is given below.

2.2.1 Closure models

Anderson & Jackson (1967) and Jackson (1997) derived mass and momentum equations for fluid-solid [1] systems by the use of a formal mathematical definition of local mean variables to translate the point Navier-Stokes equations for the fluid and the Newton's equation of motion

[1] fluid-solid here refers to gas-solid and liquid-solid systems

Table 2.1: *Governing momentum equations applied to mono-component gas-solid flow according to Jackson (2001)*

Continuity equations
$$\frac{\partial \varepsilon}{\partial t} + \nabla \cdot \left(\varepsilon \langle \boldsymbol{u} \rangle^f \right) = 0$$ $$\frac{\partial \phi}{\partial t} + \nabla \cdot \left(\phi \langle \boldsymbol{u} \rangle^s \right) = 0$$
Momentum Equations of Jackson (1997)
$$\rho_f \left[\frac{\partial \varepsilon}{\partial t} + \nabla \cdot \left(\varepsilon \langle \boldsymbol{u} \rangle^f \langle \boldsymbol{u} \rangle^f \right) \right] = \nabla \cdot \mathfrak{T}^f - n \left\langle \boldsymbol{f}^f \right\rangle + \varepsilon \rho_f \boldsymbol{g}$$ $$\rho_s \left[\frac{\partial \phi}{\partial t} + \nabla \cdot \left(\phi \langle \boldsymbol{u} \rangle^s \langle \boldsymbol{u} \rangle^s \right) \right] = \nabla \cdot \mathfrak{T}^s + n \left\langle \boldsymbol{f}^f \right\rangle + \phi \rho_s \boldsymbol{g}$$
Fluid and Solid phase stress tensors
$$\mathfrak{T}^f = - \langle p \rangle^f \boldsymbol{I} + \mu_f \left[\nabla \langle \boldsymbol{u} \rangle^f + \left(\nabla \langle \boldsymbol{u} \rangle^f \right)^T \right] + \left(\kappa_f - \frac{2}{3} \mu_f \right) \nabla \cdot \langle \boldsymbol{u} \rangle^f \boldsymbol{I}$$ $$\mathfrak{T}^s = - \langle p \rangle^s \boldsymbol{I} + \mu_s \left[\nabla \langle \boldsymbol{u} \rangle^s + \left(\nabla \langle \boldsymbol{u} \rangle^s \right)^T \right] + \left(\kappa_s - \frac{2}{3} \mu_s \right) \nabla \cdot \langle \boldsymbol{u} \rangle^s \boldsymbol{I}$$
Fluid-particle interaction force
$$n \left\langle \boldsymbol{f}^f \right\rangle = - \phi \nabla \langle p \rangle^f + \beta \left(\langle \boldsymbol{u} \rangle^f - \langle \boldsymbol{u} \rangle^s \right)$$

for a single particle directly into continuum equations. The point variables are averaged over regions large with respect to the particle diameter but small with respect to the characteristic dimension of the complete system. The continuity and averaged momentum equations for the fluid phase and solid phases are reported in Table 2.1. The proposed equations of change, as it is well known, are not mathematically closed and necessitate empirical closures for contributions mainly related to the stress tensors associated to each phase and to the fluid-particle interaction force.

2.2.1.1 Fluid stress tensor

A first approximation commonly employed for closure of the effective stress tensors (fluid and solid) is to assume a Newtonian behaviour for each continuum, albeit there are clear indications that such a view is over simplistic (Jackson, 2001). In this approach the effective stress tensor for the fluid phase, $\mathcal{T}^f$, takes the form as given in Table 2.1. The closure problem reduces to finding appropriate constitutive expressions for the pressure $\langle p \rangle$, the shear viscosity μ and the dilatational viscosity κ pertaining to each phase. The fluid is usually considered incompressible, accordingly its pressure need not be specified constitutively; moreover, μ_f is often assumed to be constant and κ_f entirely neglected. Thus, the problem simplifies to specifying values for the pressure of the fluid and the fluid viscosity.

2.2.1.2 Fluid particle interaction force

The resultant force exerted by the fluid on the solid phase is termed the *fluid particle interaction force*, $n\langle \boldsymbol{f}^f \rangle$ (see Table 2.1). One contribution to this averaged force is the buoyancy whilst it is the generally agreed in literature (see Anderson & Jackson, 1967, Jackson, 1997, Fan & Zhu, 1998) that other contributors to this force are the drag force, which is dependent on the particle concentration and the resultant slip velocity $\langle \boldsymbol{u}^f \rangle - \langle \boldsymbol{u}^s \rangle$, the virtual mass, which is dependent on the concentration and the relative acceleration and the lift force which is a force that acts in a normal direction to the slip velocity $\langle \boldsymbol{u}^f \rangle - \langle \boldsymbol{u}^s \rangle$. Other contributors, which are usually neglected, include the Faxen force and a history dependent term analogous to the Basset force for the motion of an isolated particle (Jackson, 2001). However, in this work, attention has been restricted to the dominant contribution to these forces *i.e.* the drag force. The above approximation leads to the following form for the resultant force exerted by the fluid on the particle phase.

$$n\langle \boldsymbol{f}^f \rangle = -\phi \nabla \langle p \rangle^f + \beta \left(\langle \boldsymbol{u} \rangle^f - \langle \boldsymbol{u} \rangle^s \right) \tag{2.1}$$

The first term on the R.H.S of eq.(2.1), which is the isotropic part of the fluid phase stress tensor, $\mathfrak{T}^f$, shown in Table 2.1, is the buoyant force whilst the second term is the drag force being exerted by the fluid phase on the solid phase represented as the product of a drag coefficient, β, and resultant velocity,$\left(\langle \boldsymbol{u}^f \rangle - \langle \boldsymbol{u}^s \rangle\right)$. The buoyant force of a fluidized suspension is now briefly discussed, this is followed by an assessment of the relations for the drag coefficient for mono-component systems.

2.2.1.3 Buoyancy

There exists a major disagreement in literature concerning the correct representation of the buoyant force in a fluidized bed. The conventional formula eq. (2.2) advocated for example by Clift et al. (1987), Clift (1993), Jean & Fan (1992), is simply the force experienced by the particle under static conditions (no flow):

$$f_b = \nabla \langle p \rangle^f V \quad ; \quad \nabla \langle p \rangle^f = -\rho_f g \tag{2.2}$$

where the density of the fluid is given by ρ_f and V is the volume of the fluid displaced (equivalent to the volume of the particle). However, under equilibrium conditions the pressure gradient has been argued (see Rietema & van den Akker, 1983, Gibilaro et al., 1985, Astarita, 1993, Gibilaro, 2001) to be a function of the bulk density of the *fluidized suspension*:

$$f_b = \nabla \langle p \rangle^f V \quad ; \quad \nabla \langle p \rangle^f = -\left(\rho_p (1-\varepsilon) + \rho_f \varepsilon\right) g \tag{2.3}$$

The implication of eq. (2.3) is that the *dynamic buoyancy* in the fluidized state is considerably greater than under static conditions. In the present author's view either of the alternative formulations is acceptable as long as the correct expressions for the drag force is used. Regarding the buoyancy as proportional to the pressure gradient of the fluidized bed suspension, requires that the *form drag*, which usually part of the drag force, be lumped with the *buoyant force*. While, regarding the buoyant force as *static* requires that the "non-static" pressure distribution contribution be lumped within the drag force. In this thesis, the initial

mono-component simulations have been performed using the *dynamic buoyancy* in line with Gibilaro (2001) has opposed to employing the *static buoyancy*.

2.2.1.4 Interphase Transfer Coefficient

The transfer of momentum between the fluid and solid phase is accounted for via the inter-phase transfer co-efficient, β (see Table 2.1). The interphase transfer drag models available in literature are either derived from the correlations for the drag coefficient for one particle in a suspension, C_D, or from the pressure drop per unit length in a suspension, $\Delta P/L$. The former approach takes the following form:

$$\beta = \frac{3}{4} C_D \frac{(1-\phi)\,\phi\,\rho_f \left|\langle \boldsymbol{u} \rangle^f - \langle \boldsymbol{u} \rangle^s\right|}{d_p} E \tag{2.4}$$

E in eq (2.4) is a correction coefficient introduced in order to take into account for the presence of high particle concentration in the bed. In Table 2.2, some of the drag models used in literature are reported. Wen & Yu (1966) proposed that the coefficient E is an exponential of the form, ε^p, where the power p assumes a value of – 2.65 over a whole range of fluidization. Gidaspow (1994) suggested the same value for p, but only for low Reynolds solid volume fractions *i.e.* $\phi \leq 0.2$. For $\phi \geq 0.2$ the Ergun (1952) equation is used. Di Felice (1994), instead suggested using $p = 2 - \gamma$, where γ is a function of the Reynolds number. Recently, Mazzei et al. (2006) proposed that the drag expression to be as follows:

$$\beta = \frac{3}{4} C_D \frac{\phi\,\rho_f \left|\langle \boldsymbol{u} \rangle^f - \langle \boldsymbol{u} \rangle^s\right|}{d_p} E \quad ; \quad E = \varphi(\varepsilon, Re) \quad ; \quad \varphi(\varepsilon, Re) = \frac{C_D^*}{C_D} \varepsilon^{2(1-n)} \tag{2.5}$$

where C_D^* is the drag coefficient based on the dimensionless Richardson & Zaki (1954a) relation. Di Felice (1988b) derived an alternative form for the pressure drop per unit length in a suspension similar to the Ergun (1952) equation. The expression is applicable for both

fixed and fluidized beds and is expressed as the following:

$$\beta = \left[\left(\frac{17.3}{Re}\right)^{\alpha} + (0.336)^{\alpha}\right]^{\frac{1}{\alpha}} \frac{\rho_f \left|\langle \boldsymbol{u}\rangle^f - \langle \boldsymbol{u}\rangle^s\right| \phi}{d_p} \varepsilon^{-1.8} \tag{2.6}$$

where d_p is the diameter of the particle. The Reynolds number and the exponent α are given by:

$$Re = \frac{\rho_f \varepsilon \left|\langle \boldsymbol{u}\rangle^f - \langle \boldsymbol{u}\rangle^s\right| d_p}{\mu_f} \quad ; \quad \alpha = 2.55 - 2.1\left[\tanh(20\,\varepsilon - 8)^{0.33}\right]^3 \tag{2.7}$$

Eq. (2.6) is used later in this work (see Chapter 4) to develop a constitutive expression for the fluid particle interaction force in a binary mixture. Many of the models proposed lead to different predictions for the interphase transfer coefficient (see Ergun, 1952, Wen & Yu, 1966, Di Felice, 1994, Gidaspow, 1994, Chen et al., 1999). In the initial analysis in this work the drag function advanced by Di Felice (1994) together with the drag coefficient by DallaValle (1948) has been employed.

2.2.1.5 Solid stress tensor

As mentioned, the complexity of describing the solid stress tensor, $\mathcal{T}^s$, is reduced by assuming that continuum is Newtonian, such that the tensor is related to the particle average velocity field $\langle \boldsymbol{u}^s\rangle$. The stress tensor is expressed as the form shown in Table 2.1 and reported here again for convenience.

$$\mathcal{T}^s = -\langle p\rangle^s \boldsymbol{I} + \mu_s\left[\nabla\langle \boldsymbol{u}\rangle^s + (\nabla\langle \boldsymbol{u}\rangle^s)^T\right] + \left(\kappa_s - \frac{2}{3}\mu_s\right)\nabla\cdot\langle \boldsymbol{u}\rangle^s \boldsymbol{I} \tag{2.8}$$

Closure for the tensor then requires only expressions for the scalar quantities $\langle p\rangle^s, \mu_s, \kappa_s$. There are three main strategies, reported in the literature, for the closure of the solids shear stress tensor for mono-component systems. **1)** The first method is the "traditional approach" in which closure of the solids normal stress $\langle p\rangle^s \boldsymbol{I}$ is based on the particle properties and the local voidage, whilst the viscous shear contribution μ_s is ignored or accounted for via theoretical mixture viscosity models. **2)** The second closure used is based on the Granular Kinetic Theory (GKT)which is derived from the kinetic theory of gases (Chapman & Cowling,

Table 2.2: *Examples of Drag Models Proposed in Literature*

Wen & Yu (1966)

$$\beta = \frac{3}{4} C_D \frac{(1-\phi)\,\phi\,\rho_f \left|\langle \boldsymbol{u} \rangle^f - \langle \boldsymbol{u} \rangle^s\right|}{d_p} \varepsilon^{-2.65}$$

with C_D given by Rowe (1961)

$$C_D = \begin{cases} \dfrac{24}{Re_p (1-\phi)} \left[1 + 0.15 \left((1-\phi) Re_p\right)^{0.687}\right] & \text{if } (1-\phi)\, Re_p < 1000 \\ 0.44 & \text{if } (1-\phi)\, Re_p \geq 1000 \end{cases}$$

$$Re_p = \frac{\rho_f \varepsilon \left|\langle \boldsymbol{u} \rangle^f - \langle \boldsymbol{u} \rangle^s\right| d_p}{\mu_f}$$

Gidaspow (1994) applied the Ergun (1952) equation for higher volume fractions

$$\beta = \begin{cases} 150 \dfrac{\phi^2 \mu_f}{(1-\phi)\, d_p^2} + \dfrac{7}{4} \dfrac{\phi \rho_f \left|\langle \boldsymbol{u} \rangle^f - \langle \boldsymbol{u} \rangle^s\right|}{d_p} & \text{if } \phi > 0.2 \\ \beta = \dfrac{3}{4} C_D \dfrac{(1-\phi)\,\phi\,\rho_f \left|\langle \boldsymbol{u} \rangle^f - \langle \boldsymbol{u} \rangle^s\right|}{d_p} \varepsilon^{-2.65} & \text{if } \phi \leq 0.2 \end{cases}$$

Di Felice (1994)

$$\beta = \frac{3}{4} C_D \frac{(1-\phi)\,\phi\,\rho_f \left|\langle \boldsymbol{u} \rangle^f - \langle \boldsymbol{u} \rangle^s\right|}{d_p} \varepsilon^{2-\gamma}$$

$$\gamma = 3.7 - 0.65 e^{\left(-\frac{\left[1.5 - \log\left(\varepsilon Re_p\right)\right]^2}{2}\right)}$$

with C_D given by DallaValle (1948):

$$C_D = \left(0.63 + 4.8\, Re_p^{-0.5}\right)^2$$

1970). **3)** The third approach is a combined *hybrid* approach that involves the use of frictional models together with the GKT model to account for the solid pressure and viscous shear stress. These models can be combined either additively, via a switching transition or a vie smooth transition. A brief description of the above mentioned strategies follows.

1 Exponential Equation

In this approach the solid normal stress is accounted for via a compaction modulus, $\mathscr{E}$, which is a function of the local voidage, ε. The main effect of the compaction modulus is only to prevent the particulate phase from becoming too densely packed and thus only becomes of numerical significance when the fluid voidage goes below the minimum fluidization voidage. The two main types of expressions used by researchers for this expression are shown in eq. (2.9) and (2.10).

$$-\nabla \langle p \rangle^s = G(\varepsilon) \cdot \nabla \varepsilon \tag{2.9}$$

$$\text{where } G(\varepsilon) = \begin{cases} -10^{B_1 \varepsilon + B_2} \\ e^{-\mathscr{E}(\varepsilon - \varepsilon^{\perp})} \end{cases} \tag{2.10}$$

where $\varepsilon^{\perp}$ is the compaction gas volume fraction, B_1 and B_2 are empirical numerical constants whose values differ in literature. Some values of B_1 and B_2 reported in literature are shown in Table 2.3 below. An overview of different models for $G(\varepsilon)$ has been given by Massoudi et al. (1992).

Table 2.3: *Empirical constants for Eq.*(2.9)

$G(\varepsilon) = -10^{B_1 \varepsilon + B_2}$		
B_1	B_2	Source
−9.76	7.8	Shih et al. (1987)
−10.46	6.577	Ettehadieh et al. (1984)
−8.76	5.43	Gidaspow & Ettehadieh (1983)
$G(\varepsilon) = e^{-\mathscr{E}(\varepsilon - \varepsilon^{\perp})}$		
$\mathscr{E}$	$\varepsilon^{\perp}$	Source
20	0.62	Gidaspow & Ettehadieh (1983)
600	0.376	Bouillard et al. (1989)

2 Granular Kinetic Model

Its description is provided by the kinetic theory (Gidaspow, 1994) which is analogous to

Table 2.4: *The Constitutive equations for the Granular Kinetic Theory (GKT) used in the closure of the Solid Stress Tensor*

Solid Pressure	$\langle p \rangle^s = \phi \rho_s \Theta_s \left(1 + 2 g_o \phi \left(1 + e_s\right)\right)$
Bulk viscosity	$\kappa_s = \frac{4}{3} \phi \rho_s d_p g_o \left(1 + e_s\right) \left(\frac{\Theta_s}{\pi}\right)^{0.5}$
Shear viscosity	$\mu_s = \frac{4}{5} \phi \rho_s d_p g_o \left(1 + e_s\right) \left(\frac{\Theta_s}{\pi}\right)^{0.5} + \frac{\frac{10 \pi^{0.5}}{96} \rho_s d_p \Theta_s^{0.5}}{\left(1 + e_s\right) \phi g_o} \left[1 + \frac{4}{5} g_o \phi \left(1 + e_s\right)\right]^2$
Radial distribution function	$g_o = \frac{3}{5} \left[1 - \left(\frac{\phi}{\phi^{max}}\right)^{1/3}\right]^{-1}$
Granular temperature balance	$\gamma_{\Theta_s} = \mathfrak{T}^s : \nabla \langle \boldsymbol{u} \rangle^s$
Dissipation of granular energy	$\gamma_{\Theta_s} = 3 \left(1 - e^2\right) g_o \phi^2 \rho_s \Theta \left[\frac{4}{d_p} \sqrt{\frac{\Theta}{\pi}} - \nabla \cdot \langle \boldsymbol{u} \rangle^s\right]$

the gas kinetic theory (Chapman & Cowling, 1970), here the normal stresses are said to originate from particle streaming (kinetic contribution) and direct collisions (collisional contribution). The thermodynamic temperature of the gases, the granular temperature, Θ_s, is introduced to describe the kinetic energy associated with the particle fluctuations, $\left\langle \boldsymbol{u}'^2_s \right\rangle$:

$$\frac{3}{2} \Theta_s = \frac{1}{2} \left\langle \boldsymbol{u}'^2_s \right\rangle \tag{2.11}$$

Since the effective stress tensor is dependent upon the magnitude of the particle fluctuations a balance of the granular temperature associated with this fluctuation is also required, this is given by eqn. (2.12):

$$\frac{3}{2} \left[\frac{\partial}{\partial t} \left(\phi \rho_s \Theta\right) + \nabla \cdot \left(\phi \rho_s \Theta \langle \boldsymbol{u} \rangle^s\right)\right] = \mathfrak{T}^s : \nabla \langle \boldsymbol{u} \rangle^s - \nabla \cdot \left(\kappa_s \nabla \Theta\right) - \gamma_{\Theta_s} - J_s \tag{2.12}$$

where the first term on the right hand side represents the creation of fluctuating energy due to shear stress in the solid phase, the second term stands for the diffusion of fluctuating energy along gradients in Θ; γ_{Θ_s} represents the dissipation due to inelastic particle-particle collisions and J_s stands for the dissipation or creation of granular energy resulting from the working of the fluctuating force exerted by the gas through the fluctuating velocity of the particles. In the numerical implementation of the GKT model, within the commercial CFD code used in this work (CFX4.4), the granular energy is assumed to be in a steady state and the convection and diffusion terms are neglected. Thus,Eq (2.12) results in an algebraic form expressed as:

$$\gamma_{\Theta_s} = \mathfrak{T}^s : \nabla\langle \boldsymbol{u} \rangle^s \tag{2.13}$$

The algebraic balance eqn. (2.13) is then appended to the continuity and momentum equations (van Wachem et al., 1999) shown in Table 2.1. Table 2.4 summaries the equations that describe the solid phase stress tensor and the quantities required for the calculation of the solids phase pressure and viscosities used in this work. The coefficient of restitution, e_s, shown in Table 2.4, is used to account for the inelasticity of the solid phase (where $0 < e_s < 1$). It should be noted here that a value of 0.9 was used in this work. g_o, represents the radial distribution function which allows for the tight control of the solid volume fraction, so that the maximum packing is not exceeded; the expression by Gidaspow (1994) is employed in this work. The solids pressure term $\langle p \rangle^s$ stands for the solid phase normal stresses due to particle-particle interactions. The solids bulk viscosity, κ_s describes the resistance of the particle suspension against compression, this term was neglected in the numerical implementation in this work.

3 Hybrid Modelling

At high solid volume fraction concentrations the transmission of stresses in dense gas-solid fluidized beds occurs increasingly via points of mutual contact between the particles. The way in which these stresses are transmitted could take the form of *long or short duration* contact forces. The former contact force dominates in the limit, where the concentration of particles is sufficiently high and particles are in semi-permanent contact with each other, *i.e.*

when there is zero fluidizing gas flow. Continuum frictional models which are often empirical in origin are commonly employed in the description of the solid stresses in this *slow deformation flow* regime. The latter contact force becomes more relevant in the limit where the assembly of particles is widely spaced and in vigorous motion, *i.e.* when the fluidizing gas is turned on above minimum fluidization. In this regime particle collisions are caused by bubble motion, the kinetic theory of granular flow provides an adequate description for the solid stresses in this *rapid flow* regime. Unfortunately there are no satisfactory constitutive models that span the intermediate situation between the two extreme limits presented above. Present research has focused on accounting for the intermediate situation through *ad hoc* methods. Savage (1982) for instance suggested the simple solution of adding the results of stresses predicted by the two limiting cases. In this method the frictional (normal and shear) stress is added on to the stress predicted by a rapid flow model for $\phi > \phi^{min}$ where ϕ^{min} is the solid volume fraction when frictional stresses become important.

$$\langle p \rangle^s = \begin{cases} \langle p \rangle^s_\Theta + \langle p \rangle^s_{fric} & \text{if } \phi > \phi^{min} \\ \langle p \rangle^s_\Theta & \text{if } \phi < \phi^{min} \end{cases} \quad ; \quad \mu_s = \begin{cases} \mu_s^\Theta + \mu_s^{fric} & \text{if } \phi > \phi^{min} \\ \mu_s^\Theta & \text{if } \phi < \phi^{min} \end{cases} \tag{2.14}$$

This approach was adopted by Johnson & Jackson (1987), Ocone et al. (1993), van Wachem et al. (1998), Syamlal et al. (1993). Johnson & Jackson (1987) reported some success with using this method in the prediction of the behaviour of granular materials in plane shear. van Wachem et al. (1998) used this approach to successively simulate the bubbling phenomena of Geldart group B particles. A switching mechanism is another approach which is employed by researchers to account for the solid stress in the intermediate flow regime. This method involves switching from a *rapid flow* model to a *slow deformation* frictional model by selecting the maximum of the two acting shear stresses, *i.e.* max $|\mu_s^\Theta, \mu_s^{fric}|$ for $\phi \geq \phi^{min}$. The value of ϕ^{min} is usually around 0.5.

$$\mu_s = \begin{cases} \max |\mu_s^\Theta, \mu_s^{fric}| & \text{if } \phi \geq \phi^{min} \\ \mu_s^\Theta & \text{if } \phi < \phi^{min} \end{cases} \tag{2.15}$$

The only apparent problem with this methodology is the discontinuous transition from a rapid flow model to a slow deformation model. Recent work by Tardos et al. (2003) has rectified this situation by the development of a *slow and intermediate* deformation model for the frictional shear stress. The model has recently been employed by Makkawi & Ocone (2006) to model gas-solid flow in a horizontal duct. In their model they employed the switching mechanism in the transition from a rapid flow model to a *slow and intermediate* deformation model. Results from their simulation showed good qualitative agreement with corresponding experimental results over the whole range of horizontal gas-solid flow behaviour. Table 2.5 shows a summary of constitutive frictional expressions commonly used in literature.

Table 2.5: *Frictional Models commonly applied in literature*

Johnson & Jackson (1987) $$\langle p \rangle^s_{fric} = \mathrm{Fr}\,\frac{\left(\phi - \phi^{min}\right)^n}{(\phi - \phi^{max})^p}$$ Coulomb (1776) $$\mu_s^{fric} = \langle p \rangle^s_{fric} \sin\psi$$
Syamlal et al. (1993)
$$\langle p \rangle^s_{fric} = A\left(\phi - \phi^{min}\right)^n$$ $$\mu_s^{fric} = \frac{\langle p \rangle^s_{fric} \cdot \sin\psi}{\phi\sqrt{\frac{1}{6}\left(([\nabla \times \langle \boldsymbol{u} \rangle^s]_z)^2 + \left(\nabla \langle \boldsymbol{u} \rangle^s_y\right)^2 + (\nabla \langle \boldsymbol{u} \rangle^s_x)^2 - \frac{1}{4}([\nabla \times \langle \boldsymbol{u} \rangle^s]_z)^2\right)}}$$ $$A = 10^{25}\,;\; n = 10\,;\; \phi^{min} = 0.59\,;\; \psi = 25°$$
Tardos et al. (2003)
$$\mu_s^{fric} = \langle p \rangle^s_{fric} \sin\psi \tanh\left(\frac{a\sqrt{\pi}}{2}\right)$$ $$a = \frac{(\nabla \langle \boldsymbol{u} \rangle^s \cdot \boldsymbol{j})\,\boldsymbol{j}}{2\sqrt{2}\sigma} \quad ; \quad \sigma = \frac{\sqrt{\Theta}}{4 d_p}$$

The values of the empirical constants in the expression by Johnson & Jackson (1987) and Coulomb (1776) are summarized in Table 2.6:

Table 2.6: *The values for emprical parameters for frictional models shown in Table 2.5 as suggested by various researchers (van Wachem, 2000)*

Fr $[N/m^2]$	n	p	ϕ^{min}	ψ	d_p $[\mu\, m]$	ρ_s $[kg/m^3]$	material
0.05	2	3	0.5	28°	150	2500	unknown[1]
$3.65 \cdot 10^{-32}$	0	40	-	25°	1800	2980	glass[2]
$4.0 \cdot 10^{-32}$	0	40	-	25°	1000	1095	polystrene[2]
0.05	2	5	0.5	28.5°	1000	2900	glass[2]

Sources: Ocone et al. (1993)[1]
Johnson & Jackson (1987)[2]

2.2.2 The Particle Bed Model- An Alternative Eulerian-Eulerian Model Approach

The Particle Bed Model (PBM) orginated from a study of fluidized bed stability based on the stability theory of Wallis (1969). The model predicts the transition between homogenous and bubbling fluidization by comparing the propagation velocities of kinematic and dynamic one dimensional waves through the fluidized bed, u_K and u_D respectively. A kinematic wave, u_K, is a velocity disturbance caused by an increase of the superficial gas velocity which moves up in the bed. A dynamic wave, u_D on the other hand, occurs when a net force on a flowing material is produced by a concentration gradient, thus accelerating the material through the wave. Foscolo & Gibilaro (1984) assumed that in homogeneous fluidization, where the fluidized bed is assumed to be stable, the mechanism of propagation of void disturbances across the bed can be considered similar to pressure wave propagation in a compressible fluid. The inference led to the consideration of the particle phase as an *elastic* fluid, which is capable of opposing deformation. Following the approach of Verloop & Heertjes (1970) based on Wallis (1969) theory, Foscolo & Gibilaro (1984) developed a model to predict the voidage at the onset of bubbling, ε_{mb} in a fluidized bed and they expressed their stability

criterion as follows:

$$\left[\frac{g\,d_p\,(\rho_s-\rho_f)}{u_t^2\,\rho_s}\right]^{0.5} - 0.56\,n\,(1-\varepsilon_{mb})^{0.5}\varepsilon_{mb}^{n-1} = \left\{\begin{matrix}\text{positive, stable}\\ \text{negative, unstable}\end{matrix}\right\} \qquad (2.16)$$

where n ia an exponent that depends on the fluid dynamic regime (*i.e.* $n \approx 4.8$ in the *viscous* regime, $n \approx 2.4$ in the *inertial* regime). Foscolo & Gibilaro (1984) and Gibilaro et al. (1985) obtained a resonable agreement between theoretical predictions from eq. (2.16) and experimental data available at ambient and high pressure conditions. The model was described through one-dimensional equations by Foscolo & Gibilaro (1987) and applied in linearized form to carry out the stabilty analysis mentioned above. An extension to two dimensions was formulated by Chen et al. (1999), who presented a full set of mass and momentum balance equations for describing the gas solid flow. In the original model, Foscolo & Gibilaro (1987) assumed a *total primary force* exerted by the fluid on a single particle as being composed of the effective weight (gravitational force minus the *dynamic* buoyancy) and the drag force. This total force is in fact the sum of the fluid-particle interaction force and gravitational term.

$$n\langle \boldsymbol{f}^{\mathcal{P}_\mathcal{F}}\rangle = n\langle \boldsymbol{f}^{f}\rangle + \varepsilon\rho_f\,\boldsymbol{g} \qquad (2.17)$$

They also introduced an additional term in the solid phase momentum equation, the so called *Elastic force*, see eq. (2.31), which expresses the functional dependence of the fluid particle interaction force on the bed voidage under non-steady state and non-equilibrium conditions. The force was assumed to act only in the direction parallel to the drag force. In this thesis, concepts from the Particle Bed Model are employed in deriving a model for binary systems. Thus, It is deemed necessary to present the mathematical formalism behind the elastic force. The assumptions of Foscolo & Gibilaro (1987) can be elucidated as follows:

Under Steady state conditions:

$$n\langle \boldsymbol{f}^{\mathcal{P}_\mathcal{F}}\rangle = \varsigma\left\{U_o(t)\,,\,U_p(z,t),\varepsilon(z,t)\right\} \qquad (2.18)$$

where U_o and U_p refer to the superficial fluid and particle velocities repectively. ς is representative of consitutive expressions for the total force acting on the particle volume. Here, z refers to the axial direction. In non-equilibrium conditions eq. (2.18) can be modified to the following expression (Gibilaro, 2001):

Under non-Steady state conditions:

$$n\langle f^{\mathcal{P}_\mathcal{F}}\rangle^+ = \varsigma\left\{U_o(t)\ ,\ U_p(z\ ,\ t)\ ,\varepsilon(z-\theta\ ,\ t)\right\} \tag{2.19}$$

The above equation simply means that in non-equilibrium conditions the total primary force is only a function of the voidage perturbation wave in the, z, vertical direction where θ represents the penetration distance in the axial direction measured downwards from the particle center. This finite region of influence must be preserved so that the ability of a particle to respond to an approaching concentration pertubation is not lost. A few authors have argued about the validity of the above dependency in eq.(2.19), Joseph (1990) for instance argues that eqn.(2.19) should be modified to take into consideration changes in the local particle velocity, U_p, in this case eqn.(2.19) would become:

$$n\langle f^{\mathcal{P}_\mathcal{F}}\rangle^+ = \varsigma\left\{U_o(t)\ ,\ U_p(z-\theta\ ,\ t)\ ,\varepsilon(z-\theta\ ,\ t)\right\} \tag{2.20}$$

Indeed changes in the local particle acceleration was noted by Gibilaro (2001) and deemed negligable. The penetration distance expression according to Gibilaro (2001) is given by:

$$\theta = \frac{2}{3}.d_p \tag{2.21}$$

Since θ represents a differential length in the z direction, we can write:

$$\left(\frac{\partial\varsigma}{\delta\varepsilon}\right)_{U_o,U_p} = \frac{\varsigma\left[U_o(t),U_p(z,t),\varepsilon(z\ ,\ t)\right]-\varsigma\left[U_o(t),U_p(z\ ,\ t),\varepsilon(z-\theta,t)\right]}{\varepsilon(z\ ,\ t)-\varepsilon(z-\theta,t)} \tag{2.22}$$

Eq. (2.22) can be rewritten as:

$$n\left(\frac{\partial\langle f^{\mathcal{P}_\mathcal{F}}\rangle}{\partial\varepsilon}\right)_{U_o,U_p} = \frac{n\langle f^{\mathcal{P}_\mathcal{F}}\rangle\left[U_o,U_p,\varepsilon\right] - n\langle f^{\mathcal{P}_\mathcal{F}}\rangle^{+}\left[U_o,U_p,\varepsilon\right]}{\varepsilon(z,t)-\varepsilon(z-\theta,t)} \tag{2.23}$$

Re-arranged to obtain the following relationship:

$$n\langle f^{\mathcal{P}_\mathcal{F}}\rangle^{+}\left[U_o,U_p,\varepsilon\right] = n\langle f^{\mathcal{P}_\mathcal{F}}\rangle\left[U_o,U_p,\varepsilon\right] - \left[\varepsilon(z,t)-\varepsilon(z-\theta,t)\right] n\left(\frac{\partial\langle f^{\mathcal{P}_\mathcal{F}}\rangle}{\partial\varepsilon}\right)_{U_o,U_p} \tag{2.24}$$

Eq. (2.24) can be can further modified by noting the following relationship:

$$\left(\frac{\partial\varepsilon}{\partial z}\right)_t = \frac{\varepsilon(z,t)-\varepsilon(z-\theta,t)}{\theta} \tag{2.25}$$

Substituing eq. (2.25) into eq.(2.24) we obtain:

$$n\langle f^{\mathcal{P}_\mathcal{F}}\rangle^{+}\left[U_o,U_p,\varepsilon\right] = n\langle f^{\mathcal{P}_\mathcal{F}}\rangle\left[U_o,U_p,\varepsilon\right] - \theta\left(\frac{\partial\varepsilon}{\partial z}\right)_t \cdot n\left(\frac{\partial\langle f^{\mathcal{P}_\mathcal{F}}\rangle}{\partial\varepsilon}\right)_{U_o,U_p} \tag{2.26}$$

From eq. (2.26), the Elastic force in the axial direction, is given by:

$$n\langle f^{e}\rangle = -\theta\left(\frac{\partial\varepsilon}{\partial z}\right)_t \cdot n\left(\frac{\partial\langle f^{\mathcal{P}_\mathcal{F}}\rangle}{\partial\varepsilon}\right)_{U_o,U_p} \tag{2.27}$$

The elastic force was expressed as the scalar product of the *elastic modulus*, E, and the gradient of voidage in the vertical direction in the original model (Foscolo & Gibilaro, 1987). The elastic modulus is given by the substitution of θ into eq. (2.27) and subsequently multiplying it by the number of particles per unit volume, n. The above manipulation gives:

$$E = -\frac{4\cdot(1-\varepsilon)}{\pi\cdot d_p^2}\cdot\left(\frac{\partial\langle f^{\mathcal{P}_\mathcal{F}}\rangle}{\partial\varepsilon}\right)_{U_o,U_p} \quad ; \quad n = \frac{6(1-\varepsilon)}{\pi d_p^3} \tag{2.28}$$

Foscolo & Gibilaro (1987) in their work adpoted the following form for $\langle f^{\mathcal{P}_\mathcal{F}}\rangle$:

$$\langle f^{\mathcal{P}_\mathcal{F}}\rangle = \frac{\pi d_p^3}{6}\left[\left(\rho_p-\rho_f\right) g\left(\frac{U_o-U_p}{U_t}\right)^{\frac{4.8}{n}}\varepsilon^{-3.8} - \frac{\partial p}{\partial z} - \rho_s g\right] \tag{2.29}$$

where U_t is the terminal velocity of the particle. In obtaining the derivative of the primary force function with respect to ε, Foscolo & Gibilaro (1987) made the following approximations to eq. (2.29)

$$-\frac{\partial p}{\partial z} \approx -\rho_{sp} g \quad ; \quad \left(\frac{U_o - U_p}{U_t}\right)^{\frac{4.8}{n}} \approx \varepsilon^{4.8} \tag{2.30}$$

which lead them to the following expression for the *elastic modulus*:

$$E = 3.2\, g\, d_p\, (1-\varepsilon)\left(\rho_s - \rho_f\right) \tag{2.31}$$

The momentum equations of Foscolo & Gibilaro (1987) can be summarised as:

$$\rho_f\left[\frac{\partial}{\partial t}\left(\varepsilon \langle \boldsymbol{u}\rangle^f\right) + \nabla\cdot\left(\varepsilon \langle \boldsymbol{u}\rangle^f \langle \boldsymbol{u}\rangle^f\right)\right] = \varepsilon \nabla\langle p\rangle^f - n\left\langle \boldsymbol{f}^f\right\rangle + \varepsilon\rho_f \boldsymbol{g} \tag{2.32}$$

$$\rho_s\left[\frac{\partial}{\partial t}\left(\phi \langle \boldsymbol{u}\rangle^s\right) + \nabla\cdot\left(\phi \langle \boldsymbol{u}\rangle^s \langle \boldsymbol{u}\rangle^s\right)\right] = -E\ (\nabla\varepsilon\cdot\boldsymbol{k})\,\boldsymbol{k} + n\left\langle \boldsymbol{f}^f\right\rangle + \phi\rho_s \boldsymbol{g} \tag{2.33}$$

The fluid-solid interaction force, $n\left\langle \boldsymbol{f}^f\right\rangle$, is assumed to be the sum of the fluid pressure gradient acting on the solid phase and the drag force, expressed in terms of the interphase transfer coefficient, β, and the relative velocity.

$$n\left\langle \boldsymbol{f}^f\right\rangle = -\phi\nabla\langle p\rangle^f + \beta\left(\langle \boldsymbol{u}\rangle^f - \langle \boldsymbol{u}\rangle^s\right) \quad ; \quad \nabla\langle p\rangle^f = -\left(\rho_p\,(1-\varepsilon) + \rho_f\varepsilon\right) g \tag{2.34}$$

From eq. (2.34) it can be observed that Foscolo & Gibilaro (1987) appended the *Elastic Force* to the solid phase momentum equation. They described the elastic force as being analogous to the solid pressure term, $\langle p\rangle^s$, to account for the *the transfer of momentum between particles*. No proper justification was offered for this step initally[2], however, Gibilaro (2001) later justified the addition of the elastic force in the particle phase momentum equation via *mathematical linearisation* considerations. [3].

[2]Although Gibilaro (2001) in his book does not refer to the elastic force as been analogous to the solid pressure. The force nevertheless still only features in the solid phase momentum equation in his book.

[3]More on the mathematical linearisation consideration can be found in pg 64-65 and 78-79 in the book by Gibilaro (2001).

2.2.2.1 A Revised formulation of the Particle Bed Model

Mazzei et al. (2006) re-analysed the original particle bed model by revising the equations of change partially and proposing new closure relationships for the drag force and the elastic force. The revised momentum equations are as follows:

$$\rho_f\left[\frac{\partial}{\partial t}\left(\varepsilon\langle\boldsymbol{u}\rangle^f\right)+\nabla\cdot\left(\varepsilon\langle\boldsymbol{u}\rangle^f\langle\boldsymbol{u}\rangle^f\right)\right]=\nabla\cdot\mathfrak{T}^f-n\left\langle\boldsymbol{f}^f\right\rangle+\varepsilon\rho_f\boldsymbol{g} \tag{2.35}$$

$$\rho_s\left[\frac{\partial}{\partial t}\left(\phi\langle\boldsymbol{u}\rangle^s\right)+\nabla\cdot\left(\phi\langle\boldsymbol{u}\rangle^s\langle\boldsymbol{u}\rangle^s\right)\right]=n\left\langle\boldsymbol{f}^f\right\rangle+\phi\rho_s\boldsymbol{g} \tag{2.36}$$

The fluid-solid interaction force is modified by excluding the pressure gradient term see eq. (2.37), thus the fluid pressure is no longer shared by the two phases in proportion to their volume fractions, but accounted for only in the fluid phase momentum equation. The elastic force is instead included as a contribution to the fluid solid interaction force so that the principle of action and reaction to which the force is subjected is fulfilled. The latter modification is also employed in this thesis for binary systems. The fluid-solid interaction force is given by:

$$n\left\langle\boldsymbol{f}^f\right\rangle=\beta\left(\langle\boldsymbol{u}\rangle^f-\langle\boldsymbol{u}\rangle^s\right)+E\left(\nabla\varepsilon\cdot\frac{n\left\langle\boldsymbol{f}^d\right\rangle}{\left|n\left\langle\boldsymbol{f}^d\right\rangle\right|}\right) \tag{2.37}$$

where $n\langle\boldsymbol{f}^d\rangle$ is the drag force per unit volume. The interphase transfer coefficient β is given by:

$$\beta=\frac{3}{4}C_D\frac{\left|\langle\boldsymbol{u}\rangle^f-\langle\boldsymbol{u}\rangle^s\right|\rho_f(1-\varepsilon)}{d_p}\varphi(\varepsilon,Re)\quad;\quad\varphi(\varepsilon,Re)=\frac{C_D^*}{C_D}\varepsilon^{2(1-n)} \tag{2.38}$$

where C_D^* is the drag coefficient based on the dimensionless Richardson & Zaki (1954a) relation. The Elastic Modulus, E is as follows:

$$E=-\frac{2}{3}d_p\Omega(\varepsilon,Re^*) \tag{2.39}$$

where Ω is a dimensionless constitutive function and Re^* is the Reynolds number based on the dimensionless Richardson & Zaki (1954a) relation (see Mazzei et al., 2006).

2.2.2.2 Solid Compaction Control

The particle-bed model, as developed, does not impose any restriction to the values of the solid volume fraction and thus initial CFD simulations of Geldart group B mono-component dense fluidized beds resulted in solids overpacking. Lettieri et al. (2003) found it was necessary to apply a correction mechanism in order to ensure that the condition of maximum packing was not exceeded and more realistic flow predictions could be achieved.

The justification for such a correction can be explained by noting that the solid phase is considered as a fluid and as such is able to fully occupy a given volume, with the solid volume fraction ranging from 0 to 1 (*i.e* < 1). Additionally, the particle bed model in its formulation does not explicitly account for the stresses internal to the solid phase.

Nevertheless, other authors (Gidaspow, 1994, Syamlal et al., 1993, Chen et al., 2003) have proposed numerical procedures for correcting the solids volume fraction when it exceeds the physical maximum packing limit. Syamlal et al. (1993) for instance proposed the addition of an extra equation for the correction of the solids volume fraction based on the assumption of a constitutive model for the solids pressure as a function of the solids volume fraction.

The solids volume fraction correction was derived by setting a transport equation for the correction term where the velocity field is expressed in terms of the extra solids pressure, which in turn is a function of the solids volume fraction correction term. The solids volume fraction correction equation is then solved numerically by means of an iterative procedure. The actual solids volume fraction and solids velocity are calculated after the solids volume fraction correction equation has been solved.

Chen et al. (2003) also proposed a similar approach, where the normal component of the internal stress arises above a limiting value for the solid volume fraction. Although their approach aims to mimic the same contacting phenomenon as proposed by Syamlal et al. (1993), the numerical procedure adopted was different. Chen et al. (2003) proposed an iterative procedure through which the solids contact pressure is introduced in the solids mo-

mentum balance equation at a certain time-increment and for a given grid-point, where the solids volume fraction is above the maximum packing limit. For that grid point, the solids volume fraction is set to the maximum packing limit and a first estimate of the solids pressure and its gradient is evaluated. The gas and solids velocity fields are then recalculated from the augmented momentum equations. The new values of the solids velocity and volume fraction are then substituted in the solids mass balance to satisfy the solid phase continuity. If the mass residual does not fall below a chosen value, an updated value of the solids pressure is calculated and the iterative procedure restarts from the computation of the gas and solid velocity fields.

However, the numerical algorithm used herein, *the excess volume correction algorithm*, works out a *posteriori* redistribution of the solid volume in excess for each computational cell. The redistribution of the solid volume in excess within each cell is carried out after each time step for cells where the solid volume fraction ϕ is greater than the maximum compaction value ϕ^{max} set by the user. The correction is expressed in terms of volume and not mass since the system is assumed incompressible. The redistribution of the excess volume, which is defined as $\phi^{ex} = \phi - \phi^{max}$, is in the form of an overall balance for the particle phase volume in each cell, where the over packing condition is detected. In a 2D computational domain with cells of equal size, the cell in question gives away its overall particle phase volume excess to the neighboring cells in equal parts, *i.e.* the excess divided by the number of neighboring cells, and in turn receives the relevant part of the excess coming from the neighbouring cells. The corrected value of the solid volume fraction in the cell is then computed on the basis of the value provided by the code and the net excess solid volume exchanged between the cell under exam and the neighbouring cells (see Fig.2.4). The balance may be expressed in terms of solid volume fraction, since all the cells have the same volume.

$$\phi_{i,j}^{new} = \phi_{i,j}^{old} - \phi_{i,j}^{ex} + \frac{\phi_{i+1,j}^{ex}}{4} + \frac{\phi_{i,j+1}^{ex}}{4} + \frac{\phi_{i-1,j}^{ex}}{4} + \frac{\phi_{i,j-1}^{ex}}{4} \tag{2.40}$$

The strength of this procedure is to correct numerically the solid volume fraction only when this is needed, without introducing any additional terms in the conservation equations that

could alter the physical modelling of the system. Since this correction takes place at every time step, its effectiveness is expected to increase by decreasing the time step interval. In this way, the correction will be kept as small as possible, thus preventing the correction from altering significantly the dynamics of the system. However, the smaller the computational time step interval, the longer the computational time required.

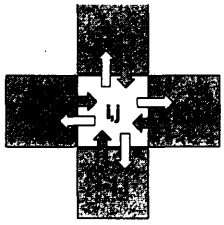

Figure 2.4: *Computational domain representation of excess volume correction, Lettieri et al. (2003)*

In this thesis, the original algorithm has been extended for the case of binary systems and is discussed later in Chapter 4.

2.3 Eulerian-Eulerian Modelling of Binary Systems

A mono-size system of particles seldom occurs in a fluidized bed of practical importance. Industrially operated fluidized beds typically consist of particles which have a wide size distribution as well as different densities. The phenomenon of mixing and segregation becomes of major importance in these non-ideal systems. A vast amount of experimental work has already been carried out by many authors looking at the behaviour of binary mixtures in gas-fluidized beds and in particular at the rate of segregation which they display (see Nienow et al., 1972, 1978, Nienow & Chessman, 1980, Marzocchella et al., 2000). The rate of segregation is often measured using the bed freeze test, where particles are taken from the fluidized bed layer by layer and sieved separately in order to measure the concentrations of different species (Wu & Baeyens, 1998). The computational modelling of binary systems, conversely, has not met with the same resounding success as that experienced in modelling mono-component systems. As mentioned earlier, the continuum modelling of binary mixtures is typically carried out using two approaches. The first is characterized by the use of

separate momentum equations to cater for each particle species whilst the second makes use of averaged mixture properties for the formulation of a mixture momentum equation coupled with the use of averaged constitutive relations.

The theoretical description of the internal particle stress associated with each of the above mentioned approaches has been primarily carried out through modifications to the granular energy balance, see eq. (2.12). A description of the internal stress based on the first approach was first advanced by Jenkins & Mancini (1989) this was followed by a contribution from Zamankhan (1995) who developed a kinetic theory for binary mixtures of spheres involving perturbations to the maxwellian velocity distribution. The aforementioned developments assume an equipartition of granular energy between the respective particle phases. This assumption as argued by Gidaspow et al. (1996) holds only for particulate systems where dissipative effects are absent. Gidaspow et al. (1996) went on to develop an extended version of the kinetic theory of dense gases for binary mixtures with an unequal granular temperature between the particle phases. This theory has recently been further extended by Iddir & Arastoopour (2005) to include a non-maxwellian velocity distribution. The theoretical description of the solid phase stress using the second approach has instead been pioneered by van Wachem et al. (2001). They extended the Granular kinetic theory (GKT) to binary mixtures by using a mixture granular balance within the framework of the two-fluid model for dense gas-solid flows.

The work presented in this thesis is primarily concerned with the modelling of non-cohesive binary fluidized suspensions of solid particles. The internal stress associated with the solid phases has been neglected and a new numerical algorithm has been developed to control local solid packing. The new numerical scheme is based on the algorithm for the *excess solid volume* correction originally developed by Lettieri et al. (2003) for mono-component systems presented earlier in § 2.2.2.2. A brief description of the modelling strategies discussed above follows.

2.3.1 Eulerian Modelling of Binary Systems using separate Momentum Equations

A summary of the mass and momentum equations which describe a binary system using separate momentum equations is shown in Table 2.7. The equations of change are an extension of those originally put forward by Anderson & Jackson (1967) and Jackson (1997) for systems of mono-size particles in Newtonian fluids, where the averaged equations of conservation for mass, linear and angular momentum where derived and phase interactions modelled phenomenologically. A detailed mathematical derivation of these equations is given later in Chapter 3.

Table 2.7: *Equations of Motion for a Binary System using separate momentum equations.*

Continuity Equation - Fluid Phase

$$\frac{\partial \varepsilon}{\partial t} + \nabla \cdot \left(\varepsilon \langle \boldsymbol{u} \rangle^{f} \right) = 0$$

Continuity Equation - Solid Phase k

$$\frac{\partial \phi_k}{\partial t} + \nabla \cdot \left(\phi_k \langle \boldsymbol{u} \rangle^{\mathscr{F}_k} \right) = 0$$

Momentum Equation - Fluid Phase

$$\rho_f \left[\frac{\partial}{\partial t} \left(\varepsilon \langle \boldsymbol{u} \rangle^{f} \right) + \nabla \cdot \left(\varepsilon \langle \boldsymbol{u} \rangle^{f} \langle \boldsymbol{u} \rangle^{f} \right) \right] = \nabla \cdot \mathfrak{T}^{f} - n_1 \left\langle \boldsymbol{f}^{f} \right\rangle^{\mathscr{F}_1} - n_2 \left\langle \boldsymbol{f}^{f} \right\rangle^{\mathscr{F}_2} + \varepsilon \rho_f \boldsymbol{g}$$

Momentum Equation - Solid Phase 1

$$\rho_1 \left[\frac{\partial}{\partial t} \left(\phi_1 \langle \boldsymbol{u} \rangle^{\mathscr{F}_1} \right) + \nabla \cdot \left(\phi_1 \langle \boldsymbol{u} \rangle^{\mathscr{F}_1} \langle \boldsymbol{u} \rangle^{\mathscr{F}_1} \right) \right] = \nabla \cdot \mathfrak{T}^{1} + n_1 \left\langle \boldsymbol{f}^{f} \right\rangle^{\mathscr{F}_1} + n_1 \langle \boldsymbol{f}^{p} \rangle^{\mathscr{F}_1} + \phi_1 \rho_1 \boldsymbol{g}$$

Momentum Equation - Solid Phase 2

$$\rho_2 \left[\frac{\partial}{\partial t} \left(\phi_2 \langle \boldsymbol{u} \rangle^{\mathscr{F}_2} \right) + \nabla \cdot \left(\phi_2 \langle \boldsymbol{u} \rangle^{\mathscr{F}_2} \langle \boldsymbol{u} \rangle^{\mathscr{F}_2} \right) \right] = \nabla \cdot \mathfrak{T}^{2} + n_2 \left\langle \boldsymbol{f}^{f} \right\rangle^{\mathscr{F}_2} - n_1 \langle \boldsymbol{f}^{p} \rangle^{\mathscr{F}_1} + \phi_2 \rho_2 \boldsymbol{g}$$

2.3.1.1 Closure Models

2.3.1.1.1 Fluid Particle Interaction force : The fluid-particle interaction force accounts for the resultant force which is exerted by the fluid on the particles of both phases. Most numerical models for binary systems available in literature only account for the force due to the pressure gradient of the fluid phase and the drag force. In this work this force is assumed to be made up of three contributions, namely: buoyant force, drag force and elastic force, see eq. (2.41) and eq. (2.42). Mono-component constitutive relations are often employed as closures for drag force in each phase $\mathscr{F}_k$. Mathiesen et al. (2000a) for instance used the Ergun (1952) equation for porosities up to 0.8 combined with the drag relation by Wen & Yu (1966) for higher porosities, see also Huilin et al. (2003) and Huilin & Gidaspow (2003).

$$n_k \left\langle \boldsymbol{f}^f \right\rangle^{\mathscr{F}_k} = n_k \langle \boldsymbol{f}^s \rangle^{\mathscr{F}_k} + n_k \left\langle \boldsymbol{f}^d \right\rangle^{\mathscr{F}_k} + n_k \langle \boldsymbol{f}^e \rangle^{\mathscr{F}_k} \tag{2.41}$$

$$n_k \left\langle \boldsymbol{f}^d \right\rangle^{\mathscr{F}_k} = \beta_k \left(\langle \boldsymbol{u} \rangle^f - \langle \boldsymbol{u} \rangle^{\mathscr{F}_k} \right) \tag{2.42}$$

2.3.1.1.2 Particle-Particle interaction force The use of separate momentum equations for each particulate phase in the modelling of binary mixtures requires an extra term to account for the collisions between particles that belong to different size classes. This "extra" contribution should be termed *particle-particle interaction force*, but is often referred to as *particle-particle drag force*. Indeed, strictly speaking, the two forces are not equivalent since the former might encompass several contributions of which the drag is just one. The earliest attempt to quantify the nature of this force was made by Soo (1967) where a derivation was given for the force acting on a single particle of species $\mathscr{F}_1$ in a cloud of colliding particles of species $\mathscr{F}_2$. This was followed by a similar development by Nakamura & Capes (1976). An experimentally related theoretical development was carried out by Arastoopour et al. (1982), where a semi-empirical expression was derived for dilute gas-solid systems. Several expressions have since been put forward by other authors (Gidaspow et al., 1985, Srinivasan & Doss, 1985, Syamlal, 1987b, Bell, 2000, Gera et al., 2004) with most correlations being variations of earlier pioneering developments. In general, the force is expressed as the product of a drag coefficient ζ and the relative slip velocity between the two solid

phases. A summary of the mathematical expressions for the particle-particle drag force models is given in Table. 2.8. In the Syamlal (1987b) correlation equation, the radial distribution function at contact g_o derived by Lebowitz (1964) is applied.

$$n_1 \langle f^p \rangle^{\mathscr{F}_1} = \zeta \left(\langle \boldsymbol{u} \rangle^{\mathscr{F}_2} - \langle \boldsymbol{u} \rangle^{\mathscr{F}_1} \right) = - n_2 \langle f^p \rangle^{\mathscr{F}_2} \tag{2.43}$$

2.3.1.1.3 Solid Stress Tensor A granular energy balance is usually employed by researchers for the description of the internal stress associated with each phase $\mathscr{F}_k$. The typical expression used in literature is shown in eq. (2.44) (see also Huilin et al., 2003, Huilin & Gidaspow, 2003, Mathiesen et al., 2000a, Iddir & Arastoopour, 2005, Gidaspow et al., 1996). The main drawback of this approach is that each species requires a closure for both the fluctuating particle velocities and the interactions between these fluctuating particle velocities as highlighted by Curtis & van Wachem (2004).

$$\frac{3}{2}\left[\frac{\partial}{\partial t}(\phi_k \rho_k \Theta_k) + \nabla \cdot \left(\phi_k \rho_k \Theta_k \langle \boldsymbol{u} \rangle^{\mathscr{F}_k}\right)\right] = \mathfrak{T}^k : \nabla \langle \boldsymbol{u} \rangle^{\mathscr{F}_k} - \nabla \cdot q - \gamma_{\Theta_k} - 3\beta_k \Theta_k \tag{2.44}$$

2.3.2 Eulerian Modelling of binary Systems using mixture momentum equations

In this approach the two fluid model is applied to describe the flow of the dense gas-solid binary mixture. Mixture continuity and momentum equations are employed in the description of the particle phase. The equations of change that describe the fluid and particle mixture are summarized in Table 2.9.

2.3.2.1 Closure Models

2.3.2.1.1 Fluid Particle Interaction force The drag force contribution is the only closure applied by researchers to describe the fluid particle interaction force using this approach (van Wachem et al., 2001). Drag models for mono-component systems are typ-

Table 2.8: *Particle-particle drag models used in this work.*

The indices 1 and 2 must be chosen so that the following condition holds: $d_1 \geqslant d_2$; Φ_1 and Φ_2 are the maximum values for ϕ_1 and ϕ_2 respectively.

Syamlal (1987b)

$$\zeta = \frac{3(1+e)\left(\frac{\pi}{2} + C_f \frac{\pi^2}{8}\right)\phi_1 \rho_1 \phi_2 \rho_2 (d_1 + d_2)^2 g_o}{2\pi\left(\rho_1 d_1^3 + \rho_2 d_2^3\right)} \left|\langle \boldsymbol{u} \rangle^{\mathscr{F}_1} - \langle \boldsymbol{u} \rangle^{\mathscr{F}_2}\right|$$

$$\text{where } g_o = \frac{1}{\varepsilon} + \frac{3}{\varepsilon^2} \frac{d_1 d_2}{(d_1 + d_2)} \left(\frac{\phi_1}{d_1} + \frac{\phi_2}{d_2}\right)$$

Bell (2000)

$$\zeta = \frac{2(1+e)\phi_1 \rho_1 \phi_2 \rho_2 (d_1 + d_2)^2 \left[1 + \frac{3}{4}\left(\frac{\phi_{12}^{max}}{\phi_1 + \phi_2}\right)^{1/3}\right]}{\left(\rho_1 d_1^3 + \rho_2 d_2^3\right)\left(\frac{\phi_{12}^{max}}{\phi_1 + \phi_2}\right)^{1/3}} \left|\langle \boldsymbol{u} \rangle^{\mathscr{F}_1} - \langle \boldsymbol{u} \rangle^{\mathscr{F}_2}\right|$$

Gidaspow et al. (1985)

$$\zeta = F(1+e) \frac{\phi_1 \rho_1 \phi_2 \rho_2 (d_1 + d_2)^2}{\rho_1 d_1^3 + \rho_2 d_2^3} \left|\langle \boldsymbol{u} \rangle^{\mathscr{F}_1} - \langle \boldsymbol{u} \rangle^{\mathscr{F}_2}\right|$$

$$\text{where } F = \frac{3\left(\phi_{12}^{max}\right)^{1/3} + (\phi_1 + \phi_2)^{1/3}}{4\left[\left(\phi_{12}^{max}\right)^{1/3} - (\phi_1 + \phi_2)^{1/3}\right]}$$

Solid packing correction (Fedors & Landel, 1979)

$$a = \sqrt{\frac{d_2}{d_1}} \; ; \; X_{12} = \frac{\phi_1}{\phi_1 + \phi_2}$$

$$\phi_{12}^{max} = \left[(\Phi_1 - \Phi_2) + (1-a)(1-\Phi_1)\Phi_2\right]\left[\Phi_1 + (1-\Phi_1)\Phi_2\right] \frac{X_{12}}{\Phi_1} + \Phi_2$$

$$\text{for } X_{12} \leqslant \frac{\Phi_1}{\Phi_1 + (1-\Phi_1)\Phi_2}$$

$$\phi_{12}^{max} = (1-a)\left[\Phi_1 + (1-\Phi_1)\Phi_2\right](1 - X_{12}) + \Phi_1$$

$$\text{for } X_{12} \geqslant \frac{\Phi_1}{\Phi_1 + (1-\Phi_1)\Phi_2}$$

Table 2.9: *Equations of Motion for a Binary System using particle mixture momentum equations*

Continuity equations
$$\frac{\partial \varepsilon}{\partial t} + \nabla \cdot \left(\varepsilon \langle \boldsymbol{u} \rangle^f\right) = 0$$ $$\frac{\partial \phi}{\partial t} + \nabla \cdot \left(\phi \langle \boldsymbol{u} \rangle^m\right) = 0$$
Momentum Equations
$$\rho_f \left[\frac{\partial}{\partial t}\left(\varepsilon \langle \boldsymbol{u} \rangle^f\right) + \nabla \cdot \left(\varepsilon \langle \boldsymbol{u} \rangle^f \langle \boldsymbol{u} \rangle^f\right)\right] = \nabla \cdot \mathfrak{T}^f - n\left\langle f^f \right\rangle + \varepsilon \rho_f \boldsymbol{g}$$ $$\rho_m \left[\frac{\partial}{\partial t}\left(\phi \langle \boldsymbol{u} \rangle^m\right) + \nabla \cdot \left(\phi \langle \boldsymbol{u} \rangle^m \langle \boldsymbol{u} \rangle^m\right)\right] = \nabla \cdot \mathfrak{T}^m + n\left\langle f^f \right\rangle + \phi \rho_m \boldsymbol{g}$$
Definitions
$$\rho_m = \frac{\rho_1 \phi_1}{\rho_1 \phi_1 + \rho_2 \phi_2} + \left(1 - \frac{\rho_1 \phi_1}{\rho_1 \phi_1 + \rho_2 \phi_2}\right) \rho_2$$

ically modified to take into consideration the presence of other particles in the mixture. van Wachem et al. (2001) and Dahl & Hrenya (2005) applied a modified version of the Wen & Yu (1966) equation proposed by Pirog (1998) to simulate the dynamics of a particle mixture. van der Hoef et al. (2004) developed an average drag force relationship for a polydisperse particle system using the Lattice Boltzmann Modelling (LBM) approach. Howley & Glasser (2002) developed a general drag coefficient model to account for particle mixtures. A summary of some of the closures available in literature is detailed in Table 2.10.

2.3.2.1.2 Solid Stress Tensor A description of the collisional and kinetic contributions to the internal stress of the mixed particle phase has been provided by van Wachem et al. (2001) using the kinetic theory. Whilst, most investigators neglect the contribution of the kinetic and collisional pressure originating from particle fluctuations to the total solid phase stress of the mixed particle species instead van Wachem et al. (2001) assume a predomi-

Table 2.10: *Examples of averaged drag models proposed in literature for binary mixtures*

Pirog (1998)

$$\beta = \frac{3}{4} C_D \frac{\left(\prod_{k=1}^{2} (1-\phi_k)^{-2\alpha_k}\right) \phi \rho_f \left|\langle \boldsymbol{u} \rangle^f - \langle \boldsymbol{u} \rangle^s\right|}{\langle d_p \rangle} \varepsilon^3$$

where C_D is by Rowe (1961)

$$C_D = \begin{cases} \dfrac{24}{Re_p (1-\phi)} \left[1 + 0.15 \left((1-\phi) Re_p\right)^{0.687}\right] & \text{if } (1-\phi)\, Re_p < 1000 \\ 0.44 & \text{if } (1-\phi)\, Re_p \geq 1000 \end{cases}$$

$$Re_p = \frac{\rho_f \varepsilon \left|\langle \boldsymbol{u} \rangle^f - \langle \boldsymbol{u} \rangle^s\right| \langle d_p \rangle}{\mu_f} \; ; \; \alpha_k = 11.28 - 9.69 \frac{d_{pk}}{\langle d_p \rangle} + 1.49 \left(\frac{d_{pk}}{\langle d_p \rangle}\right)^2 \; ; \; \langle d_p \rangle = \frac{1}{\sum_{k=1}^{n} \frac{x_k}{d_{pk}}}$$

Howley & Glasser (2002) applied the Ergun (1952) equation

$$\beta = y_1 (\beta_1 - \Delta\beta_{12}) + y_2 (\beta_2 - \Delta\beta_{21})$$

$$\Delta\beta_{12} = \beta_1 - \langle \beta \rangle \; ; \; \Delta\beta_{21} = \beta_2 - \langle \beta \rangle \; ; \; y_k = \frac{\phi_k}{\phi} \text{ where k=1 or 2}$$

$$\beta_k = 150 \frac{\phi^2 \mu_f}{(1-\phi)\, d_{pk}^2} + \frac{7}{4} \frac{\phi \rho_f \left|\langle \boldsymbol{u} \rangle^f - \langle \boldsymbol{u} \rangle^s\right|}{d_{pk}}$$

$$\langle \beta \rangle = 150 \frac{\phi^2 \mu_f}{(1-\phi)\, \langle d_p \rangle^2} + \frac{7}{4} \frac{\phi \rho_f \left|\langle \boldsymbol{u} \rangle^f - \langle \boldsymbol{u} \rangle^s\right|}{\langle d_p \rangle}$$

nance of the frictional contact forces. The constitutive frictional models described earlier in Table 2.5 are often employed as closure relationships. For completeness however, the granular temperature equation which was developed by van Wachem et al. (2001) is briefly presented in eqn. (2.47). The main drawback of this approach is that the granular temperature of each particle species is averaged and thus an equipartition of granular energy is assumed intrinsically (Curtis & van Wachem, 2004). In trying to account for the particle velocity of each particle species van Wachem et al. (2001) defined a peculiar velocity $\langle \boldsymbol{C} \rangle^{\mathcal{F}_k}$, for each solid phase:

$$\langle \boldsymbol{C} \rangle^{\mathcal{F}_k} = \langle \boldsymbol{c}^{\mathcal{F}_k} - \boldsymbol{u}^m \rangle \tag{2.45}$$

The granular temperature, $\mathscr{T}^{\mathscr{F}_k}$, is related to the peculiar velocity and to the mass of the individual particle species $m^{\mathscr{F}_k}$. The mixture granular temperature, $\mathscr{T}$, is given by an average of the granular temperature of the mixture:

$$\frac{3}{2}\mathscr{T}^{\mathscr{F}_k} = \frac{1}{2} m^{\mathscr{F}_k} \left\langle C^2 \right\rangle^{\mathscr{F}_k} \quad ; \quad \mathscr{T} = \frac{1}{n}\left(n^{\mathscr{F}_1}\mathscr{T}^{\mathscr{F}_1} + n^{\mathscr{F}_2}\mathscr{T}^{\mathscr{F}_2} \right) \tag{2.46}$$

where $n^{\mathscr{F}_k}$ refers to the number of each particle species present in the mixture. The mixture balance of granular energy is:

$$\frac{3}{2} n\left[\frac{\partial \mathscr{T}}{\partial t} + \nabla \cdot (\mathscr{T} \langle \boldsymbol{u} \rangle^m) \right] - \frac{3}{2}\mathscr{T}\nabla \cdot \left(n^{\mathscr{F}_1} \langle \boldsymbol{C} \rangle^{\mathscr{F}_1} + n^{\mathscr{F}_2} \langle \boldsymbol{C} \rangle^{\mathscr{F}_2} \right) = -\langle p \rangle^s : \nabla \langle \boldsymbol{u} \rangle^m$$

$$-\nabla \cdot q - \gamma + \sum_{k=1,2} \left(\boldsymbol{F}^{\mathscr{F}_k} + \rho_k \boldsymbol{g} \right) \cdot \left(n^{\mathscr{F}_1} \langle \boldsymbol{C} \rangle^{\mathscr{F}_1} + n^{\mathscr{F}_2} \langle \boldsymbol{C} \rangle^{\mathscr{F}_2} \right) \tag{2.47}$$

where $\boldsymbol{q}$ is the mixture energy flux, $\langle p \rangle^s$ is the total solids stress tensor of the mixture. $\boldsymbol{F}^{\mathscr{F}_k}$ is the total force acting on particle phases $\mathscr{F}_k$, and γ is the rate of granular energy dissipation. The first term on the left hand side denotes the time dependency of the mixture granular energy, the second term is the convection of the mixture granular energy and the third term denotes the convection of mixture granular energy due to the relative species movement. On the right hand side, the first term denotes the creation of mixture granular energy due to shear in the particle phase, the second term denotes diffusion of the mixture granular energy along the gradients in the mixture granular temperature, the third term denotes the creation or dissipation of mixture granular energy due to external forces.

2.4 Particle Mixing in Binary Systems

Fluidized beds can either be operated to promote particle mixing or segregation. Particle mixing has been the subject of several experimental investigations. Rowe (1971) and Rowe et al. (1972) carried out experiments by injecting bubbles into two separate layers of *flotsam* and *jetsam* as the starting mixture. The flotsam is the lighter of the two components, which tends to remain at the top layer of the bed upon fluidization while the jetsam is the

layer of the heavier or larger component, which tend to stay close to the bottom of the bed upon fluidization. Their studies showed that the passage of bubbles is the main mechanism responsible for particle mixing in gas fluidized beds. Rowe (1971) and Rowe et al. (1972) demonstrated, through photographs taken in 2D beds, that particles are carried upwards in the *wake* of the bubble close to the gas distributor plate and carried up to the top of the fluidized bed. Along the way up, the bubble wakes exchange their content with the rest of the bed in a phenomenon known as *wake shedding*. This overall upward vertical movement is counter balanced by mass circulation downward in the bubble free region of the bed.

A number of analytical mathematical models have been proposed to predict mixing behaviour in bubbling gas fluidized beds. Amongst the many models available the countercurrent back mixing model (CCBM) has gained greater acceptance due to its representation of the transport process in a gas fluidized bed. The countercurrent back mixing model was originally proposed by van Deemter (1961) and refined and generalized later by Gwyn et al. (1970). The model depicts the bed as a multiple phase system, with an upward flow of gas in the wake and a downward flow in the dense phase. Exchange occurs between the phases. Mass balances over the individual systems are represented by a system of hyperbolic partial differential equations (Lim et al., 1995). The model has proved quite successful in representing the mixing in bubbling beds despite the fact that it ignores other possible mixing mechanisms such solids splashing at the bed surface and turbulent mixing near the distributor.

The use of computational fluid dynamics in the studying of particle mixing has been pioneered by Syamlal (1985). In his work constitutive expressions mentioned earlier in § 2.3.1 were used to simulate the hydrodynamics of a binary mixture. Results from his studies confirmed qualitative experimental observations of mixing being induced by bubbles in gas-fluidized beds. Copper & Coronella (2005) investigated the effect of bubbling on the mixing of a bed consisting of two Geldart Group B materials using a commercial CFD code, FLUENT. From their simulations they were able to qualitatively identify the mixing mechanisms of particle exchange and circulation. More recent work concerning the simulation of mix-

ing phenomenon has been published by Huilin et al. (2003), Huilin & Gidaspow (2003), Bokkers et al. (2004).

2.5 Particle Segregation in Binary Systems

The presence of two kinds of particles in a fluidized bed leads to the superimposition of segregation on the mixing process. The are two primary objectives for investigating particle segregation phenomenon in gas fluidized beds. In one respect, studies are carried out to determine the operating conditions required to promote bed mixing and minimize particle segregation whilst the other objective, contrary to the above statement is, to study the conditions under which clean separation can be accomplished between different materials in the bed (Yang, 2003). In this case, the degree of separation and rate of particle separation are important aspects of investigation. The mechanisms of particle segregation in a gas fluidized bed was first studied by Rowe (1971) and Rowe et al. (1972) using binary systems of near spherical particles in both two dimensional and three dimensional cylindrical beds. Three distinctly different mechanisms were found to be important in creating the relative movement of particles in a bed. The lifting of particles in the wake of the rising gas bubble, which serves as the main means by which flotsam particles are carried to the upper part of the bed. The migration of the bigger jetsam particles by falling through bubbles and the percolate of the smaller, denser particles through the interstices created by the bigger jetsam particles constitute the remaining mechanism through which segregation takes place. Experimental studies have been carried out by many researchers (Nienow et al., 1972, 1978, Nienow & Chessman, 1980, Nienow & Chiba, 1985, Ho et al., 1987, Bilbao et al., 1988, 1991) looking at the behaviour of *jetsam* and *flotsam* rich systems as well as the segregation patterns. Nienow et al. (1987) extended the segregation study from binary systems to quaternary systems in beds of different sized particles.

A conceptual mathematical model for the calculation of segregation patterns in gas fluidized bed was first proposed by Gibilaro & Rowe (1974). The generalized model depicts the bed

in terms of a bulk (dense) phase and a dispersed wake phase in which the solid flows are controlled by four mechanisms: convective, segregating, dispersive and particle exchange. The model gives qualitative agreement with the segregation patterns observed in some typical cases. The use of computational fluid dynamics (CFD) to study segregation has been pioneered by Syamlal (1985) and Gera et al. (2004) who used the **M**ultiphase **F**low with **I**nterphase e**X**changes (MFIX) code to model the hydrodynamics of particle segregation in gas fluidized beds using Geldart Group D particles. Quantitative results on the bed height was compared with the experimental findings of Goldschmidt et al. (2001). Huilin et al. (2003) used a modified version of the K-FIX(3D) code to model the segregation dynamics of a Geldart Group D binary system consisting of particles which only differed in size. Results obtained indicated that particle segregation depended on the degree of bubbling in the fluid bed in agreement with experimental observations. van Wachem et al. (2001) used the commercial CFD code by Ansys, CFX4.3, to model qualitatively *bed inversion* phenomenon in gas fluidized beds using Geldart Group B particles which differ in density and size.

2.5.1 Classification of flotsam and jetsam

As discussed earlier, when a binary mixture or a mono component system with a very wide size distribution, is fluidized the segregating tendency of particles of different sizes or density leads to a top to bottom variation in concentration in the bed (Nienow & Chiba, 1985). Rules governing the classification of a *flotsam* and a *jetsam* component for a binary system were suggested by Chiba et al. (1980) and are presented in Table 2.11 where ρ_R refers to the density ratio, d_b is the diameter of the bigger particle and d_s is the diameter of the smaller particle. However, the distinction between a jetsam particle and a flotsam particle becomes less clear in systems where there is a mixture of wide size and density distribution. This is because one particular component may be a flotsam with respect to some components in the bed, while simultaneously being a jetsam to other components.

Table 2.11: *Which Component Is Jetsam?*

Case 1	$d_b/d_s \leq 10$; $\rho_R = \rho_b/\rho_s$
1a.	Density ratio $\rho_R = 1$; Bigger component is jetsam
1b.	Density ratio $\rho_R > 1$; Heavier component is jetsam
Case 2	$d_b >> d_s$; % smaller → 100%
2a.	Bigger component denser than bulk density of smaller ; bigger is jetsam
2b.	Bigger component less dense than bulk density of smaller; smaller is jetsam
Case 3.	$d_b >> d_s$; % bigger → 100%
3a.	Bigger component denser than smaller; bigger is jetsam
3b.	Bigger component less dense than smaller ; either may be jetsam
Case 4.	The minor component is plate like with sphericity < 0.5
4a.	Platelike particle is denser ; platelike particle is jetsam
4b.	Platelike particle is lighter; either component may be jetsam

Source: Chiba et al. (1980)

2.5.2 Minimum fluidization velocity of a binary mixture

Three types of behaviour can be observed when a binary or a mono component system with a very wide size distribution is fluidized. These are represented by the pressure drop curves shown in Figure 2.5 and diagrams shown in Figure 2.6. In the first case where the two components segregate completely (see Fig 2.6 a), the fluidization curve will follow curve (b) in Fig. 2.5 for the ascending portion but descend along curve (a), this is due to the fact that the mixture will have already separated into the two distinct layers of flotsam and jetsam when the gas velocity is higher than the minimum fluidization velocity of the jetsam (Yang, 2003). For an ideal system (Fig 2.6b) where the particles are of small size difference and equal density both the ascending and descending portions will coincide with curve (b) in Fig. 2.5. The third type of behaviour (Fig. 2.6 c) occurs in binary systems where the density difference is small but size difference is large or in single component systems with a very wide size distribution.

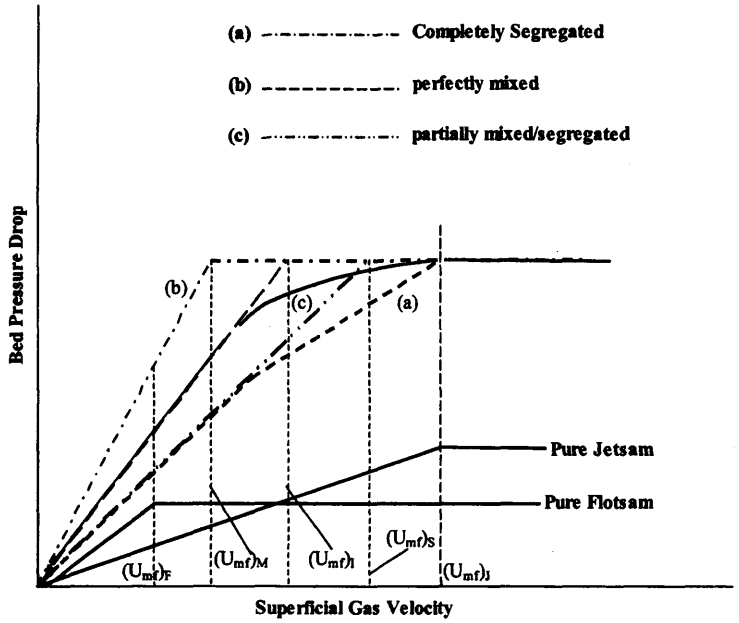

Figure 2.5: *Determination of minimum fluidization velocity of a binary mixture*
Source: Yang (2003)

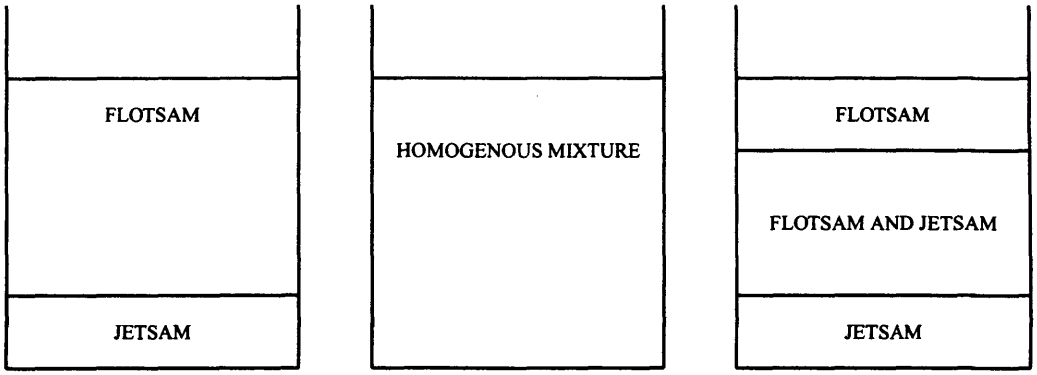

Figure 2.6: *Concentration Profiles in the Strongly Segregating (a), Perfect Mixing (b) and Partial Mixing (c) regimes*
Source: Chiba et al. (1979)

Most minimum fluidization velocities reported in literature correspond to $(U_{mf})_M$, the minimum fluidization velocity of the homogeneous mixture, or $(U_{mf})_J$, the minimum fluidization velocity of the jetsam particle in the mixture. Empirical correlations have been proposed for calculating the minimum fluidization velocity of a binary mixture by many authors some of which include Gossens et al. (1971), Cheung et al. (1974), Chiba et al. (1979). However many of the correlations proposed in literature tend to be particle system specific. The mini-

mum fluidization velocity U_{mf} used in this work is the correlation proposed by Gossens et al. (1971):

$$U_{mf} = \frac{\mu_f}{\rho_f d_m}\left[\left(33.7^2 + 0.0408\,Ar\right)^{0.5} - 33.7\right] \tag{2.48}$$

where the Archimedes number Ar of the mixture is given by:

$$Ar = \frac{\rho_m - \rho_f}{\rho_f} Ga \quad ; \quad \frac{1}{\rho_m} = \frac{\omega_1}{\rho_1} + \frac{\omega_2}{\rho_2} \tag{2.49}$$

and the Galileo number Ga is equal to:

$$Ga = \frac{d_m^3 \rho_f^2 g}{\mu_f^2} \quad ; \quad d_m = \frac{\omega_1 \rho_2 + \omega_2 \rho_1}{\omega_1 \rho_2 d_2 + \omega_2 \rho_1 d_1} d_1 d_2 \tag{2.50}$$

In equations (2.49) and (2.50) the quantities ω_1 and ω_2 denote the mass fractions of the larger and smaller particles respectively in the powder devoid of fluid; these therefore take the expressions:

$$\omega_1 = \frac{\phi_1 \rho_1}{\phi_1 \rho_1 + \phi_2 \rho_2} \quad ; \quad \omega_2 = \frac{\phi_2 \rho_2}{\phi_1 \rho_1 + \phi_2 \rho_2} \tag{2.51}$$

2.5.3 Mixing and Segregation indexes

A proper description of the state of particle distribution in a binary gas-fluidized bed can be achieved by means of two established parameters, the mixing index M and the coefficient of segregation C_s. The use of either depends on the approach of interest. If the mixedness of the system is of primary concern, then the mixing index is more appropriate; if, on the other hand, the degree of segregation is of direct interest, then the coefficient of segregation is more suitable. The two however, even if not directly related, should ultimately provide the same physical information. The mixing index was first defined by Rowe (1971) as:

$$M = \frac{\langle \omega_{jet} \rangle_t}{\langle \omega_{jet} \rangle_o} \tag{2.52}$$

where $\langle \omega_{jet} \rangle_t$ is the average mass fraction of the jetsam phase in the top region of the bed and $\langle \omega_{jet} \rangle_o$ is the average mass fraction of the jetsam phase evaluated over the entire bed. The top region of the bed is not uniquely defined, but can be chosen somewhat arbitrarily. The above definition intrinsically equates a state of perfect jetsam segregation *at the bottom of the bed* to a mixing index of $M = 0$ and a state of perfect mixing to a mixing index of $M = 1$. Perfect jetsam segregation *at the top of the bed*, which is usually imposed before the system is fluidized, is instead given by a mixing index of $M = \left(m_{jet} + m_{flot}\right)/m_{jet}$, where m_{jet} and m_{flot} are the overall masses of jetsam and flotsam in the bed, respectively. The coefficient of segregation, introduced by Geldart (1986), is given by:

$$C_s = \frac{\langle \omega_{jet} \rangle_b - \langle \omega_{jet} \rangle_t}{\langle \omega_{jet} \rangle_b + \langle \omega_{jet} \rangle_t} \cdot 100 \tag{2.53}$$

where $\langle \omega_{jet} \rangle_b$ and $\langle \omega_{jet} \rangle_t$ are the mass fractions of the jetsam phase in the bottom and top halves of the bed. Clearly C_s varies between -100 and $+100$, with -100 denoting perfect jetsam segregation at the top of the bed, 0 being representative of perfect mixing, and $+100$ indicating perfect jetsam segregation at the bottom of the bed.

2.5.4 Effect of gas velocity and particle size on segregation

The resulting pattern which is displayed by a binary system is dependent upon whether the *flotsam* or *jetsam* particle is present in excess. We consider first a system rich in flotsam particles. From Fig. 2.7a it is seen that at gas velocities in the region of the minimum fluidization velocity of the flotsam particle, a layer of pure jetsam settles to the bottom of the bed whilst there is a fairly uniform distribution of jetsam particles in the upper part of the bed. Increasing the gas velocity results (see Fig. 2.7 b) in an increase in the concentration of the jetsam particles in the upper part of the bed which results in the development of a concentration gradient in the bottom part of the bed. Further increase in the gas velocity results in the state of *perfect mixing* [4] (see Fig. 2.7 c) where the bed is uniformly mixed throughout.

[4] Experimental observations during this work however showed that the perfect mixing is never achieved. This has also been noted by Nienow et al. (1978)

Conversely the situation of having a system rich in jetsam particles presents a different scenario. In Fig. 2.8 a the flotsam is initially lying on top of the bed which predominantly has jetsam particles. Increase in the gas velocity , Fig. 2.8 b, results in the flotsam being gradually *buried* in the bed. This is caused by the bubbles which form and rise initially through *pure* jetsam (Nienow et al., 1978). The bubbles would carry, in their wake, the jetsam phase to the top of the bed which would result in the layer of flotsam, initially at the top, being progressively buried. Further gas velocity increase leads to the equilibrium situation, where flotsam sinking through the bed are *picked up* by passing bubbles and deposited near the upper part (see Fig. 2.8 c). From the above discussion it is clear that a link exists between

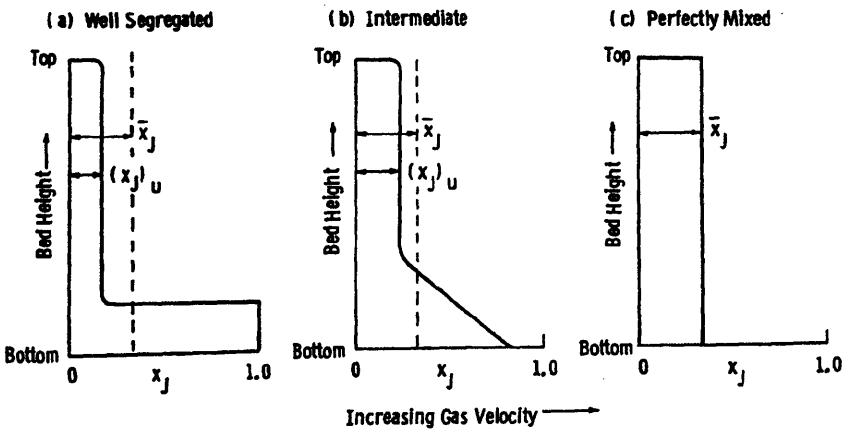

Figure 2.7: *Practical states of equilibrium for flotsam rich binary systems*

Source: (Yang, 2003) and Nienow et al. (1978)

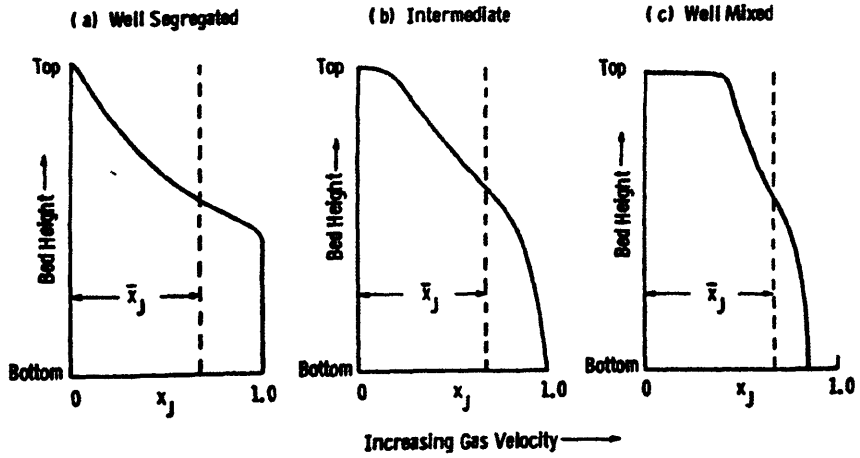

Figure 2.8: *Practical states of equilibrium for Jetsam rich binary systems*
Source: (Yang, 2003, Nienow et al., 1978)

the gas velocity and the mixing state of the binary system. It is thus of great importance to have correlations capable of linking to the *desired mixing* required to the superficial gas velocity. An analytical representation of this link was first given by Nienow et al. (1987). They related the mixing index, M, with the superficial gas velocity, U, through the following equation:

$$M = \frac{1}{(1 + e^{-Z})} \tag{2.54}$$

where Z is given by:

$$Z = \left[\frac{U - U_{To}}{U - (U_{mf})_F}\right] \cdot e^{\frac{U}{U_{To}}} \tag{2.55}$$

where the takeover velocity U_{To} is estimated from empirical equations (Yang, 2003). However eq.(2.54) was only valid for jetsam concentrations of less than 50%. A more recent study by Wu & Baeyens (1998) has yielded an equation which relates the mixing index M to the visible bubble flow rate Q_B/A throughout the bed. The equations are presented as follows:

$$M = 1 - 0.0067\, d_R\, 1.33 \left(\frac{Q_B}{A}\right)^{-0.75} \tag{2.56}$$

In eq. (2.56), d_R is the ratio d_1/d_2 of the larger diameter to the smaller diameter of the particles. Q_B/A and is a modification of the original correlation derived in the *two-phase theory of fluidization* proposed by Toomey & Johnstone (1952) and successively developed by Davidson & Harrison (1963b). The modified correlation takes the form:

$$\frac{Q_B}{A} = \gamma\left(U_o - U_{mf}\right) \tag{2.57}$$

where U_{mf} is the minimum fluidization velocity of the system and γ is a *throughflow* empirical corrective factor. The two-phase theory was a first attempt at quantifying Q_B/A. The theory modelled a fluidized bed as consisting of an emulsion phase of voidage ε_{mf} wherein the fluid flow rate is equal to that at incipient fluidization conditions and a bubble phase which carries the additional flow of fluid. The visible bubble flow rate was considered to be equal to the excess gas flow above that required for minimum fluidization, *i.e.* $\gamma = 1$ in equation (2.57). It was noted, however, that in practice Q_B/A was rather smaller than the

one predicted by the original theory. This led to the introduction of the corrective factor γ featuring in equation (2.57). The form of γ advanced by Wu & Baeyens (1998) has been used in this work:

$$\gamma(Ar) = \begin{cases} 1 & \text{for } Ar \leqslant 50 \\ 2.27\,Ar^{-0.21} & \text{for } Ar > 50 \end{cases} \tag{2.58}$$

2.6 Conclusion

This chapter has sought to outline the various modelling strategies used by researchers in tackling gas-solid flow problems. The challenges currently been faced by workers in this area was also presented. Whilst, the Lagrangian-Eulerian approach for modelling gas-solid flows, represents a greater level of mathematical detail. However, it is not suited for the modelling of large scale fluidized beds due to the sheer computational effort required to model such realistic systems. The Eulerian-Eulerian approach, which is the strategy that has been adopted in this work, describes the gas-solid system as an interpenetrating continuum. This approach has been used to study the mixing and segregation patterns of the industrial materials provided for this work. However, there are issues concerning an appropriate theoretical description for the behaviour of the solid particles in a continuum for binary systems as well as constitutive expressions for the fluid particle interaction force. The rest of this work will seek to address and elucidate (where possible) solutions to the above problems.

Chapter 3

Experimental materials and methods

Summary

This chapter describes the powders and the particle characterization techniques employed to classify the materials used in this work. Particle properties such as mean particle diameter, size distribution and particle shape are reported. This chapter also details fluidization tests as well as results from scanning electron microscope (SEM) technique used to investigate the surface properties of the powders provided for this project. The materials used include slag, natural and synthetic rutile as well as two different sizes of ballotini glass beads. All powders aside from the ballotini glass beads were provided by Huntsman Tioxide Ltd.

3.1 Mono-component systems

3.1.1 Particle size and particle size distribution

Analytical samples of the materials investigated were obtained by riffling large batches. The mean particle diameter and particle size distribution were determined by sieve analysis. For each powder, the sieve test was repeated three times and average values for the mean particle diameter were taken. In this thesis, the surface-volume diameter, d_{sv}, has been used to

calculate the mean particle diameter. The surface-volume diameter is defined as follows:

$$d_p = d_{sv} = \frac{1}{\sum_i x_i/d_{pi}} \tag{3.1}$$

where x_i is the weight fraction of particles in each size range. The relative diameter spread, σ/d_{50}, was used to compare the width of the size distribution of the powders provided for this work. The relative spread is obtained by plotting the cumulative percentage undersize versus the sieve aperture size. The spread is defined the following way (Geldart, 1986):

$$\sigma = \frac{d_{84\%} - d_{16\%}}{2} \tag{3.2}$$

The relative spread is then calculated using the following:

$$\text{Relative spread} = \frac{\sigma}{d_{50}} \tag{3.3}$$

where d_{50} represents the median size corresponding to the 50% value on the graph of cumulative percentage undersize versus size. The classification by Geldart (1986), which is reported in Table 3.1 for convenience, was used to elucidate the type of size distribution corresponding to the calculated relative diameter spread. Plots showing the PSD and relative diameter spread of the industrial powders and ballotini investigated in this thesis are shown in Figures 3.2-3.9. The natural and synthetic rutile materials exhibited a fairly wide distribution 0.21 and 0.31 respectively (see Table 3.1). The synthetic rutile shows a slightly larger PSD than the natural rutile because of the presence of agglomerates as a result of the process of manufacture as later shown in Fig. 3.13, whilst the slag material exhibited a very wide size distribution (0.50). The ballotini glass beads, as expected, showed a narrow size distribution based on the above classification with the larger particle having a relative spread of 0.077 and the smaller particle a relative spread of 0.135. The physical properties of the all the powders employed are summarized in Table 3.2

Table 3.1: *Width of size distribution based on relative spread*

Number of sieves on which the middle 70% (approx.) of the powder is found	σ/d_{50}	Type of distribution
1	0	Very narrow
2	0.03	Narrow
3	0.17	Fairly Narrow
4	0.25	Fairly wide
5	0.33	
6	0.41	Wide
7	0.48	
9	0.60	Very wide
11	0.70	
> 13	> 0.80	Extremely wide

Source: Geldart (1986)

Table 3.2: *Particle physical properties*

Acronym	NR	SR	SG	BI-1	BI-2
Material	Natural Rutile	Synthetic Rutile	Slag	Ballotini	Ballotini
$d_p, \mu m$	186	156	305	350	212
ρ_p, kgm^{-3}	4200	3200	4200	2500	2500
Geldart Group	B	B	B	B	B
σ/d_{50}	0.21	0.31	0.50	0.077	0.135

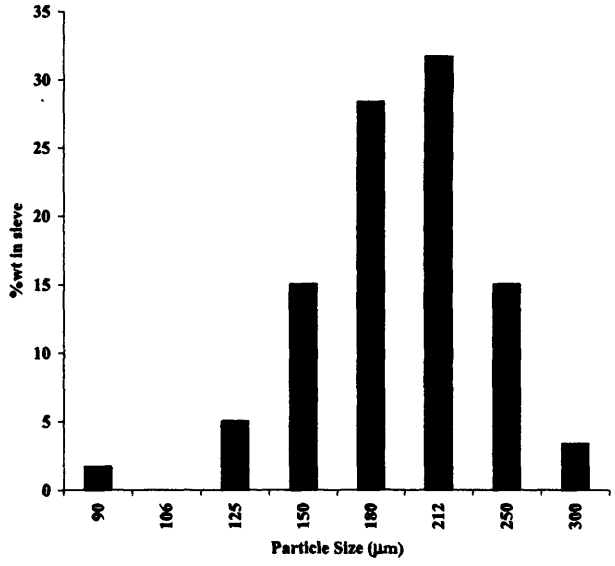

Figure 3.1: *Natural Rutile, particle size distribution, d_p = 186µm*

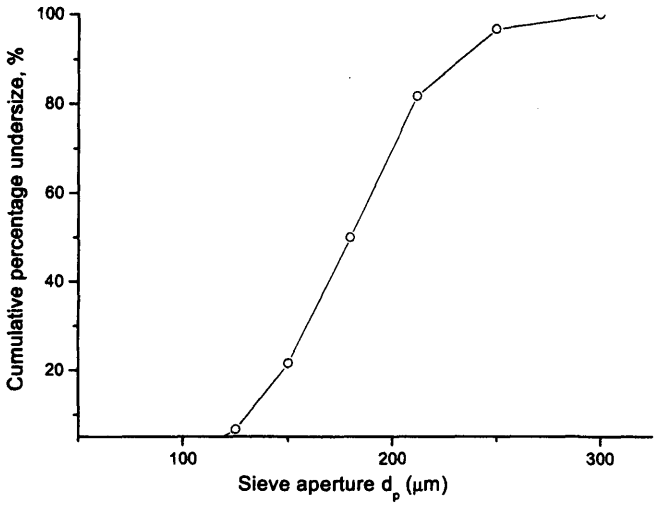

Figure 3.2: *Natural Rutile, Relative spread of natural rutile, d_p = 186μm*

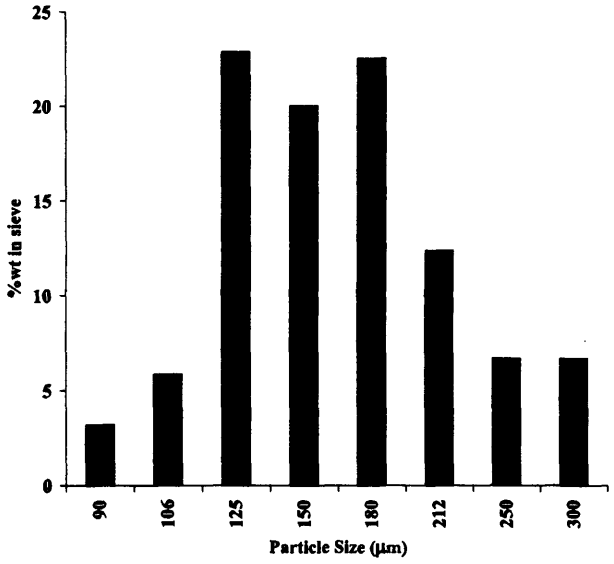

Figure 3.3: *Synthetic Rutile, particle size distribution, d_p = 156 μm*

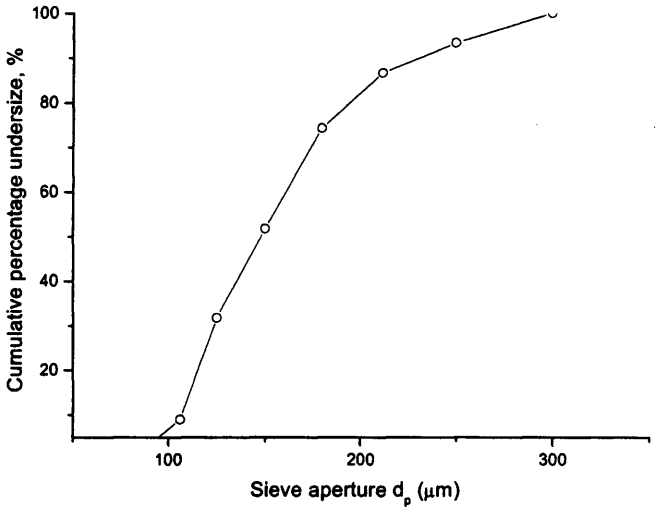

Figure 3.4: *Synthetic Rutile, Relative spread of synthetic rutile, d_p = 156μm*

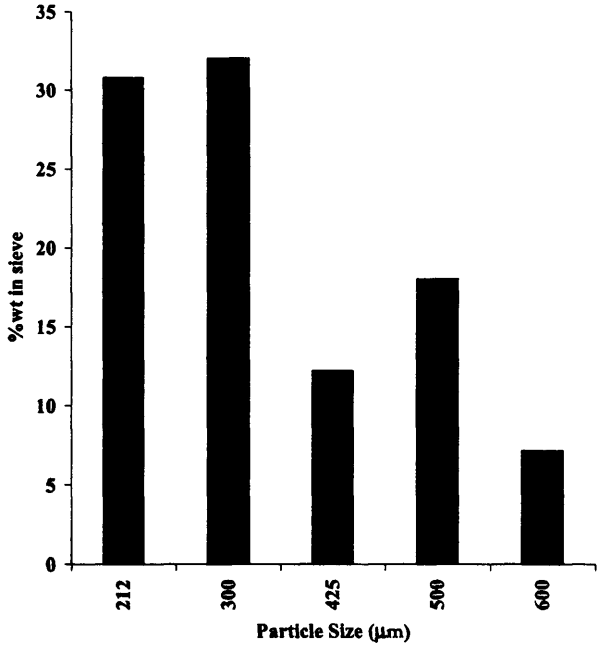

Figure 3.5: *Slag, particle size distribution, d_p = 305 μm*

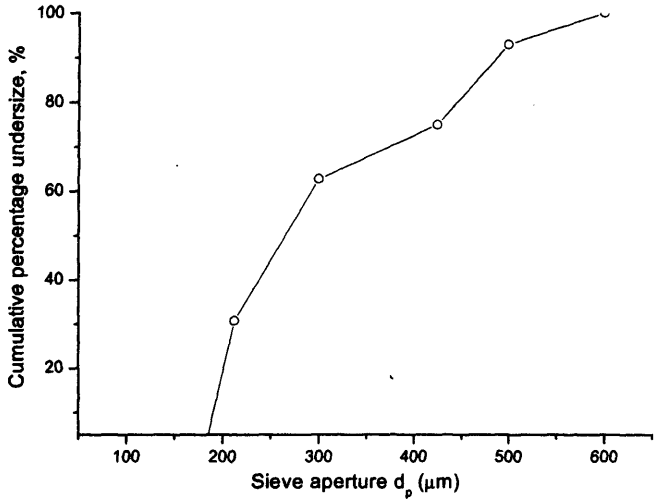

Figure 3.6: *Slag, Relative spread of slag material, d_p = 305μm*

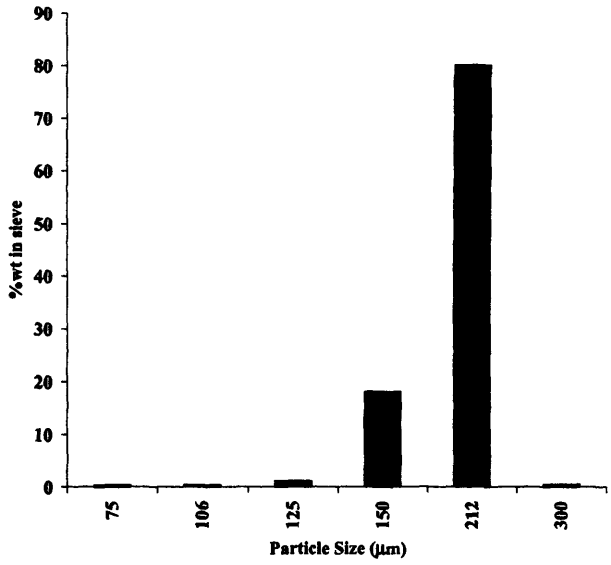

Figure 3.7: *Ballotini, particle size distribution, d_p = 212 μm*

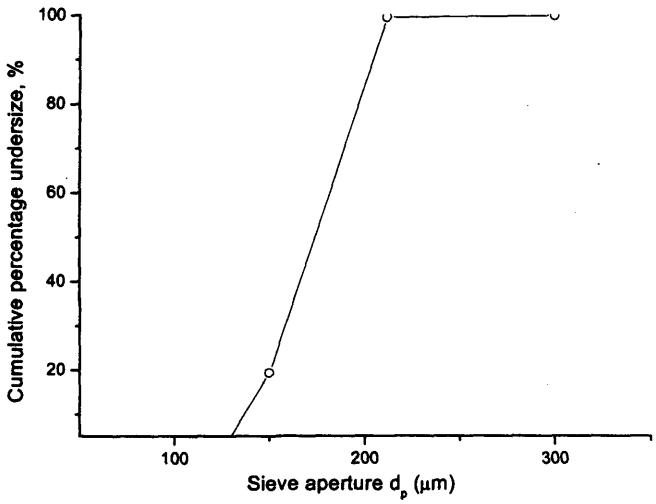

Figure 3.8: *Ballotini, Relative spread of ballotini glass beads, d_p = 212μm*

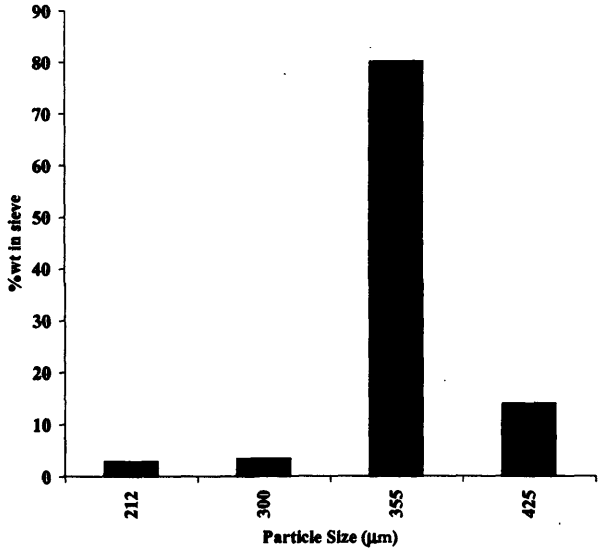

Figure 3.9: *Ballotini, particle size distribution, d_p = 350 μm*

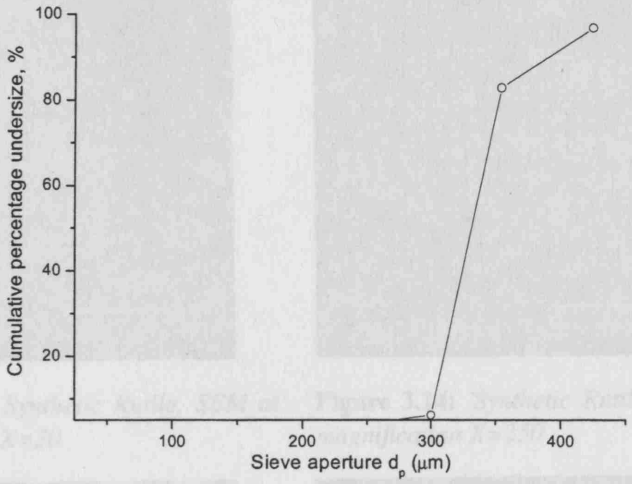

Figure 3.10: *Ballotini, Relative spread of ballotini glass beads, d_p = 350μm*

3.1.2 Particle shape - Scanning Electron Microscope (SEM)

Using a scanning electron microscope (SEM) the surface morphology of the materials under investigation were observed and photographs taken. SEM photographs of the natural and synthetic rutile as well as slag are reported in Figures 3.11 - 3.16. The natural rutile and slag particle are observed to be more irregularly shaped whilst the synthetic rutile, Figure 3.14, is more spherical. From fig 3.13, the presence of agglomerates can be observed; this is as a result of the process of manufacture of the synthetic rutile powder.

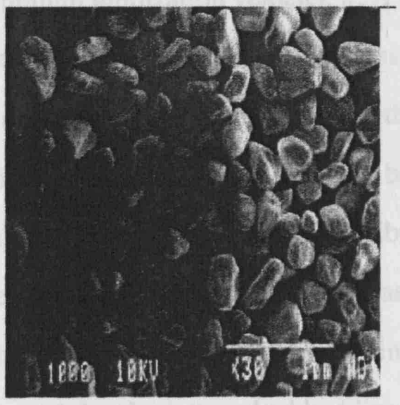

Figure 3.11: *Natural Rutile, SE magnification X=30*

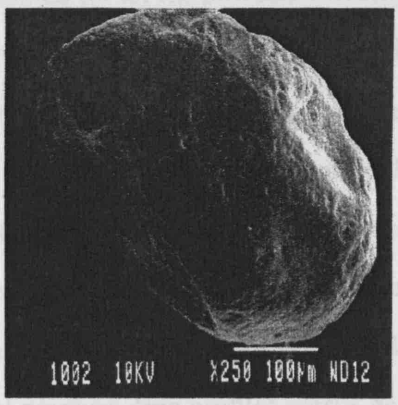

Figure 3.12: *Natural Rutile, SEM at magnification X=250*

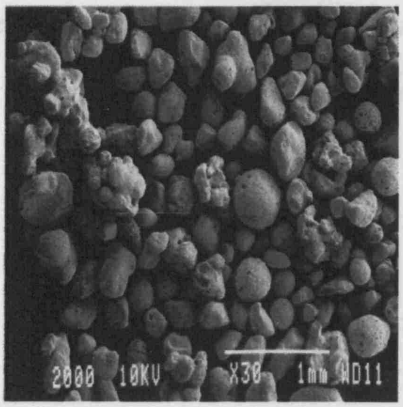

Figure 3.13: *Synthetic Rutile, SEM at magnification X=30*

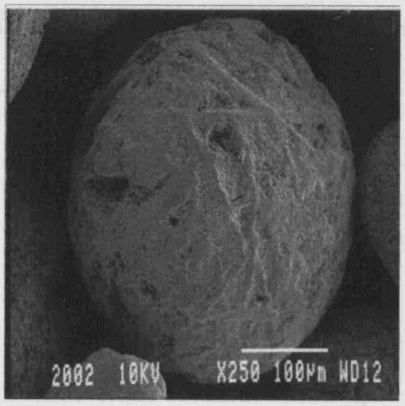

Figure 3.14: *Synthetic Rutile, SEM at magnification X=250*

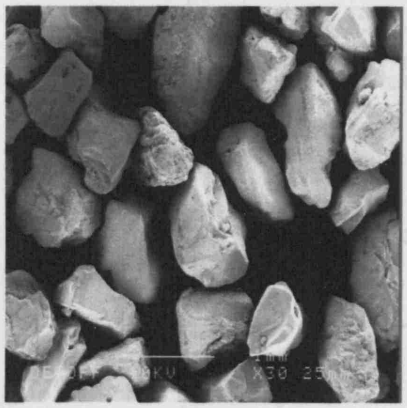

Figure 3.15: *Slag, SEM at magnification X=30*

Figure 3.16: *Slag, SEM at magnification X=100*

3.1.3 Fluidization tests

The minimum fluidization velocity, u_{mf}, was measured for all the powders investigated. u_{mf} was obtained from diagrams of the pressure drop profile across the bed as a function of the fluidizing gas velocity. For all powders, the minimum bubbling velocity, u_{mb}, was determined from visual observations and found to be equal to the u_{mf} as expected. The fluidizing gas used, nitrogen, was increased via a calibrated rotameter. Pressure drop measurements were recorded during the increase and decrease of the inlet gas flowrate. The experimental minimum fluidization velocity was determined from the intersection of the horizontal fluidized bed line and the sloping packed bed line. Typical pressure drop profiles versus gas velocity are shown for the industrial powders used in this work (slag, natural and synthetic rutile) in Figure 3.18, 3.17 and 3.19 respectively. Similar tests were also carried out for the ballotini

powders used. The values for u_{mf} obtained from the experiments were compared with the

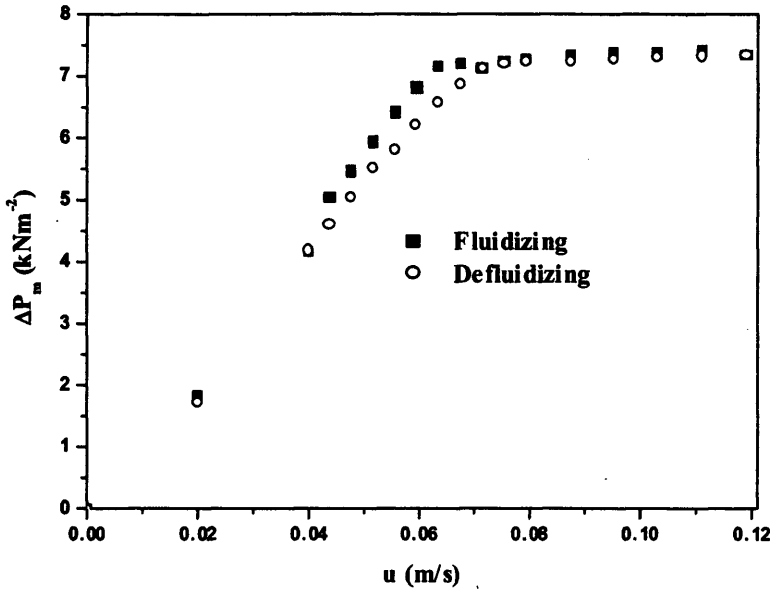

Figure 3.17: *Measured pressure drop versus superficial gas velocity for Natural Rutile*

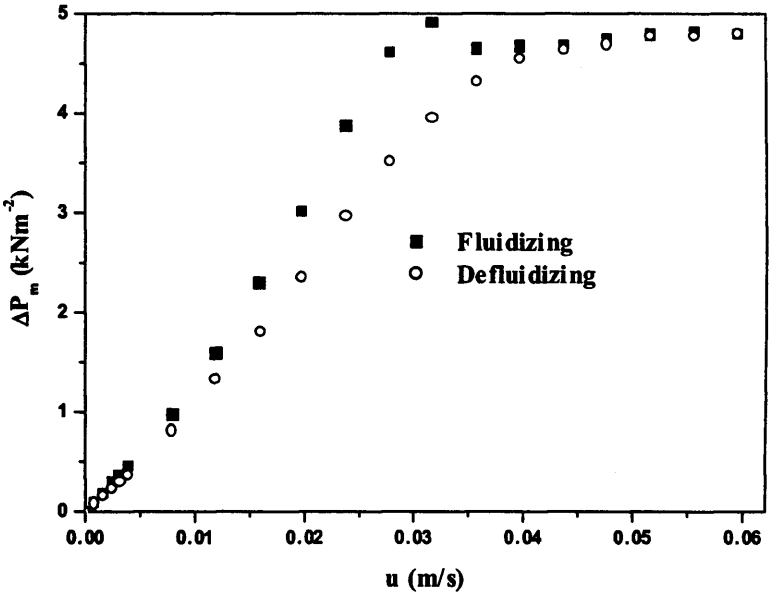

Figure 3.18: *Measured pressure drop versus superficial gas velocity for Synthetic Rutile*

experimental correlations of Baeyens & Geldart (1974) and Wen & Yu (1966) reported in eq's. (3.4) and (3.5):

$$u_{mf} = \frac{(\rho_p - \rho_g)^{0.934} g^{0.934} d_p^{1.8}}{1,111 \mu^{0.87} \rho_g^{0.066}} \tag{3.4}$$

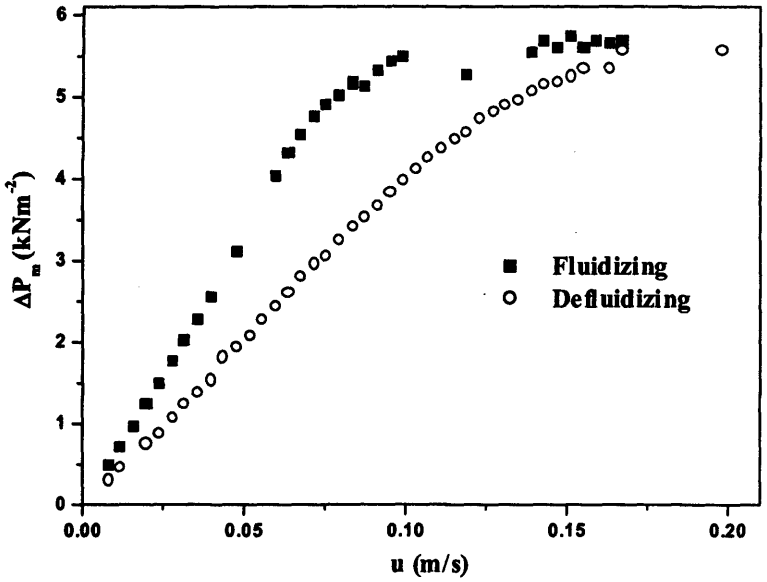

Figure 3.19: *Measured pressure drop versus superficial gas velocity for Slag*

$$u_{mf} = \frac{\mu}{\rho_f d_p}\left[(1,135.7 + 0.0408\,Ar)^{1/2} - 33.7\right] \quad ; \quad Ar = \frac{\rho_g d_p^3 \left(\rho_p - \rho_g\right) g}{\mu^2} \tag{3.5}$$

Results in Figures 3.17 - 3.19 show that the curves obtained increasing the fluidizing gas velocity deviate progressively more from those obtained when decreasing the gas velocity when comparing natural rutile, synthetic rutile and slag respectively; this is consistent with the results reported for the PSD which showed the natural rutile to have the narrowest PSD whilst slag had the widest. Interestingly, a comparison between experimental and predicted values for u_{mf} is reported in Table 3.3. Results show overall a match of within 25% for the powders investigated.

Table 3.3: *Comparison of experimental u_{mf} values with empirical correlations*

Material	Exp. m/s	Baeyens & Geldart (1974) m/s	Wen & Yu (1966) m/s
Natural Rutile	0.062	0.045	0.046
Synthetic Rutile	0.032	0.026	0.025
Slag	0.133	0.110	0.120

3.2 Binary systems

3.2.1 System properties

Table 3.5 reports the two systems of binary mixtures that have been specifically investigated in this thesis, system 1 has been obtained by mixing natural rutile, 186 μm, and slag material, 305 μm, at varying particle concentrations as illustrated in Table 3.4. Conversely, system 2

Table 3.4: *Binary mixture fractions investigated*

Experimental	$\langle \omega_{flot} \rangle$	$\langle \omega_{jet} \rangle$
1	0.25	0.75
2	0.50	0.50
3	0.75	0.25

has been obtained by mixing equal concentrations of ballotini particles of sizes 212 μm and 350 μm respectively. The systems selected represent a study of the fluidization patterns of binary mixtures composed of powders having the same density. It should also be noted that the size ratio, d_{jet}/d_{flot} , for both systems investigated is ≈ 1.6.

Table 3.5: *Properties of binary mixtures investigated*

	Solids Notation as in Table 3.2		Comparison of:
System	Jetsam	Flotsam	Size
1	SG	NR	$d_{jet}/d_{flot} \approx 1.64$
2	BI-1	BI-2	$d_{jet}/d_{flot} \approx 1.65$

3.2.2 Fluidization tests

The minimum fluidization velocity as well as bed voidage tests were carried out for the binary mixture of particles that belong to the system 1 (NR-SG), which was reported earlier in Table 3.5. In all the experiments, the flotsam particles are filled first; the jetsam particles are then added on top up to a height of 300 mm. Initially, the mixture was fluidized at a high superficial gas velocity for 10 mins[1]. Afterwards, the fluidizing gas was shutoff and

[1] This was done ensure the experimental bed was well mixed

the fluidization tests were then carried out. The local bed density (ρ_b) under fluidized bed conditions was calculated as $\rho_b = \Delta P/(g\,\Delta h)$, where Δh is the distance between pressure taps, see Figure 3.25. The bed voidage, ε, was evaluated as $\varepsilon = 1 - \rho_b/\rho_p$ in order to enable direct comparison with corresponding CFD simulations. Figures 3.20 - 3.22 report the variation of pressure drop with increasing superficial gas velocity using the Natural Rutile-Slag (system 1) mixture characterized by jetsam volumetric concentration of 25%, 50% and 75% respectively. The pressure gradients increasing and decreasing values of superficial gas velocity at three different heights in the bed are shown. From Figures 3.20 - 3.22 it can

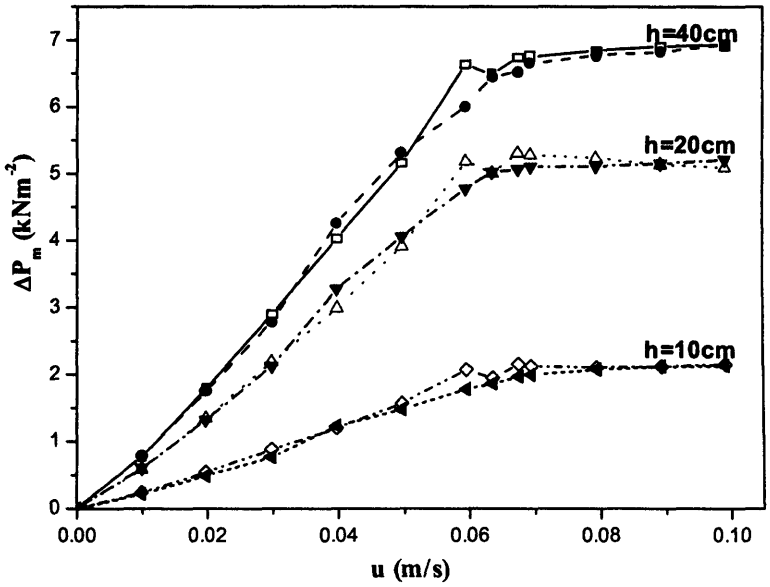

Figure 3.20: *Measured pressure drop versus superficial gas velocity for system 1 mixture: 25% average jetsam (slag) volumetric fraction, $\langle\omega_{jet}\rangle$; hollow symbols: increasing u; closed symbols: decreasing u*

be observed that as the superficial gas velocity is steadily increased, the pressure measured at the bottom of the bed ($h = 10cm$) increases until it reaches a value that is approximately constant ($\approx 2\,kPa$), whereas the pressure measured at higher pressure taps decreases as a result of the progressive increase in concentration of jetsam (slag) particles. The increase in jetsam concentration also leads to a higher settled bed voidage as shown in Figure 3.23. This result is as a consequence of the increasing the overall PSD given that the slag powder has a wide PSD. Overall all the pressure profiles obtained display similar characteristics to that observed for systems with a wide size distribution (Nienow & Chiba, 1985). The measured

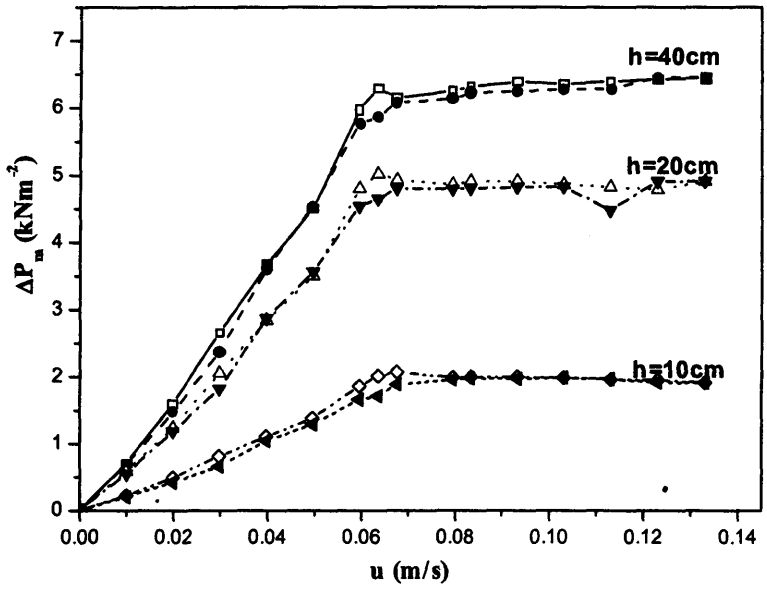

Figure 3.21: *Measured pressure drop versus superficial gas velocity for system 1 mixture: 50% average jetsam (slag) volumetric fraction, $\langle\omega_{jet}\rangle$; hollow symbols: increasing u; closed symbols: decreasing u*

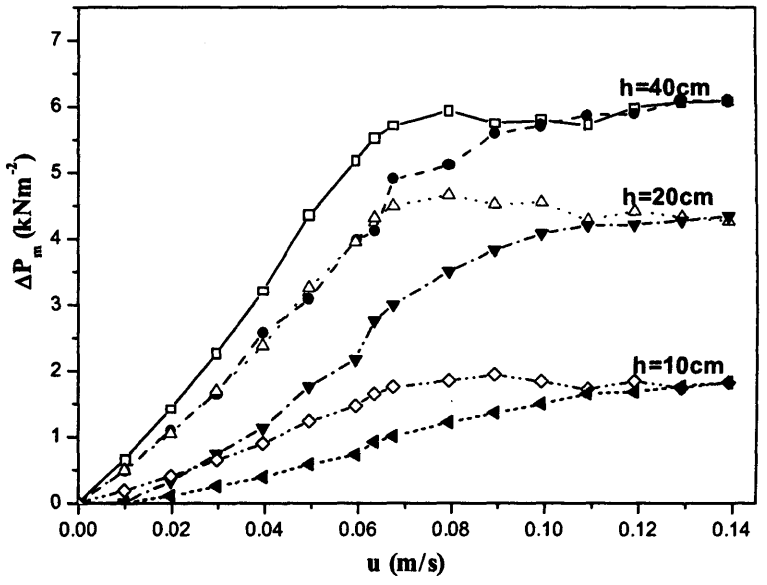

Figure 3.22: *Measured pressure drop versus superficial gas velocity for system 1 mixture: 75% average jetsam (slag) volumetric fraction, $\langle\omega_{jet}\rangle$; hollow symbols: increasing u; closed symbols: decreasing u*

minimum fluidization velocity u_{mf} obtained for different jetsam fractions of system 1 was compared with the empirical correlation proposed by Gossens et al. (1971), reported earlier

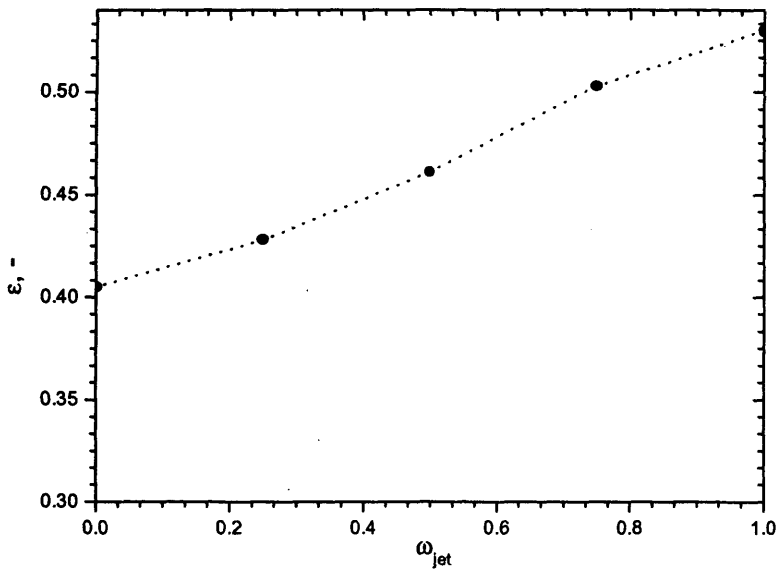

Figure 3.23: *Average bed voidage of mixtures as a function of the average jetsam volumetric fraction* $\langle \omega_{jet} \rangle$

in § 2.5.2 and presented again below for convenience:

$$u_{mf} = \frac{\mu_f}{\rho_f d_m}\left[\left(33.7^2 + 0.0408\,Ar\right)^{0.5} - 33.7\right] \tag{3.6}$$

where the Archimedes number Ar of the mixture is given by:

$$Ar = \frac{\rho_m - \rho_f}{\rho_f} Ga \quad ; \quad \frac{1}{\rho_m} = \frac{\omega_1}{\rho_1} + \frac{\omega_2}{\rho_2} \tag{3.7}$$

and the Galileo number Ga is equal to:

$$Ga = \frac{d_m^3 \rho_f^2 g}{\mu_f^2} \quad ; \quad d_m = \frac{\omega_1 \rho_2 + \omega_2 \rho_1}{\omega_1 \rho_2 d_2 + \omega_2 \rho_1 d_1} d_1 d_2 \tag{3.8}$$

It is noted that in equations (3.7) and (3.8) the quantities ω_1 and ω_2 denote the mass fractions of the larger and smaller particles respectively in the powder devoid of fluid; and take the expressions:

$$\omega_1 = \frac{\phi_1 \rho_1}{\phi_1 \rho_1 + \phi_2 \rho_2} \quad ; \quad \omega_2 = \frac{\phi_2 \rho_2}{\phi_1 \rho_1 + \phi_2 \rho_2} \tag{3.9}$$

Table 3.6 shows a comparison between the experimental values obtained for u_{mf} and val-

ues derived from the empirical correlation by Gossens et al. (1971) for minimum fluidization velocity for system 1. An agreement of 10 – 20% with the empirical correlation of Gossens et al. (1971) was obtained.

Table 3.6: *Comparison of experimental u_{mf} values for system 1 (NR-SG) with the empirical correlation of Gossens et al. (1971)*

Jetsam fraction $\langle\omega_{jet}\rangle$	Exp. m/s	Gossens et al. (1971) m/s
0.25	0.065	0.059
0.50	0.070	0.078
0.75	0.090	0.110

3.3 Experimental rig and Image analysis

The experimental set-up consisted of a two-dimensional plexiglass rectangular column, 600 *mm* high, 350 *mm* wide and 10 *mm* thick. The distributor was a uniform permeable sintered bronze rectangular plate with a thickness of 3.5 *mm*. The bed was filled to an initial height of 300 *mm*, for all experiments. Fluidizing gas, nitrogen, was supplied via flowmeters. Pressure taps are installed 100 *mm* apart along the height of the bed from which pressure readings as a function of the superficial gas velocity are collected via a digitron electronic manometer. A system of two interlocked on/off valves operated simultaneously is installed on the rig to allow for instantaneous evacuation of the fluidizing gas during the "bed freeze tests" performed for the analysis of the mixing and segregation that occurs in the bed. A photograph of the set-up is given in Figure 3.24 and a schematic representation of the rig is shown in Figure 3.25. In the bed freeze test the fluidizing air supply is shut off abruptly. The bed at rest is then split into four horizontal layers, the powder is collected by means of a sampling probe attached to a vacuum pump, which is described later and each layer is subsequently sieved to obtain the percentage by weight of the different components. The sampling probe was designed on purpose by the author, shown in Figure 3.26. The suction required by the probe is provided by means of a vacuum pump. This is operated by embedding the probe

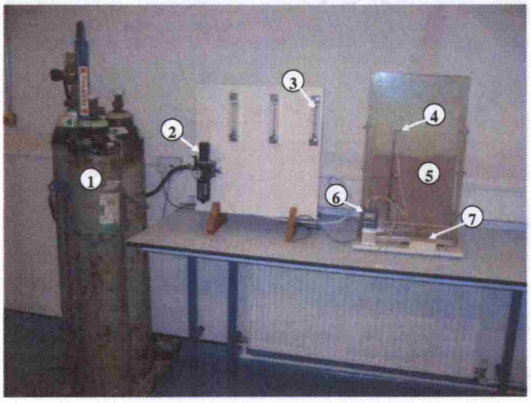

KEY

1 Nitrogen gas

2 Pressure regulator

3 Flowmeter

4 Pressure tap

5 Fluidized bed

6 Electronic manometer

7 On/off valve control switch

Figure 3.24: *2D Experimental vessel: 350 mm wide, 600 mm height, 10 mm depth*

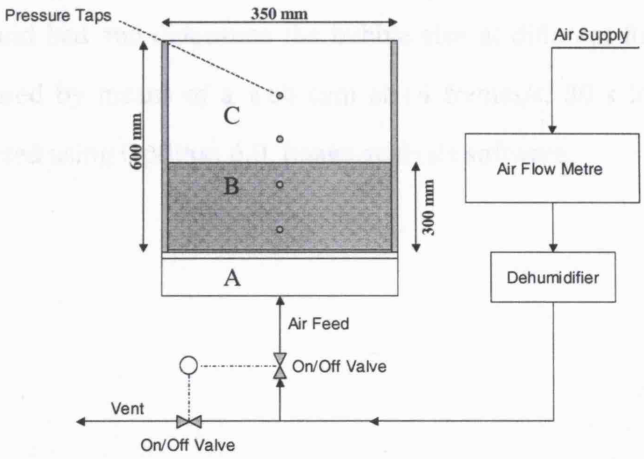

Figure 3.25: *Experimental Apparatus. (A) Windbox; (B) Fluidized bed; (C) Freeboard.*

vertically into the fixed bed, at a set location, after gas supply is hsut off and the bed is at rest material is collected into the sampling container attached (see Figure 3.26) via suction when the actuator attached to the probe is depressed. In this thesis, the probe has only been used for offline measurements (*i.e.* when the fluidzing gas is shut off).

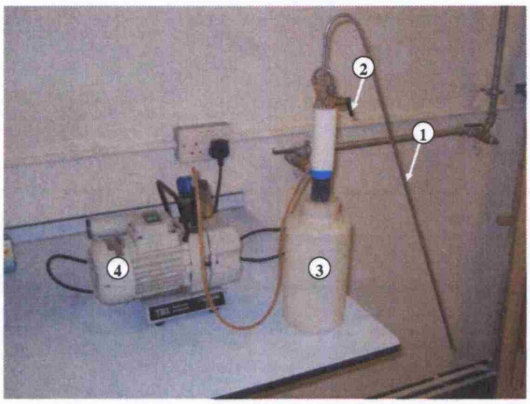

KEY

1 Steel probe

2 Vacuum actuator

3 Sample collector

4 Vacuum pump

Figure 3.26: *Sampling probe for extracting material from the fluid bed*

Digital video recordings of the fluid bed were made to analyse the development of bubble dynamics in the fluid bed and determine the bubble size at different fluidizing velocities. Images were captured by means of a web cam at 14 frames/s, 80 s long and were then subsequently analysed using Optimas 6.0, image analysis software.

Chapter 4

Derivation of the averaged equations of motion for a binary system and numerical control of solids compaction

Summary

This chapter presents a model for the CFD simulation of binary gas-solid fluidized beds. The averaged equations of motion for the fluid and solid phases are derived by extending the two-fluid equations of change for identical spheres in a Newtonian fluid, developed by Anderson & Jackson (1967) and Jackson (1997). A new equation of closure for the fluid-particle interaction force is developed and a new numerical algorithm is used to control the solid phase compaction of each particle phase.

This chapter has been submitted for publication:

Owoyemi, O., Mazzei, L., Lettieri P., (2006). CFD modeling of binary-fluidized suspensions and investigation of role of particle-particle drag on mixing and segregation. *AIChE Journal.*, **53**, 1924 – 1940

Owoyemi, O., Lettieri, P., (2006). A Hydrodynamic Model for the Simulation of Binary Particle Systems in Gas-Fluidized Beds. In *Proceedings of the 10th International Conference on Multiphase Flow in Industrial Plant*, 459-470

4.1 Introduction

The various two-fluid models employed by many authors (Boemer et al., 1997, van Wachem et al., 1998, Peirano et al., 2001, Gelderbloom et al., 2003, Lettieri et al., 2004, Owoyemi et al., 2005) have common origins in the spatially averaged Eulerian-Eulerian equations of motion first put forward by Anderson & Jackson (1967) and successively rigorously derived by several other researchers (Drew & Segel, 1971, Drew, 1971, Whitaker, 1973, Drew, 1983, Drew & Lahey, 1993, Jackson, 1997). Such equations, as it is well known, are not mathematically closed and necessitate empirical closures for contributions mainly related to the stress tensors associated to each phase and to the fluid-particle interaction force. The need for suitable closures, indispensable for predicting the dynamics of multi-phase systems with a satisfactory degree of accuracy, has stimulated a vast amount of original research that has led to the pervasiveness of many empirical closures in literature today.

In this chapter a derivation of the Eulerian-Eulerian averaged equations of motion for binary mixtures of particles in Newtonian fluids is presented. These equations are an extension of those originally put forward by Anderson & Jackson (1967) and Jackson (1997) for systems of mono-size particles in Newtonian fluids, where the averaged equations of conservation for mass, linear and angular momentum where derived and phase interactions modelled phenomenologically. In our derivation, however, only the mass and linear momentum equations of conservation shall be considered. These suffice to provide a rich description of the fluid-solid interaction forces at play in binary mixtures and a logical justification for the emergence of terms such as the particle-particle interaction force or the stress tensors associated with each phase. A brief introduction of a new fluid dynamic model developed in this work for binary fluidized mixtures and implemented in the commercial CFD code CFX4.4 follows thereafter. In this model, the fluid dynamic interaction between fluid and solid is based on the "elastic force" concept originally proposed by Wallis (1969). The solid stress tensors are neglected and a new numerical scheme is proposed in order to control the compaction of each solid phase.

4.2 Equations of change for binary mixtures in newtonian fluids

In this section we seek to derive the averaged equations of motion for binary mixtures, in order to elucidate the fluid-solid and particle-particle interaction forces at play in such systems and provide a mathematical basis for the origin of the particle-particle interaction force. This derivation is achieved by extending earlier work carried out by Anderson & Jackson (1967) and Jackson (1997) for mono-component systems. The formal process of local space averaging is used to obtain the macroscopic *binary system conservation equations* from microscopic equations of conservation. This form of local averaging was first advanced by Anderson & Jackson (1967) and has since been used by a few authors (Whitaker, 1973, Guogh & Zwarts, 1979), though in slightly different form. In this method a weighting function is defined to obtain the averaged values of point properties which could be a scalar, vector or tensorial property. The weighting function, in this case, is used as a device to give "weight" to elements closer to the spatial position wherein the average is computed. The point variables are averaged over regions which are large with respect to the particle diameter but small with respect to the macroscopically length scale of interest. In what follows we extend the earlier work done by deriving new averages associated with the fluid phase for the case of a binary system in a Newtonian fluid. Furthermore, a new contact force in the particle phase momentum equations that accounts for the force which is exerted by particles that belong to different solid phases at their mutual point of contact as proposed [1].

Following Anderson & Jackson (1967) we start by defining a weighting function $g(r)$, where $r = |x - y|$ represents the separation of two points in space. From now onwards, x shall be used to denote the spatial point in which the average is worked out, whereas y shall represent a mute variable of integration. The weighting function is assumed to be a monotonic decreasing function of the radial distance r, and to possess derivatives $g^n(r)$ of all orders for

[1] It is worth noting here that the formal process of averaging will only be applied to the microscopic equation of linear momentum for the binary mixture in this thesis.

each value of r. The integral of g is also normalized so that:

$$4\pi \int_0^\infty g(r) r^2 dr = 1 \tag{4.1}$$

The "radius" l of the weighting function is defined as the scalar which fulfills the following equation:

$$\int_0^l g(r) r^2 dr = \int_l^\infty g(r) r^2 dr \tag{4.2}$$

with $a \ll l \ll L$, where a is the particle radius (regardless of which particular solid phase $\mathscr{F}_i$ is chosen, since the diameters of all the particles present in the mixture are assumed to have the same order of magnitude) and L is the smallest macroscopic length scale of interest, insensitive to variations in the function g. The averaging radius l can be regarded as defining the spherical neighbourhood of $\boldsymbol{x}$ wherein the spatial points have appreciable weight in the averaging process.

4.2.1 Fluid phase averages

The void fraction $\varepsilon(\boldsymbol{x}, t)$ at time t and location $\boldsymbol{x}$ is defined as:

$$\varepsilon(\boldsymbol{x}, t) = \int_{V_f(t)} g(|\boldsymbol{x} - \boldsymbol{y}|)\, dV_y \tag{4.3}$$

where $V_f(t)$ is the volume occupied by the fluid at time t and dV_y is a differential volume in the neighbourhood of the point $\boldsymbol{y}$ (the subscript is used to stress that the mute variable of integration is $\boldsymbol{y}$ and not $\boldsymbol{x}$). From Jackson (1997) the fluid phase average, $\langle \psi \rangle^f(\boldsymbol{x}, t)$, of a generic point property $\psi(\boldsymbol{x}, t)$ is defined by:

$$\langle \psi \rangle^f(\boldsymbol{x}, t) = \frac{1}{\varepsilon(\boldsymbol{x}, t)} \int_{V_f(t)} \psi(\boldsymbol{y}, t)\, g(|\boldsymbol{x} - \boldsymbol{y}|)\, dV_y \tag{4.4}$$

The spatial derivative of a mean quantity can be expressed, through mathematical derivation, as per eq.(4.5) (see Appendix A.1 for a detailed derivation); here two arbitrary size classes

are considered, $\mathscr{F}_1$ and $\mathscr{F}_2$, which represent the two different types of particles, differing in diameter, present in the mixture. It can be seen that eq.(4.5) is a modification of the original expression developed by Jackson (1997) for the fluid-phase spatial derivative for the case of mono-component particle systems. The new term in our case is the last contribution featuring on the R.H.S. of the equation; this is the summation of integrals evaluated on the surfaces which bound the fluid-solid interface of the particles belonging to the phase $\mathscr{F}_2$.

$$\varepsilon(\boldsymbol{x},t)\left\langle\frac{\partial\psi}{\partial x_k}\right\rangle^f(\boldsymbol{x},t)=\frac{\partial}{\partial x_k}\left[\varepsilon(\boldsymbol{x},t)\langle\psi\rangle^f(\boldsymbol{x},t)\right]$$
$$-\sum_{\mathscr{F}_1}\int_{S_1(t)}\psi(\boldsymbol{y},t)\,g(|\boldsymbol{x}-\boldsymbol{y}|)\,n_k(\boldsymbol{y},t)\,dS_y-\sum_{\mathscr{F}_2}\int_{S_2(t)}\psi(\boldsymbol{y},t)\,g(|\boldsymbol{x}-\boldsymbol{y}|)\,n_k(\boldsymbol{y},t)\,dS_y \qquad (4.5)$$

Similarly, through mathematical derivation (see Appendix A.2 for a detailed derivation), the time derivative of a mean quantity for a binary system, with regard to the fluid phase, is given by:

$$\varepsilon(\boldsymbol{x},t)\left\langle\frac{\partial\psi}{\partial t}\right\rangle^f(\boldsymbol{x},t)=\frac{\partial}{\partial t}\left[\varepsilon(\boldsymbol{x},t)\langle\psi\rangle^f(\boldsymbol{x},t)\right]+\sum_{\mathscr{F}_1}\int_{S_1(t)}\psi(\boldsymbol{y},t)\,g(|\boldsymbol{x}-\boldsymbol{y}|)\,\boldsymbol{u}(\boldsymbol{y},t)\cdot\boldsymbol{n}(\boldsymbol{y},t)\,dS_y$$
$$+\sum_{\mathscr{F}_2}\int_{S_2(t)}\psi(\boldsymbol{y},t)\,g(|\boldsymbol{x}-\boldsymbol{y}|)\,\boldsymbol{u}(\boldsymbol{y},t)\cdot\boldsymbol{n}(\boldsymbol{y},t)\,dS_y \qquad (4.6)$$

The integrals herein are taken over the surfaces $S_1(t)$ and $S_2(t)$ of the particles belonging to phases $\mathscr{F}_1$ and $\mathscr{F}_2$ respectively. $\boldsymbol{n}(\boldsymbol{x},t)$ denotes the outward unit normal to the particle surface and $\boldsymbol{u}(\boldsymbol{x},t)$ is the fluid velocity. The last term present on the R.H.S. of eq.(4.6) is the modification being advanced in this work by the present author. Hitherto, the dependence on time t and position $\boldsymbol{x}$ has been stated explicitly; from now onwards, however, in order to simplify the notation, such dependence will be left out unless deemed necessary.

4.2.2 Averaged equations of motion for the fluid phase

In the following, the aforementioned relationships and definitions will now be applied to obtain the macroscopic continuity and linear momentum equations of conservation for the fluid

phase. In what follows the convention is adopted that repeated *lower* indices are summed over the values one to three; upper indices are *not* to be regarded as dummy indices implying summation.

4.2.2.1 Continuity

The continuity equation for the fluid is given by setting $\psi = u_k$ in eq.(4.5) and $\psi = 1$ in eq.(4.6) and then adding the results. The incompressibility assumption, $\langle \partial u_k/\partial x_k \rangle_f (\boldsymbol{x}, t) = 0$, is also applied herein. Implementing the above the following locally averaged equation of mass conservation for the fluid phase is obtained:

$$\frac{\partial \varepsilon}{\partial t} + \frac{\partial}{\partial x_k}\left[\varepsilon \langle u_k \rangle^f\right] = 0 \tag{4.7}$$

4.2.2.2 Momentum

The assumption here is that the fluid is incompressible and satisfies the point Navier-Stokes equation. The Navier-Stokes equation for a single fluid is given by:

$$\rho_f\left[\frac{\partial u_i}{\partial t} + \frac{\partial}{\partial y_k}(u_i u_k)\right] = \frac{\partial \xi_{ik}}{\partial y_k} + \rho_f g_i \tag{4.8}$$

where $\xi_{ik}(\boldsymbol{x}, t)$ is the point value of the ik-th component of the fluid stress tensor and g_i is the i-th component of the gravity vector. The process of averaging this equation involves multiplying both sides by the weighting function $g(|\boldsymbol{x} - \boldsymbol{y}|)$ and integrating over $V_f(t)$ with respect to $\boldsymbol{y}$. By the application of eq.(4.6) with $\psi \equiv u_i$ and of eq.(4.5) with $\psi \equiv u_i u_k$ on the L.H.S. of eq.(4.8), and of eq.(4.6) with $\psi \equiv \xi_{ik}$, on the R.H.S. of eq.(4.8), the following is obtained:

$$\rho_f\left[\frac{\partial}{\partial t}\left(\varepsilon \langle u_i \rangle^f\right) + \frac{\partial}{\partial x_k}\left(\varepsilon \langle u_i u_k \rangle^f\right)\right] = \frac{\partial}{\partial x_k}\left(\varepsilon \langle \xi_{ik} \rangle^f\right) + \varepsilon \rho_f g_i$$

$$- \sum_{\mathscr{F}_1} \int_{S_1(t)} \xi_{ik}(\boldsymbol{y})\, n_k(\boldsymbol{y})\, g(|\boldsymbol{x} - \boldsymbol{y}|)\, dS_y - \sum_{\mathscr{F}_2} \int_{S_2(t)} \xi_{ik}(\boldsymbol{y})\, n_k(\boldsymbol{y})\, g(|\boldsymbol{x} - \boldsymbol{y}|)\, dS_y \tag{4.9}$$

From eq.(4.9) it is immediately evident that the averaging procedure for the case of a binary mixture leads to the emergence of an "extra traction force" appearing in the averaged linear momentum equation for the fluid. This "additional" force is that which is exerted on particles belonging to the additional solid phase $\mathscr{F}_2$. Now the traction terms:

$$-\sum_{\mathscr{F}_1}\int_{S_1(t)} \xi_{ik}(\boldsymbol{y})\, n_k(\boldsymbol{y})\, g(|\boldsymbol{x}-\boldsymbol{y}|)\, dS_y - \sum_{\mathscr{F}_2}\int_{S_2(t)} \xi_{ik}(\boldsymbol{y})\, n_k(\boldsymbol{y})\, g(|\boldsymbol{x}-\boldsymbol{y}|)\, dS_y \qquad (4.10)$$

appearing in eq.(4.9), are the summation of the mean resultant forces exerted by the fluid on the particles of phases $\mathscr{F}_1$ and $\mathscr{F}_2$ respectively. It is worth pointing out that, for each single particle, the mean resultant force is worked out as follows: the differential traction forces acting at each point of the particle surface are first weighted using the local values of the weighting function at the locations under consideration and then summed. The term featuring in eq.(4.10) is the *fluid-solid interaction force* which couples the fluid phase equations of motion to those pertaining to each solid phase present in the mixture. It is however useful to transform eq.(4.10) from a situation where the traction forces exerted at every differential element of the fluid-solid interface are first weighted using the values of the weighting function at the location of the surface elements and then summed, to one where the overall force acting on the entire surface of each particle is first calculated and then weighted by using the value of the weighting function at the particle centre. The latter method of averaging represents a closer physical interpretation of the fluid-solid interaction force (Jackson, 1997) and fulfills Newton's third law of dynamics (principle of action and reaction). The transformation can be achieved by expanding the weighting function in a Taylor series about the centre $\boldsymbol{x}^{\mathscr{C}_i}(t)$ of the generic particle of phase $\mathscr{F}_i$. For particles belonging to phase $\mathscr{F}_1$ we have:

$$g(|\boldsymbol{x}-\boldsymbol{y}|) = g\left(\left|\boldsymbol{x}-\boldsymbol{x}^{\mathscr{C}_1}\right|\right) - \frac{\partial g\left(\left|\boldsymbol{x}-\boldsymbol{x}^{\mathscr{C}_1}\right|\right)}{\partial x_m}\left(y_m - x_m^{\mathscr{C}_1}\right)$$
$$+ \frac{1}{2!}\frac{\partial^2 g\left(\left|\boldsymbol{x}-\boldsymbol{x}^{\mathscr{C}_1}\right|\right)}{\partial x_m \partial x_r}\left(y_m - x_m^{\mathscr{C}_1}\right)\left(y_r - x_r^{\mathscr{C}_1}\right) - \cdots \qquad (4.11)$$

Jackson (1997) has shown that the Taylor series can be truncated at its second order term with acceptably small error. The form of the Taylor series for the particles which belong to the species $\mathscr{F}_2$ is exactly the same as eq.(4.11) and will not be presented for brevity. The following relationships hold true on the surface of each particle species: $\boldsymbol{y}-\boldsymbol{x}^{\mathscr{C}_1}(t) = a_1\,\boldsymbol{n}(\boldsymbol{y},t)$ and $\boldsymbol{y}-\boldsymbol{x}^{\mathscr{C}_2}(t) = a_2\,\boldsymbol{n}(\boldsymbol{y},t)$ where $\boldsymbol{n}(\boldsymbol{y},t)$ is the outward unit normal to the particle surface, and a_1 and a_2 are the radii of the particles belonging to species $\mathscr{F}_1$ and $\mathscr{F}_2$ respectively. The truncated Taylor series above becomes:

$$g(|\boldsymbol{x}-\boldsymbol{y}|) = g\left(\left|\boldsymbol{x}-\boldsymbol{x}^{\mathscr{C}_1}\right|\right) - a_1\,\frac{\partial g\left(\left|\boldsymbol{x}-\boldsymbol{x}^{\mathscr{C}_1}\right|\right)}{\partial x_m}\,n_m(\boldsymbol{y}) + \frac{1}{2!}\,a_1^2\,\frac{\partial^2 g\left(\left|\boldsymbol{x}-\boldsymbol{x}^{\mathscr{C}_1}\right|\right)}{\partial x_m \partial x_r}\,n_m(\boldsymbol{y})\,n_r(\boldsymbol{y}) \tag{4.12}$$

Here again the same applies for particles of type $\mathscr{F}_2$. Introducing eq.(4.12) into eq.(4.10), we obtain for the $\mathscr{F}_1$ particle species:

$$\sum_{\mathscr{F}_1}\int_{S_1(t)} \xi_{ik}(\boldsymbol{y})\,n_k(\boldsymbol{y})\,g(|\boldsymbol{x}-\boldsymbol{y}|)\,dS_y = \sum_{\mathscr{F}_1}\left\{g\left(\left|\boldsymbol{x}-\boldsymbol{x}^{\mathscr{C}_1}\right|\right)\int_{S_1(t)} \xi_{ik}(\boldsymbol{y})\,n_k(\boldsymbol{y})\,dS_y\right\}$$

$$-a_1\,\frac{\partial}{\partial x_m}\sum_{\mathscr{F}_1}\left\{g\left(\left|\boldsymbol{x}-\boldsymbol{x}^{\mathscr{C}_1}\right|\right)\int_{S_1(t)} \xi_{ik}(\boldsymbol{y})\,n_k(\boldsymbol{y})\,n_m(\boldsymbol{y})\,dS_y\right\}$$

$$+\frac{1}{2!}\,a_1^2\,\frac{\partial^2}{\partial x_m \partial x_r}\sum_{\mathscr{F}_1}\left\{g\left(\left|\boldsymbol{x}-\boldsymbol{x}^{\mathscr{C}_1}\right|\right)\int_{S_1(t)} \xi_{ik}(\boldsymbol{y})\,n_k(\boldsymbol{y})\,n_m(\boldsymbol{y})\,n_r(\boldsymbol{y})\,dS_y\right\} \tag{4.13}$$

It is convenient at this point to define the following quantities:

$$n_1 \left\langle f_i^f \right\rangle^{\mathscr{F}_1}(x,t) = \sum_{\mathscr{F}_1} \left\{ g\left(\left|x - x^{\mathscr{C}_1}\right|\right) \int_{S_1(t)} \xi_{ik}(y)\, n_k(y)\, dS_y \right\} \tag{4.14}$$

$$n_1 \left\langle s_{im}^f \right\rangle^{\mathscr{F}_1}(x,t) = a_1 \sum_{\mathscr{F}_1} \left\{ g\left(\left|x - x^{\mathscr{C}_1}\right|\right) \int_{S_1(t)} \xi_{ik}(y)\, n_k(y)\, n_m(y)\, dS_y \right\} \tag{4.15}$$

$$n_1 \left\langle s_{imr}^f \right\rangle^{\mathscr{F}_1}(x,t) = a_1^2 \sum_{\mathscr{F}_1} \left\{ g\left(\left|x - x^{\mathscr{C}_1}\right|\right) \int_{S_1(t)} \xi_{ik}(y)\, n_k(y)\, n_m(y)\, n_r(y)\, dS_y \right\} \tag{4.16}$$

where $n_1(x,t)$ represents the particle number density (number of particles per unit volume) of phase $\mathscr{F}_1$; this term will be formally defined later on in eq.(4.25). By substitution of eqs.(4.14), (4.15) and (4.16) into eq.(4.13), we have:

$$\sum_{\mathscr{F}_1} \int_{S_1(t)} \xi_{ik}(y)\, n_k(y)\, g(|x-y|)\, dS_y$$

$$= n_1 \left\langle f_i^f \right\rangle^{\mathscr{F}_1} - \frac{\partial}{\partial x_m}\left(n_1 \left\langle s_{im}^f \right\rangle^{\mathscr{F}_1}\right) + \frac{1}{2!}\frac{\partial^2}{\partial x_m x_r}\left(n_1 \left\langle s_{imr}^f \right\rangle^{\mathscr{F}_1}\right) \tag{4.17}$$

As stated earlier, the manipulations which have been carried out with regard to particles of species $\mathscr{F}_1$ in eqs.(4.13), (4.14), (4.15) and (4.16) have the same form for particles of species $\mathscr{F}_2$. Bearing this in mind, eq.(4.10) becomes:

$$-n_1 \left\langle f_i^f \right\rangle^{\mathscr{F}_1} - n_2 \left\langle f_i^f \right\rangle^{\mathscr{F}_2}$$

$$+\frac{\partial}{\partial x_m}\left(n_1 \left\langle s_{im}^f \right\rangle^{\mathscr{F}_1} + n_2 \left\langle s_{im}^f \right\rangle^{\mathscr{F}_2}\right) - \frac{1}{2!}\frac{\partial^2}{\partial x_m x_r}\left(n_1 \left\langle s_{imr}^f \right\rangle^{\mathscr{F}_1} + n_2 \left\langle s_{imr}^f \right\rangle^{\mathscr{F}_2}\right) \tag{4.18}$$

Here the corresponding terms for the $\mathscr{F}_2$ particle have been included. Substituting eq.(4.18) into eq.(4.9) results in:

$$\rho_f \left[\frac{\partial}{\partial t}\left(\varepsilon \langle u_i \rangle^f\right) + \frac{\partial}{\partial x_k}\left(\varepsilon \langle u_i u_k \rangle^f\right)\right] = \frac{\partial}{\partial x_k}\left[\varepsilon \langle \xi_{ik} \rangle^f + n_1 \left\langle s_{ik}^f \right\rangle^{\mathscr{F}_1} + n_2 \left\langle s_{ik}^f \right\rangle^{\mathscr{F}_2}\right.$$

$$\left. - \frac{1}{2!}\frac{\partial}{\partial x_r}\left(n_1 \left\langle s_{ikr}^f \right\rangle^{\mathscr{F}_1} + n_2 \left\langle s_{ikr}^f \right\rangle^{\mathscr{F}_2}\right)\right] - n_1 \left\langle f_i^f \right\rangle^{\mathscr{F}_1} - n_2 \left\langle f_i^f \right\rangle^{\mathscr{F}_2} + \varepsilon \rho_f g_i \tag{4.19}$$

The average of the dyadic product featuring on the L.H.S. of eq.(4.19) can be decomposed according to Jackson (1997) in the following way:

$$\langle u_i u_k \rangle^f = \langle u_i \rangle^f \langle u_k \rangle^f + \langle u_i' u_k' \rangle^f \tag{4.20}$$

where $u_i'(\boldsymbol{x}, t)$ denotes the deviation $u_i(\boldsymbol{x}, t) - \langle u_i \rangle^f(\boldsymbol{x}, t)$ of the i-th component of the point fluid velocity from its fluid phase average. By substituting into eq.(4.19) and by carrying out the relevant manipulations, we have:

$$\rho_f \left[\frac{\partial}{\partial t} \left(\varepsilon \langle u_i \rangle^f \right) + \frac{\partial}{\partial x_k} \left(\varepsilon \langle u_i \rangle^f \langle u_k \rangle^f \right) \right] = \frac{\partial}{\partial x_k} \left[\varepsilon \langle \xi_{ik} \rangle^f + n_1 \left\langle s_{ik}^f \right\rangle^{\mathscr{F}_1} + n_2 \left\langle s_{ik}^f \right\rangle^{\mathscr{F}_2} \right.$$
$$\left. - \frac{1}{2!} \frac{\partial}{\partial x_r} \left(n_1 \left\langle s_{ikr}^f \right\rangle^{\mathscr{F}_1} + n_2 \left\langle s_{ikr}^f \right\rangle^{\mathscr{F}_2} \right) - \varepsilon \rho_f \langle u_i' u_k' \rangle^f \right] - n_1 \left\langle f_i^f \right\rangle^{\mathscr{F}_1} - n_2 \left\langle f_i^f \right\rangle^{\mathscr{F}_2} + \varepsilon \rho_f g_i \tag{4.21}$$

Eq.(4.21) can be more conveniently arranged in the form:

$$\rho_f \left[\frac{\partial}{\partial t} \left(\varepsilon \langle u_i \rangle^f \right) + \frac{\partial}{\partial x_k} \left(\varepsilon \langle u_i \rangle^f \langle u_k \rangle^f \right) \right] = \frac{\partial \mathcal{T}_{ik}^f}{\partial x_k} - n_1 \left\langle f_i^f \right\rangle^{\mathscr{F}_1} - n_2 \left\langle f_i^f \right\rangle^{\mathscr{F}_2} + \varepsilon \rho_f g_i \tag{4.22}$$

where the term $\mathcal{T}_{ik}^f(\boldsymbol{x}, t)$ is defined by:

$$\mathcal{T}_{ik}^f = \varepsilon \langle \xi_{ik} \rangle^f + n_1 \left\langle s_{ik}^f \right\rangle^{\mathscr{F}_1} + n_2 \left\langle s_{ik}^f \right\rangle^{\mathscr{F}_2} - \frac{1}{2!} \frac{\partial}{\partial x_r} \left(n_1 \left\langle s_{ikr}^f \right\rangle^{\mathscr{F}_1} + n_2 \left\langle s_{ikr}^f \right\rangle^{\mathscr{F}_2} \right) - \varepsilon \rho_f \langle u_i' u_k' \rangle^f \tag{4.23}$$

and denotes the ik-th component of the effective stress tensor pertaining to the fluid phase. The last term on the R.H.S. of eq.(4.23), $\varepsilon \rho_f \left\langle u_i' u_k' \right\rangle^f$, is analogous to the "Reynolds stress contribution" in turbulent flow and is representative of the fluctuations of the fluid velocity about its mean value. It is evident that finding an analytical closure for the effective fluid stress tensor appears to be a problem of extraordinary complexity; however, a closure has been derived by Jackson (1997) on theoretical grounds in the limiting case of diluted, Stokesian mono-component mixtures fluidized by Newtonian fluids. Appropriate closures for the terms on the R.H.S. of eq.(4.22) are described later on in §4.3. The same principles used in deriving the averaged fluid phase equations of motion to shall now be applied to the case of the solid phases.

4.2.3 Solid phase volume fraction

In the present section we provide the expressions for the volume fraction of each solid phase present in the mixture. The local volume fraction $\phi_i(\boldsymbol{x}, t)$ of the generic particle species $\mathscr{F}_i$ is defined as:

$$\phi_i(\boldsymbol{x}, t) = \sum_{\mathscr{F}_i} \int_{V_i(t)} g(|\boldsymbol{x} - \boldsymbol{y}|)\, dV_y \tag{4.24}$$

where $V_i(t)$ denotes the volume occupied by the generic particle belonging to the solid phase $\mathscr{F}_i$ at the time t of interest.

By following a similar approach to the one shown in the previous section, it could be possible to define also local space averages of point variables with reference to each solid phase $\mathscr{F}_i$; in what follows, however, such averages will not be employed and therefore their definition shall not be reported.

4.2.4 Particle phase averages

In order to derive the mass and linear momentum equations of conservation for each particle phase, *particle phase averages* are required; these, as we shall presently see, are based on properties of the particles as a whole. Examples of such properties are, for instance, the resultant force and the resultant torque exerted by the fluid on each single particle of the system. Applying similar averages to those advanced by Jackson (1997), the number density $n_i(\boldsymbol{x}, t)$ for the particle species $\mathscr{F}_i$ is given by:

$$n_i(\boldsymbol{x}, t) = \sum_{\mathscr{F}_i} g\left(\left|\boldsymbol{x} - \boldsymbol{x}^{\mathscr{C}_i}\right|\right) \tag{4.25}$$

where $\boldsymbol{x}^{\mathscr{C}_i}(t)$ is the position of the centre of the generic particle belonging to phase $\mathscr{F}_i$. The solid volume fraction $\phi_i(\boldsymbol{x}, t)$ is related to the number density $n_i(\boldsymbol{x}, t)$ by the following approximate relationship (here reported without proof for the sake of brevity):

$$\phi_i(\boldsymbol{x}, t) = n_i(\boldsymbol{x}, t)\, V_i \tag{4.26}$$

Eq.(4.26) can be derived by expanding the function $\phi_i(\boldsymbol{x}, t)$ as a Taylor series about the particle centre $\boldsymbol{x}^{\mathscr{C}_i}(t)$ and by retaining only the constant term of the series (Jackson, 1997). The particle-phase average $\langle\psi\rangle^{\mathscr{F}_i}(\boldsymbol{x}, t)$ for the phase $\mathscr{F}_i$ of a particle property $\psi^p(t)$ is defined as:

$$\langle\psi\rangle^{\mathscr{F}_i}(\boldsymbol{x}, t) = \frac{1}{n_i(\boldsymbol{x}, t)} \sum_{\mathscr{F}_i} \left[\psi^p(t)\, g\left(\left|\boldsymbol{x} - \boldsymbol{x}^{\mathscr{C}_i}\right|\right) \right] \tag{4.27}$$

It can be shown that the particle-phase time derivative of an averaged variable $\langle\psi\rangle^{\mathscr{F}_i}(\boldsymbol{x}, t)$ is given by Jackson (1997):

$$n_i(\boldsymbol{x}, t) \left\langle \frac{d\psi}{dt} \right\rangle^{\mathscr{F}_i}(\boldsymbol{x}, t) = \frac{\partial}{\partial t}\left[n_i(\boldsymbol{x}, t)\, \langle\psi\rangle^{\mathscr{F}_i}(\boldsymbol{x}, t) \right] + \frac{\partial}{\partial x_k}\left[n_i(\boldsymbol{x}, t)\, \langle\psi\, u_k\rangle^{\mathscr{F}_i}(\boldsymbol{x}, t) \right] \tag{4.28}$$

where $u_k^p(t)$ denotes the k-th component of the velocity of the centre of the generic particle p. Since the particle properties $\psi^p(t)$ are pure functions of time, no analogous expression to equation (4.5) can be derived for this kind of averages.

4.2.5 Averaged equations of motion for the particle phase

The mass and linear momentum averaged equations of conservation for each particle species in the system will now be derived. The equations shall be developed by making reference only to phase $\mathscr{F}_1$ as the mathematical manipulations involved are the same for both phases.

4.2.5.1 Continuity

The continuity equation for solid phase $\mathscr{F}_1$, in terms of phase averages, can be derived by setting $\psi^p \equiv 1$ in equation (4.28); doing so yields:

$$\frac{\partial n_1}{\partial t} + \frac{\partial}{\partial x_k}\left(n_1 \langle u_k\rangle^{\mathscr{F}_1} \right) = 0 \tag{4.29}$$

4.2.5.2 Momentum

In writing the linear momentum equation for the particles present in the binary mixture, Newton's second law of motion is applied. The forces to be taken into consideration include the traction forces exerted by the fluid on the particles, the forces arising as a result of collisions between particles of the same species at their mutual points of contact, those arising as a result of collisions between particles of different species at their mutual points of contacts and the effect of gravity. Accordingly, the linear momentum equation for the generic particle p of phase $\mathscr{F}_1$ takes the form:

$$\rho_1 V_1 \frac{du_i^p}{dt} = \int_{S_1(t)} \xi_{ik}(y)\, n_k(y)\, dS_y + \sum_{\substack{q \neq p \\ q \in \mathscr{F}_1}} f_i^{pq} + \sum_{\substack{z \neq p \\ z \in \mathscr{F}_2}} f_i^{pz} + \rho_1 V_1 g_i \tag{4.30}$$

The first term on the R.H.S. is the traction force exerted on the surface of the generic particle p of phase $\mathscr{F}_1$ by the surrounding fluid. The second term is the sum of the forces $f_i^{pq}(t)$ exerted on the particle p by the particles q belonging to phase $\mathscr{F}_1$. Finally, the third term is the sum of the forces $f_i^{pz}(t)$ exerted on the particle p by the particles z belonging to phase $\mathscr{F}_2$. Indeed the terms $f_i^{pq}(t)$ and $f_i^{pz}(t)$ do not vanish only for a limited number of particles, namely those which happen to be in direct contact with the particle p at the time t of interest. The third contribution on the R.H.S. of eq.(4.30) represents the "additional force" that has to be taken into account when considering binary mixtures. This term, as we shall see, gives rise to the inter-phase particle-particle interaction force acting between the two solid phases (which are, in a eulerian framework, continuous and no longer dispersed). Eq.(4.30) is averaged by multiplying both sides by $g\left(\left|x - x^{\mathscr{C}_1}\right|\right)$ and by summing over all the particles p belonging to the phase under consideration (in the present instance $\mathscr{F}_1$).

$$\rho_1 V_1 \sum_{\mathscr{F}_1}\left[g\left(\left|x - x^{\mathscr{C}_1}\right|\right) \frac{du_i^p}{dt} \right] = \sum_{\mathscr{F}_1}\left\{ g\left(\left|x - x^{\mathscr{C}_1}\right|\right) \int_{S_1(t)} \xi_{ik}(y)\, n_k(y)\, dS_y \right\} \tag{4.31}$$

$$+ \sum_{\mathscr{F}_1}\left\{ g\left(\left|x - x^{\mathscr{C}_1}\right|\right) \sum_{\substack{q \neq p \\ q \in \mathscr{F}_1}} f_i^{pq} \right\} + \sum_{\mathscr{F}_1}\left\{ g\left(\left|x - x^{\mathscr{C}_1}\right|\right) \sum_{\substack{z \neq p \\ z \in \mathscr{F}_2}} f_i^{pz} \right\} + \rho_1 V_1 g_i \sum_{\mathscr{F}_1} g\left(\left|x - x^{\mathscr{C}_1}\right|\right)$$

Using eqs.(4.14), (4.25), (4.27) and (4.28), choosing $\psi^p \equiv u_i^p$, we can write eq.(4.31) as:

$$\rho_1 V_1 \left[\frac{\partial}{\partial t} \left(n_1 \langle u_i \rangle^{\mathscr{F}_1} \right) + \frac{\partial}{\partial x_k} \left(n_1 \langle u_i u_k \rangle^{\mathscr{F}_1} \right) \right] = n_1 \left\langle f_i^f \right\rangle^{\mathscr{F}_1} + n_1 \rho_1 V_1 g_i$$

$$+ \sum_{\mathscr{F}_1} \left\{ g\left(|x - x^{\mathscr{C}_1}| \right) \sum_{\substack{q \neq p \\ q \in \mathscr{F}_1}} f_i^{pq} \right\} + \sum_{\mathscr{F}_1} \left\{ g\left(|x - x^{\mathscr{C}_1}| \right) \sum_{\substack{z \neq p \\ z \in \mathscr{F}_2}} f_i^{pz} \right\} \tag{4.32}$$

The first term on the R.H.S. of eq.(4.32) is the fluid-particle interaction force relevant to phase $\mathscr{F}_1$ which has its exact analogue in eq.(4.22). The last two terms of the equation, instead, refer respectively to the resultant forces arising from the particle-particle contacts between a) particles belonging to the same phase, b) particles belonging to different phases. In consideration of this, such contributions are conceptually different; the former is representative of the stress *internal* to the phase under exam, whereas the second can be interpreted as a contact force acting *between* the two eulerian solid phases. In order for the solid stress tensor associated to phase $\mathscr{F}_1$ to appear explicitly in eq.(4.32), further mathematical manipulations are required. Following (Jackson, 1997), we start by considering the following double sum over the particles p of phase $\mathscr{F}_1$:

$$\sum_{\mathscr{F}_1} \sum_{\substack{q \neq p \\ q \in \mathscr{F}_1}} \left[g\left(|x - x^{pq}| \right) f_i^{pq} \right] \tag{4.33}$$

where $x^{pq}(t)$ is the position of the point of mutual contact between the particles p and q, where also q belongs to the same phase $\mathscr{F}_1$. The double sum vanishes since $x^{pq}(t) = x^{qp}(t)$ and $f_i^{pq}(t) = -f_i^{qp}(t)$ (principle of action and reaction). By expanding the function $g(|x - x^{pq}|)$ as a Taylor series in the variable x^{pq} about the centre $x^{\mathscr{C}_1}(t)$ of the particles,

we obtain:

$$0 = \sum_{\mathscr{F}_1}\left\{g\left(|\boldsymbol{x}-\boldsymbol{x}^{\mathscr{C}_1}|\right)\sum_{\substack{q\neq p\\ q\in\mathscr{F}_1}} f_i^{pq}\right\} - a_1\frac{\partial}{\partial x_k}\sum_{\mathscr{F}_1}\left\{g\left(|\boldsymbol{x}-\boldsymbol{x}^{\mathscr{C}_1}|\right)\sum_{\substack{q\neq p\\ q\in\mathscr{F}_1}}\left(f_i^{pq}n_k^{pq}\right)\right\}$$

$$+\frac{1}{2!}a_1^2\frac{\partial^2}{\partial x_k\partial x_m}\sum_{\mathscr{F}_1}\left\{g\left(|\boldsymbol{x}-\boldsymbol{x}^{\mathscr{C}_1}|\right)\sum_{\substack{q\neq p\\ q\in\mathscr{F}_1}}\left(f_i^{pq}n_k^{pq}n_m^{pq}\right)\right\} - \cdots \tag{4.34}$$

where the unit vector $\boldsymbol{n}^{pq}(t)$ is given by the relation:

$$\boldsymbol{n}^{pq}(t) = \frac{1}{a_1}\left[\boldsymbol{x}^{pq}(t) - \boldsymbol{x}^{\mathscr{C}_1}(t)\right] \tag{4.35}$$

It is now convenient to define the following functions:

$$n_1\left\langle s_{ik}^p\right\rangle^{\mathscr{F}_1}(\boldsymbol{x},t) = a_1\sum_{\mathscr{F}_1}\left\{g\left(|\boldsymbol{x}-\boldsymbol{x}^{\mathscr{C}_1}|\right)\sum_{\substack{q\neq p\\ q\in\mathscr{F}_1}}\left[f_i^{pq}(t)\,n_k^{pq}(t)\right]\right\} \tag{4.36}$$

$$n_1\left\langle s_{ikm}^p\right\rangle^{\mathscr{F}_1}(\boldsymbol{x},t) = a_1^2\sum_{\mathscr{F}_1}\left\{g\left(|\boldsymbol{x}-\boldsymbol{x}^{\mathscr{C}_1}|\right)\sum_{\substack{q\neq p\\ q\in\mathscr{F}_1}}\left[f_i^{pq}(t)\,n_k^{pq}(t)\,n_m^{pq}(t)\right]\right\} \tag{4.37}$$

Replacing eqs.(4.36) and (4.37) into eq.(4.34), and retaining only the first three terms of the series, yields:

$$\sum_{\mathscr{F}_1}\left\{g\left(|\boldsymbol{x}-\boldsymbol{x}^{\mathscr{C}_1}|\right)\sum_{\substack{q\neq p\\ q\in\mathscr{F}_1}} f_i^{pq}\right\} = \frac{\partial}{\partial x_k}\left(n_1\left\langle s_{ik}^p\right\rangle^{\mathscr{F}_1}\right) - \frac{1}{2!}\frac{\partial^2}{\partial x_k\partial x_m}\left(n_1\left\langle s_{ikm}^p\right\rangle^{\mathscr{F}_1}\right) \tag{4.38}$$

Substitution of eq.(4.38) into eq.(4.32) gives:

$$\rho_1 V_1\left[\frac{\partial}{\partial t}\left(n_1\langle u_i\rangle^{\mathscr{F}_1}\right) + \frac{\partial}{\partial x_k}\left(n_1\langle u_i u_k\rangle^{\mathscr{F}_1}\right)\right] = \frac{\partial}{\partial x_k}\left[n_1\left\langle s_{ik}^p\right\rangle^{\mathscr{F}_1} - \frac{1}{2!}\frac{\partial}{\partial x_m}\left(n_1\left\langle s_{ikm}^p\right\rangle^{\mathscr{F}_1}\right)\right]$$

$$+ n_1\left\langle f_i^f\right\rangle^{\mathscr{F}_1} + \sum_{\mathscr{F}_1}\left\{g\left(|\boldsymbol{x}-\boldsymbol{x}^{\mathscr{C}_1}|\right)\sum_{\substack{z\neq p\\ z\in\mathscr{F}_2}} f_i^{pz}\right\} + n_1\rho_1 V_1 g_i \tag{4.39}$$

We finally have to tackle the last term on the R.H.S. of eq.(4.32). This contribution is representative of the contact force acting between phases $\mathscr{F}_1$ and $\mathscr{F}_2$. Accordingly, the force must fulfill the principle of action and reaction; that is, the following relationship should hold:

$$\sum_{\mathscr{F}_1}\left\{g\left(\left|x-x^{\mathscr{C}_1}\right|\right)\sum_{\substack{z\neq p\\ z\in\mathscr{F}_2}} f_i^{pz}\right\} = -\sum_{\mathscr{F}_2}\left\{g\left(\left|x-x^{\mathscr{C}_2}\right|\right)\sum_{\substack{p\neq z\\ p\in\mathscr{F}_1}} f_i^{zp}\right\} \tag{4.40}$$

It is not difficult to see that such condition cannot be met. Even if Newton's third law of motion guarantees that $f_i^{pz}(t)$ is equal and opposite to $f_i^{zp}(t)$, eq.(4.40) is not fulfilled since $g\left(\left|x-x^{\mathscr{C}_1}\right|\right)$ differs from $g\left(\left|x-x^{\mathscr{C}_2}\right|\right)$. In other words, since in the particle averages of eq.(4.40) the forces are not given the same weight (insomuch as $x^{\mathscr{C}_1} \neq x^{\mathscr{C}_2}$), their being equal and opposite does not suffice to render the summations equal to one another in magnitude. This conceptual paradox is very similar to the one encountered by (Jackson, 1997, 2001) in connection with the interaction force between fluid and particles in mono-component systems. It is intrinsically related to the way in which the averages are mathematically performed, and directly stems form the use of *particle averages* rather than *solid averages* in the derivation of the macroscopic dynamical equations for the dispersed phases of the system. For more details concerning these alternative averaging procedures, their advantages and drawbacks, and the implications that their employment entails, the reader should refer to Jackson (1997, 2001). In our specific instance, In order to overcome this conceptual paradox, we operate as follows; we first expand the function $g\left(\left|x-x^{\mathscr{C}_1}\right|\right)$ as a Taylor series in the variable $x^{\mathscr{C}_1}$ about the point $x^{pz}(t)$ representative of the position of mutual contact between the generic particle p of phase $\mathscr{F}_1$ and the generic particle z of phase $\mathscr{F}_2$:

$$g\left(\left|x-x^{\mathscr{C}_1}\right|\right) = g\left(|x-x^{pz}|\right) - a_1\frac{\partial g\left(|x-x^{pz}|\right)}{\partial x_k}n_k(y) + \frac{1}{2!}a_1^2\frac{\partial^2 g\left(|x-x^{pz}|\right)}{\partial x_k \partial x_r}n_k(y)\,n_r(y) - \cdots \tag{4.41}$$

We then introduce eq.(4.41) into the L.H.S. of eq.(4.40), retaining only the first three terms of the series; this leads to:

$$\sum_{\mathscr{F}_1}\left\{g\left(|x-x^{\mathscr{C}_1}|\right)\sum_{\substack{z\neq p\\ z\in\mathscr{F}_2}} f_i^{pz}\right\} = \sum_{\mathscr{F}_1}\left\{g\left(|x-x^{pz}|\right)\sum_{\substack{z\neq p\\ z\in\mathscr{F}_2}} f_i^{pz}\right\} \tag{4.42}$$

$$-a_1\frac{\partial}{\partial x_k}\sum_{\mathscr{F}_1}\left\{g\left(|x-x^{pz}|\right)\sum_{\substack{z\neq p\\ z\in\mathscr{F}_2}}\left(f_i^{pz}n_k^{pz}\right)\right\}+\frac{1}{2!}a_1^2\frac{\partial^2}{\partial x_k\partial x_r}\sum_{\mathscr{F}_1}\left\{g\left(|x-x^{pz}|\right)\sum_{\substack{z\neq p\\ z\in\mathscr{F}_2}}\left(f_i^{pz}n_k^{pz}n_r^{pz}\right)\right\}$$

Eq.(4.42) can be rewritten in the compact form:

$$\sum_{\mathscr{F}_1}\left\{g\left(|x-x^{\mathscr{C}_1}|\right)\sum_{\substack{z\neq p\\ z\in\mathscr{F}_2}} f_i^{pz}\right\} = n_1\left\langle f_i^p\right\rangle^{\mathscr{F}_1}-\frac{\partial}{\partial x_k}\left(n_1\left\langle r_{ik}^p\right\rangle^{\mathscr{F}_1}\right)+\frac{1}{2!}\frac{\partial^2}{\partial x_k\partial x_r}\left(n_1\left\langle r_{ikm}^p\right\rangle^{\mathscr{F}_1}\right) \tag{4.43}$$

where:

$$n_1\left\langle f_i^p\right\rangle^{\mathscr{F}_1}(x,t) = \sum_{\mathscr{F}_1}\left\{g\left(|x-x^{pz}|\right)\sum_{\substack{z\neq p\\ z\in\mathscr{F}_2}} f_i^{pz}(t)\right\} \tag{4.44}$$

$$n_1\left\langle r_{ik}^p\right\rangle^{\mathscr{F}_1}(x,t) = a_1\sum_{\mathscr{F}_1}\left\{g\left(|x-x^{pz}|\right)\sum_{\substack{z\neq p\\ z\in\mathscr{F}_2}}\left[f_i^{pz}(t)\,n_k^{pz}(t)\right]\right\} \tag{4.45}$$

$$n_1\left\langle r_{ikm}^p\right\rangle^{\mathscr{F}_1}(x,t) = a_1^2\sum_{\mathscr{F}_1}\left\{g\left(|x-x^{pz}|\right)\sum_{\substack{z\neq p\\ z\in\mathscr{F}_2}}\left[f_i^{pz}(t)\,n_k^{pz}(t)\,n_r^{pz}(t)\right]\right\} \tag{4.46}$$

Upon substitution of eq.(4.43) into eq.(4.39), we have:

$$\rho_1 V_1\left[\frac{\partial}{\partial t}\left(n_1\langle u_i\rangle^{\mathscr{F}_1}\right)+\frac{\partial}{\partial x_k}\left(n_1\langle u_i u_k\rangle^{\mathscr{F}_1}\right)\right] = \frac{\partial}{\partial x_k}\left[n_1\left\langle s_{ik}^p\right\rangle^{\mathscr{F}_1}-n_1\left\langle r_{ik}^p\right\rangle^{\mathscr{F}_1}\right.$$

$$\left.-\frac{1}{2!}\frac{\partial}{\partial x_m}\left(n_1\left\langle s_{ikm}^p\right\rangle^{\mathscr{F}_1}-n_1\left\langle r_{ikm}^p\right\rangle^{\mathscr{F}_1}\right)\right]+n_1\left\langle f_i^f\right\rangle^{\mathscr{F}_1}+n_1\left\langle f_i^p\right\rangle^{\mathscr{F}_1}+n_1\rho_1 V_1 g_i \tag{4.47}$$

The term $n_1\left\langle f_i^p\right\rangle^{\mathscr{F}_1}$ fulfills the principle of action and reaction and therefore can be regarded as the effecting inter-phase interaction force between the solid phases. The remaining terms

of the Taylor series which constitute the L.H.S. of eq.(4.43) are instead lumped within the solid stress tensor of the phase under exam. The average of the dyadic product on the L.H.S. of eq.(4.47) can be related to the dyad of the averaged particle velocities following similar considerations to those presented earlier for the fluid phase (refer to eq.(4.20)). This leads to the final result:

$$\rho_1 V_1 \left[\frac{\partial}{\partial t} \left(n_1 \langle u_i \rangle^{\mathscr{F}_1} \right) + \frac{\partial}{\partial x_k} \left(n_1 \langle u_i \rangle^{\mathscr{F}_1} \langle u_k \rangle^{\mathscr{F}_1} \right) \right] = \frac{\partial \mathcal{T}_{ik}^1}{\partial x_k} + n_1 \left\langle f_i^f \right\rangle^{\mathscr{F}_1} + n_1 \left\langle f_i^p \right\rangle^{\mathscr{F}_1} + n_1 \rho_1 V_1 g_i \tag{4.48}$$

where the term $\mathcal{T}_{ik}^1 (\boldsymbol{x}, t)$ is defined by:

$$\mathcal{T}_{ik}^1 = n_1 \left\langle s_{ik}^p \right\rangle^{\mathscr{F}_1} - n_1 \left\langle r_{ik}^p \right\rangle^{\mathscr{F}_1} - \frac{1}{2!} \frac{\partial}{\partial x_m} \left(n_1 \left\langle s_{ikm}^p \right\rangle^{\mathscr{F}_1} - n_1 \left\langle r_{ikm}^p \right\rangle^{\mathscr{F}_1} \right) - n_1 \rho_1 V_1 \langle u_i' u_k' \rangle^{\mathscr{F}_1} \tag{4.49}$$

and denotes the ik-th component of the effective stress tensor for the solid phase $\mathscr{F}_1$. For completeness we also report the corresponding averaged equation of conservation for the linear momentum pertaining to phase $\mathscr{F}_2$:

$$\rho_2 V_2 \left[\frac{\partial}{\partial t} \left(n_2 \langle u_i \rangle^{\mathscr{F}_2} \right) + \frac{\partial}{\partial x_k} \left(n_2 \langle u_i \rangle^{\mathscr{F}_2} \langle u_k \rangle^{\mathscr{F}_2} \right) \right] = \frac{\partial \mathcal{T}_{ik}^2}{\partial x_k} + n_2 \left\langle f_i^f \right\rangle^{\mathscr{F}_2} + n_2 \left\langle f_i^p \right\rangle^{\mathscr{F}_2} + n_2 \rho_2 V_2 g_i \tag{4.50}$$

where attention should be drawn to the fact that for the principle of action and reaction the following relation holds:

$$n_2 \left\langle f_i^p \right\rangle^{\mathscr{F}_2} = - n_1 \left\langle f_i^p \right\rangle^{\mathscr{F}_1} \tag{4.51}$$

Using the approximation eq.(4.26), the Eulerian-Eulerian averaged equations of motion for binary fluidized mixtures of solid particles in Newtonian fluids can be summarized, in tensorial form, as shown in Table 4.1. At first inspection, the analytical form of the final equations does not differ significantly from other formulations already present in literature (this is somewhat encouraging since formally the general expressions of such equations is indeed well established); the method of averaging, however, considerably does.

Table 4.1: *Equations of motion for a binary system.*

Continuity Equation - Fluid Phase

$$\frac{\partial \varepsilon}{\partial t} + \nabla \cdot \left(\varepsilon \langle \boldsymbol{u} \rangle^{f} \right) = 0$$

Continuity Equation - Solid Phase k

$$\frac{\partial \phi_k}{\partial t} + \nabla \cdot \left(\phi_k \langle \boldsymbol{u} \rangle^{\mathscr{F}_k} \right) = 0$$

Momentum Equation - Fluid Phase

$$\rho_f \left[\frac{\partial}{\partial t} \left(\varepsilon \langle \boldsymbol{u} \rangle^{f} \right) + \nabla \cdot \left(\varepsilon \langle \boldsymbol{u} \rangle^{f} \langle \boldsymbol{u} \rangle^{f} \right) \right] = \nabla \cdot \mathfrak{T}^{f} - n_1 \left\langle \boldsymbol{f}^{f} \right\rangle^{\mathscr{F}_1} - n_2 \left\langle \boldsymbol{f}^{f} \right\rangle^{\mathscr{F}_2} + \varepsilon \rho_f \boldsymbol{g}$$

Momentum Equation - Solid Phase 1

$$\rho_1 \left[\frac{\partial}{\partial t} \left(\phi_1 \langle \boldsymbol{u} \rangle^{\mathscr{F}_1} \right) + \nabla \cdot \left(\phi_1 \langle \boldsymbol{u} \rangle^{\mathscr{F}_1} \langle \boldsymbol{u} \rangle^{\mathscr{F}_1} \right) \right] = \nabla \cdot \mathfrak{T}^{1} + n_1 \left\langle \boldsymbol{f}^{f} \right\rangle^{\mathscr{F}_1} + n_1 \langle \boldsymbol{f}^{p} \rangle^{\mathscr{F}_1} + \phi_1 \rho_1 \boldsymbol{g}$$

Momentum Equation - Solid Phase 2

$$\rho_2 \left[\frac{\partial}{\partial t} \left(\phi_2 \langle \boldsymbol{u} \rangle^{\mathscr{F}_2} \right) + \nabla \cdot \left(\phi_2 \langle \boldsymbol{u} \rangle^{\mathscr{F}_2} \langle \boldsymbol{u} \rangle^{\mathscr{F}_2} \right) \right] = \nabla \cdot \mathfrak{T}^{2} + n_2 \left\langle \boldsymbol{f}^{f} \right\rangle^{\mathscr{F}_2} - n_1 \langle \boldsymbol{f}^{p} \rangle^{\mathscr{F}_1} + \phi_2 \rho_2 \boldsymbol{g}$$

To the authors knowledge, no other research group has applied the averaging scheme put forward by Anderson & Jackson (1967) and Jackson (1997) in order to derive averaged equations of motion for binary systems. In the authors opinion, the application of such a scheme, along with the various considerations previously presented, adds considerable insight into the meaning of each of the terms featuring in the equations. Moreover, the particle phase method of averaging which is advocate seems to be particularly suitable for solid fluidized suspensions since, being based on the Lagrangian equations of motion for material bodies, it captures most effectively the physics underlying the dynamics of particulate systems. Appropriate closures, which will be applied to the case studies, will now be discussed in the next section.

4.3 Closure relationships

4.3.1 Effective stress tensor closures

Eq. (4.23) and (4.49) reveal quite clearly the complex nature of the internal stress associated with each eulerian phase; this complexity arises from the several different contributions which ultimately make up the effective stress tensors obtained from the averaging process. This renders the problem of finding appropriate closure relationships, especially based on theoretical grounds, extremely difficult. A vast amount of theoretical research shall probably have to be conducted before the attainment of satisfactory closures. A first approximation commonly employed in the interim is to assume a Newtonian behaviour for each continuum, albeit there are clear indications that such a view is over simplistic (Jackson, 2001). In this approach the effective stress tensors take the form:

$$\mathcal{T}^f = -\langle p\rangle^f \boldsymbol{I} + \mu_f\left[\nabla\langle \boldsymbol{u}\rangle^f + \left(\nabla\langle \boldsymbol{u}\rangle^f\right)^T\right] + \left(\kappa_f - \frac{2}{3}\mu_f\right)\nabla\cdot\langle \boldsymbol{u}\rangle^f \boldsymbol{I} \tag{4.52}$$

$$\mathcal{T}^k = -\langle p\rangle^{\mathcal{F}_k} \boldsymbol{I} + \mu_k\left[\nabla\langle \boldsymbol{u}\rangle^{\mathcal{F}_k} + \left(\nabla\langle \boldsymbol{u}\rangle^{\mathcal{F}_k}\right)^T\right] + \left(\kappa_k - \frac{2}{3}\mu_k\right)\nabla\cdot\langle \boldsymbol{u}\rangle^{\mathcal{F}_k} \boldsymbol{I} \tag{4.53}$$

and the closure problem reduces to finding appropriate constitutive expressions for the pressure p, the shear viscosity μ and the dilatational viscosity κ pertaining to each phase. The fluid is usually considered incompressible, accordingly its pressure need not be specified constitutively; moreover, μ_f is often assumed to be constant and κ_f entirely neglected. For the solid phase, conversely, more elaborate constitutive expressions have been developed; some of them, for instance, have been derived from the application of non-equilibrium kinetic theories for granular gases (Gidaspow, 1994). Most of these closures, however, cater for mono-component systems and their extension to binary solid suspensions is not immediate. In the present work the fluid has been assumed incompressible, the shear viscosity constant and equal to that of the pure fluid, and the dilatational viscosity negligible. The internal stress associated with the solid, on the other hand, has not been modeled. However, the discretization scheme (SUPERBEE) employed in the numerical solution of the momentum conservation equations used in this work implicitly introduces a *numerical dissipation*

term (artificial viscosity), which is purely numerical in origin. This term serves to improve and guarantee the stability of the solution (Anderson, 1995).

Indeed, mathematical models have been developed without a particle-phase stress and have been found capable of correctly predicting different types of fluidization behaviour. Zhang & Brandani (2004), Zhang et al. (2005), in their work developed a mathematical model from two-fluid momentum balance considerations. They included additional terms in the fluid-particle interaction force for the solid and fluid phases whilst neglecting solid stresses. Their model correctly simulated the homogenous fluidization of Geldart Group A and bubbling fluidization of Geldart Group B powders in gas fluidized beds.

Needham & Merkin (1983) examined a number of one-dimensional models based on hyperbolic equations, either containing or excluding particle-phase viscosity, in order to determine the dominant effect of the many terms in the continuum equations of motion governing a fluidized bed. Their numerical analysis demonstrated that models which exclude particle-phase viscosity can predict the transition between two stable fluidization states. Christie et al. (1991) demonstrated that a one-dimensional hyperbolic model can qualitatively reproduce the oscillatory behaviour typical of slugging fluidization. Chen et al. (1999) performed numerical simulations using a two-dimensional hyperbolic model which does not include particle-phase viscosity and found that it can predict correctly the transition between homogenous to bubbling fluidization of Geldart Group A and B materials. Nevertheless, results from a comparative analysis on the effect of modelling the solid stress tensor with regards to the numerical prediction of mixing and segregation in binary gas-solid fluidized beds is presented in Chapter 6.

4.3.2 Fluid-Particle interaction force closures

The fluid-particle interaction force accounts for the resultant force which is exerted by the fluid on the particles of phase $\mathscr{F}_k$. In this thesis, this force is assumed to be made up of three

contributions, namely: buoyant force, drag force and elastic force.

$$n_k \left\langle \boldsymbol{f}^f \right\rangle^{\mathscr{F}_k} = n_k \langle \boldsymbol{f}^s \rangle^{\mathscr{F}_k} + n_k \left\langle \boldsymbol{f}^d \right\rangle^{\mathscr{F}_k} + n_k \langle \boldsymbol{f}^e \rangle^{\mathscr{F}_k} \tag{4.54}$$

It is worth pointing out that other contributions to the fluid-particle interaction force should, at least in principle, be considered; for instance, the virtual mass force, the lift force, the Faxen force and a history-dependent term analogous to the Basset force for the motion of isolated particles. In the present analysis, however, these additional contributions have all been neglected. With regard to the latter, it seems reasonable to believe that for dense fluidized suspensions, the space-averaging of history-dependent forces would result into a vanishing contribution; indeed, the averaging procedure would most probably erase any historical effect of the motion of the particles on the fluid in their immediate neighbourhood (Anderson & Jackson, 1967, Jackson, 2001).

For all the remaining contributions, exact expressions have been derived analytically by some authors for the case of single particles (usually of spherical or nearly spherical shape) in non-uniform flows. These closures, however, apply to very specific fluid dynamic conditions; for instance, vanishing or very low Reynolds numbers (Maxey & Riley, 1983, Nadim & Stone, 1991). These results have been used more recently by some researchers in order to develop analytically space-averaged closures catering for solid mono-component fluidized suspensions; for instance, the work of Zhang & Prosperetti (1994, 1997) and Jackson (1997, 1998). These expressions, however, are applicable under very restricting assumptions such as vanishing viscosity (Zhang & Prosperetti, 1994), small Stokes and Reynolds numbers (Jackson, 1997, 1998, Zhang & Prosperetti, 1997) or low particle concentrations (Jackson, 1997, 1998, Zhang & Prosperetti, 1997, 1994).

Generalizing these expressions to other fluid dynamic conditions is by no means straightforward and often raises conceptual issues (related, for example, to frame indifference and objectivity). It is interesting to report, for example, that the lift force on an isolated spherical particle takes quite different functional forms in the inviscid and low Reynolds number cases

(Saffman, 1965, Auton et al., 1988, Jackson, 2001); thus, finding an expression of general validity for a space-averaged closure of such term still appears, for the time being, to be a daunting task. The virtual mass force, conversely, has a quite well established functional form, even if empirical expressions for a concentration-dependent virtual mass coefficient are still to be found.

In light of these considerations, as already said, forces other than those retained in eq. (4.54) have been neglected; this approximation is indeed anything but uncommon and is found in the work of several research groups (Ding & Gidaspow, 1990, Massoudi et al., 1992, Gidaspow, 1994, van Wachem et al., 1998, van Wachem, 2000, Gelderbloom et al., 2003, Gera et al., 2004). The closures used in the present work to express the three contributions to the fluid-particle interaction force reported in eq. (4.54) will now be described. The *buoyant force* associated to the phase $\mathscr{F}_k$ is related to the isotropic contribution to the effective fluid stress tensor and the solid volume fraction ϕ_k as follows:

$$n_k \langle \boldsymbol{f}^s \rangle^{\mathscr{F}_k} = -\phi_k \nabla \langle p \rangle^f \tag{4.55}$$

Eq. (4.55) is a generalization of one of the closures commonly used for such a force. The *drag force* is expressed, as usual, as the product of a drag coefficient β_k and the relative slip velocity between the fluid and the particle phase of interest.

$$n_k \left\langle \boldsymbol{f}^d \right\rangle^{\mathscr{F}_k} = \beta_k \left(\langle \boldsymbol{u} \rangle^f - \langle \boldsymbol{u} \rangle^{\mathscr{F}_k} \right) \tag{4.56}$$

Here the closure used for the inter-phase momentum transfer coefficient is that derived by Di Felice (1988b) for the pressure drop per unit length in a suspension modified by Owoyemi (2005), Owoyemi & Lettieri (2006). The expression is applicable for both fixed and fluidized beds and has the form:

$$\beta_k = \left[\left(\frac{17.3}{Re_k} \right)^{\alpha} + (0.336)^{\alpha} \right]^{\frac{1}{\alpha}} \frac{\rho_f \left| \langle \boldsymbol{u} \rangle^f - \langle \boldsymbol{u} \rangle^{\mathscr{F}_k} \right| \phi_k}{d_k} \varepsilon^{-1.8} \tag{4.57}$$

where the Reynolds number and the exponent α are given by:

$$Re_k = \frac{\rho_f \varepsilon \left| \langle \boldsymbol{u} \rangle^f - \langle \boldsymbol{u} \rangle^{\mathcal{F}_k} \right| d_k}{\mu_f} \quad ; \quad \alpha = 2.55 - 2.1 \left[\tanh \left(20\,\varepsilon - 8 \right)^{0.33} \right]^3 \tag{4.58}$$

The *elastic force* is a specific feature of the present model. The concept of elasticity associated to multi-phase flow, and in particular to solid fluidized suspensions, has been already been discussed in § 2.2.2. Nevertheless, a short description will be given here. The concept of elasticity was initially introduced by Wallis (1969) and thereafter further developed by Foscolo & Gibilaro (1987) and Gibilaro (2001). It originally stems from a theoretical investigation into the hydrodynamic stability of homogeneous fluidized beds.

The first formulation of the averaged linear momentum equations of conservation, and more specifically of the fluid-particle interaction force featuring in them and comprising solely the drag and the buoyant forces, leads to an intrinsic instability of the homogeneous state of fluidization. The inclusion of additional contributions to the interaction force such as those previously discussed (virtual mass force, lift force and the like) does not bring about any significant qualitative change. This appears to be inconsistent with experimental evidence; there are, in fact, many systems (fluidized by either gas or liquid) that are found to expand in an unambiguously homogeneous fashion (at least, from what can be experimentally observed) up to a critical, often well-defined value of the fluid volume fraction. The physical arguments put forward by Foscolo & Gibilaro (1987) led to the introduction of an additional force, the elastic force, related to the gradients in the suspension void fraction which are generated when the homogeneity of the system is lost at the macroscopic length scale. The inclusion of this contribution into the fluid-particle interaction force results into a simple criterion for discriminating between stable and unstable fluidization.

The original formulation of the elastic force closure, developed for mono-dimensional systems of mono-sized particles near equilibrium conditions, is not adequate, however, for the study of the dynamics of fluidized suspensions far from equilibrium. A revised, multi-dimensional and somewhat generalized formulation of the force has been subsequently ad-

vanced by Mazzei et al. (2006) for mono-component systems. The force is therein regarded as a component of the drag force; more specifically, the contribution related to voidage gradients within the suspension which arise under non-equilibrium conditions. The approach of Mazzei et al. (2006) has been adopted and extended by Owoyemi (2005), Owoyemi & Lettieri (2006) for binary mixtures; the closure takes the following expression:

$$n_k \langle f^e \rangle^{\mathcal{F}_k} = E_k \left(\nabla \varepsilon \cdot \frac{n_k \langle f^d \rangle^{\mathcal{F}_k}}{\left| n_k \langle f^d \rangle^{\mathcal{F}_k} \right|} \right) \tag{4.59}$$

where E_k is given by the expression presented earlier in eq. (4.59) and reproduced below for convenience.

$$E_k = -\frac{4 \cdot (1-\varepsilon)}{\pi \cdot d_k^2} \cdot \left(\frac{\partial \langle f^{\mathcal{P}_\mathcal{F}} \rangle}{\partial \varepsilon} \right)_{U_o, U_p} \quad ; \quad n_k = \frac{6(1-\varepsilon)}{\pi d_k^3} \tag{4.60}$$

In this work, $\langle f^{\mathcal{P}_\mathcal{F}} \rangle$ is given by:

$$\langle f^{\mathcal{P}_\mathcal{F}} \rangle = \frac{\pi d_k^2}{6} \left[\left(\frac{17.3}{Re_k} \right)^{\alpha} + (0.336)^{\alpha} \right]^{\frac{1}{\alpha}} \rho_f \left(U_o - U_p \right)^2 \varepsilon^{-3.8} - \frac{\pi d_p^3}{6} \left(\rho_p - \rho_f \right) g \varepsilon \tag{4.61}$$

The evaluation of the $\left(\frac{\partial \langle f^{\mathcal{P}_\mathcal{F}} \rangle}{\partial \varepsilon} \right)_{U_o, U_p}$ function is required to obtain a general expression for the elastic modulus. A mathematical solution to the partial derivative is detailed in Appendix A.3. Following mathematical manipulations we obtain the following novel form for the *elastic modulus* E_k:

$$E_k = -\frac{2}{3} d_k \left[\left(-\frac{3.8}{\varepsilon} + \chi \right) \left| n_k \langle f^d \rangle^{\mathcal{F}_k} \right| - \phi_k \left(\rho_k - \rho_f \right) g \right] \tag{4.62}$$

The functional form of χ is:

$$\chi = \frac{1}{\alpha}\left\{-\frac{1}{\alpha}\ln\left[\left(\frac{17.3}{Re_k}\right)^{\alpha}+(0.336)^{\alpha}\right]+\frac{\left(\frac{17.3}{Re_k}\right)^{\alpha}\ln\left(\frac{17.3}{Re_k}\right)+(0.336)^{\alpha}\ln(0.336)}{\left(\frac{17.3}{Re_k}\right)^{\alpha}+(0.336)^{\alpha}}\right\}$$

$$\left\{6.3\left[\tanh(20\varepsilon-8)^{0.33}\right]^2\right\}\left\{\operatorname{sech}^2(20\varepsilon-8)^{0.33}\right\}\left\{6.6(20\varepsilon-8)^{-0.67}\right\} \tag{4.63}$$

4.3.3 Particle-Particle interaction force closures

In the present model the only constituent of the particle-particle interaction force which has been taken into consideration is the inter-phase drag. The force is expressed as the product of a drag coefficient ζ and the relative slip velocity between the two solid phases.

$$n_1 \langle \boldsymbol{f}^p \rangle^{\mathscr{F}_1} = \zeta\left(\langle \boldsymbol{u} \rangle^{\mathscr{F}_2} - \langle \boldsymbol{u} \rangle^{\mathscr{F}_1}\right) = -n_2 \langle \boldsymbol{f}^p \rangle^{\mathscr{F}_2} \tag{4.64}$$

Several investigators have put forward empirical correlations to account for the momentum transfer coefficient ζ. In this thesis three drag constitutive equations proposed by Gidaspow et al. (1985), Syamlal (1987b), Bell (2000) are compared later in Chapter 6. A summary of the mathematical expressions for the proposed models has already been presented earlier in Table. 2.8.

4.3.4 Solid phase compaction control

As previously pointed out, in the present work the internal stress associated with the solid phases has been neglected. This might give rise to local over-compaction in some regions of the simulated fluidized bed. To counter this effect a new numerical algorithm has been developed. The new numerical scheme is based on the algorithm for the *excess solid volume* correction originally developed by Lettieri et al. (2003) for mono-component systems

which has already been introduced in § 2.2.2.2. Nevertheless, for convenience the excess solid volume correction balance may be expressed in terms of solid volume fraction by the following:

$$\phi_{i,j}^{new} = \phi_{i,j}^{old} - \phi_{i,j}^{ex} + \frac{\phi_{i+1,j}^{ex}}{4} + \frac{\phi_{i,j+1}^{ex}}{4} + \frac{\phi_{i-1,j}^{ex}}{4} + \frac{\phi_{i,j-1}^{ex}}{4} \tag{4.65}$$

In the present work, the original algorithm has been extended for the case of binary systems. The new algorithm allows dynamic calculation of the total maximum solid packing ϕ_{12}^{max} in each cell within the computational grid after each time step. The parameter ϕ_{12}^{max} is equal to:

$$\phi_{12}^{max} = \phi_1^{max} + \phi_2^{max} \tag{4.66}$$

where ϕ_1^{max} and ϕ_2^{max} denote the local (*i.e.*, relative to the cell under exam) maximum value of the solid volume fractions ϕ_1 and ϕ_2 of phases $\mathscr{F}_1$ and $\mathscr{F}_2$ respectively. These two parameters are not known *a priori* but are computed by the algorithm. The computation of the instantaneous maximum packing is also necessary because each cell of the computational domain contains a unique distribution of particles which varies in time and from cell to cell. The dynamic control for ϕ_{12}^{max} was achieved by implementing the equation proposed by Fedors & Landel (1979) for the maximum packing in a binary mixture of spheres. The numerical solid compaction algorithm is described below and shown diagrammatically in Fig.4.1.

Step 1: The maximum allowable solid compaction Φ_1 and Φ_2 are set manually, *e.g* to the value of 0.60, for both phases $\mathscr{F}_1$ and $\mathscr{F}_2$ present in the mixture.

Step 2: The algorithm collects, as an input, the values of the local solid volume fractions ϕ_1^{old} and ϕ_2^{old} at the current time step. The values are then used in order to compute the local maximum solid volume fraction ϕ_{12}^{max} for the mixture, in each computational cell, using the Fedors & Landel (1979) equation.

Step 3: The calculated maximum packing volume fraction for the mixture is then shared between phase $\mathscr{F}_1$ and $\mathscr{F}_2$ using a simple redistribution based on proportionality. The above enables the calculation of the excess volume fractions ϕ_1^{ex} and ϕ_2^{ex}.

Step 4: The new "corrected" solid volume fractions ϕ_1^{new} and ϕ_2^{new} for each phase is then calculated using eq. (4.65).

It is worth noting that the algorithm does not necessarily drop the excess solid volume out of the cell, but it rather rearranges the solid volume field so that the solid volume excess is transported towards domain regions where no excess is present.

The strength of this procedure lies in the implementation of a local numerical correction of the solid volume fraction only in the computational cells where this is required, without the introduction of additional terms in the equations of motion (such as additional pressure gra-

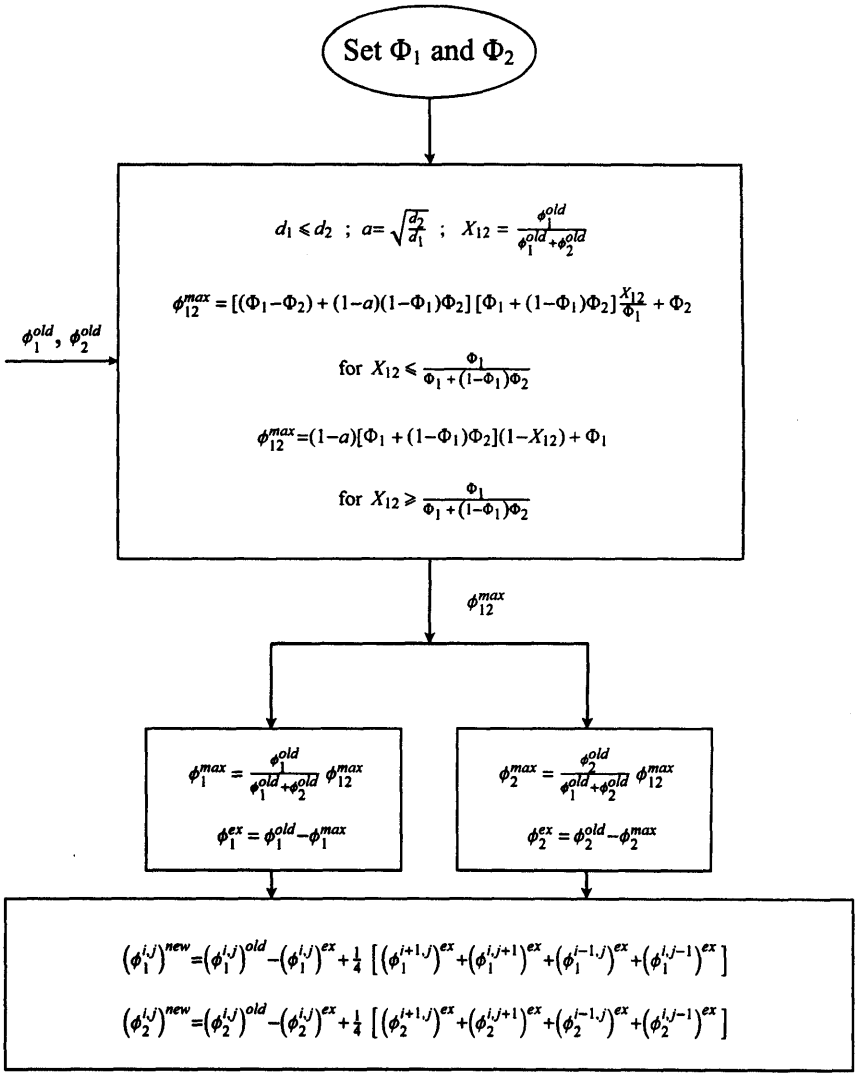

Figure 4.1: *Solid compaction correction algorithm*

dients for the solid phase) devoid of physical meaning and which would affect the numerical solution globally.

4.4 Conclusion

This chapter has described the derivation of the Eulerian-Eulerian averaged equations of change for binary mixtures of particles fluidized by means of a Newtonian fluid. The origin of the particle-particle interaction force has also been clearly presented. Description of the closure equations developed in this work for the fluid-particle drag and those used for the particle-particle drag has also been reported.

Chapter 5

Eulerian model predictions for mono-component fluidized systems

Summary

This chapter describes the various simulations that have been performed for the mono-component gas fluidized systems reported in Chapter 3. The chapter is a three part study into the substantiation of the Eulerian-Eulerian approach against the physical world. Firstly, a linear stability analysis of the *mono-component* version of the model presented earlier in Chapter 4 is performed. Thereafter, a numerical validation of the closure drag model proposed in Chapter 1 of this thesis is carried out by using modelling materials for the test cases. The chapter concludes with an experimental verification of the Eulerian-Eulerian mono-component CFD simulations of the rutile industrial powders supplied for this project.

Parts of this chapter has been published :

Owoyemi, O., Lettieri, P., Place, R., (2005). Experimental Validation of Eulerian-Eulerian Simulations of Rutile Industrial Powders. *Ind Eng Chem Res*, 44, 9996-10004.

5.1 Introduction

The overall aim of this thesis, as stated earlier in Chapter 1, is the application of computational fluid dynamics (CFD) to the modelling of the dense gas-solid fluidization of binary mixtures, specifically industrial rutile powders provided by Huntsman Tioxide Ltd. This task was split into several stages, as highlighted in Chapter 1. In this section, the substantiation of using the Eulerian-Eulerian approach for the modelling of the mono-component industrial materials is addressed. Results obtained from the numerical simulations are compared with results obtained from corresponding experimental data. This was considered as a first step in verifying the suitability of the modelling approach adopted in this thesis and also a necessary precursor to its application for the simulation of binary systems.

In addressing the above question, this section has been split into three parts, in the first study the mono-component version of the proposed equations of change which have been elucidated in Chapter 4 are examined analytically. Here, linear stability analysis theory is applied to the proposed equations of change in the face of small fluctuations in the voidage or particle velocity. The effort leads to the development of a new stability criterion for homogenous gas fluidized beds with better predictive capability than the Foscolo & Gibilaro (1984) criterion.

The second part validates the drag force closure relation which has been used in this thesis, through predictions of bed height and bed voidage as well as through other macroscopic fluidization indicators obtained from CFD simulations of Geldart Group A materials such as FCC catalyst (70 μm). Results are compared with predictions from the Richardson & Zaki (1954a) correlation.

In the third part, an experimental validation of numerical simulations of the mono-component industrial materials, Slag, Natural and Synthetic Rutile particles is reported. In this study predictions using the well established granular kinetic theory (GKT) presented earlier in Chapter 2, and available within CFX4.4, are compared with the mono-component version of the model proposed to model the behavior of the individual rutile powders. The simulations

are performed at different superficial gas velocities. Simulation results obtained for bed expansion, bubble size and voidage profiles are compared with dedicated experimental results obtained using a 2D fluid bed experimental rig which is reported in Chapter 3. Empirical bubble size values obtained using Darton et al. (1977) correlation are also compared with the simulated values and experimental bubble size measurements.

5.2 Stability analysis of the mono-component equations of change

The hydrodynamic stability analysis of the uniform fluidized state has generated a lot of research interest over the years (Jackson, 1963, Pigford & Baron, 1965, Foscolo & Gibilaro, 1984), where earlier studies had suggested that all fluidized suspensions should be unstable (Jackson, 1963). However, Foscolo & Gibilaro (1984) derived a criterion which predicted the existence of a boundary separating particulate behaviour, on the stable side, from aggregative behaviour on the unstable side.

In this section, the hydrodynamic stability of the uniform fluidized state is revisited. Here, the *fluid-particle interaction* closure derived earlier in Chapter 4 is applied together with the mono-component equations of change proposed in this thesis to investigate the effect of small perturbations in the void fraction to the state of uniform fluidization. The aim of the stability analysis is to establish a new criterion for discriminating between particulate and aggregative behaviour in fluidized beds. This part is important for the subsequent validation of the equation of closure for the drag and elastic force proposed in this thesis. Following the derivation reported in Chapter 4, the equations of change proposed in this thesis for mono-component systems are summarized in Table 5.1.

The development of the stability criterion is carried out by writing down a closed formulation of the conservation equations for the particle and fluid phases that defines the one-dimensional mono-component model presented in Table 5.1.

Table 5.1: *Proposed governing conservation equations applied to mono-component gas-solid flow.*

Continuity equations
$$\frac{\partial \varepsilon}{\partial t} + \nabla \cdot \left(\varepsilon \langle \boldsymbol{u} \rangle^f\right) = 0$$ $$\frac{\partial \phi}{\partial t} + \nabla \cdot \left(\phi \langle \boldsymbol{u} \rangle^s\right) = 0$$
Momentum Equations
$$\rho_f \left[\frac{\partial}{\partial t}\left(\varepsilon \langle \boldsymbol{u} \rangle^f\right) + \nabla \cdot \left(\varepsilon \langle \boldsymbol{u} \rangle^f \langle \boldsymbol{u} \rangle^f\right)\right] = \nabla \cdot \mathcal{T}^f - n\left\langle \boldsymbol{f}^f \right\rangle + \varepsilon \rho_f \boldsymbol{g}$$ $$\rho_s \left[\frac{\partial}{\partial t}\left(\phi \langle \boldsymbol{u} \rangle^s\right) + \nabla \cdot \left(\phi \langle \boldsymbol{u} \rangle^s \langle \boldsymbol{u} \rangle^s\right)\right] = n\left\langle \boldsymbol{f}^f \right\rangle + \phi \rho_s \boldsymbol{g}$$
Fluid phase stress tensor
$$\mathcal{T}^f = -\langle p \rangle^f \boldsymbol{I} + \mu_f \left[\nabla \langle \boldsymbol{u} \rangle^f + \left(\nabla \langle \boldsymbol{u} \rangle^f\right)^T\right] + \left(\kappa_f - \frac{2}{3}\mu_f\right) \nabla \cdot \langle \boldsymbol{u} \rangle^f \boldsymbol{I}$$
Fluid-particle interaction force
$$n\left\langle \boldsymbol{f}^f \right\rangle = -\phi \nabla \langle p \rangle^f + \beta\left(\langle \boldsymbol{u} \rangle^f - \langle \boldsymbol{u} \rangle^s\right) + E\left(\nabla \varepsilon \cdot \frac{n\left\langle \boldsymbol{f}^d \right\rangle}{\left| n\left\langle \boldsymbol{f}^d \right\rangle \right|}\right)$$

The *particle phase conservation* equations can be summarized in one dimensional form (z direction) by the following [1]:

$$-\frac{\partial \varepsilon}{\partial t} + \frac{\partial}{\partial z}\left((1-\varepsilon) u^s\right) = 0 \tag{5.1}$$

$$(1-\varepsilon)\rho_p \left(\frac{\partial u^s}{\partial t} + u^s \frac{\partial u^s}{\partial z}\right) = -(1-\varepsilon)\frac{\partial p}{\partial z} + n\left\langle f^d \right\rangle + E\frac{\partial \varepsilon}{\partial z} + (1-\varepsilon)\rho_s g_z \tag{5.2}$$

Similarly the fluid phase one dimensional conservation equations can be represented by the

[1] averaged brackets have been dropped for the sake of clarity

following:

$$\frac{\partial \varepsilon}{\partial t} + \frac{\partial}{\partial z}\left(\varepsilon u^f\right) = 0 \tag{5.3}$$

$$\varepsilon \rho_f \left(\frac{\partial u^f}{\partial t} + u^f \frac{\partial u^f}{\partial z}\right) = \varepsilon \frac{\partial p}{\partial z} - n\left\langle f^d \right\rangle - E\frac{\partial \varepsilon}{\partial z} + \varepsilon \rho_f g_z \tag{5.4}$$

where $n\left\langle f^d \right\rangle$ is given by:

$$n\left\langle f^d \right\rangle = \beta\left(u^f - u^s\right) \tag{5.5}$$

The stability of the homogeneously fluidized state is now going to be analyzed. Here the underlining assumption is that the system is incompressible and the particle density is far greater that that of the fluid phase, i.e. $\rho_s >> \rho_f$, thus terms in the fluid phase momentum equation proportional to the fluid phase density will be negligible when compared to the drag, pressure gradient and Elastic force terms eq. (5.4) reduces to the following:

$$n\left\langle f^d \right\rangle = \varepsilon \frac{\partial p}{\partial z} - E\frac{\partial \varepsilon}{\partial z} \tag{5.6}$$

Substituting eq. (5.6) into eq. (5.2) gives a fully decoupled expression for the particle phase given by:

$$(1-\varepsilon)\rho_s \left(\frac{\partial u^s}{\partial t} + u^s \frac{\partial u^s}{\partial z}\right) = f^{\mathcal{P}_{\mathcal{F}}^+} \tag{5.7}$$

where the $f^{\mathcal{P}_{\mathcal{F}}^+}$ represents the net force (fluid-particle interaction plus gravity) acting on the particle phase and is given by the following:

$$f^{\mathcal{P}_{\mathcal{F}}^+} = \frac{n\left\langle f^d \right\rangle}{\varepsilon} - (1-\varepsilon)\rho_p g + \frac{E}{\varepsilon}\frac{\partial \varepsilon}{\partial z} \tag{5.8}$$

The trivial solution to the eq.(5.7) is the steady state condition of $u^s = 0$ and $\varepsilon = \varepsilon^o$ which reduces the particle momentum equation to $f^{\mathcal{P}_{\mathcal{F}}^+} = 0$. The stability of the above steady state conditions to small perturbations in the void fraction will now be investigated. Eq. (5.2) and (5.4) will be cast in terms of deviations in the voidage $\varepsilon^{\mathcal{D}}$ from its steady state level ε^o, $\varepsilon = \varepsilon^o + \varepsilon^{\mathcal{D}}$ and the particle velocity [2] u^s and eliminating terms that contain the product of

[2] u^s is already a deviation about the steady state value of zero

two or more quantities which approach zero, such as u^s and $\varepsilon^{\mathscr{D}}$ (Gibilaro, 2001).

$$\frac{\partial \varepsilon^{\mathscr{D}}}{\partial t} = \frac{\partial u^s}{\partial z}(1-\varepsilon^o) \quad ; \quad \textit{Continuity} \tag{5.9}$$

The net force acting on the particle is a non-linear function of the two variables, u^s and ε^o. A reasonable linear approximation for the net force, for small deviation from the steady state, would be a first order Taylor series expansion of the continuous function, $f^{\mathcal{P}_{\mathcal{F}}^+}$. In order to carry out the linearization, the function $f^{\mathcal{P}_{\mathcal{F}}^+}$ will be split into the following parts:

$$f^{\mathcal{P}_{\mathcal{F}}^+} = F + \frac{E}{\varepsilon}\frac{\partial \varepsilon}{\partial z} \quad ; \quad F = \frac{n\langle f^d \rangle}{\varepsilon} - (1-\varepsilon)\rho_p g \tag{5.10}$$

where $n\langle f^d \rangle$ is given by the following:

$$n\langle f^d \rangle = \left[\left[\frac{17.3\mu}{\rho_f (u^o - u^s) d_p}\right]^{\alpha} + 0.336^{\alpha}\right]^{\frac{1}{\alpha}} \frac{\rho_f}{d_p}(1-\varepsilon)\varepsilon^{-3.8}(u^o - u^s)^2 \tag{5.11}$$

the term u^o is the superficial gas velocity, d_p is the diameter of the particle and the exponent α is given by:

$$\alpha = 2.55 - 2.1\left[\tanh(20\varepsilon - 8)^{0.33}\right]^3 \tag{5.12}$$

The continuous function F and the Elastic modulus E can be linearized as follows:

$$F\left(0 + u^s, \varepsilon^o + \varepsilon^{\mathscr{D}}\right) = F(0, \varepsilon^o) + \left[\left\{\frac{\partial F}{\partial u^s}\right\}_{F=0} u^s + \left\{\frac{\partial F}{\partial \varepsilon}\right\}_{F=0} \varepsilon^{\mathscr{D}}\right] \tag{5.13}$$

$$\frac{E}{\varepsilon}\frac{\partial \varepsilon}{\partial z}\left(0 + u^s, \varepsilon^o + \varepsilon^{\mathscr{D}}\right) = \frac{E^o}{\varepsilon^o}\frac{\partial \varepsilon^{\mathscr{D}}}{\partial z}(0, \varepsilon^o) + \frac{\partial \varepsilon^{\mathscr{D}}}{\partial z}\left[\left\{\frac{\partial}{\partial u^s}\frac{E}{\varepsilon}\right\}_0 u^s + \left\{\frac{\partial}{\partial \varepsilon}\frac{E}{\varepsilon}\right\}_0 \varepsilon^{\mathscr{D}}\right] \tag{5.14}$$

Following the linearization process the linearized momentum equation can be written as follows:

$$(1-\varepsilon^o)\frac{\partial u^s}{\partial t} = \frac{f_{u^s}^*}{\rho_s} u^s + \frac{f_\varepsilon}{\rho_s}\varepsilon^{\mathscr{D}} + \frac{E^o}{\varepsilon^o \rho_s}\frac{\partial \varepsilon^{\mathscr{D}}}{\partial z} \quad ; \quad \textit{Momentum} \tag{5.15}$$

where f_{u^s} and f_ε is given by $\left\{\frac{\partial F}{\partial u^s}\right\}_{F=0}$ and $\left\{\frac{\partial F}{\partial \varepsilon}\right\}_{F=0}$ respectively. In steady state conditions, the first term on the R.H.S of eq. (5.13), $F(u_o, 0, \varepsilon_o)$, is equal to zero with this consideration

the task therefore is to evaluate the terms, $\left\{\frac{\partial F}{\partial u^s}\right\}_{F=0}$ and $\left\{\frac{\partial F}{\partial \varepsilon}\right\}_{F=0}$ [3]. The last term in braces on the R.H.S of eq .(5.14) is also eliminated because it represents the product of functions that approach zero as the deviations u^s and $\varepsilon^{@}$ approach zero. The evaluation of f_{u^s} and f_ε leads to the following form:

$$f_{u^s} = \frac{n\langle f^d \rangle}{u^o}\left[\frac{\left[\frac{17.3}{Re_p}\right]^\alpha}{\left[\left[\frac{17.3}{Re_p}\right]^\alpha + 0.336^\alpha\right]^{\frac{1}{\alpha}}} - 2\right] \quad ; \quad f_\varepsilon = (1-\varepsilon)\rho_s g\left(\left[-3.8\varepsilon^{-1} + \chi\right] - \frac{1}{\varepsilon}\right) \tag{5.16}$$

where the functional form of χ is given by eq. (5.17):

$$\chi = \frac{1}{\alpha}\left\{-\frac{1}{\alpha}\ln\left[\left(\frac{17.3}{Re_p}\right)^\alpha + (0.336)^\alpha\right] + \frac{\left(\frac{17.3}{Re_p}\right)^\alpha \ln\left(\frac{17.3}{Re_p}\right) + (0.336)^\alpha \ln(0.336)}{\left(\frac{17.3}{Re_p}\right)^\alpha + (0.336)^\alpha}\right\}$$

$$\left\{6.3\left[\tanh(20\varepsilon - 8)^{0.33}\right]^2\right\}\left\{\operatorname{sech}^2(20\varepsilon - 8)^{0.33}\right\}\left\{6.6(20\varepsilon - 8)^{-0.67}\right\} \tag{5.17}$$

The expressions for the kinematic and dynamic wave velocities, u_K and u_D, introduced earlier in § 2.2.2, which determine the boundary of stability for the uniform fluidized state can now be extracted from eq. (5.14) through the following considerations.

$$u_D = \sqrt{\frac{E}{\varepsilon\rho_s}} \quad ; \quad u_K = \frac{f_\varepsilon(1-\varepsilon)}{f_{u^s}} \tag{5.18}$$

where E refers to the elastic modulus. Following the above consideration we obtain the

[3] The differentiation procedure has been carried out using the MathCAD software

following for the kinematic and dynamic velocities:

$$u_K = u^o(1-\varepsilon)\frac{-4.8\,\varepsilon^{-1}+\chi}{\left[\left(\dfrac{\left[17.3/Re_p\right]^{\alpha}}{\left[17.3/Re_p\right]^{\alpha}+0.336^{\alpha}}\right)-2\right]} \tag{5.19}$$

$$u_D = \sqrt{\frac{\frac{2}{3}d_p\left(n\langle f^d\rangle\left(-3.8\varepsilon^{-1}+\chi\right)-(1-\varepsilon)\left(\rho_s-\rho_f\right)g\right)}{\varepsilon\rho_s}} \tag{5.20}$$

The numerator in eq. (5.20) represents the Elastic modulus which has been derived earlier in Chapter 4. The criterion for stability can be generalized as follows (Gibilaro, 2001): If $u_K > u_D$, the bed starts to bubble at the minimum fluidization condition: $\epsilon_{mb} = \epsilon_{mf} = 0.4$. If $u_K < u_D$, the bed is initially homogeneous and will start to bubble where $u_K = u_D$. If the condition $u_K < u_D$, persists over the full expansion range, $1 > \varepsilon > 0.4$, then the bed is always homogeneous. The stability criterion can be further summarized into eq. (5.21)

$$\left(\frac{d_p}{\rho_s u_t^2}\right)^{0.5}\left(\frac{\mathscr{W}}{1-\varepsilon}-\left(\rho_s-\rho_f\right)g\right)^{0.5}-1.5^{0.5}(1-\varepsilon)\,\varphi\,\varepsilon^{n-0.5}=\left\{\begin{matrix}\text{positive, stable}\\ \text{negative, unstable}\end{matrix}\right\} \tag{5.21}$$

where u_t refers to the particle terminal velocity and n is an exponent that depends on the fluid dynamic regime (*i.e.* $n \approx 4.8$ in the *viscous* regime, $n \approx 2.8$ in the *inertial* regime). $\mathscr{W}$ and φ represent the following:

$$\mathscr{W} = n\langle f^d\rangle\left(-3.8\varepsilon^{-1}+\chi\right) \quad ; \quad \varphi = \frac{-4.8\,\varepsilon^{-1}+\chi}{\left[\left(\dfrac{\left[17.3/Re_p\right]^{\alpha}}{\left[17.3/Re_p\right]^{\alpha}+0.336^{\alpha}}\right)-2\right]} \tag{5.22}$$

5.2.1 Stability analysis results for Geldart group A powders

Eq. (5.19), (5.20) and (5.21) were used to perform a fluid-bed stability analysis on range of Geldart Group A gas-fluidized powders. Figure 5.1 shows a comparison of the predicted "sta-

bility limit"(where the dynamic and kinematic wave velocities intersect) using the new model as compared with the Foscolo & Gibilaro (1984) criterion, presented earlier in eq.(2.16), for Group A powder of diameter 70μm . It can be seen that eq's (5.19) and (5.20) give a better prediction for the stability limit than that obtainable using the Foscolo & Gibilaro (1984) criterion. Quantitatively, there is a per cent error of 10 % when the Foscolo & Gibilaro (1984) criterion is compared to experimental measurements[4] whilst the criterion proposed herein matches exactly with the experimental data.

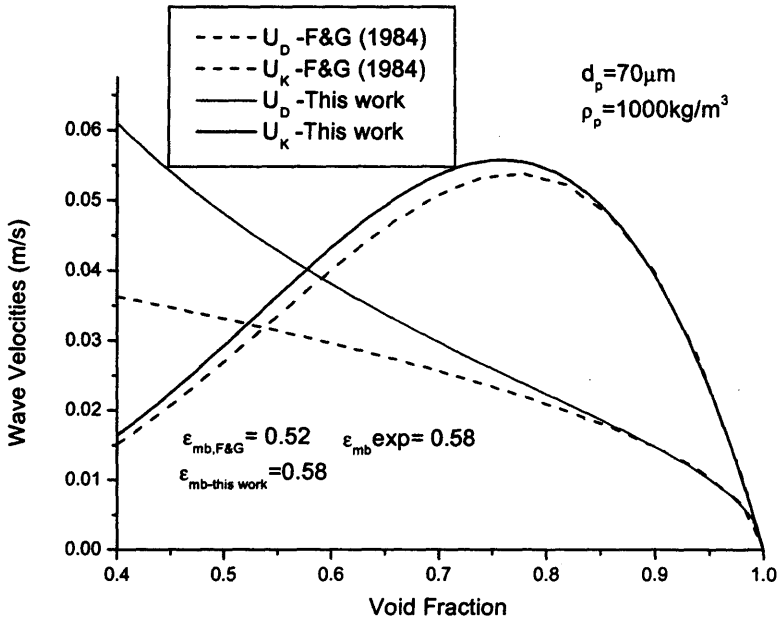

Figure 5.1: *A comparison of the Dynamic and Kinematic-wave velocities as functions of void fraction for the fluidization of alumina particles by air.*

The better predictive capability of the proposed model is a result of two factors, the first factor is the difference in the predicted dynamic wave velocity, the new dynamic wave expression eq. (5.20) is a function of the concentration of the particles ε, a dependence which is not present in the Foscolo & Gibilaro (1984) model[5]. This inverse relationship simply means that the propagation of the dynamic wave is slower in dense beds and faster in dilute beds. Consequently, dense beds will experience a greater bed expansion before bubbling and as a result a higher value for ε_{mb}. The second factor which gives the new criterion better predictive capability is the *fluid-particle interaction force*. The elastic modulus is a function of the *fluid-*

[4]Experimental data has been obtained from Lettieri (1999)

[5]This dependence has also been independently arrived at by other authors using different considerations (see Jean & Fan, 1992, Mazzei et al., 2006)

particle interaction force and by inference a better closure for the *fluid-particle interaction force* should give a better prediction of the Elastic modulus.

Values for the minimum bubbling voidage, ε_{mb}, predicted by the model have also been compared with those predicted by the eq. (2.16) (Foscolo & Gibilaro, 1984) and experimental data for other Geldart A powders. Figure 5.2 reports the minimum bubbling voidage as a function of the mean particle diameter for different Geldart Group A powders (diameter: $26\,\mu m - 137\,\mu m$, density: $1210\,kg/m^3 - 1420\,kg/m^3$); the experimental data refers to ambient conditions and have been obtained by Xie & Geldart (1995).

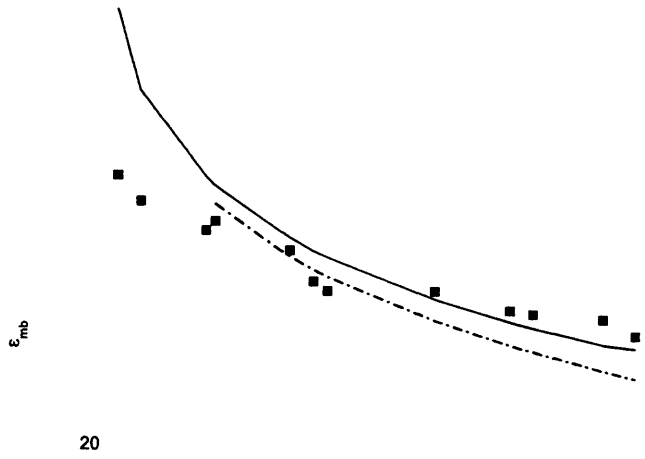

Figure 5.2: *Model comparison with experimental data of the minimum bubbling voidage as a function of mean particle diameter for different powders at ambient temperature*

A good agreement is found between predictions of the new model and experimental data (error within ± 5%) in the "high" range of mean particle diameters (greater than about 90 μm). However, it can be observed that the more the mean particle diameter is reduced the less accurate the predictions of the model become (the same holding true also for the original PBM (Foscolo & Gibilaro, 1984)). A possible explanation for the poor quality of the theoretical predictions obtained for very low mean particle diameters can be attributed to the predominance of the effects of interparticle forces (IPF's), at smaller particle diameters, which are not accounted for in any of the models compared above. The importance of these forces

have been discussed by Lettieri et al. (2001). In the work presented therein, Lettieri et al. (2001) suggested that both hydrodynamic forces (HDF's) and interparticle forces (IPF's) were present in Group A powders but HDFs dominate the behaviour of coarser Group A powders while IPFs are more important for the finer Group A powders. However, they concluded that the flow behavior of Group B powders was determined entirely by only HDFs and IPFs were absent. Nevertheless, the aim of the analysis presented so far has been to analytically demonstrate the predictive capability of the fluid particle interaction closure relation developed in this thesis where HDF's dominate over the IPF's.

5.3 Numerical validation of the implemented drag model

In this section, numerical simulations using the proposed model (see Table 5.1) are used to demonstrate the validity of the drag force closure used in this thesis. Predictions of bed height and bed voidage obtained from CFD simulations of Geldart Group A FCC catalyst of diameter 70 μm and density 1420 kg/m^{-3} at four different superficial gas velocities are compared with predictions from the Richardson & Zaki (1954a) equation. The superficial gas velocities have been chosen such that the bed is always in the particulate fluidization regime. The governing equations described in Table 5.1 as well as the closure relations reported for the interphase transfer coefficient and Elastic modulus in eq. (5.23) and eq. (5.25) respectively were implemented in the CFX.4.4 code. As previously pointed out in this thesis, the internal stress associated with the solid phases has been neglected. The omission of this stress might give rise to localized over compaction in some regions of the simulated fluidized bed. To counter this effect the numerical algorithm *excess solid volume correction* developed by Lettieri et al. (2003) for mono-component systems (described in Chapter 4) has also been implemented within the CFX4.4 code.

$$\beta = \left[\left(\frac{17.3}{Re_p}\right)^{\alpha} + (0.336)^{\alpha}\right]^{\frac{1}{\alpha}} \frac{\rho_f \left|\langle \boldsymbol{u} \rangle^f - \langle \boldsymbol{u} \rangle^s\right| \phi}{d_p} \varepsilon^{-1.8} \tag{5.23}$$

where the Reynolds number and the exponent α are given by:

$$Re_p = \frac{\rho_f \varepsilon \left|\langle \boldsymbol{u} \rangle^f - \langle \boldsymbol{u} \rangle^s\right| d_p}{\mu_f} \quad ; \quad \alpha = 2.55 - 2.1\left[\tanh\left(20\,\varepsilon - 8\right)^{0.33}\right]^3 \tag{5.24}$$

$$E = -\frac{2}{3} d_p \left[\left(-\frac{3.8}{\varepsilon} + \chi\right)\left|n\left\langle f^d \right\rangle\right| - \phi\left(\rho_s - \rho_f\right) g\right] \tag{5.25}$$

5.3.1 CFD simulation conditions

A 2D computational grid, in which front and back wall effects are neglected, was used. The left and right walls of the domain were modelled using no-slip velocity boundary condition for simplicity in all the phases. Dirichlet boundary conditions were employed at the bottom of the bed to specify a uniform gas inlet velocity. A pressure boundary condition, which can be arbitrary, was specified at the top of the bed and set to a reference value of 1.015×10^5 Pa – representing atmospheric pressure . The fluidization conditions used for all simulations are summarized in Table 5.2. Four different simulations were carried out at superficial gas velocities of 0.018 m/s, 0.020 m/s, 0.025 m/s and 0.035 m/s respectively. The fluidized bed was initially filled to a height of 0.30 m. All simulations were performed for a total of 45 seconds (real time); this corresponds to an overall computational time of roughly 1 day for each simulation. The simulations were carried out using three Dell Xeon P4 3.2 Ghz Machines.

5.3.2 CFD simulation results- bed voidage

The experimental determination of the expansion characteristics of a homogenously fluidized bed involves simply the measurement of the steady state height as a function of the superficial gas velocity, u_o, with results usually presented as a relationship between u_o and the void fraction, ε. Researchers have found that the plot of superficial gas velocity, u_o against ε on a logarithmic scale yields an approximate straight line behaviour, over a full range of bed expansion. This relationship was expressed empirically by Richardson & Zaki (1954a) as

Table 5.2: *Computational parameters used in the numerical validation of the implemented drag model.*

Description	Symbol	Value	Units	Comments
Solids density	ρ_s	1420	kg/m^3	
Particle diameter	d_p	70	μm	Geldart Group A
Gas density	ρ_f	1.29	kg/m^3	
Gas viscosity	μ_f	1.85×10^{-5}	Pa s	
Minimum fluidization velocity	u_{mf}	0.00230	m/s	from Ergun (1952)
Superficial gas velocity	u_o	0.018 – 0.035	m/s	a range is used
Bed height	H_b	0.60	m	
Settled bed height	H_s	0.30	m	
Grid cell size	Δx and Δy	0.005	m	Square cells
Time step	Δt	10^{-2}	s	

the following:

$$u_o = u_t \varepsilon^n \tag{5.26}$$

where u_t is the terminal velocity and n correlates with the Archimedes number Ar, and are given by the following Gibilaro (2001):

$$u_t = \left[-3.809 + \left(3.809^2 + 1.832Ar^{0.5}\right)^{0.5}\right]^2 \cdot \mu_f / \left(d_p/\rho_f\right) \tag{5.27}$$

$$Ar = gd_p^3\rho_f\left(\rho_p - \rho_f\right)/\mu_f^2 \quad ; \quad n = \frac{4.8 + 0.1032Ar^{0.57}}{1 + 0.043Ar^{0.57}} \tag{5.28}$$

In this thesis, predictions derived from the Richardson & Zaki (1954a) correlation which have been computed using eq.(5.26), (5.27) and (5.28) are compared with results on bed voidage at different superficial gas velocities obtained from the CFD simulations. Figure 5.3 shows a comparison between the results obtained from the Richardson & Zaki (1954a) correlation and predictions obtained from CFD simulations. From Figure 5.3, it can be seen that there is a very good agreement between prediction from the CFD numerical model and the Richardson & Zaki (1954a) correlation. Table 5.3 reports a comparison between the average macroscopic predictions obtained from numerical simulations compared with predictions from the Richardson & Zaki (1954a) correlation. From Table 5.3, quantitative numerical results are found to deviate between 0.34% - 1.73% from predictions obtained

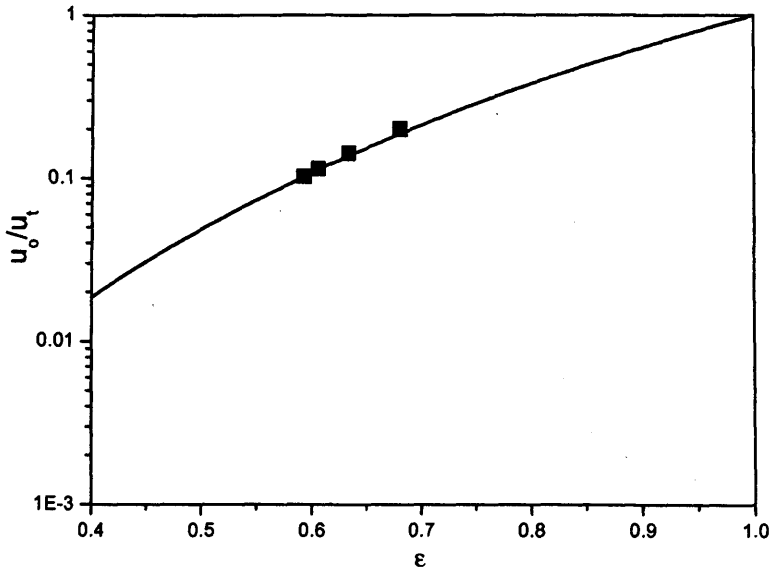

Figure 5.3: *Bed expansion characteristics: Comparison of CFD model results with Richardson & Zaki (1954a) correlation, Continuous curve, the R-Z form; solid squares, CFD model results*

from the Richardson & Zaki (1954a) correlation. This result demonstrates the good predic-

Table 5.3: *Comparison of computational averaged bed voidage prediction with predictions from the Richardson & Zaki (1954a) equation*

u_o, ms^{-1}	Bed Voidage		% Error
	Model Prediction	Richardson & Zaki (1954a)	
0.018	0.592	0.594	0.34
0.020	0.605	0.608	0.49
0.025	0.633	0.640	1.09
0.035	0.680	0.692	1.73

tive capability of the drag force closure employed in this thesis for expanding beds although the % deviation from Richardson & Zaki (1954a) increases with increasing superficial gas velocity. Nonetheless, the results provide a conclusive validation of the drag force closure.

5.4 CFD validation of the Eulerian-Eulerian simulations of the mono-component industrial powders

In this section, an experimental validation of the simulation of the Geldart Group B industrial materials, slag, natural and synthetic rutile particles is carried out. The study is concerned with the validation of the mono-component model presented in this thesis, see Table. 5.1, with the state of art granular kinetic theory model through a comparison of prediction of both models with experiments. The equations which have been used for the granular kinetic theory used for this study are summarized in Table 5.4.

Table 5.4: *Governing conservation equations applied to the validation of mono-component gas-solid simulations of industrial powders*

Continuity equations
$$\frac{\partial \varepsilon}{\partial t} + \nabla \cdot \left(\varepsilon \langle \boldsymbol{u} \rangle^f\right) = 0$$ $$\frac{\partial \phi}{\partial t} + \nabla \cdot \left(\phi \langle \boldsymbol{u} \rangle^s\right) = 0$$
Momentum Equations
$$\rho_f \left[\frac{\partial}{\partial t}\left(\varepsilon \langle \boldsymbol{u} \rangle^f\right) + \nabla \cdot \left(\varepsilon \langle \boldsymbol{u} \rangle^f \langle \boldsymbol{u} \rangle^f\right)\right] = \nabla \cdot \mathcal{T}^f - n\left\langle \boldsymbol{f}^f \right\rangle + \varepsilon \rho_f \boldsymbol{g}$$ $$\rho_s \left[\frac{\partial}{\partial t}\left(\phi \langle \boldsymbol{u} \rangle^s\right) + \nabla \cdot \left(\phi \langle \boldsymbol{u} \rangle^s \langle \boldsymbol{u} \rangle^s\right)\right] = \nabla \cdot \mathcal{T}^s + n\left\langle \boldsymbol{f}^f \right\rangle + \phi \rho_s \boldsymbol{g}$$
Fluid and Solid phase stress tensors
$$\mathcal{T}^f = -\langle p \rangle^f \boldsymbol{I} + \mu_f \left[\nabla \langle \boldsymbol{u} \rangle^f + \left(\nabla \langle \boldsymbol{u} \rangle^f\right)^T\right]$$ $$\mathcal{T}^s = -\langle p \rangle^s \boldsymbol{I} + \mu_s \left[\nabla \langle \boldsymbol{u} \rangle^s + \left(\nabla \langle \boldsymbol{u} \rangle^s\right)^T\right] + \left(\kappa_s - \frac{2}{3}\mu_s\right) \nabla \cdot \langle \boldsymbol{u} \rangle^s \boldsymbol{I}$$
Fluid-particle interaction force
$$n\left\langle \boldsymbol{f}^f \right\rangle = -\phi \nabla \langle p \rangle^f + \beta\left(\langle \boldsymbol{u} \rangle^f - \langle \boldsymbol{u} \rangle^s\right)$$

The interphase transfer co-efficient, β advanced by Di Felice (1994) has been used to model

the drag force in this study. The function has the following form:

$$\beta = \frac{3}{4} C_D \frac{(1-\phi)\,\phi\,\rho_f\,\left|\langle u\rangle^f - \langle u\rangle^s\right|}{d_p}\,\varepsilon^{2-\gamma} \quad ; \quad \gamma = 3.7 - 0.65e^{\left(-\frac{[1.5-\log(\varepsilon Re_p)]^2}{2}\right)} \tag{5.29}$$

The drag coefficient, C_D, proposed by DallaValle (1948) was applied in Eq. (5.29) has the following form:

$$C_D = \left(0.63 + 4.8\,Re_p^{-0.5}\right) \quad ; \quad Re_p = \frac{\varepsilon\,\rho_f\,\langle u\rangle^f\,d_p}{\mu} \tag{5.30}$$

5.4.1 Experimental and simulation strategies

The reader should refer to Chapter 3 for details of the experimental rig as well as the physical properties of the industrial materials used herein. For the experimental work carried out, the experimental bed was filled, for each mono-component industrial powder, to an initial height of 300 *mm*, corresponding to 2.37 *kg*,1.89 *kg* and 1.92 *kg* of slag, natural and synthetic rutile particles respectively. Experiments and corresponding simulations were performed at three different fluidizing velocities to investigate fluidization behaviour of all the materials at **(Case A)** same superficial fluidizing velocity, **(Case B)** same excess gas velocity **(Case C)** same multiple of u_{mf}. The inlet velocity at (Case A) was set equal to 0.20 m/s for all powders - inlet velocity for (Case B) was set at 0.20 m/s for natural rutile, 0.27 m/s for slag and 0.16 m/s for the synthetic rutile giving an excess gas velocity equal to 0.14 m/s for all powders. The inlet velocity at (Case C) was set equal to 3 u_{mf} which corresponded to values for u_o = 0.20 m/s for the natural rutile 0.39 m/s for slag and 0.07 m/s for the synthetic rutile - simulation strategies are summarized in Table 5.5. The computational parameters used in this study are similar to those already presented in § 5.3.1. However, an alternative discretisation scheme was employed in this study. The selection of the discretization [6] method can have a profound effect on the behaviour of a bubbling fluidized bed. Recent work by Copper & Coronella (2005) showed that systems modelled using a first order discretization scheme produced bubbles that are not realistic. The bubbles produced in their simulations,

[6]Discretization is the process by which the governing partial differential equations are converted to algebraic equations for numerical solutions

Table 5.5: *Simulation Strategy used in the validation of the mono-component Eulerian-Eulerian simulations industrial powders*

Material	Simulation Strategy		
	Case A (m/s) Same u_o	Case B (m/s) Same u_o-u_{mf}	Case C (m/s) Same multiple of u_{mf}
Slag	$1.8\,u_{mf}$ = 0.20	$2\,u_{mf}$ = 0.27	$3\,u_{mf}$ = 0.39
Natural Rutile	$3\,u_{mf}$ = 0.20	$3\,u_{mf}$ = 0.20	$3\,u_{mf}$ = 0.20
Synthetic Rutile	$8.7\,u_{mf}$ = 0.20	$7\,u_{mf}$ = 0.16	$3\,u_{mf}$ = 0.07

using a first order scheme, were initially large followed by much smaller bullet shaped bubbles which contained little wake. Furthermore, the bubbles were found not to interact with one another. Guenther & Syamlal (2001) had earlier attributed the above effect to the numerical diffusion in the numerical solutions of the solids momentum equation caused by the use first order discretization schemes. Following the observations of Copper & Coronella (2005) and Guenther & Syamlal (2001), a second order discretization scheme, SUPERBEE [7], was used for the momentum equations of the gas and solid phases to improve the computational prediction of bubble shape and behaviour. In fact, the use of the SUPERBEE discretization scheme implicitly introduces dissipation, purely numerical in origin, in the *modified* equation which is solved by the numerical code. This modified equation is different to the momentum equations shown in Table 5.1. Numerical dissipation serves to improve the stability of the solution by the use of artificial viscosity - a term which is again purely numerical in origin.

The impact of artificial viscosity on the qualitative aspects of a flow is like that of physical viscosity. Increasing artificial viscosity, for instance, results in a smoothen effect on shock waves just like an increased physical co-efficient of viscosity would cause. Therefore, for the specific case of this work, where internal stresses relevant to the solid phase has not been modelled, more artificial viscosity will be added implicity by the numerical algorithm to ensure a stable solution.

The fluidization conditions used in the present study are summarized in Table 5.6. A total

[7] Available within CFX4.4

of seven different simulations were carried out. All simulations were performed for a total 5 secs real time which translates to about 20 days for each simulation. The simulations were carried out using 3 Dell Xeon P4 3.1 Ghz Machine.

Table 5.6: *Computational parameters used in the CFD simulations*

Description	Symbol	Value	Comments
Gas Density	ρ_g [kg/m^3]	1.2	
Gas Viscosity	μ_g [Pa s]	1.85×10^{-5}	
Restitution Coefficient	e_s	0.90	GKT model
Maximum Solids Packing	ϵ_s,max	0.60	
Bed height	H_{bed} [m]	0.60	
Settled bed height	H_S	0.30	
Grid cell size	Δx and Δy [m]	0.005	Square cells
Time step	Δt [s]	10^{-4}	Time step

5.4.2 Results using the Granular Kinetic Theory model

5.4.2.1 Voidage profiles and bed expansion

A major initial objective of this work is to validate results obtained from CFD simulations with experimental results. In this section, snapshots showing the fluidization of slag, natural and synthetic rutile are compared with voidage contour maps obtained from CFD simulations using the GKT model. Figures. 5.4 - 5.6 show the voidage profiles for all the powders when fluidized at the same gas velocity, u_o = 0.2 m/s (Case A). The bubbles that form in the natural rutile are smaller in comparison to the synthetic rutile, as can be observed in the snapshots reported in Figure 5.4. This material is characterized by a higher u_{mf} than the synthetic rutile and thus a smaller excess gas velocity at the same superficial gas velocity.

The experimental and simulated snapshots of the synthetic rutile, Figure 5.5, shows a more vigorous bubbling regime when compared to the natural rutile ones. This behavior is expected because of the lower minimum fluidization velocity of the synthetic rutile material, see Table. 3.3. From the snapshots, it can also be seen that bubbles start to coalesce near the bottom of the bed and increase in size as the process of coalescence develops higher up in

the bed. Experimental and computational voidage profiles for the slag material, Figure 5.6, show very little fluid bed activity at the fluidizing velocity applied. From the experimental snapshot, it can be seen that there is no bubble activity in the bottom half of the bed, this might be related to the *wide* particle size distribution of the powder (see Figure 3.5). The computational snapshot in concurrence with the experimental snapshot depicts very small bubbles, this is due to the larger u_{mf} of the slag material which results in a small amount of excess gas in the fluid bed and consequently small bubbles.

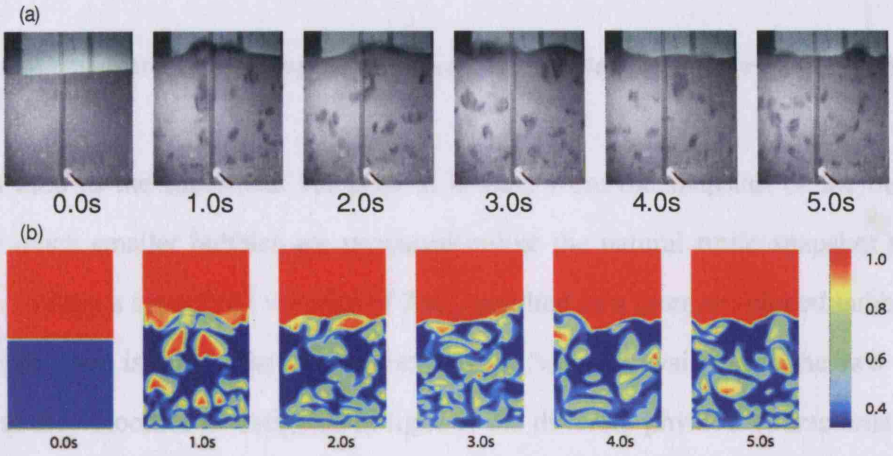

Figure 5.4: *Comparison between experimental (a) and simulated (b) voidage profile for Natural Rutile Material at U_o = 0.20 m/s*

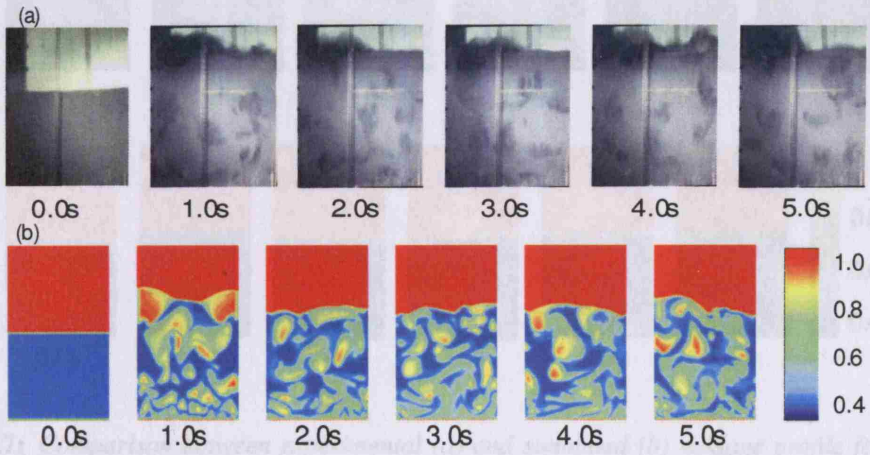

Figure 5.5: *Comparison between experimental (a) and simulated (b) voidage profile for Synthetic Rutile Material at U_o = 0.20 m/s (Case A)*

Figure 5.7 shows the voidage contour map for the synthetic rutile where 3 u_{mf} (Case C)

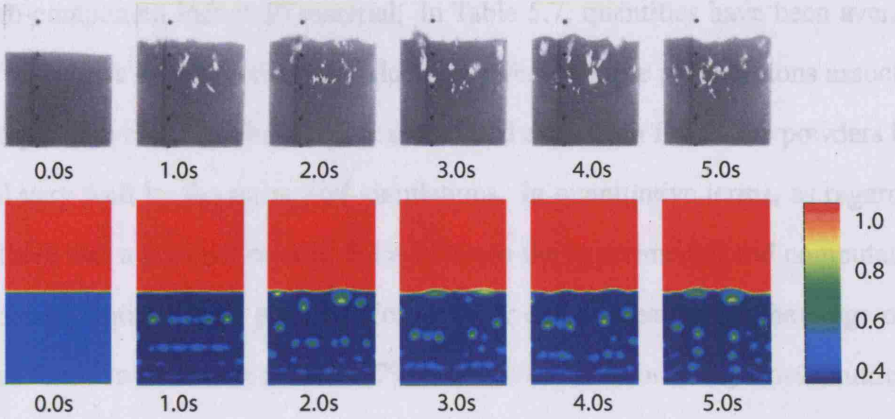

Figure 5.6: *Comparison between experimental (a) and simulated (b) voidage profile for Slag at U_o = 0.20 m/s (Case A)*

has been used as the superficial velocity. It is clear from the snapshot of the bed that in this case much smaller bubbles are produced unlike the natural rutile snapshot shown in Figure 5.4 where a superficial velocity of 3 u_{mf} resulted in a more developed bubbling bed. This phenomenon is due to the different excess gas velocity available in the two fluid bed systems at the velocities investigated in light of the different physical characteristics of all the materials and the flow rate needed to achieve fluidization.

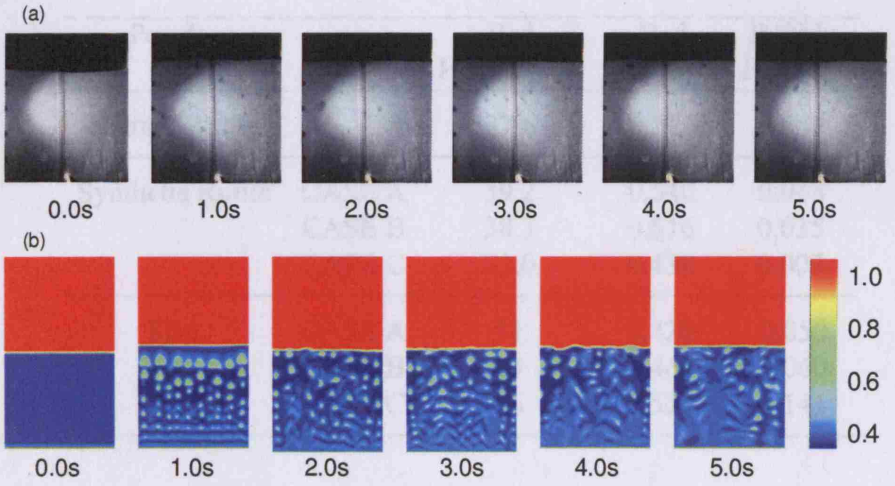

Figure 5.7: *Comparison between experimental (a) and simulated (b) voidage profile for Synthetic Rutile Material at U_o = 0.07 m/s (Case C)*

Table 5.7 and 5.8 show the time averaged macroscopic fluidization indicators obtained from the numerical computations and data from the experimental investigations carried out on

the mono-component industrial material. In Table 5.7, quantities have been averaged after the first 2 seconds of simulations to reduce the effect of large perturbations associated with the startup of the bed. Qualitatively, observed bed expansion for all the powders have been captured very well by the numerical simulations. In quantitative terms, as regards the bed height, there was a per cent error of 4.4% between the experimental and computational prediction for the natural rutile powder. For all other cases investigated, the range of per cent error was found to be within 5.9% - 6.7% and 8.3% - 11% for the synthetic rutile and slag. The disparity between the experimental and numerical results could be due to the influence of the particle size distribution (PSD) of the powders used for the experimental study, a property which has not been accounted for in the computational simulations, earlier work by Grace & Sun (1991) suggested that the particle size distribution can have a major influence on the bed expansion. According to them, the bed expansion increases the PSD widens. Thus, the wider PSD of the slag particle is responsible for bigger disparity noted between experimental and numerical results.

Table 5.7: *Comparison of time averaged macroscopic fluidization indicators for the industrial materials used in the mono-component Eulerian-Eulerian simulations*

Powder		Bed Height (cm)	Bed Voidage	Bubble Hold-up
Natural Rutile		37.6	0.521	0.053
Synthetic Rutile	CASE A	39.2	0.540	0.048
	CASE B	38.3	0.516	0.035
	CASE C	32.0	0.438	0.007
Slag	CASE A	31	0.420	0.050
	CASE B	33	0.460	0.060
	CASE C	38	0.522	0.141

Figures 5.8 and 5.9 , obtained by averaging the values for the bed height at different superficial velocities for the synthetic rutile and slag powder respectively, show a comparison of the numerical predictions for bed expansion with experimental data. The light gray lines on the plot indicate the region of 10% experimental error. From Figures 5.8 and 5.9, the numerical

Table 5.8: *Experimental results from the mono-component fluidization of the industrial powders*

Powder	u_o m/s	H_{mf} (cm)	Bed height (cm) at U_o	Voidage at U_o	ϵ_{mb}
Natural Rutile	0.20	30	36	0.66	0.58
Synthetic Rutile	0.20	33	42	0.59	0.48
	0.16	33	40	0.57	0.48
	0.07	33	34	0.50	0.48
Slag	0.20	30	35	0.59	0.53
	0.27	30	36	0.61	0.53
	0.39	30	38	0.63	0.53

predictions are observed to be within experimental error for most of the cases investigated.

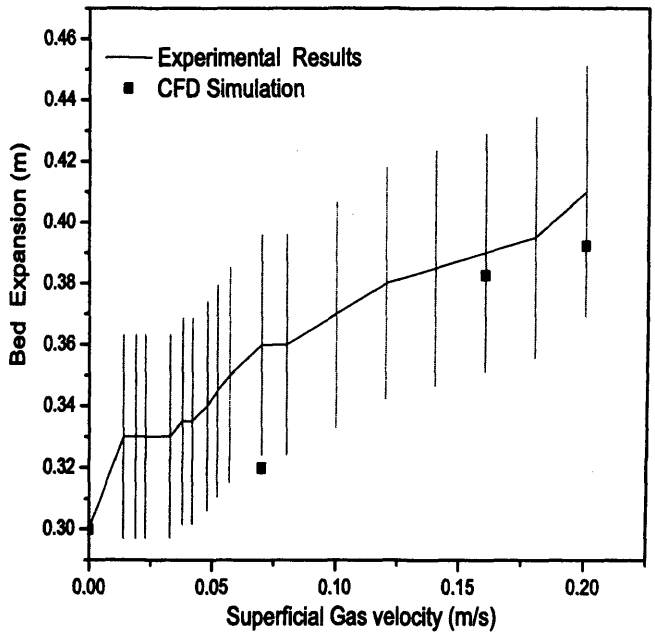

Figure 5.8: *Synthetic Rutile: Comparison between experimental and simulated averaged bed expansion*

The bubble hold up, shown in Table 5.7, is a measure of the fraction of gas that passes through the bed as bubbles. From Table 5.7, for Case B, where the same excess gas velocity is employed in all the simulations, the bubble holdup is seen to increase with increasing particle size. On the other hand, the trend also shows a decrease in bed expansion with an

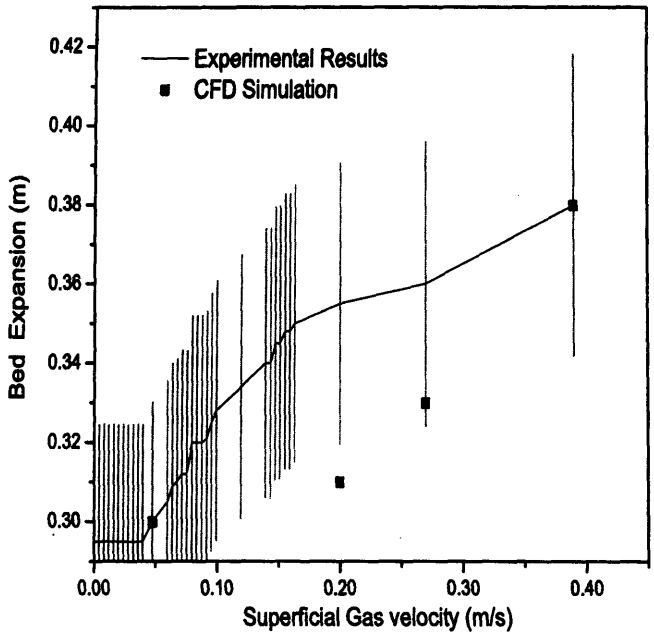

Figure 5.9: *Slag: Comparison between experimental and simulated averaged bed expansion*

increase of bubble holdup for Case B. The physical manifestation of an increase in bubble holdup is the presence of more bubbles in the fluid bed, for example see Figure 5.4.

5.4.2.2 Bubble Properties

For Case A, where the same fluidizing gas velocity is used (u_o = 0.2 m/s) the analysis of bubble diameter data has been conducted by comparing simulated values with results obtained from empirical bubble growth correlations and experimental data analysis. In this thesis, the semi-empirical model for bubble growth proposed by Darton et al. (1977) is used. This equation gives the bubble diameter as a function of the bed height as follows:

$$d_b = 0.54\left(u - u_{mf}\right)^{0.4}\left(h + 4\sqrt{A_0}\right)^{0.8}/g^{0.2} \tag{5.31}$$

where d_b is the bubble diameter, h is the height above the distributor and A_0 is the 'catchment area', which characterizes the gas distributor. The constant 0.54 has been obtained experi-

mentally. In absence of available data on the distributor characteristics, Darton et al. (1977) suggested a value for A_0 equal to 0. This fairly corresponds to the inlet boundary conditions set-up during this work, where no distributor has been simulated. In defining a bubble, an appropriate voidage has to be selected as the boundary between the emulsion and the gas phase. In this work, a voidage contour of 0.80 has been assumed for both experimental and simulation measurements (Yates et al., 1994). However, there is no broad agreement on the definition of a bubble in literature. Yates et al. (1994) for instance reported on a gas voidage distribution around a bubble, which was measured experimentally by means of an X-ray technique, as 0.627 for the cloud region surrounding the bubble core and a voidage of 1.0 for the core of the injected bubble. Nevertheless, the voidage used in this work is in also line with values used in literature by other authors (see Witt et al., 1998, Kuipers et al., 1993, van Wachem et al., 1998, 1999). The analysis of experimental bubble diameter was carried out using Optimas 6.0, image analysis software. A total of 60 bubble diameters were collated from the experimental analysis.

Figures. 5.10 and 5.11 show a comparison between the CFD simulations, experimentally obtained bubble diameter measurements and predictions from Darton et al. (1977) correlation for the synthetic rutile and natural rutile powders respectively. The results show, in agreement with experiments and predictions from Darton et al. (1977), that the simulated bubbles size increases as they travel up through the bed.

The simulated values are however always below the experimental ones for all the powders, with the scatter between experimental and simulated bubble size being greater at higher heights in the bed, in particular for the case of the natural rutile. On the other hand, Darton et al. (1977) correlation always over predicts the bubble size for both materials. In previous work, Cammarata et al. (2003) had shown similar results when comparing bubble size obtained from 2D and 3D simulations of a Group B material with predictions using the Darton et al. (1977) equation. In this case, results from 2D simulations were always lower than that predicted by Darton et al. (1977). That paper had also demonstrated that results from 3D simulations were always higher than those obtained from 2D runs - this may be seen

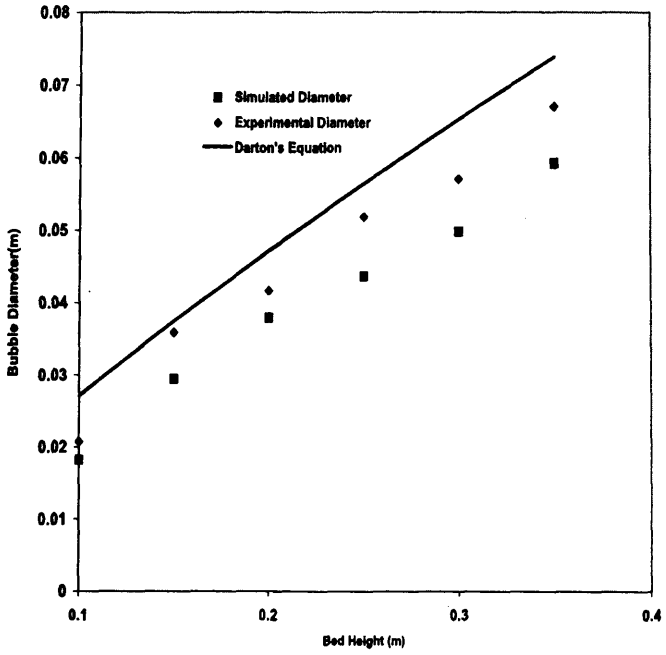

Figure 5.10: *Comparison of experimental and simulated bubble diameters with Darton et al. (1977) correlation for Synthetic Rutile material at u_o = 0.2 m/s*

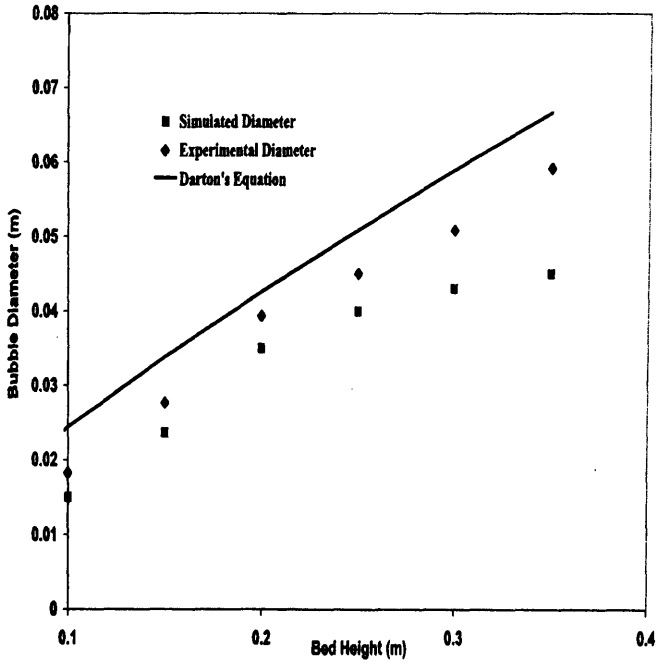

Figure 5.11: *Comparison of experimental and simulated bubble diameters with Darton et al. (1977) correlation for Natural Rutile material at u_o = 0.2 m/s*

in agreement with the results reported in this thesis where the "3D experimental bubbles" are always greater than the 2D simulated ones.

5.4.3 Comparison of results between the GKT and the proposed mono-component model

In this section, predictions obtained from the proposed mono-component model reported in Table 5.1 and implemented within CFX4.4 are compared with numerical predictions obtained from the GKT presented in the previous section and with existing experimental data. The same simulation strategy was employed when using the new proposed mono-component model, by which the same case studies reported in Table 5.5 were investigated.

5.4.3.1 Voidage profile and bed expansion

Figure 5.12 shows a voidage snapshot of the comparison between the experimental and computational voidage profiles for the Natural rutile material, the chosen velocity corresponds to 0.20 m/s. Figure 5.12 c shows qualitatively, that the proposed model is able capture bub-

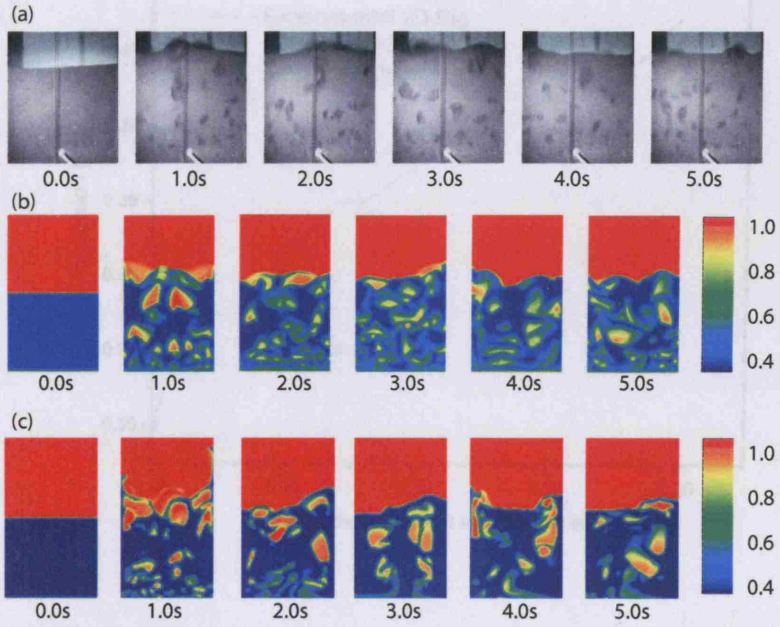

Figure 5.12: *Comparison between experimental (a) and simulated voidage profile for Natural Rutile Material (b) using the GKT model and (c) using the proposed mono-component model at u_o = 0.20 m/s (Case A)*

ble growth and the phenomenon of bubble coalescence which is present in the experimental snapshot. From Figure 5.12 b and c, it can also be observed that the marked inhomogeneities

present in the fluid bed in the GKT snapshot has been reproduced (although to a lesser extent) by the proposed model as shown in Figure 5.12 c. The simulated bubble sizes from the proposed model shown in figure 5.12 c also appears to be bigger, and more similar to the experimental snapshot than that which was predicted by GKT model. This inference is rendered in a more quantitative footing later.

Figure 5.13 shows a comparison between the experimental and simulated bed height predictions. From Figure 5.13, it can be observed that the predictions from the proposed mono-component model are closer to the experimentally determined values. Nevertheless, there is still a very good match between predictions obtained from the GKT and that predicted by the new mono-component model. Table 5.9 shows a comparison between experimental and model predictions obtained for bed height from the GKT and mono-component model proposed in this thesis.

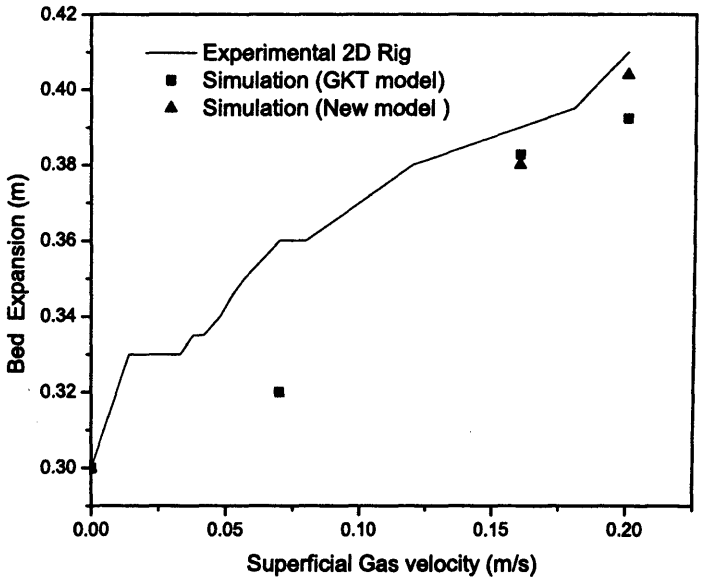

Figure 5.13: *Comparison between experimental and simulated bed height for Synthetic Rutile Material using the (GKT) and the proposed mono-component model at different superficial gas velocities*

Quantitatively, there is very little difference between the bed height prediction obtained from both numerical models. There was a per cent error of 2.8% between the experimental and

computational prediction for the natural rutile powder using the new model, as opposed to 4.4% obtained when experimental data is compared to predictions from the GKT. For all other cases investigated, the range of per cent error was found to be to be within 5% and 14% for the synthetic rutile and slag respectively when experimental data and numerical results from the new model are compared.

Table 5.9: *Comparison of model predictions for the bed height using the proposed model and GKT with experimental data*

		Bed Height		
Material	Case	Model Prediction	GKT Prediction	Experimental
Natural Rutile	-	0.37	0.38	0.36
Synthetic Rutile	Case A	0.40	0.39	0.42
	Case B	0.38	0.38	0.40
Slag	Case A	0.30	0.31	0.35
	Case B	0.32	0.33	0.36

The very little difference between the numerical predictions from both models highlights the very good predictive capability of the model developed herein. On the other hand, the result also demonstrates that the collisional stresses which are predicted by the GKT have little influence on macroscopic fluid bed predictions in dense gas solid systems. Indeed, this observation was noted in investigations carried out by van Wachem (2000) using bubbling dense gas-solid fluidized beds. Therein, the predicted granular temperature in dense regions of flow was found be very low $\left(\Theta \approx 10^{-5}\ \mathrm{m^2 s^{-2}}\right)$ due to the magnitude of the dissipation term. Thus, the magnitude of the solid phase stress predicted in the simulated dense gas solid beds were very small.

5.4.3.2 Power Spectral Density of pressure waves

The power spectral density (PSD) of time series of pressure fluctuations has become increasedly used by researchers (van Wachem et al., 1998, van der Schaaf et al., 2002, 2004) to characterize the gas bubble characteristics in freely bubbling beds. A power-law decay is normally observed with increasing frequency, with the decay often having a slope with

non-integer values in a log-log plot. The underlying physics of the power-law decay at increasing frequency, is believed to originate from hydrodynamic phenomena, such as rising, coalescing and exploding gas bubbles. Experimental observations by van der Schaaf et al. (2002) have shown that the slope of the power law decay of the PSD of pressure fluctuations in a bubbling fluidized bed in a log-log plot lies between -2 and -5. In this thesis, the PSD function has been estimated using the Origin ©graphical software. The PSD function of the time series is estimated from a length of 65536 points and is averaged over the length of the time series.

Figure 5.14, shows a comparison of the simulated pressure fluctuation of the natural rutile material using the GKT model available within CFX and the newly proposed model for the natural rutile material.

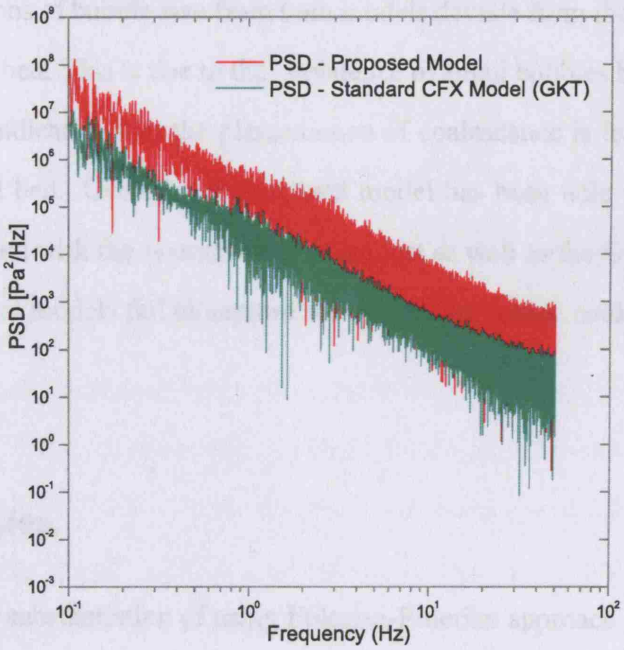

Figure 5.14: *A comparison of the PSD function of the simulated pressure fluctuation of the natural rutile material , $u_o = 0.20m/s$*

The most prominent difference between the two curves lies in the *total power* predicted of

the PSD. Here, a total power of $\approx 10^8\ Pa^2/Hz$ and $\approx 10^7\ Pa^2/Hz$ was predicted for the proposed model and the GKT respectively. The physical interpretation of the above effect is the prevalence of bubble activity in the fluidized bed simulated using the proposed model. This has already been observed in the computational voidage snapshots shown earlier in Figure 5.12.

5.4.3.3 Bubble properties

The predicted values of bubble diameter with increasing bed height have been analysed for the two models and compared with results obtained from empirical bubble growth equation proposed by Darton et al. (1977) and the experimental data results for the natural rutile powder at $u_o = 0.20m/s$. From Figure 5.15, it can be seen that initially (bedheight < $0.2m$), both models predict bubble growth via coalescence in agreement with experimental observations. However, predictions of bubble size from both models deviate from the experimental predictions higher in the bed. This is due to the prevalence of small bubbles higher up in the bed in both simulations indicating that the phenomenon of coalescence is less pronounced higher up in the fluidized bed. Overall, the proposed model has been able to capture the bubble properties associated with the system under exam just as well as the GKT model. Nevertheless, both numerical models fail to capture the physics of bubble coalescence higher in the fluidized bed.

5.4.4 Conclusion

In this section, the substantiation of using Eulerian-Eulerian approach for modelling the industrial materials has been addressed. The study was split into three parts, in the first part a linear stability analysis of the equations of change proposed in this thesis was carried out. Results obtained yielded a criterion which gives a better prediction than established criterions (Foscolo & Gibilaro, 1984) for the minimum bubbling voidage in a mono-component system. The better predictive capability was attributed to a better expression for the dynamic

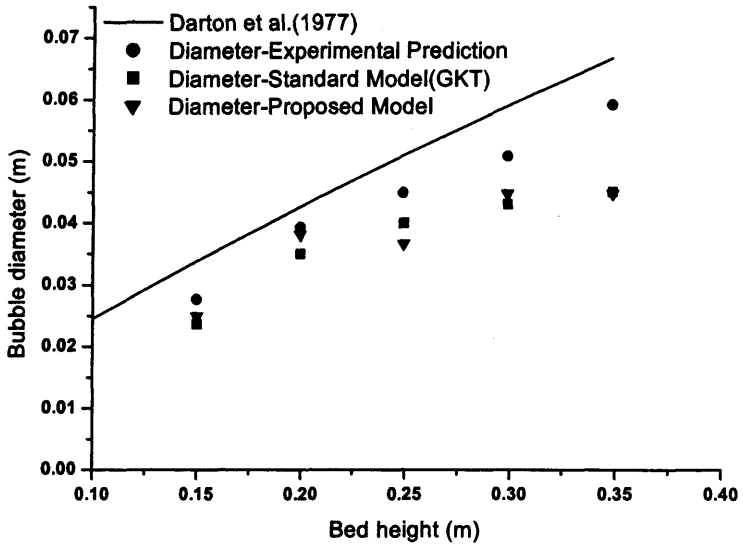

Figure 5.15: *Comparison of the experimental and simulated bubble diameters with Darton et al. (1977) correlation for Natural Rutile material at u_o = 0.2 m/s*

wave velocity, which is now a function of the local concentration of the particles, as well as the fluid-particle interaction force closure developed in this thesis. The second part centered around the validation of the drag force closure relation which has been used in this thesis, through macroscopic fluidization indicators. Results obtained, as regards the bed expansion, from the numerical study showed a very good agreement with predictions obtained from the Richardson & Zaki (1954a) equation.

In the third part, an experimental validation of numerical simulations of the mono-component industrial materials, Slag, Natural and Synthetic Rutile particles was carried out. In this study numerical results obtained from the well established granular kinetic theory (GKT) were initially compared with experimental results obtained using a 2D fluid bed and subsequently compared with results from the mono-component version of the model proposed in this thesis. For all velocities investigated, a good qualitative and quantitative match was found between the GKT predictions and experiments. Simulated values for bed expansion were found overall to be within 11% of experimentally measured values at the velocities investigated. Experimental results as well as an empirical bubble correlation were used to validate predicted simulation results for bubble size. The results show in agreement with

experiments and predictions from Darton et al. (1977), that the simulated bubbles size increases as they travel up through the bed. However, the phenomenon of bubble coalescence was found to be less pronounced higher in the bed.

A comparison between the model results from the GKT and the mono-component model proposed in this thesis, revealed on one hand very little difference between the numerical predictions from both models, thus highlighting the very good predictive capability of the model developed herein. Nevertheless, the results on the other hand, seem to indicate that the collisional stresses which are predicted by the GKT might have a limited influence on macroscopic fluid bed predictions in homogenous and bubbling dense gas solid systems.

Chapter 6

Eulerian-Eulerian model predictions for the binary systems

Summary

This chapter reports on the validation of the mathematical model developed for binary systems during this work and presented in Chapter 4. At first, simulation results are compared with experiments for Geldart B ballotini powders. In this part, a sensitivity analysis of the closure models describing the *particle-particle drag* force required for the modelling of a binary system described as a *three fluid* system is also carried out. Secondly, this chapter presents results on the mixing and segregation study of the industrial rutile materials provided by Huntsman Tioxide for this project.

The chapter then concludes by presenting simulation results on the numerical validation of a new fluid particle interaction force framework for binary mixture using an alternative modelling approach based on the virial equation of state for binary systems.

Parts of this chapter has been published in:

Owoyemi, O., Mazzei, L., Lettieri P., (2006). CFD modeling of binary-fluidized suspensions and investigation of role of particle-particle drag on mixing and segregation. *AIChE Journal.*, **53**, 1924 – 1940

6.1 Effect of particle-particle drag force on the dynamics of binary gas fluidized systems

In this section, a substantiation of the effect of the particle-particle drag force on the mixing and bubble dynamics of a binary gas-solid fluidized bed is examined. Here, three different closures available in literature and catering for this contribution are considered namely Gidaspow et al. (1985), Syamlal (1987b) and Bell (2000). The simulations are compared with a reference simulation where inter-phase particle-particle interactions are entirely neglected and also with dedicated experimental results. The particles used for experiments and computational studies are ballotini belonging to the Geldart Group B classification having 200 μm and 350 μm in diameter respectively and same density of 2500 kg/m^3. To conclude this study, a sensitivity analysis into the effect of solid stresses and numerical parameters (computational grid and time resolution) on the simulation dynamics is presented.

6.1.1 Simulation strategy

In the present study, all the simulations were carried out using a commercial CFD package, CFX 4.4. This package allows the free implementation of extra equations, boundary conditions and differencing schemes. The closure relations reported in § 4.3.2 were implemented in the code. In this part of the study, the internal stress associated with the solid phases has been neglected. The omission of this stress might give rise to localized over compaction in some regions of the simulated fluidized bed. To counter this effect the numerical algorithm *excess solid volume correction* developed in this thesis for binary systems (described in § 4.3.4) has also been implemented within the CFX4.4 code.

A 2D computational grid, in which front and back wall effects are neglected, was used. The left and right walls of the domain were modelled using no-slip velocity boundary conditions (for simplicity) for all phases. Dirichlet boundary conditions were employed at the bottom of the bed to specify a uniform gas inlet velocity. A pressure boundary condition was specified

at the top of the bed and set to a reference value of 1.015×10^5 Pa. The distributor was made impenetrable to the solid phase. As before, a second order discretization scheme, SUPERBEE [1], was used for all equations in order to improve the computational prediction of bubble shape and behaviour (Copper & Coronella, 2005). Here again, the SUPERBEE discretization scheme *implicitly* introduces dissipation, purely numerical in origin, in the *modified* equation which is solved by the numerical code. This would improve numerical convergence as well as the stability of the final solution since the internal stresses relevant to the solid phase has not been modelled.

The fluidization conditions used for all simulations are summarized in Table 6.1. A total of four different simulations was carried out. The fluidized bed was initially filled with two layers in which the flotsam particles (smaller particles) occupied the bottom half of the bed whilst the jetsam particles (bigger particles) occupied the top half of the bed. The particle-particle drag constitutive equations shown earlier in Table 2.8 were implemented for three of the cases. A fourth reference simulation was carried out in which no particle-particle drag was accounted for. All simulations were performed for a total of 10 seconds (real time); this is roughly twice the time required by the simulated system to achieve steady-state conditions and corresponds to an overall computational time of roughly 92 days for each simulation. The simulations were carried out using three Dell Xeon P4 3.2 Ghz Machines.

Table 6.1: *Computational parameters used in the CFD simulations.*

Description	Symbol	Value	Units	Comments
Gas density	ρ_f	1.29	kg/m^3	
Gas viscosity	μ_f	1.85×10^{-5}	Pa s	
Bed height	H_b	0.60	m	
Settled bed height	H_s	0.30	m	
Grid cell size	Δx and Δy	0.005	m	Square cells
Time step	Δt	10^{-4}	s	
Superficial gas velocity	U_o	0.25	m/s	
Coefficient of restitution	e	0.97	-	Syamlal (1987b)
Coefficient of friction	C_f	0.15	-	Syamlal (1987b)

[1] Available within CFX4.4

The grid resolution and time step adopted were based on previous work by Lettieri et al. (2002), *i.e.* 5 mm square cells using a time step of 10^{-4} secs. These values are in concurrence with figures recommended by several other researchers. In this regard, the work by Samuelsberg & Hjertager (1996), Enwald & Almstedt (1999), Mathiesen et al. (2000b), van Wachem (2000) and Mckeen & Pugsley (2003), to name just a few, is mentioned. In these works , the cells size length is usually of the order of one centimeter (varying between 0.5 cm and 4.0 cm); the time step (when specified) is in the range 10^{-5} s to 10^{-3} s. In both cases, choice of timestep used in this thesis is conservative and should be adequate and sufficiently small. However, a grid and time step dependence study is clearly desirable and a sensitivity analysis on this has been reported in § 6.1.5.

6.1.2 Experimental strategy

The experimental set-up used in this work, shown in Figure 6.1, consists of a two-dimensional plexiglass rectangular column, 600 mm high, 350 mm wide and 12 mm thick. The distributor is a uniformly permeable sintered bronze rectangular plate with a thickness of 3.5 mm. The fluidizing gas, air, is supplied via rotameters. The gas is dehumidified and filtered in order to remove possible impurities present in the stream. Pressure taps are installed 100 mm apart along the height of the bed from which pressure readings are collected via an electronic manometer. A system of two interlocked on/off valves operated simultaneously is installed on the rig to allow for instantaneous evacuation of the fluidizing gas during the "bed freeze tests" performed for the analysis of the mixing and segregation that occurs in the bed.

The binary system investigated is characterized by components that differ in size and have the same density. Ballotini powder samples of sizes $200\,\mu$m and $350\,\mu$m with a density of $2500\,\mathrm{kg/m^3}$ were used in the fluidization experiments. The larger and smaller ballotini particles represent the *jetsam* and *flotsam* particles respectively, as shown earlier in Table 3.5. The bed is initially completely segregated. The flotsam particles are filled first up to a height of 150 mm; the jetsam particles are then added on top up to a height of 300 mm. This

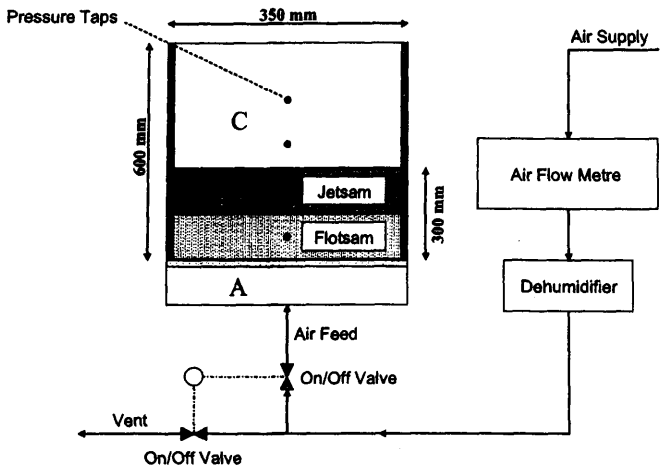

Figure 6.1: *Experimental Apparatus. (A) Windbox; (B) Fluidized bed; (C) Freeboard.*

corresponds to 0.88 kg and 0.97 kg of the flotsam and jetsam particles respectively.

The experiments were carried out at a superficial gas velocity u_o of 0.25 m/s. This value was determined using the procedure described earlier in § 2.5.4. Digital video recordings of the fluid bed were also made to analyse the development of the bubble dynamics within the bed and to determine the bubble size at the operating conditions employed. A "bed freeze analysis", for the experimental investigation of mixing and segregation, was carried out one minute after the initiation of the experiments (time required by the real system to achieve steady-state conditions). In the bed freeze tests the fluidizing air supply was shut off abruptly. The bed at rest was then split into four horizontal layers and each layer was sieved to obtain the percentage by weight of the different components. Samples used for sieving in this work were collected by means of a probe attached to a vacuum pump, described earlier in Chapter 3. Results of the bed freeze analysis are reported in Table 6.2 and Figure 6.3 and shall be discussed later on.

6.1.3 CFD Simulation results

6.1.3.1 Mixing and Segregation

A description of the mixing and segregation index has already been given in § 2.5.3. There, the mixing index was defined as:

$$M = \frac{\langle \omega_{jet} \rangle_t}{\langle \omega_{jet} \rangle_o} \tag{6.1}$$

where $\langle \omega_{jet} \rangle_t$ is the average mass fraction of the jetsam phase in the top region of the bed and $\langle \omega_{jet} \rangle_o$ is the average mass fraction of the jetsam phase evaluated over the entire bed. The top region of the bed is not uniquely defined, but can be chosen somewhat arbitrarily. Here, following van Wachem et al. (2001), the region was assumed to be the top 25% of the bed. In this study, since m_{jet} = 0.97 kg and m_{flot} = 0.88 kg, the index varies between 0 and 1.91. On the other hand, the coefficient of segregation, introduced by Geldart (1986), is given by:

$$C_s = \frac{\langle \omega_{jet} \rangle_b - \langle \omega_{jet} \rangle_t}{\langle \omega_{jet} \rangle_b + \langle \omega_{jet} \rangle_t} \cdot 100 \tag{6.2}$$

where $\langle \omega_{jet} \rangle_b$ and $\langle \omega_{jet} \rangle_t$ are the mass fractions of the jetsam phase in the bottom and top halves of the bed. Clearly C_s varies between −100 and +100, with −100 denoting perfect jetsam segregation at the top of the bed, 0 being representative of perfect mixing, and +100 indicating perfect jetsam segregation at the bottom of the bed.

Table 6.2 reports the mixing index M and the coefficient of segregation C_s calculated from experiments and after 10 seconds of simulation for all the different case studies examined. The values of M are also compared with the prediction obtained from the semi-empirical correlation developed by Wu & Baeyens (1998) and presented formerly in § 2.5.4. All the simulations show a good agreement with the experimental data and the semi-theoretical expression with the exception of the case where the particle-particle drag was neglected.

In quantitative terms, as regards the mixing index, the correlation by Wu & Baeyens (1998) yields predictions which deviate from experimental measurements by 1.6 %, the numerical

simulations accounting for the particle-particle drag present a deviation in the range 9% (Bell (2000) closure) - 13 % (Syamlal (1987b) closure), whereas when the foregoing contribution is neglected a percent error is found in excess of 28 %. The theoretical results obtained when the particle-particle drag contribution was accounted for are not noticeably affected by the specific closure adopted and always appear to slightly overpredict the degree of mixing within the bed compared with experiments.

In particular, the equation by Syamlal (1987b) yields an almost perfect mixing with a mixing index of roughly 1. Conversely, in the reference simulation, where no drag force was implemented, the segregation of the jetsam phase was somewhat overestimated as clearly indicated by the low mixing index and high coefficient of segregation obtained in this instance. In the light of these results, it seems reasonable to conclude that the absence of particle-particle drag causes the jetsam phase to migrate swiftly towards the bottom of the bed on account of the lack of hindrance (friction) that would otherwise have hampered this motion.

Table 6.2: *Experimental and theoretical values of the mixing index M and the coefficient of segregation C_s for all simulations.*

Drag Model	Mixing Index	Coefficient of Segregation
Experimental	0.886	+ 3.520
Wu & Baeyens (1998)	0.900	–
Bell (2000)	0.972	+ 2.456
Gidaspow et al. (1985)	0.984	+ 1.312
Syamlal (1987b)	0.999	– 0.620
No particle drag implemented	0.637	+ 17.177

Figure 6.2 and 6.3 show a comparison between theoretical and experimental concentration profiles of the jetsam phase throughout the bed. The computational values were determined after 10 seconds of simulation by splitting the bed into 28 horizontal layers of equal volume and by calculating the average jetsam mass fraction in each layer. The experimental results were obtained as described earlier on in § 3.3; in this case only four horizontal layers were considered. The profiles shown are consistent with the figures reported in Table 6.2 and confirm the conclusions previously drawn.

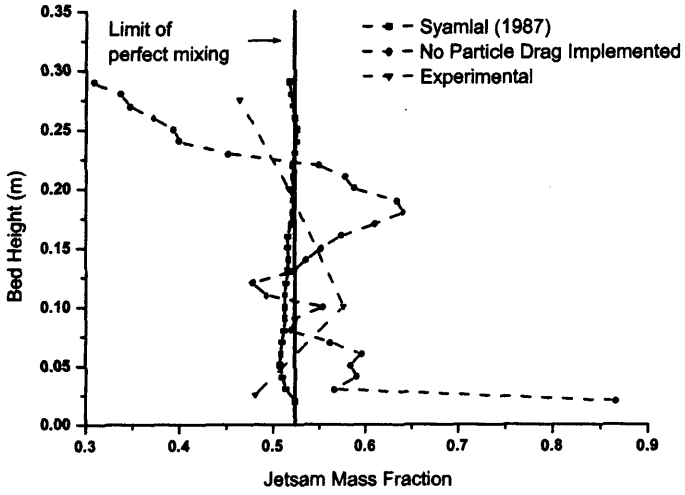

Figure 6.2: *Comparison of computational and experimental segregation patterns obtained from numerical simulations using (a) Syamlal (1987b) and (b) No particle-particle drag force.*

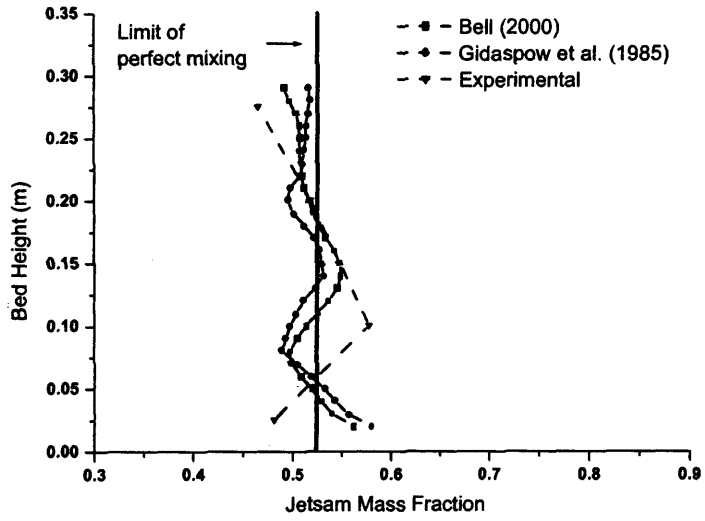

Figure 6.3: *Comparison of computational and experimental segregation patterns obtained from numerical simulations using (a) Bell (2000) and (b) Gidaspow et al. (1985) particle-particle drag force.*

In the case study where the Syamlal (1987b) equation was used we find an almost flat vertical profile with a constant jetsam mass fraction throughout the bed equal to roughly 0.52. This corresponds to a state of almost perfect mixing where the jetsam mass fraction would be equal to $\langle \omega_{jet} \rangle_o = 0.97/(0.97 + 0.88) = 0.524$. The degree of mixing is also slightly overestimated in the case studies where the equations of closure by Gidaspow et al. (1985)

and Bell (2000) were used. Here, as expected, the jetsam mass fraction profiles almost overlap with the limit of perfect mixing, with a jetsam concentration on the bottom of the bed slightly higher than on top. This is in agreement with the values of M and C_s formerly calculated and shown in Table 6.2. The effect due to lack of hindrance on the jetsam phase is again clearly found when no particle-particle drag was considered. In this instance the jetsam distribution throughout the bed is highly uneven.

In the upper region of the bed the jetsam mass fraction drops to values as low as 0.3 and the profile lies on the left of the limit of perfect mixing. In the remainder of the bed, conversely, the jetsam concentration is appreciatively higher, the profile shifts to the right of the limit of perfect mixing, and the mass fraction reaches values up to 0.66. This is clearly indicative of a state of segregation within the bed and confirms what was previously found from the analysis of the segregation and mixing parameters. This prediction is in sharp contrast with the experimental findings which present a jetsam phase far more evenly distributed and with a mass fraction spanning a quite narrow range (0.464 – 0.577).

Figure 6.4 shows the evolution of the jetsam mass fraction profile with time obtained using the Syamlal (1987b) drag correlation as an example.

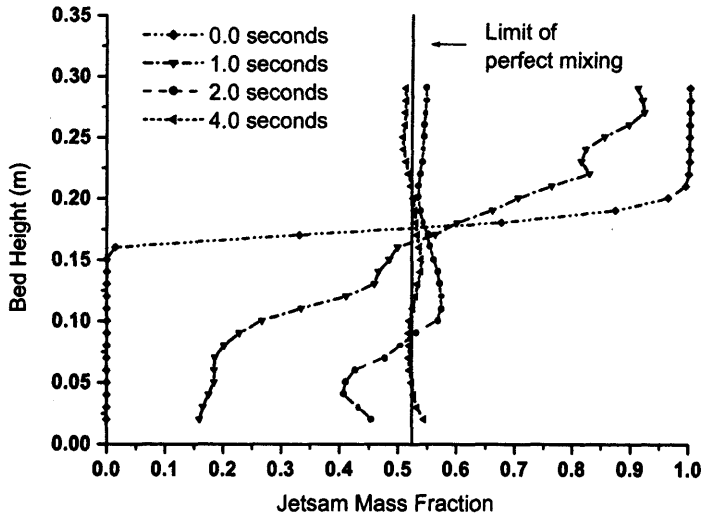

Figure 6.4: *Evolution of the jetsam mass fraction profile with time using the Syamlal (1987b) drag correlation*

From the figure, it can be seen that during the first 2 seconds, the jetsam phase spreads rapidly throughout the system; its mass fraction is seen to gradually increase at the bottom of the bed until an even distribution is attained (fully mixed state) after about 4 seconds of simulation. The jetsam mixing profile varies little thereafter and therefore is not reported.

In terms of the time required by the system to reach steady-state conditions, the above computational prediction is found to be at variance with experimental observations, where the bed becomes fully mixed after roughly 1 minute. The difference in mixing time between experimental and computational predictions clearly reveals a limitation in the predictive capability of the model. One may possibly attribute this to neglecting the collisional and frictional contribution in the model used in this thesis. However, the extent to which either factor predominates is presently unknown; to this end, it is worth pointing out that similar disparities have also been encountered by other researchers who have carried out analogous investigations while taking into account the collisional solid stress contribution. It is worth mentioning in this regard, the work of Huilin et al. (2003) where the fluid dynamic behaviour of a gas-fluidized binary mixture of Geldart Group D particles is simulated starting from initial conditions of perfect mixing. In the operating conditions chosen, the system tends to segregate and within roughly 10 seconds almost complete segregation is predicted. In light of the above, a sensitivity study on the effect of the collisional stress on the simulations is presented later in § 6.1.4.

6.1.3.2 Bubble Dynamics

An analysis of the bubble dynamics within the bed was carried out by comparing results in terms of computational bubble diameter with data obtained from experimental investigation. In defining a bubble, an appropriate voidage had to be selected as the boundary between emulsion and gas phases. A voidage contour of 0.80 was assumed in the simulations. This subjective figure is in conformity with values used in literature; in this regard, reference is made, for instance, to the work by Yates et al. (1994) and Mazzei & Lettieri (2006). The experimental analysis of the bubble diameter was conducted using Optimas 6.0, an image

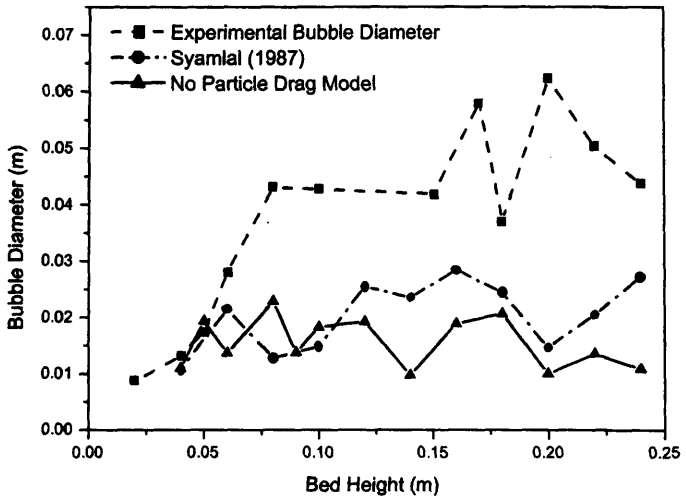

Figure 6.5: *Comparison of experimental with the simulated bubble diameter for (a) Syamlal (1987b) particle drag model and (b) no implemented drag model.*

analysis software. The computational analysis, on the other hand, was performed using the numerical algorithm recently developed by Mazzei & Lettieri (2006), where bubble diameters are assessed by capturing void regions within the simulated fluidized bed and then gauging their equivalent diameter (diameter of the circle of equivalent area).

Figure 6.5 shows a comparison between experimental and simulated bubble diameters. The data reported refer to experimental findings, results from the reference simulation where the particle-particle drag was neglected and predictions obtained using the closure by Syamlal (1987b). Results relevant to other constitutive equations have not been reported since these did not appreciably differ from those based on the Syamlal (1987b) equation. Indeed, as the figure clearly shows, the theoretical predictions in terms of bubble diameter are not significantly affected by the inclusion of the particle-particle drag force; this contribution seems therefore not to have a dominant effect on the bubble dynamics of the system. The experimental bubbles are always found to be larger than the simulated ones. Experimental evidence also indicates an increase in bubble size with increasing bed height due to coalescence, a phenomenon which appears less pronounced in the numerical results. A possible cause which might contribute in the underestimation of the computed bubble size might be

found in the dimensionality of the computational domain used in the simulations. In previous investigations carried out by Owoyemi et al. (2005) and Cammarata et al. (2003) using a 2D computational domain, the disparity between experimental and predicted bubble sizes was attributed to the subtle dissimilarity in geometry between the 2D computational domain and the experimental 3D, "thin 2D", domain. Another possible reason for the disparity between experimental and computational prediction of bubble size might be the underlying assumptions that have been made in the simulations. In this work, the individual particles have been assumed to have a monosize distribution whereas the experimental powders actual have a particle size distribution. Figure 6.6 reports a comparison between experimental and simulated bed voidage profiles obtained using the different constitutive expressions for the particle-particle drag force previously presented. All the simulations predict the bubbling phenomenon, albeit modestly, alongside other macroscopic phenomena like bubble coalescence and bed expansion without however highlighting the different behaviour of the bed when a particle-particle drag is included or not.

To complete the analysis, Figure 6.7 shows a comparison of the instantaneous velocity distribution of the jetsam particles superimposed on the voidage profile for two case studies. Here, the Syamlal (1987b) particle drag case study is compared with the case in which no drag is implemented. Both profiles show jetsam particles ascend upwards through the bed due to bubble motion and descend downwards towards the bottom of the bed at the walls of the vessel. A slight difference in the predicted magnitude of the particle velocity vectors of the jetsam phase can be discerned between each computational snapshot, with the snapshot produced using the Syamlal (1987b) drag law predicting a slightly higher velocity for jetsam velocity vector in localized regions of the bed.

However, once again, this specific kind of investigation does not seem to discriminate between different particle-particle drag force closures and this type of representation of the results appears to be quite insensitive to the inclusion of such term.

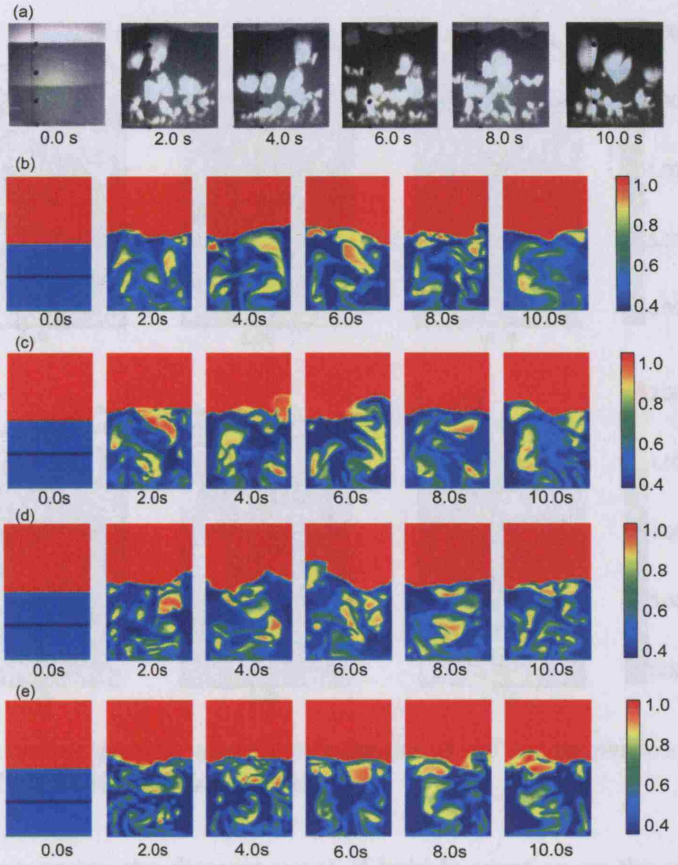

Figure 6.6: *Snapshots showing a comparison between: (a) experimental bed, (b) computational bed obtained using the drag closure by Bell (2000), (c) computational bed obtained using the drag closure by Gidaspow et al. (1985), (d) computational bed obtained using the drag closure by Syamlal (1987b) and (e) computational bed obtained using no particle drag expression.*

6.1.3.3 Bed height and voidage

A quantitative comparison of the bulk properties of the bed is shown in Table 6.3 in which results for bed height and voidage are reported. The properties were time-averaged ignoring the first two seconds of simulation in order to reduce the effect of perturbations associated with the bed start-up [2]. Very little difference is found between the various cases examined, the percent error spanning the range 3.3% (Syamlal (1987b) closure) - 5.8 % (no particle drag implemented), this is shown in diagrammatic form in Figure 6.8 which shows the comparison of the time evolution of bed height using the Syamlal (1987b) drag model and the case where no particle drag is implemented. The fluctuations in bed height with time in Fig-

[2]Although full mixing happens after 4 secs, it is not thought that either averaging after 4 secs or 2 secs will have a big effect on the time averaged results. The time of 2 secs was chosen because it corresponds to the point where semi-oscillatory response starts being observed (see Figure 6.8)

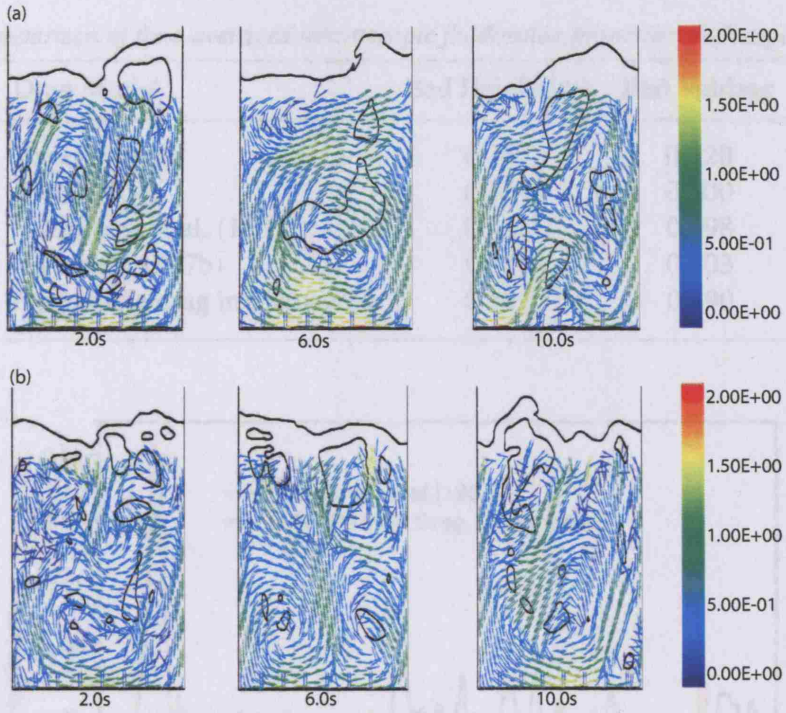

Figure 6.7: *Instantaneous particle velocity distribution of the jetsam particle using(a) Syamlal (1987b) drag model (b) No Particle drag Model*

ure 6.8 can be attributed to the discrete event of bubble eruption on the surface of the bed, which are similar for both case studies. Although, the case study where the Syamlal (1987b) particle drag is implemented has a slightly higher fluctuating frequency than the case where no particle-particle drag term has been implemented. Nevertheless, it is reasonable to conclude that the computational predictions of macroscopic properties of the fluid bed are quite insensitive to the specific particle-particle drag force closure adopted and again do not seem to be significantly affected by the inclusion of such contribution. This is not entirely surprising, since the concentration profiles of the solid phases within the bed are not expected to have a marked effect on overall bed properties such as bed height and mean bed void fraction.

6.1.3.4 Power Spectral Density (PSD) of pressure waves

Figure 5.14 shows a comparison of the power of pressure fluctuations between the numerical prediction obtained from the Syamlal (1987b) particle drag law and the case study where

Table 6.3: *Comparison of time-averaged macroscopic fluidization properties with experimental data.*

Drag Model	Bed Height (m)	Bed Voidage
Experimental	0.365	0.520
Bell (2000)	0.354	0.500
Gidaspow et al. (1985)	0.353	0.498
Syamlal (1987b)	0.355	0.503
No particle drag implemented	0.347	0.490

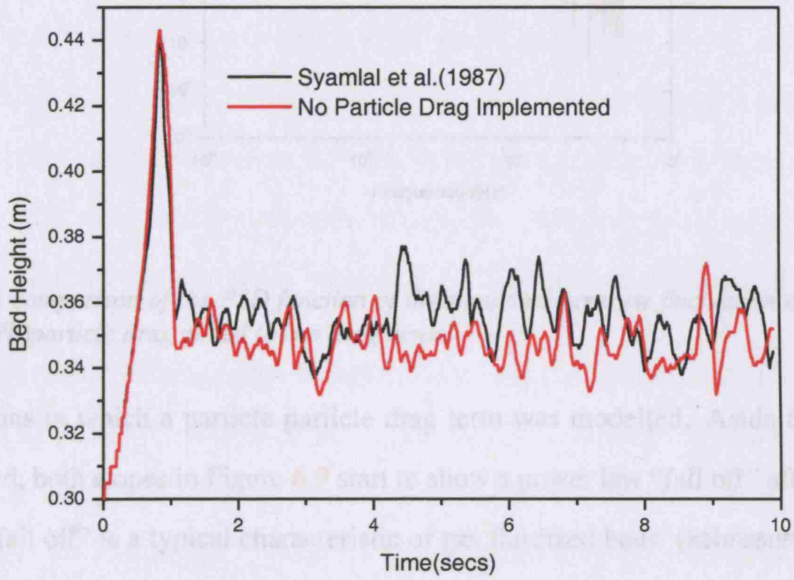

Figure 6.8: *A comparison of the averaged bed height fluctuations with time at $u_o = 0.20m/s$ using numerical results obtained from (a) Syamlal (1987b) drag model and (b) No particle drag model.*

no particle drag model was implemented. The PSD function has been estimated using Origin © graphical software. The PSD function of the time series is estimated from a length of 1084 points and is averaged over the length of the time series.

From Figure 5.14, it can be observed that both curves have the same *total power* of PSD ($\approx 10^9\ Pa^2/Hz$). However, the PSD shift appears to be higher using the Syamlal (1987b) drag model. It is imagined that the above phenomenon would have an effect on the frequency of bed height fluctuations with time, such that bed height fluctuations would be greater for simulations in which the particle-particle drag term is included (van der Schaaf et al., 2004). Nevertheless, an increased frequency of bed height fluctuation was not observed in any of

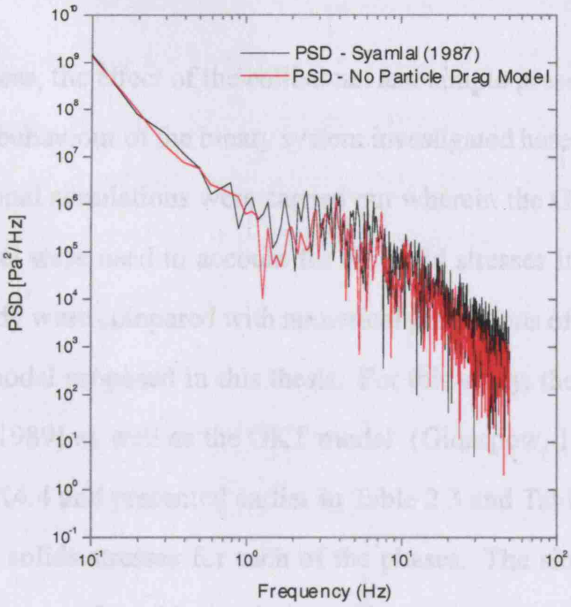

Figure 6.9: *A comparison of the PSD function of the simulated pressure fluctuation of using the (a) Syamlal (1987b)particle drag model (b) no drag model*

the simulations in which a particle-particle drag term was modelled. Aside from the PSD shift observed, both slopes in Figure 6.9 start to show a power law "fall off" after 5 Hz. This power law "fall off" is a typical characteristic of gas fluidized beds (Johnsson et al., 2000). However, the true underlining physics of the power at higher frequencies remain unknown (van Wachem, 2000). Overall, the PSD curves for both simulations are seen to have a similar shape irrespective of the inclusion of the particle-particle drag force term.

6.1.4 Effect of solid phase collisional and simple pressure stresses on the simulation dynamics

The effect of modelling the solid phase collisional stress on the numerical prediction of macroscopic fluidization properties for mono-component systems was presented earlier in § 5.4.3. There, it was found that the collisional stresses which are predicted by the GKT (Granular Kinetic Theory) model have little influence on macroscopic fluid bed predictions such as bed height and voidage as well as predictions of the bubble diameter. Thence, the

stresses were deemed non-dominant.

Here, for completeness, the effect of the collisional and simple pressure stresses on the mixing and segregation behaviour of the binary system investigated herein will be elucidated. To this end, two additional simulations were carried out wherein the GKT theory and a simple solids pressure model were used to account for the solid stresses in the particulate phases. Results from the study were compared with numerical predictions of mixing and segregation obtained from the model proposed in this thesis. For this study, the simple pressure model of Bouillard et al. (1989) as well as the GKT model (Gidaspow, 1994), both of which are available within CFX4.4 and presented earlier in Table 2.3 and Table 2.4 respectively, were used to describe the solids stresses for each of the phases. The simulation conditions employed in § 6.1.1 were used for both simulations. The particle drag law by Syamlal (1987b) was used to describe the interaction between the solid phases in all the simulations.

Table 6.4 reports the mixing index M and the coefficient of segregation C_s calculated from experiments and after 10 seconds of simulation for all the different simulations. The values of M are also compared with the prediction obtained from the semi-empirical correlation developed by Wu & Baeyens (1998). All the simulations, in agreement with experimental

Table 6.4: *A comparison of experimental and theoretical values of the mixing index M and the coefficient of segregation C_s obtained using different particle stresses.*

		System Properties	
Study	Solid Stress Model	Mixing Index	Coefficient of Segregation
Experimental	–	0.886	+ 3.520
Wu & Baeyens (1998)	–	0.900	–
Simulation 1	Bouillard et al. (1989)	0.972	+ 1.160
Simulation 2	GKT (Gidaspow, 1994)	0.975	+ 1.617
Simulation 3‡	–	0.999	– 0.620

‡Refers to the model proposed in this thesis

findings, yield similar results for the mixing index and coefficient of segregation without regard for the presence of a solid phase stress model. Quantitatively, as regards the mixing index, the numerical predictions which account for a solid phase stress model deviate from experimental measurements by 8.84% (Bouillard et al., 1989) and 9.14%(GKT, Gidaspow

(1994)) respectively, a per cent error of 13% is found between numerical predictions and experimental measurements when the particle stress is neglected. Thus, it seems that collisional and simple pressure stresses have a very minimal influence on the numerical prediction of the mixing index and coefficient of segregation in dense binary gas solid beds. Figures 6.10 and 6.11 shows the evolution of the jetsam mass fraction profile with time obtained when solid phase stresses are modelled.

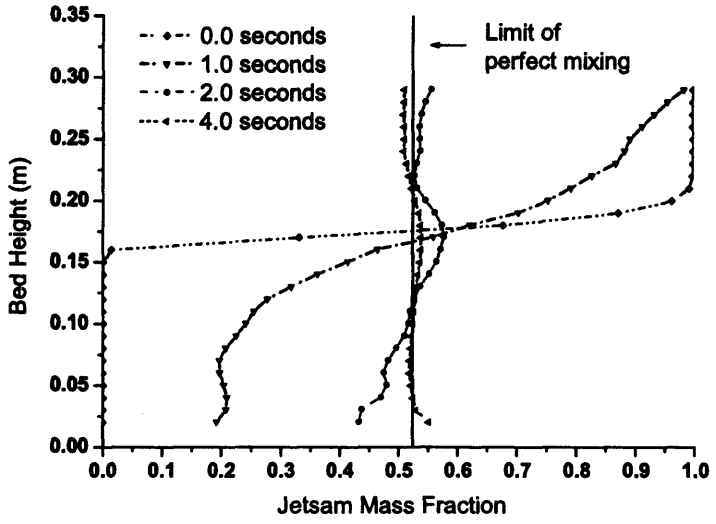

Figure 6.10: *Evolution of the jetsam mass fraction profile with time obtained using the GKT theory to model the solid phase stresses*

From the figures, it can be seen that during the first 2 seconds, the jetsam phase spreads rapidly throughout the system in concurrance with Figure 6.4, wherein the solid stress was neglected. The mass fraction gradually increases at the bottom of the bed in Figures 6.10 and 6.11 until an even distribution is attained (fully mixed state) after about 4 seconds of simulation, in agreement with earlier results in Figure 6.4. Hence, it seems that the computational predictions of computational mixing time is quite insensitive to collisonal stress (GKT) and the simple pressure model adopted and as such do not seem to be significantly affected by the inclusion of such contribution for the solid phases. However, the numerical dicretization scheme used in this work , SUPERBEE, might possibly be overwhelming the effects of the collisonal stress (GKT) and the simple pressure model adopted due to numer-

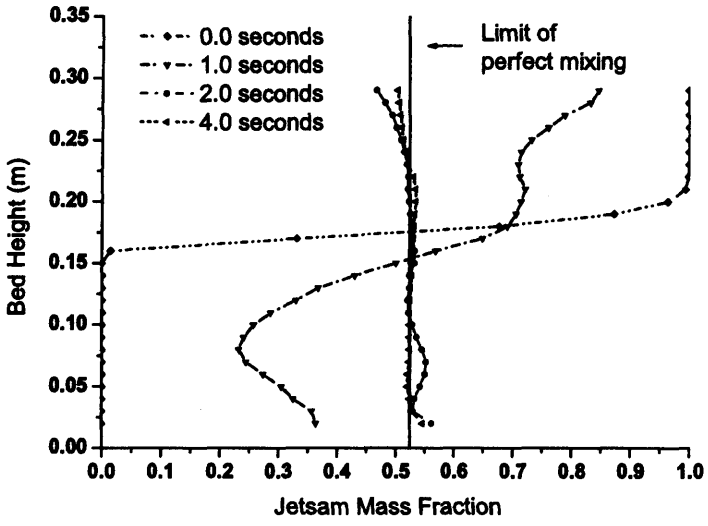

Figure 6.11: *Evolution of the jetsam mass fraction profile with time obtained using the simple pressure model of Bouillard et al. (1989) to model the solid phase stresses*

ical dissipation. Further studies might need to be carried out to delineate the effects of the second order discretization scheme on the dynamics of the fluidized system.

6.1.5 Effect of grid and time resolution on the simulation dynamics

The size of the grid spacing determines to a large extent the computational effort (time) required as well as the extent of numerical diffusion. The size of the time step on the other hand influences the numerical convergence of the differential equations as well as the overall computational time. Thus, it is important for an optimum to be found between the above quantities (grid size and time step). To this end, this section presents a study into the effect of the time and grid resolution on the numerical prediction of macroscopic fluidization properties. Here, four simulations were carried out using grid sizes of 5 and 10mm square cells as well as time steps of 10^{-04} and 10^{-03} secs. The simulations were carried out following the *matrix* shown in Table 6.5. The simulation conditions employed in § 6.1.1 were used for all the numerical investigations. Here again, the particle drag law by Syamlal (1987b) was used to describe the interaction between the solid phases in all the simulations.

Table 6.5: *Simulation matrix used for the numerical investigation of grid and time resolution*

	Grid Size	
Time Step	5mm	10mm
10^{-04} secs	Simulation 1	Simulation 2
10^{-03} secs	Simulation 3	Simulation 4

Table 6.6 shows results of a comparison of the averaged macroscopic fluidization properties obtained after 10 seconds of simulation for all the different simulations.

Table 6.6: *A comparison of the numerical predictions of averaged fluidization properties for the numerical investigation of grid and time resolution.*

		Averaged macroscopic fluidisation properties			
Time step	Grid size	Bed height (m)	Bed Voidage	Mixing Index	Coefficient of Segregation
10^{-04} secs	5 mm	0.355	0.503	0.998	− 0.620
10^{-03} secs	5 mm	0.350	0.496	0.985	+ 0.951
10^{-04} secs	10 mm	0.355	0.501	0.988	+ 0.132
10^{-03} secs	10 mm	0.350	0.496	0.987	+ 0.211

From Table 6.6, a change in the grid cell size is observed to have very little influence on the averaged numerical predictions of fluidization indicators. For instance, using a constant time step of either 10^{-03} or 10^{-04} secs and increasing the grid cell size from 5mm to 10mm results in no appreciable change in the predicted numerical values for the bed height and voidage. However, there is a subtle effect on the numerical prediction of the mixing index and coefficient of segregation. Nevertheless, this effect is small and deemed negligible within the range of variation of the two indexes, refer to § 6.1.3.1

Conversely, a reduction in the time step, for instance, from 10^{-03}s to 10^{-04}s whilst using a constant grid cell size of 5mm, results in a 2% change in the numerical prediction of bed height and voidage. Here again, it appears that the effect of a time step reduction on the predictions for mixing and coefficient of segregation is minimal. Overall, it seems that a change in time step has a more appreciable effect on numerical prediction than a corresponding change in grid cell size.

A smaller grid and time step dependence study would be clearly desirable, however a quick

calculation reveals that with the computational resources available for this work at present, simulations performed using a time step of 10^{-4} s and square cells of 5 mm side length required, as previously mentioned, an overall computational time of roughly 2200 hours (92 days). For the same time step, if the side length of the cells is halved (2.5 mm), the computational time rises to about 4800 hours (200 days) for the same amount of real time simulation. Similarly, for the same grid resolution, if the time step is lowered to 10^{-5} s, the computational time rises to about 9950 hours (415 days). Thus, the long computational times involved renders such a study unfeasible.

6.1.6 Conclusions

The model presented earlier in Chapter 4 has been solved using the commercial CFD code CFX 4.4. Four simulations have been carried out: three wherein different constitutive equations for the particle-particle drag force were used and a final one where the force was entirely neglected. The first three case studies yielded similar results in terms of jetsam particle distribution within the bed, with an almost perfect mixing and a good agreement with the experimental data. In the forth case study, conversely, an overprediction of the jetsam mobility was found with a resulting tendency of such phase to segregate towards the bottom of the bed. This was in clear contrast with the experimental evidence. An investigation into the bubble dynamics and bulk properties of the system was also conducted showing that this study did not discriminate between different particle-particle drag force closures and appeared to be quite insensitive to the inclusion of such a contribution. A sensitivity analysis on the influence of the collisional stress together with the effect of the grid cell size and time step was performed. Results obtained showed a minimal effect on the numerical prediction of mixing and segregation on the materials studied.

6.2 Mixing and segregation of binary fluidized beds using industrial materials

In this section, the mixing and segregation behaviour of a binary mixture of industrial powders supplied for this project is studied using the model presented in Chapter 4 for binary mixtures. Computational results obtained are validated quantitatively and qualitatively with experimental data. The materials used in this study are natural rutile and slag which differ only in size, having a mean diameter of 186 μm and 305 μm respectively, and same density of 4200 kg/m^3.

6.2.1 Simulations Strategy

In this study, all the simulations were carried out using a commercial CFD package, CFX 4.4. The simulations were carried out using the same conditions described earlier in § 6.1.1. The Syamlal (1987b) drag law was used to model the particle particle drag term in all the simulations. The fluidization conditions used for all the simulations are summarized in Table 6.7. In this investigation, three different average compositions, corresponding to the

Table 6.7: *Computational parameters used in the CFD simulations.*

Description	Symbol	Value	Units	Comments
Gas density	ρ_f	1.29	kg/m^3	
Gas viscosity	μ_f	1.85×10^{-5}	Pa s	
Bed height	H_b	0.60	m	
Settled bed height	H_s	0.30	m	
Grid cell size	Δx and Δy	0.005	m	Square cells
Time step	Δt	10^{-4}	s	
Superficial gas velocity	U_o	–	m/s	see Table 6.9
Coefficient of restitution	e	0.97	-	Syamlal (1987b)
Coefficient of friction	C_f	0.15	-	Syamlal (1987b)

average mass fraction of jetsam particles (slag) of 0.25, 0.50, 0.75 in the bed were considered, so that the hydrodynamic behavior of three binary mixtures in all was studied. The various mixtures of natural rutile and slag (*NR-SG*) investigated is summarized in Table 6.8.

The mixture fractions of the powders were initially filled in two layers in which the flotsam particles (Natural Rutile, NR, smaller particles) occupied the bottom half of the bed whilst the jetsam particles (bigger particles, Slag, SG) occupied the top half of the bed. The mixtures were then fluidized at a constant excess gas velocity, u_{xs}. This value was determined using the procedure described earlier in § 2.5.4 which uses the expression developed by Wu & Baeyens (1998) that relates the mixing index M representative of the bed mixedness to the visible bubble flow rate. Here, the excess gas velocity is given by the following:

$$u_{xs} = u_o - u_{mf} \tag{6.3}$$

where u_o refers to the superficial gas velocity and u_{mf} is the minimum fluidization velocity. For each of the three cases reported in Table 6.8 the investigation was carried out at two excess gas velocities, u_{xs} equal to 0.20 m/s and to 0.10m/s and each simulation was carried out for 10 seconds real time. In all, a total of six numerical simulations were performed for this study. The overall computational time was roughly 85 days for each simulation. The simulations were carried out using three Dell Xeon P4 3.2 Ghz Dual processor Machines. The superficial gas velocities employed for the various mixture fractions used the simulations are summarized in the form of a "matrix" in Table 6.9. Here, the superficial gas velocities used for the investigations on mixing, for instance, can be discerned by selecting a particular column (jetsam mixture fraction) and thereafter selecting the desired excess gas velocity, in this case 0.20, and lastly adding the desired excess gas velocity to the minimum fluidization velocity specified in the chosen column.

Table 6.8: *Binary mixture fractions investigated*

Simulation	$\langle\omega_{flot}\rangle$	$\langle\omega_{jet}\rangle$
1	0.25	0.75
2	0.50	0.50
3	0.75	0.25

Table 6.9: *Superficial gas velocities used in the study of mixing and segregation patterns for industrial materials*

Quantities, m/s	Average mass fraction of jetsam, $\langle \omega_{jet} \rangle$					
	0.25		0.50		0.75	
u_{xs}	0.20	0.10	0.20	0.10	0.20	0.10
u_{mf}	0.060		0.078		0.107	
u_o	0.260	0.160	0.278	0.178	0.307	0.207

6.2.2 Experimental strategy

The experimental apparatus and strategy used in this study is similar to that which was described earlier in § 6.1.2. In this case, the natural rutile and slag particles represent the *flotsam* and *jetsam* particles respectively. In all the experiments performed, the bed is initially completely segregated. The flotsam particles are filled first and the jetsam particles are then added on top up to a height of 300 mm. The amount of flotsam and jetsam particles which have been used in for the all experiments have been summarised in Table 6.10.

Table 6.10: *The amount of flotsam and jetsam particles used in the experimental study of the industrial powders*

$\langle \omega_{jet} \rangle$	m_{jet} (kg)	m_{flot} (kg)
0.75	1.660	0.631
0.50	1.110	1.085
0.25	0.577	1.804

The experiments were also carried out at the superficial gas velocities summarized in Table 6.9. Digital video recordings of the fluid bed were also made to analyse the development of the bubble dynamics within the bed and to determine the bubble size at the operating conditions employed.

6.2.3 CFD simulation results

6.2.3.1 Mixing

Table 6.11 reports a comparison of the mixing index M obtained from experiments with numerical results obtained after 10 seconds of simulation, using an excess gas velocity of 0.20m/s, for all the different jetsam fractions. The values of M are also compared with the prediction obtained from the semi-empirical correlation developed by Wu & Baeyens (1998). All the simulations show a good agreement with the experimental data and the semi-theoretical expression.

Table 6.11: *Experimental and theoretical values for mixing index M obtained for different jetsam fractions at an excess gas velocity of 0.20m/s*

	Mixing Index		
$\langle\omega_{jet}\rangle$	CFD	Experimental	Wu & Baeyens (1998)
0.75	1.00	0.92	0.90
0.50	0.98	1.00	0.90
0.25	0.95	1.00	0.90

In quantitative terms, results from the numerical simulations are within 8% and 10% of the experimental results and the prediction from the semi-empirical correlation developed by Wu & Baeyens (1998) respectively. However, the correlation by Wu & Baeyens (1998) seems to underpredict the experimental and computational mixing indexes in all the cases investigated. Nonetheless, a fluidized bed with a mixing index greater than 0.9 is usually considered to be in well mixed state (Wu & Baeyens, 1998).

Figure 6.12 shows an experimental snapshot of the typical evolution of mixing in the fluidized bed for a mixture fraction, $\langle\omega_{jet}\rangle$, of 0.75 jetsam (slag) at an excess gas velocity of 0.20m/s. From the snapshot, it can be observed that the flotsam particles (Natural rutile), which originally occupy the bottom part of the bed, are transported upwards by rising bubbles. This mechanism of transport has also been identified by other researchers (Nienow & Chessman, 1980, Nienow & Chiba, 1985). In the present case, experimental ob-

servations showed that particles which gather in the wake of a rising bubble, are carried from near the bottom of the bed to the surface of the bed. En-route, natural rutile particles from the wake of the rising bubble is constantly exchanged with new particles from the dense surrounding region. This mode of suffusion of the natural rutile particles to the surface of the bed appears as the "finger like" propagation of the particles in the snapshot. At the same time, slag particles seem to"rain down" through approaching bubbles as a mode of transport towards the bottom of the bed. The large presence of bubbles of different sizes in the fluidized bed adds complexity to the mixing pattern observed. Hence, the overall mixing process can be approximated as a random mixing process.

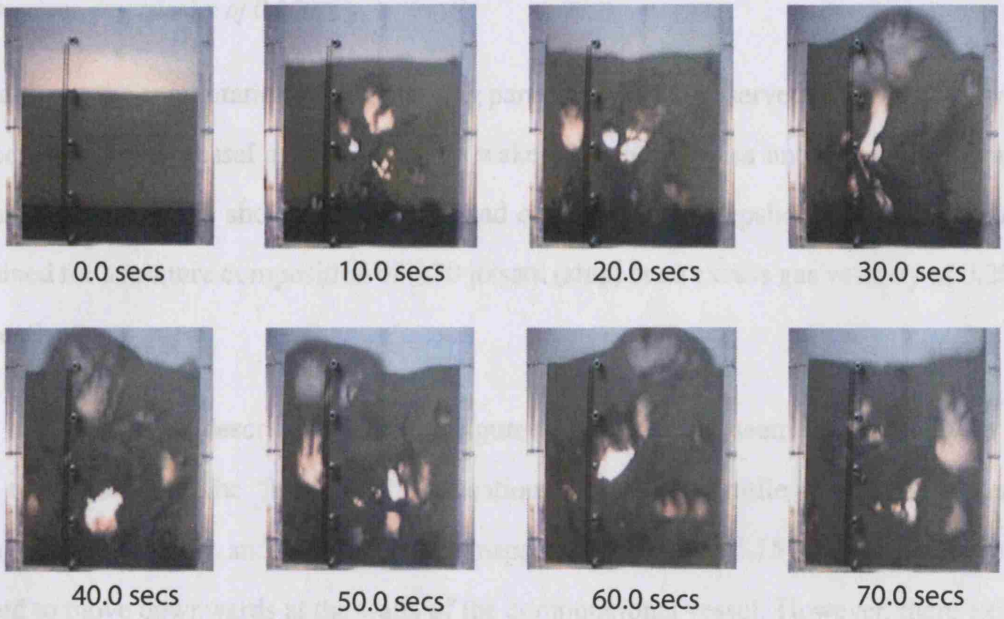

Figure 6.12: *Experimental snapshots of the fluidized bed using a mixture fraction of 0.75 slag at an excess gas velocity of 0.20m/s.*

Figure 6.13 shows a computational snapshot of the mixing mechanism in the simulated fluidized bed for a mixture fraction of 0.75 slag particles at an excess gas velocity of 0.20m/s. From Figure 6.13, It can be seen that the experimentally observed mixing mechanism has been captured by the numerical simulation; natural rutile particles are observed to permeate to the top of the bed in a "finger like" manner in concurrence with earlier experimental findings. This transportation of natural rutile particles to the top of the bed is also facilitated by bubble motion, which has been captured by the simulation causing substantial agitation

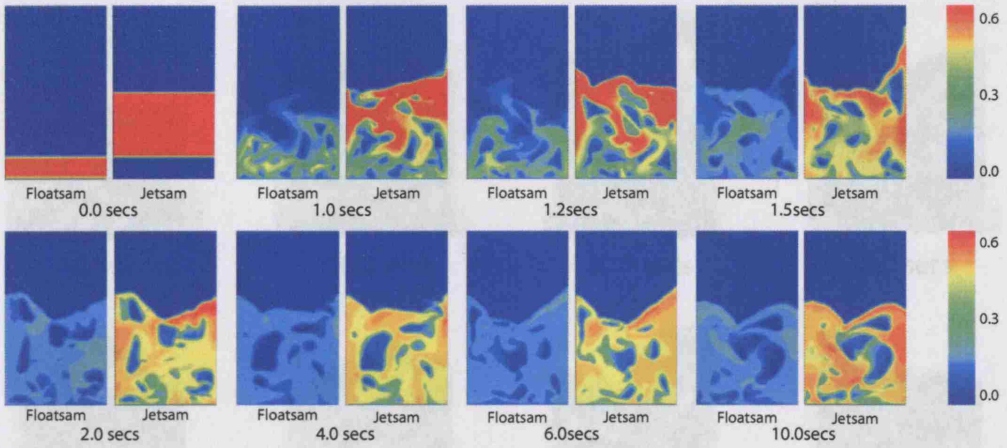

Figure 6.13: *Computational snapshots of the simulated fluid bed using a mixture fraction of 0.75 slag at an excess gas velocity of 0.20m/s.*

through out the computational bed. The slag particles are also observed to travel downwards at the walls of the vessel as well as in the wake of rising bubbles until evenly distributed. Figures 6.14 and 6.15 show experimental and computational snapshots of voidage profiles obtained for a mixture composition of 0.50 jetsam (slag) at an excess gas velocity of 0.20m/s respectively.

The mixing process described earlier in Figures 6.12 and 6.13 seem to be at play in Figures 6.14 and 6.15. The 'finger like' permeation of the natural rutile particles is present in both the experimental and computational snapshots. In Figure 6.15 slag particles are observed to move downwards at the walls of the computational vessel. However, there exist in the computational snapshot, localized areas where the volume fraction the slag particles are higher than average, particularly near the walls of the vessel where there is very little bubble motion. Higher volume fractions of natural rutile particles also predominate in areas where the gas volume fraction is high *i.e* around bubbles. Qualitatively, it is reasonable to conclude from the experimental and computational results, that a change in average mixture of the jetsam fraction has no effect on the overall mixing mechanism in the bed. Furthermore, for all the cases investigated computational beds when fully mixed remains well mixed throughout.

Figure 6.16 shows the evolution of the jetsam mass fraction profile with time obtained using

Figure 6.14: *Experimental snapshots of the fluidized bed using a mixture fraction of 0.50 jetsam at an excess gas velocity of 0.20m/s.*

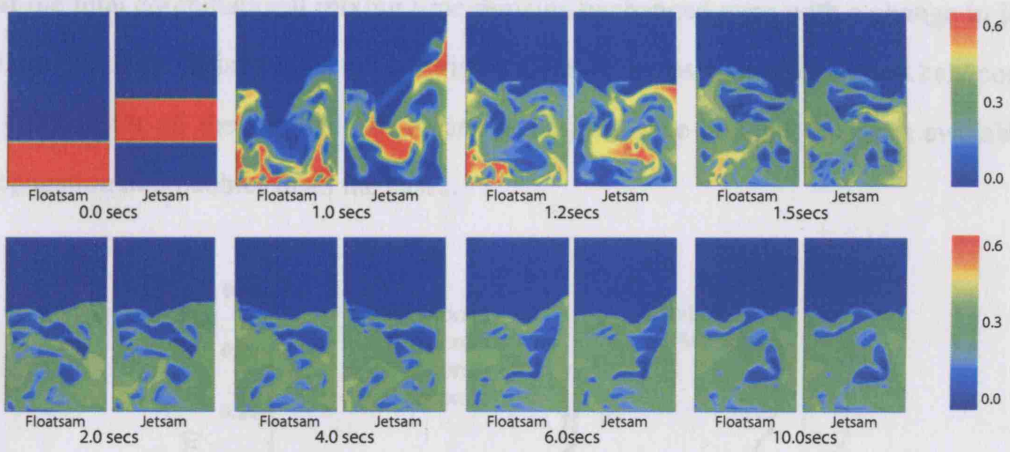

Figure 6.15: *Computational snapshots of the simulated fluid bed using a mixture fraction of 0.50 jetsam at an excess gas velocity of 0.20m/s.*

a binary mixture fraction of 0.75 slag particles. From figure 6.16, it can be seen that during the first 2 seconds, the jetsam phase spreads rapidly throughout the system; its mass fraction is seen to increase at the bottom of the bed until an even distribution is attained throughout the bed after about 4 seconds of simulation. There is little variation in the jetsam mixing profile thereafter and therefore subsequent profiles not reported. Figures 6.17 and 6.18, show the computational evolution of the slag particles with time for 50% and 25% jetsam concentration. In both profiles, the bed becomes fully mixed around 4 secs. Hence, it seems

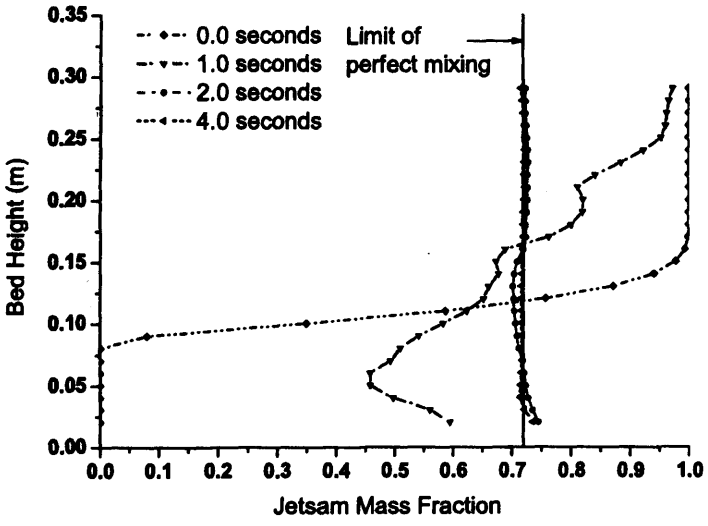

Figure 6.16: *Evolution of the jetsam mass fraction profile with time for a mixture concentration of 75% Slag*

that the total computational mixing time remains unchanged even with a change in jetsam mixture fraction. This result is not surprising since the excess gas velocity was held constant at 0.20m/s for all the simulations; meaning that the same amount of gas is available for propagation into bubbles in all the cases.

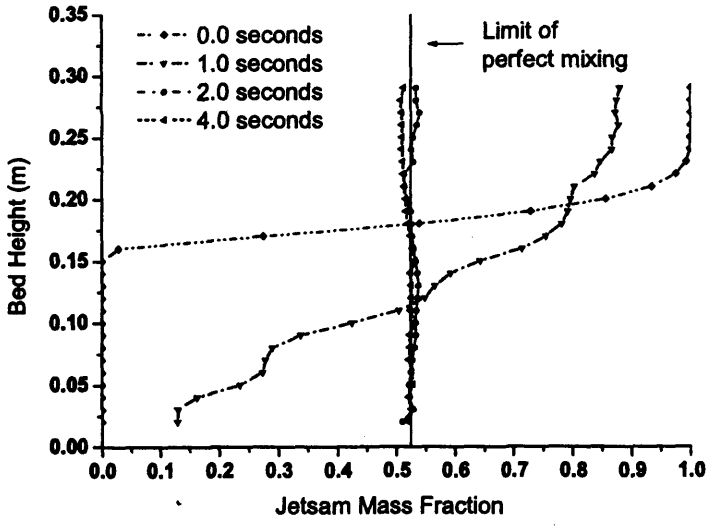

Figure 6.17: *Evolution of the jetsam mass fraction profile with time for a mixture fraction of 50% Slag*

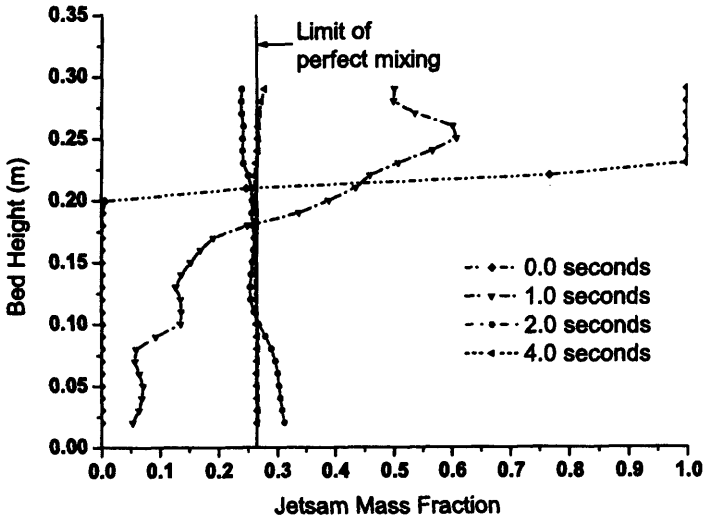

Figure 6.18: *Evolution of the jetsam mass fraction profile with time for a mixture fraction of 25% Slag*

Similar to what has been observed earlier for the modelling materials in § 6.1.3.1, there is a disparity in mixing time between the computational and experimental snapshots. For all the mixture fractions investigated, the experimental fluid bed becomes fully mixed after roughly 70secs, whilst the computational fluid bed becomes fully mixed after 4 secs.

6.2.3.2 Macroscopic bed properties

A quantitative comparison of the bulk properties of the bed is shown in Table 6.12 in which results for bed height, voidage and bubble holdup are reported for simulations carried out at an excess gas velocity of 0.20m/s. The properties have been time-averaged ignoring the first two seconds of simulation in order to reduce the effect of perturbations associated with the bed start-up.

From Table 6.12, varying differences are observed between numerical predictions and experimental findings for the different jetsam mass fractions investigated. Quantitatively, a percent error spanning the range 2.0% (25% jetsam fraction) - 4.0 % (75% jetsam fraction) was found for bed height when computational and experimental results were compared, this is represented in diagrammatic form in Figure 6.19, in which the experimental data has been

Table 6.12: *A comparison of experimental and numerical predictions of averaged fluid bed macroscopic quantities at an excess gas velocity of 0.20m/s*

	Bed Height			Bed Voidage			Bubble holdup		
Slag, $\langle \omega_{jet} \rangle$	Exp	CFD	% diff	Exp	CFD	% diff	Exp	CFD	% diff
0.75	37	35.5	4.0	0.537	0.499	7.0	0.360	0.182	97.8
0.50	37.5	36.2	3.5	0.545	0.510	6.4	0.236	0.175	34.9
0.25	38.5	37.7	2.0	0.552	0.521	5.6	0.190	0.178	6.7

plotted with a scatter of 20%. From Figure 6.19, It can be seen that the numerical predictions of the bed height deviates slightly from experimental results with higher jetsam fractions, but is not in disagreement. The slight deviation of computational predictions from experimental results might be due to the deficiency in accounting for a wide particle size distribution for the jetsam (slag) in the numerical model.

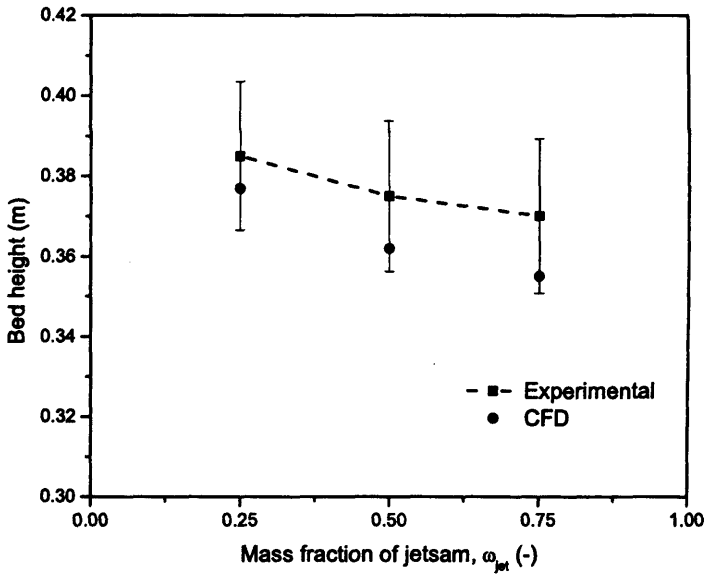

Figure 6.19: *A comparison of the experimental and numerical averaged bed height results for slag at different mixture fractions using constant excess gas velocity of 0.20m/s*

A range between 5.6% (25% jetsam fraction) - 7.0 % (75% jetsam fraction) percent error can be observed for the bed voidage in Table 6.12. Here again, the results have been illustrated graphically in Figure 6.20. It can be observed from Figure 6.20, that the agreement between numerical and experimental results is better at lower jetsam mass fractions. A possible reason

for this might be the modelling assumptions used in this work. In the model developed in this thesis, particles have been assumed to be spherical and as a result a bed voidage of 0.40 is intrinsically assumed in all the simulations. The above assumption is in disparity with experimental observations; where the bed voidage at rest is a lot higher.

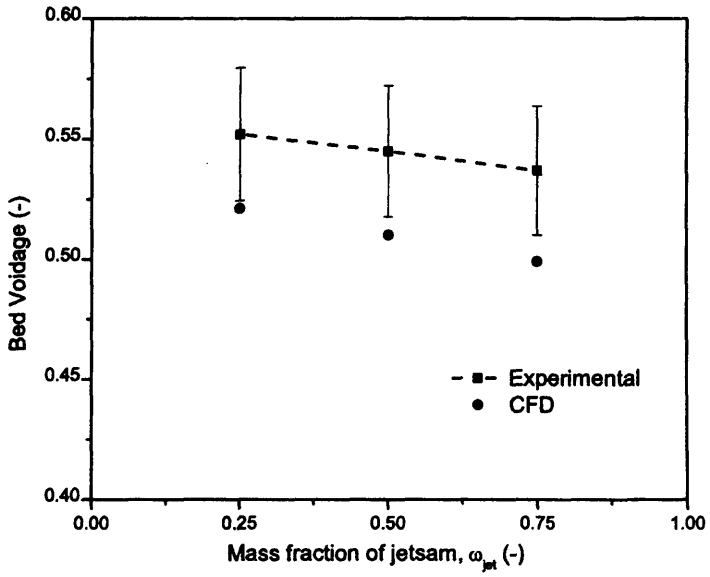

Figure 6.20: *A comparison of the experimental and numerical averaged bed voidage results for slag at different mixture fractions using constant excess gas velocity of 0.20m/s*

A comparison between numerical predictions and experimental results yielded a percent error in the range of 6.7% (25% jetsam fraction) - 97.8 % (75% jetsam fraction) for the bubble holdup. The bubble holdup in this thesis is defined, as the fraction of gas, above that required for minimum fluidization, that leaves the fluid bed through bubbles. Experimentally from Table 6.12, the bubble holdup was seen to increase with increasing slag mass fraction. Thus, it seems that an increase in the mass fraction of large particles causes the excess gas to preferentially leave the bed via bubbles. This trend is in agreement with earlier experimental bed height observations, which showed a larger bed expansion for the beds with a higher fraction of natural rutile particles (flotsam). In this case, it seems that a larger proportion of excess gas leaves the bed via the interstices of the particle matrix rather than through bubbles.

Computationally, numerical values obtained for bubble holdup are constant and seem to only show good agreement at lower jetsam fractions, within 10%. This agreement becomes poorer with increasing jetsam concentration. This might be caused by the deficiency in the computational prediction of bubbles in the fluidized bed by the numerical model. Computational bubbles obtained during this study were found to be smaller in size than the experimentally observed ones. This is discussed in greater detail in the next section. Results obtained from computational and experimental investigations have been also been plotted in Figure 6.21.

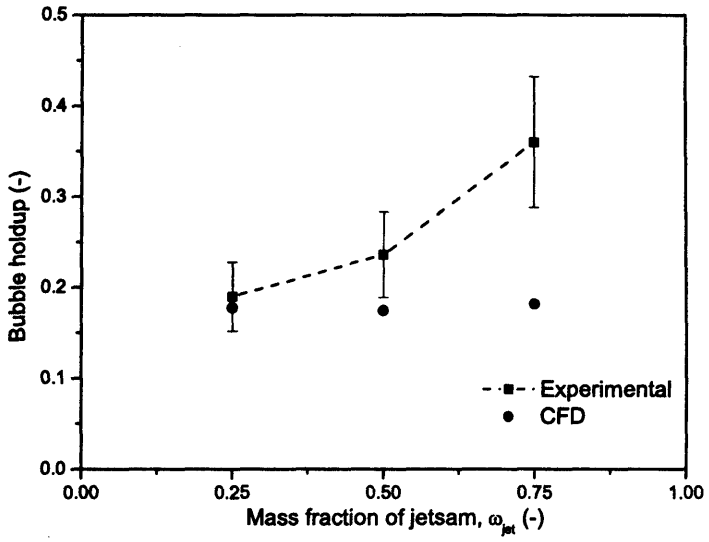

Figure 6.21: *A comparison of the experimental and numerical averaged bubble holdup results for slag at different mixture fractions using constant excess gas velocity of 0.20m/s*

6.2.3.3 Bubble properties

The analysis of the bubble dynamics within the bed was carried out by comparing results obtained from numerical computations with the Darton et al. (1977) bubble growth equation as well as with data obtained from experimental investigations. As with previous simulations, a voidage of 0.80 was assumed to represent a computational bubble. The experimental analysis of the bubble diameter was conducted using Optimas 6.0. The computational bubble analysis, on the other hand, was performed using the numerical algorithm recently devel-

oped by Mazzei & Lettieri (2006). Darton et al. (1977)'s equation has been already been described earlier in §5.1, there the semi empirical equation had the following form:

$$d_b = 0.54\left(u - u_{mf}\right)^{0.4}\left(h + 4\sqrt{A_0}\right)^{0.8}/g^{0.2} \tag{6.4}$$

where d_b is the bubble diameter, h is the height above the distributor and A_0 is the 'catchment area', which characterizes the gas distributor and u is the superficial gas velocity. A value of 0 has been suggested by Darton et al. (1977) for A_0 in absence of available data on the distributor characteristics.

Figure 6.22 shows a plot of the bubble diameter versus bed height for all the simulated bubbles computed at a constant excess gas velocity of 0.20m/s using a jetsam concentration of 75%. The figure also shows predictions obtained from eq. (6.4). Over 5000 bubbles [3], obtained from simulations, have been plotted on the graph. Figure 6.22 shows an enormous spread in predicted bubble diameters due to coalescence, breakup and the interaction of bubbles with the wall of the computational vessel. It can be seen that the predicted bubble diameters are smaller in the higher part of the fluidized bed, but are not in complete disagreement (± 20%) with predictions from the Darton et al. (1977) equation. The prominence of small bubbles in the bed may be due to less pronounced bubble coalescence higher up in the bed.

Figure 6.23 shows a plot of the experimentally obtained bubble diameters at a constant excess gas velocity of 0.20m/s and a jetsam mixture fraction of 75%. A total of over 500 points were plotted on the diagram. Predictions from Darton et al. (1977)'s semi-empirical correlation are also plotted on the diagram. The black lines in the figure indicate the experimental values that are within ± 30% of the Darton et al. (1977) equation. A general trend of an increase in bubble diameter with increasing bed height can be discerned from the experimental scatter in Figure 6.23. The Darton et al. (1977) equation is seen to give a better prediction of the bubble diameter in the lower part of the bed, with most experimental points within ± 30% of the semi-empirical correlation. However, the predictions from the semi-empirical

[3]Represents the total number of bubbles which has evolved during 10 secs of real time simulation

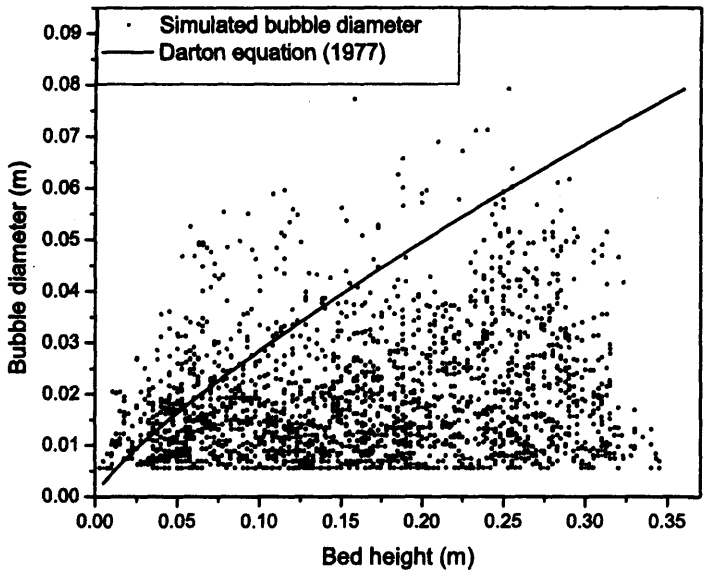

Figure 6.22: *A comparison of the simulated bubble diameter with Darton et al. (1977) equation at an excess gas velocity of 0.20m/s using a mixture fraction of 0.75 slag particles*

correlations are poorer higher up in the bed this might be as a result of the few experimental points available in that region. Nevertheless, the correlation provides a good way of testing the validity of the abundant data out of CFD simulation as well as providing a means of assessing experimental data.

Figure 6.24 shows a comparison between the simulated and experimental bubble diameters at different bed heights. The bubbles have been averaged into ten classes by method of interpolation. It can be observed that, the experimental bubble diameter prediction always larger than the simulated ones. Possible causes of this disparity have been discussed earlier in § 6.1.3.2, where the differences between experimental and simulated diameters were attributed to the dissimilarity in geometry between the 2D computational domain and the experimental 3D, "thin 2D", domain.

A change mixture composition of the jetsam was found to have no effect, as expected, on the numerical predictions of bubble size in the computational simulations. A constant value for the bubble size was in fact observed for all other cases. This is because the same excess gas flow rate was applied in all the simulations. Figures 6.25 and 6.26 show the plot of

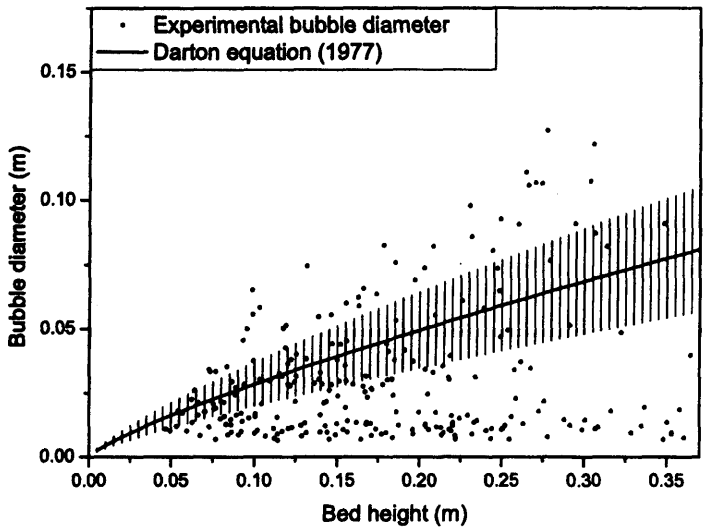

Figure 6.23: *A comparison of the experimental bubble diameter with Darton et al. (1977) equation at an excess gas velocity of 0.20m/s using a mixture fraction of 0.75 slag particles*

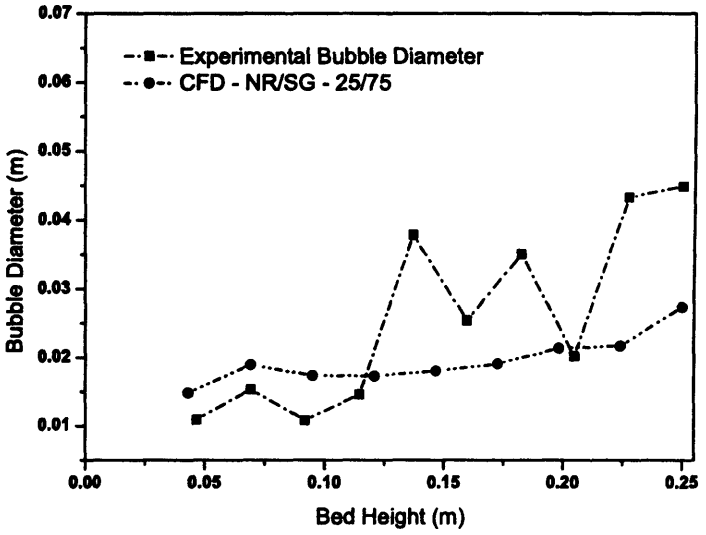

Figure 6.24: *A comparison of the simulated and experimental bubble diameter at an excess gas velocity of 0.20m/s using a mixture fraction of 0.75 slag particles*

the bubble diameter versus bed height for all the simulated bubbles computed at a constant excess gas velocity of 0.20m/s for jetsam mixture fraction of 0.50 and 0.25 respectively. Both simulations seem to give bubble size predictions that span a range of 0.005m - 0.085 m in concurrence with results reported earlier in Figure 6.22.

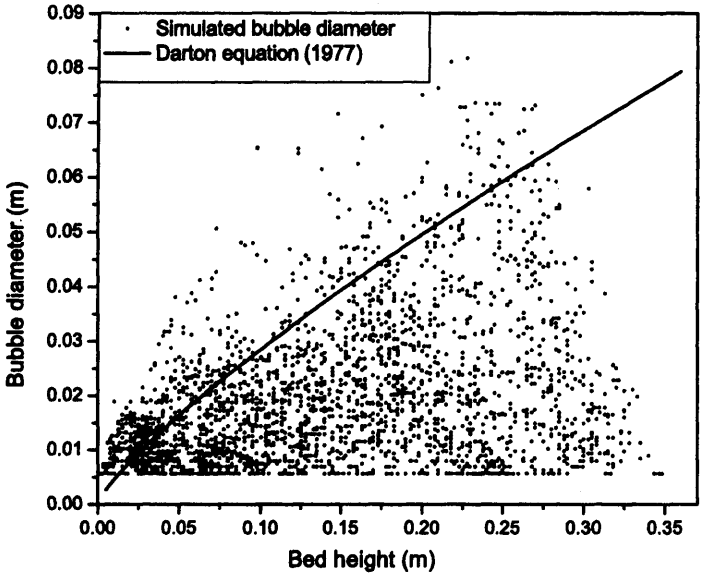

Figure 6.25: *A comparison of the simulated bubble diameter with Darton et al. (1977) equation at an excess gas velocity of 0.20m/s using a mixture fraction of 0.50 slag particles*

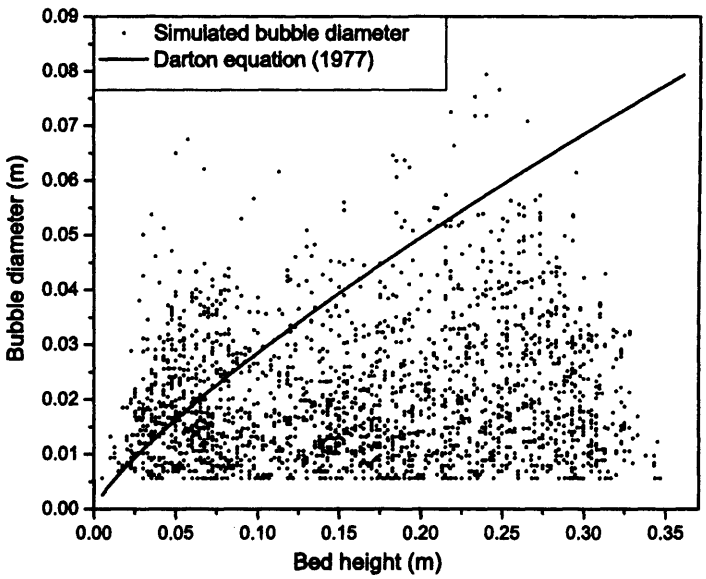

Figure 6.26: *A comparison of the simulated bubble diameter with Darton et al. (1977) equation at an excess gas velocity of 0.20m/s using a mixture fraction of 0.25 slag particles*

Similarly, experimental observations showed that a change in the mixture composition of the jetsam had no noticeable effect on the experimental bubble size predictions.

6.2.3.4 Segregation

As mentioned in § 6.2.1, the excess gas velocity, u_{xs}, was subsequently reduced to 0.10m/s after the computational bed was fully mixed and simulations were carried out for a further period of 10 seconds real time. This was done to enable the study of the segregation dynamics in the bed. The justification for not fluidizing at a superficial gas velocity slightly higher than the minimum fluidization velocity of the flotsam is based on the fact that segregation is promoted by the passage of bubbles in fluidized beds (Nienow & Chiba, 1985). Thus, neither mixing or segregation will occur in a bubble free bed at velocities slightly higher than the minimum fluidization velocity of the flotsam particle.

Table 6.13 reports the mixing index M and the coefficient of segregation C_s calculated from experiments and after 10 seconds of simulation for all the different case studies examined. The values of M are also compared with the prediction obtained from the semi-empirical correlation developed by Wu & Baeyens (1998). All the simulations show a good agreement with the experimental data and the semi-theoretical expression albeit under circumstances of modest segregation. In qualitative terms, the numerical predictions, in concurrence with experimental results, show an increasing co-efficient of segregation with decreasing jetsam fraction. This is due to the fact that a decrease in the superficial gas velocity of the system, as a result of the decrease in jetsam mass fraction, reduces the difference between the u_{mf} of the mono-component jetsam particle (slag) and the superficial gas velocity applied.

Quantitatively, as regards the mixing index, the correlation by Wu & Baeyens (1998) yields predictions which deviates from experimental and computational measurements by 18%. The reason for this discrepancy might be that the mechanism of segregation is overwhelmed by the solids recirculation and exchange mixing mechanisms present in the experimental and computational beds. Copper & Coronella (2005) arrived at similar conclusions, following their numerical investigation into the segregation dynamics of natural rutile and coke particles using a commercial CFD package, FLUENT ™. In this case, they found that the mechanism of mixing pervaded in the fluidized bed over the antagonistic effect of segregation even when simulations were carried out at superficial gas velocities comparable to the

minimum fluidization velocity of the jetsam particle. Figures 6.27-6.29 show a comparison

Table 6.13: *Experimental and theoretical values for mixing index M obtained for different jetsam fractions at an excess gas velocity of 0.10m/s*

	Mixing index			Coefficient of segregation	
$\langle \omega_{jet} \rangle$	CFD	Exp	Wu & Baeyens (1998)	CFD	Exp
0.75	1.00	0.98	0.82	− 0.304	− 0.084
0.50	0.99	1.00	0.82	+ 0.380	− 0.065
0.25	0.98	0.92	0.82	+ 0.736	+ 0.842

between theoretical and experimental concentration profiles of the jetsam phase throughout the bed at different jetsam concentrations. The computational values were determined after 10 seconds of simulation by splitting the bed into 28 horizontal layers of equal volume and by calculating the average jetsam mass fraction in each layer. The experimental results were obtained as described earlier on in § 6.1.2; in this case only four horizontal layers were considered. The profiles shown are consistent with the figures reported in Table 6.13 and confirm the conclusions previously drawn *i.e.* that the segregation mechanism is less dominant due to the overwhelming prominence of the mixing and solids recirculation mechanisms. Furthermore, from figures 6.27-6.29, the computational and the experimental jetsam mass fraction profiles almost overlap with the limit of perfect mixing, with the experimental jetsam concentration on the bottom of the bed slightly higher than on top. This is in agreement with the values of M and C_s formerly calculated and shown in Table 6.13.

6.2.4 Conclusions

In this section, an experimental validation of the numerical simulations of the mixing and segregation behaviour of a binary mixture of industrial powders supplied for this project using the model presented in § 6.1 for binary mixtures as been presented. Three different average compositions, corresponding to the averages mass fraction of big particles (slag) of 0.25, 0.50, 0.75 in the bed were considered. The mixtures were fluidized at a constant excess gas velocity, u_{xs}, of 0.20m/s for 10 secs. The excess gas velocity, u_{xs}, was subsequently reduced to 0.10m/s to enable a study of the segregation dynamics of the system. Qualita-

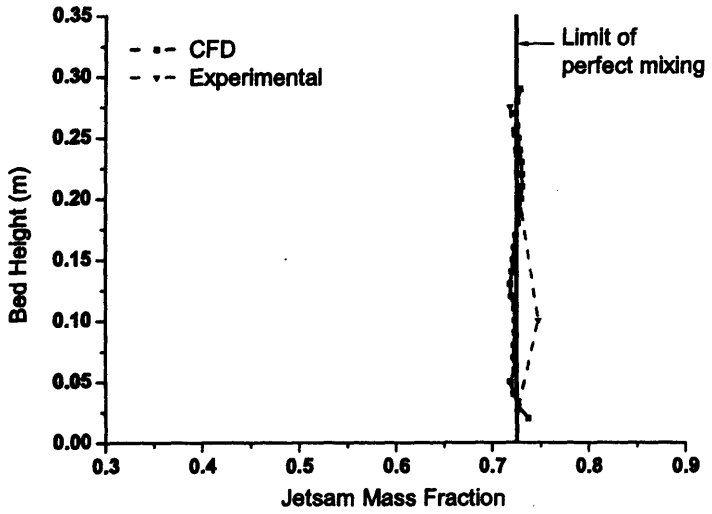

Figure 6.27: *Comparison of computational and experimental segregation patterns obtained from numerical simulations using a jetsam concentration of 75%*

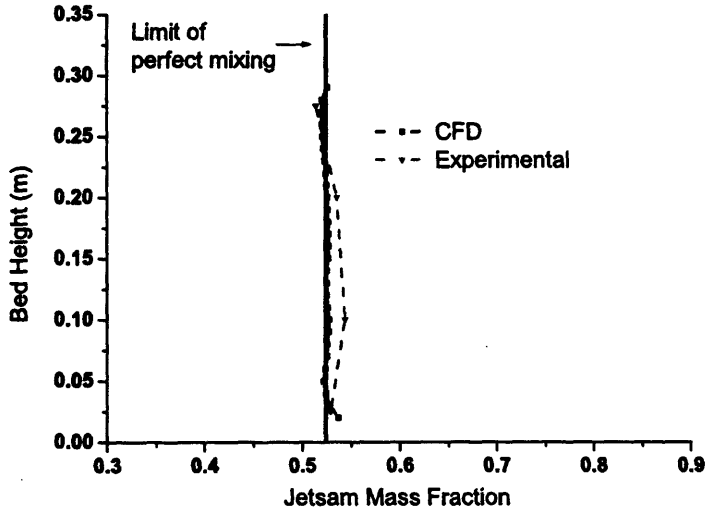

Figure 6.28: *Comparison of computational and experimental segregation patterns obtained from numerical simulations using a jetsam concentration of 50%*

tively, the numerical simulations captured the mixing mechanism experimentally observed. Quantitative results on the mixing index from the numerical simulations were also reported.

Numerical results from macroscopic bed properties showed a good agreement with the experimental findings for bed properties like the bed height and voidage. However, a difference

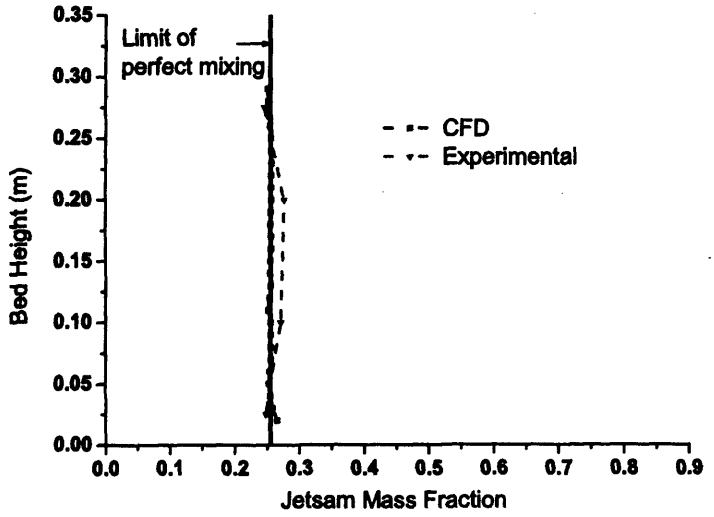

Figure 6.29: *Comparison of computational and experimental segregation patterns obtained from numerical simulations using a jetsam concentration of 25%*

in the numerical prediction of the bubble holdup from experiments data was found. An investigation into the bubble dynamics and bulk properties of the system was also conducted. In the segregation study, a modest segregation pattern was predicted both numerically and experimentally. The reason for this was attributed to the pervasiveness of the the solids recirculation and exchange mixing mechanisms over that of segregation even when low excess gas velocities are employed.

6.3 Numerical validation of a fluid particle interaction framework for binary mixtures

In this section, a mathematical framework for characterizing the fluid-particle interaction force in a binary mixture using the *two fluid* approach is presented. The main goal of this study is to demonstrate the capability of the proposed framework in simulating the flow behaviour of a binary mixture. The inherent advantage of the *two fluid* over the *three fluid* approach in the modelling of well mixed binary systems arises from the computational time saving that could be accrued. Thus, there is a need for reliable constitutive expressions

for describing fluid-particle interaction force when a binary system is modelled via the *two fluid* approach. A previous study by van Wachem (2000), carried out using the *two-fluid* approach, has already demonstrated that the bed expansion in a binary mixture of particles of different sizes and identical densities is significantly higher than that of a system consisting of mono-component particles of the same mean size as the binary mixture. In the study therein, a modified form of the Wen & Yu (1966) equation was used to characterize the drag force exerted on a particle in the binary mixture. The drag force contribution was also the only closure applied by the author in to describe the average fluid particle interaction force using this approach.

A summary of the drag relations proposed in literature was shown earlier in Table 2.10. However, rather than examining a particular drag model at this point, a new general framework for the fluid particle interaction force in a mixture of solid species will be introduced herein. As described earlier in § 2.3.2, the *two fluid* approach can be applied to describe the flow of dense gas-solid binary mixtures, mixture continuity and momentum equations are employed in the description of the particle phase. The equations of change that describe the fluid and particle mixture are presented in Table 6.14 for convenience. In this study, the fluid particle interaction force is defined as the following for mixtures:

$$n\langle \boldsymbol{f} \rangle^{f} = \varepsilon \nabla \cdot \mathcal{T}^{f} + \beta_{mix}\left(\langle \boldsymbol{u} \rangle^{f} - \langle \boldsymbol{u} \rangle^{s}\right) + E_{mix}\left(\nabla \varepsilon \cdot \langle \boldsymbol{n}^{d} \rangle^{\mathscr{F}_i}\right)\langle \boldsymbol{n}^{d} \rangle^{\mathscr{F}_i} \tag{6.5}$$

where $\langle \boldsymbol{n}^{d} \rangle$ is the unit drag force vector pertaining to the each solid phase $\mathscr{F}_i$. The fluid particle interaction framework is defined in a way that considers the presence of both particle species in the mixture, and is analogous to the virial equation of state for binary mixtures (Clifford, 1999). The fluid particle interaction framework can be defined as follows:

$$\beta_{mix} = \left(\frac{\rho_1 \phi_1}{\rho_1 \phi_1 + \rho_2 \phi_2}\right)^2 \beta_1 + \left(\frac{\rho_1 \phi_1}{\rho_1 \phi_1 + \rho_2 \phi_2}\right)\left(\frac{\rho_2 \phi_2}{\rho_1 \phi_1 + \rho_2 \phi_2}\right)\beta_{12} + \left(\frac{\rho_2 \phi_2}{\rho_1 \phi_1 + \rho_2 \phi_2}\right)^2 \beta_2 \tag{6.6}$$

where ϕ refers to the solid volume fraction and β_{12} is a function of the average diameter of

Table 6.14: *Equations of Motion for a Binary System using particle mixture momentum equations*

Continuity equations
$$\frac{\partial \varepsilon}{\partial t} + \nabla \cdot \left(\varepsilon \langle \boldsymbol{u} \rangle^f\right) = 0$$ $$\frac{\partial \phi}{\partial t} + \nabla \cdot \left(\phi \langle \boldsymbol{u} \rangle^m\right) = 0$$
Momentum Equations
$$\rho_f \left[\frac{\partial}{\partial t}\left(\varepsilon \langle \boldsymbol{u} \rangle^f\right) + \nabla \cdot \left(\varepsilon \langle \boldsymbol{u} \rangle^f \langle \boldsymbol{u} \rangle^f\right)\right] = \nabla \cdot \mathfrak{T}^f - \beta_{mix}\left(\langle \boldsymbol{u} \rangle^f - \langle \boldsymbol{u} \rangle^s\right)$$ $$-E_{mix}\left(\nabla \varepsilon \cdot \langle \boldsymbol{n}^d \rangle^{\mathcal{F}_i}\right)\langle \boldsymbol{n}^d \rangle^{\mathcal{F}_i} + \varepsilon \rho_f \boldsymbol{g}$$ $$\rho_m \left[\frac{\partial}{\partial t}\left(\phi \langle \boldsymbol{u} \rangle^m\right) + \nabla \cdot \left(\phi \langle \boldsymbol{u} \rangle^m \langle \boldsymbol{u} \rangle^m\right)\right] = \nabla \cdot \mathfrak{T}^m + \beta_{mix}\left(\langle \boldsymbol{u} \rangle^f - \langle \boldsymbol{u} \rangle^s\right)$$ $$+E_{mix}\left(\nabla \varepsilon \cdot \langle \boldsymbol{n}^d \rangle^{\mathcal{F}_i}\right)\langle \boldsymbol{n}^d \rangle^{\mathcal{F}_i} + \phi \rho_m \boldsymbol{g}$$
Definitions
$$\rho_m = \frac{\rho_1 \phi_1}{\rho_1 \phi_1 + \rho_2 \phi_2} + \left(1 - \frac{\rho_1 \phi_1}{\rho_1 \phi_1 + \rho_2 \phi_2}\right)\rho_2$$

the mixture, d_{av} which is given by the following:

$$d_{av} = \frac{1}{\frac{x_1}{d_1} + \frac{x_2}{d_2}} \tag{6.7}$$

Similarly, the Elastic modulus, E_{mix} can be expressed as follows:

$$E_{mix} = \left(\frac{\rho_1 \phi_1}{\rho_1 \phi_1 + \rho_2 \phi_2}\right)^2 E_1 + \left(\frac{\rho_1 \phi_1}{\rho_1 \phi_1 + \rho_2 \phi_2}\right)\left(\frac{\rho_2 \phi_2}{\rho_1 \phi_1 + \rho_2 \phi_2}\right)E_{12} + \left(\frac{\rho_2 \phi_2}{\rho_1 \phi_1 + \rho_2 \phi_2}\right)^2 E_2 \tag{6.8}$$

Equation (6.6) allows the implementation of mono-component drag relations within the framework to characterize the drag force binary mixture. In this study, simulations are performed for two cases. **Case 1)** investigates a comparison between a three and two fluid simulation for one of the industrial cases studied previously whilst **Case 2)** looks into the

sensitivity of the framework to differences in mean particle diameter ratio, d_b/d_s, where d_b is the diameter of the bigger particle and d_s is the diameter of the smaller particle. Modelling materials belonging to the Geldart Group B classification have been used for this numerical investigation.

6.3.1 Simulations

In this section, numerical simulations are used to demonstrate the validity of the fluid particle interaction framework proposed in eq. (6.6). The drag model proposed earlier in eq.(5.23) is implemented within the framework of eq. (6.6) in the CFX.4.4 code. The particles used for the computational studies are as follows: **Case 1)** Natural rutile and Slag with particle sizes of 186 μm and 350 μm respectively having a density of 4200 kg/m^3. An average mass fraction of jetsam particles (slag) of 0.75 in the bed was assumed in this simulation. **Case 2)** consist of ballotini particles which are 71 μm and 350 μm in diameter respectively and have a density of 2500 kg/m^3. The mean diameter ratio for Case 1 and Case 2 used for the investigations are 1.6 and 5 respectively.

The grid used for the numerical simulation was 2D computational grid, in which front and back wall effects are neglected, was used. The left and right walls of the domain were modelled using no-slip velocity boundary conditions for all phases. Dirichlet boundary conditions were employed at the bottom of the bed to specify a uniform gas inlet velocity. A pressure boundary condition was specified at the top of the bed and set to a reference value of 1.015×10^5 Pa. It is worth noting here that $\nabla \cdot \mathfrak{I}^m$, is not modelled in this study, instead the algorithm *excess solid volume correction* developed by Lettieri et al. (2003) is implemented. The fluidization conditions used for all simulations are summarized in Table 6.15. In this study, two numerical simulations are carried out at the same superficial gas velocity. The first simulation is a reference simulation in which the *three phase* model is solved whilst the second simulation solution employs the framework proposed in eq. (6.6). The fluidized bed was assumed fully mixed at initialization. The superficial gas velocity was chosen such that the bed was always fully mixed (Wu & Baeyens, 1998).

Table 6.15: *Computational parameters used in the numerical validation of the fluid particle interaction framework for binary mixtures.*

Description	Symbol	Value	Units	Comments
Gas density	ρ_f	1.29	kg/m^3	
Gas viscosity	μ_f	1.85×10^{-5}	Pa s	
Superficial gas velocity (Case 1)	u_o	0.31	m/s	
Minimum fluidization velocity (Case 1)	u_{mf}	0.11	m/s	
Superficial gas velocity (Case 2)	u_o	0.111	m/s	
Minimum fluidization velocity (Case 2)	u_{mf}	0.012	m/s	
Bed height	H_b	0.60	m	
Settled bed height	H_s	0.30	m	
Grid cell size	Δx and Δy	0.005	m	Square cells
Coefficient of restitution	e	0.97	-	Syamlal (1987b)†
Coefficient of friction	C_f	0.15	-	Syamlal (1987b)†
Time step	Δt	10^{-4}	s	

† *used in the three phase simulation*

6.3.2 CFD simulation results

6.3.2.1 Computational time

Table 6.16 shows a comparison of the computational time required to obtain numerical predictions from the proposed framework (two fluid) and the standard three fluid approach for different real time scenarios.

Table 6.16: *Comparison of computational times for "two fluid" and "three fluid" simulations*

	Computational time (hrs)‡		
Real Time (secs)	pseudo Two fluid	Three fluid	Time saving (hrs)
0.1	8.28	20	11.73
1	82.75	201	118.25
10	827.5	2018	1190.50

‡The computations are based on simulations ran on a Dell Xeon P4 3.2 Ghz Machine

From Table 6.16, the time savings range from ≈ 12hrs for a real time simulation of 0.1 secs

to a total savings of 49 days! for a real time simulation of 10 secs. From the above, it seems that the fluid-particle interaction frame work proposed herein could potentially provide a computationally economical means of accessing the behavior of well mixed binary systems.

6.3.2.2 Macroscopic Bed properties

A quantitative comparison of the bulk properties of the bed is shown in Table 6.17 and 6.18 for Case 1 and Case 2 respectively. Here, results for bed height, voidage and bubble holdup are reported for the simulations carried out using the two and thee fluid approach respectively. The properties have been time-averaged ignoring the first two seconds of simulation in order to reduce the effect of perturbations associated with the bed start-up.

Table 6.17: *Comparison of time-averaged macroscopic fluidization properties for Case 1*

Macroscopic properties	Three fluid simulation	Two fluid simulation	% Error
Bed height (m)	0.375	0.350	7.14
Bed Voidage (-)	0.499	0.484	3.00
Bubble holdup (-)	0.182	0.165	9.30

Table 6.18: *Comparison of time-averaged macroscopic fluidization properties for Case 2*

Macroscopic properties	Three fluid simulation	Two fluid simulation	% Error
Bed height (m)	0.495	0.474	4.24
Bed Voidage (-)	0.637	0.620	2.66
Bubble holdup (-)	0.098	0.100	2.04

A very good agreement is found when results from the "three phase" model are compared with numerical predictions from the proposed framework (two fluid) for both cases. From Table 6.17 (Case 1) a percentage error within 10% is found when averaged macroscopic fluidization indicators are compared between the *three fluid* and *two fluid* simulations whilst a percentage error of within 5% is found when the same quantities are compared for Case

2, see Table 6.18. The above results on one hand highlight the suitability of the framework for capturing the macroscopic bed properties of a well mixed "three fluid" binary mixtures. On the other hand, the results also demonstrate the influence of the mean diameter ratio on results from the proposed fluid particle interaction framework. In this case, an increase in the mean diameter ratio, (d_b/d_s), leads to a better "match" between predictions from the fluid particle interaction framework and corresponding *three fluid* simulations.

6.3.2.3 Bubble diameter

The predicted values of bubble diameter with increasing bed height have been analysed for the two cases and compared with results obtained from empirical bubble growth equation proposed by Darton et al. (1977). Figures 6.30 - 6.33 show the scatter of the computational bubble sizes obtained from both cases compared with the Darton et al. (1977) equation. For each case, numerical predictions of bubble size obtained from the two and three fluid models have been compared. In general, there is a good agreement with the Darton et al. (1977) equation at the bottom of the bed in both cases. All plots show an increase in bubble size at increased heights in the bed, indicating the promotion of bubble growth via coalescence in both cases. Furthermore, the predicted bubble size range is the same for both cases (0.005m-0.08m). In terms of a computational model comparison, with respect to Case 1, Figures 6.30 and 6.31 show that the "two fluid" model predicts a greater proportion of small bubbles higher up in the bed than the "three fluid" simulation. The same phenomena is also present in Case 2, Figures 6.32 and 6.33, where the mean diameter ratio has been increased to 5.6. It can be observed that proportion of small bubbles predicted by the "two fluid' model higher in the bed is greater than the corresponding prediction by the three fluid simulation. The reason for this discrepancy between the two and three fluid simulations might be the predominance of a less pronounced bubble coalescence mechanism in the "two fluid" model as compared to the three fluid model.

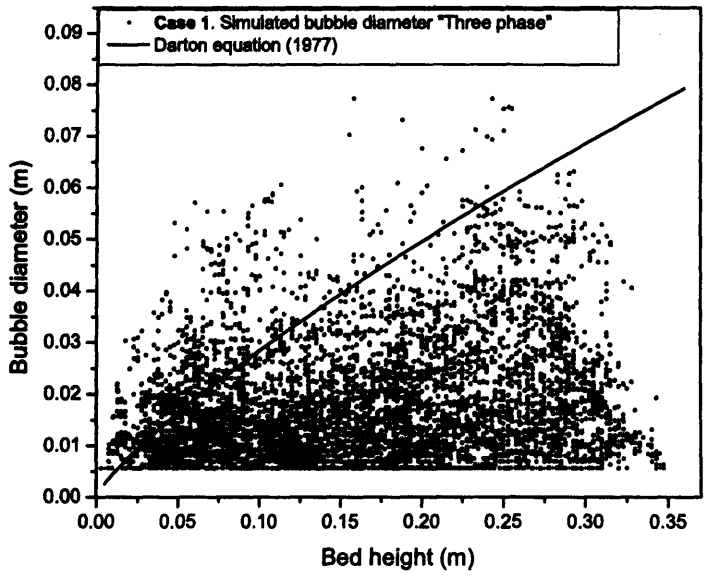

Figure 6.30: *A comparison of the "three phase" simulated bubble diameter with Darton et al. (1977) equation (Case 1)*

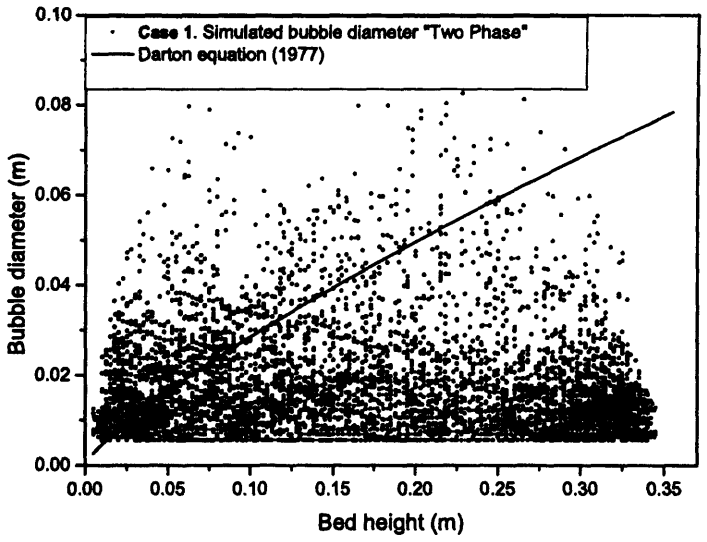

Figure 6.31: *A comparison of the "two phase" simulated bubble diameter with Darton et al. (1977) equation (Case 1)*

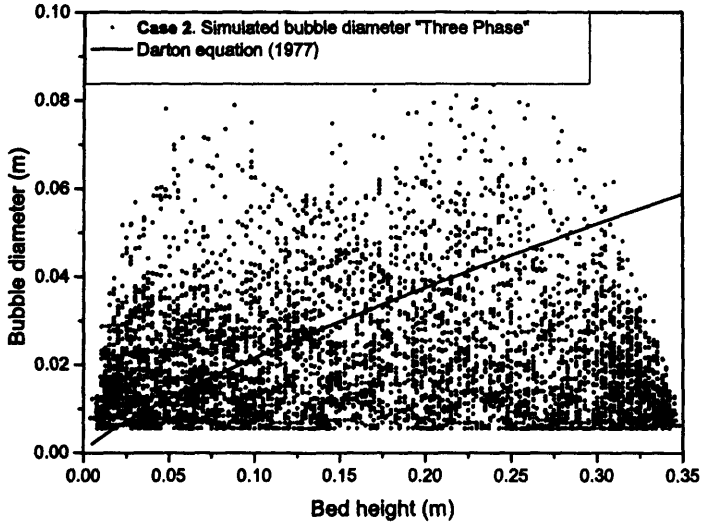

Figure 6.32: *A comparison of the "three phase" simulated bubble diameter with Darton et al. (1977) equation (Case 2)*

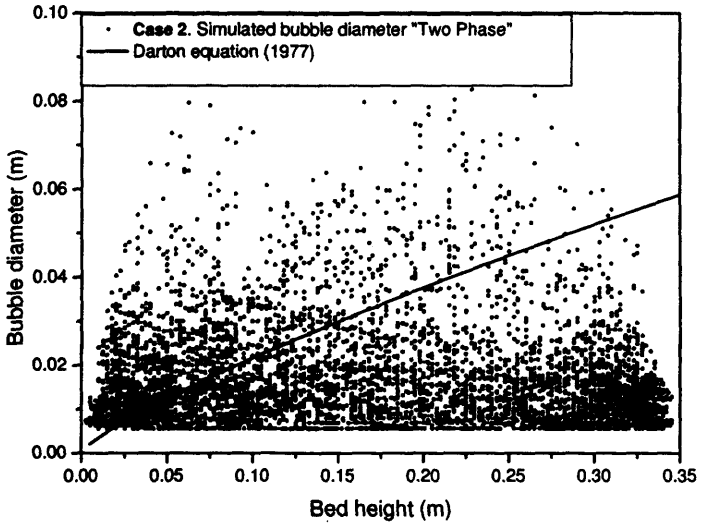

Figure 6.33: *A comparison of the "two phase" simulated bubble diameter with Darton et al. (1977) equation (Case 2)*

6.3.2.4 Power spectral density of pressure waves

Figure 6.34 and 6.35, shows a comparison of the simulated pressure fluctuation for both cases investigated. The PSD function has been estimated using Origin © graphical software. The

PSD function of the time series was estimated from a length of 1084 points and is averaged over the length of the time series.

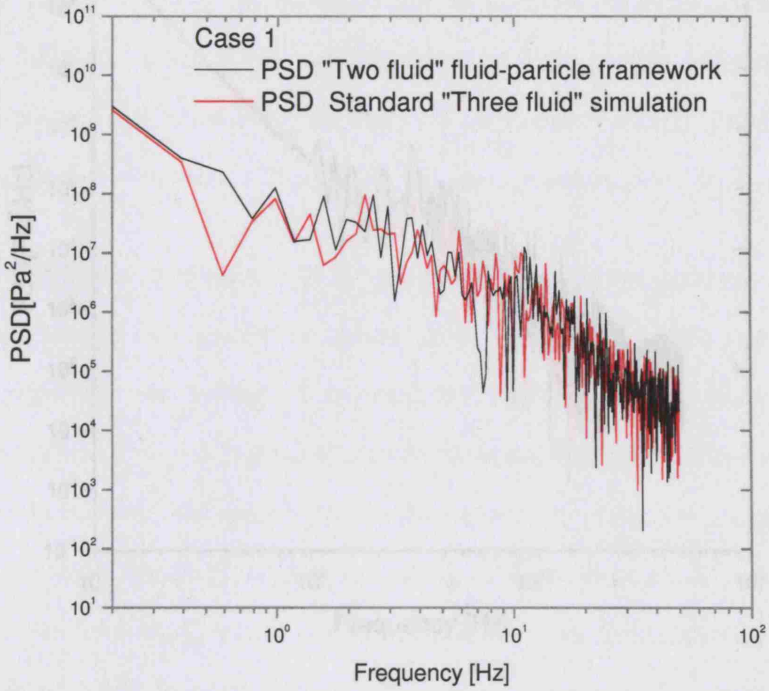

Figure 6.34: *A comparison of the PSD function of the simulated pressure fluctuation of the natural rutile material , $u_o = 0.20m/s$*

From Case 1, Figure 6.34, it can be observed that both models predict the same *total power* of PSD ($\approx$ 5.5^{10} Pa^2/Hz). Very little difference can be discerned from both curves and qualitatively the predictions seem to match for both models. Similarly, for Case 2, both PSD curves obtained are very similar with the *total power* of PSD $\approx$ 10^9 Pa^2/Hz. The above results provide more evidence of the predictive capability of the proposed fluid particle interaction framework. It is also reasonable to conclude that the mean diameter ratio has little influence on the numerical prediction of the PSD using the proposed fluid particle interaction framework.

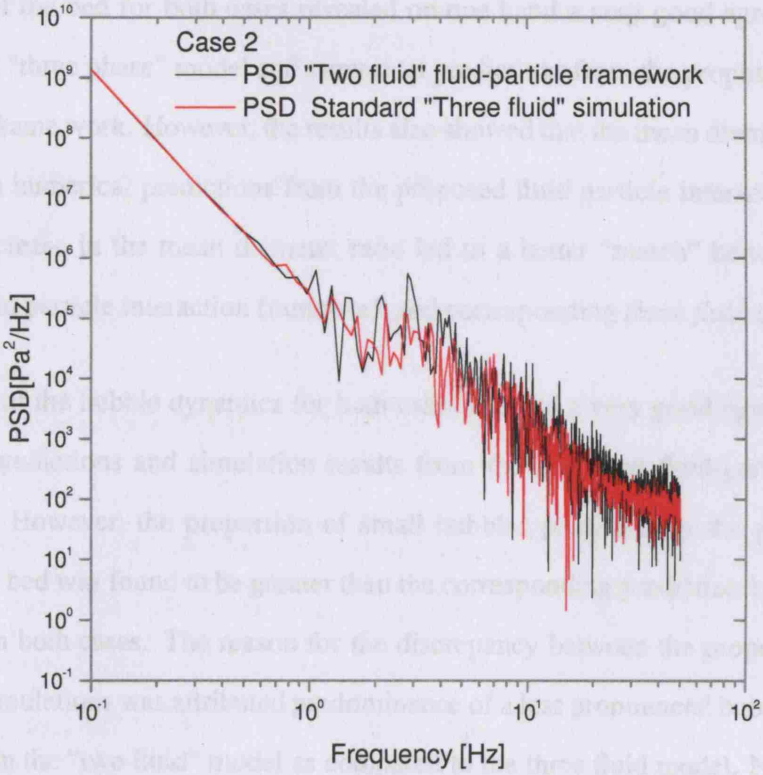

Figure 6.35: *A comparison of the PSD function of the simulated pressure fluctuation of the natural rutile material , $u_o = 0.20m/s$*

6.3.3 Conclusion

A new framework for modelling the fluid-particle interaction force in a binary mixture using the "two fluid" approach has been proposed. In this study, two different cases were investigated wherein **Case 1)** was based on an industrial mixture previously studied, here an average mass fraction of jetsam particles (slag) of 0.75 in the bed was assumed. **Case 2)** consisted of ballotini particles which are have the same density but different diameters. The mean diameter ratio for **Case 1)** and **Case 2)** used for the investigations were 1.6 and 5 respectively.

Results obtained with regards to computational time showed that a potential time saving in the range of ≈ 12hrs for a real time simulation of 0.1 secs to a total savings of 49 days for a real time simulation of 10 secs could be achieved using the fluid-particle interaction framework as compared to a standard three phase approach. A quantitative comparison of the bulk

properties of the bed for both cases revealed on one hand a very good agreement between results from "three phase" model and numerical predictions from the proposed fluid-particle interaction frame work. However, the results also showed that the mean diameter ratio had an influence on numerical predictions from the proposed fluid particle interaction framework. Here, an increase in the mean diameter ratio led to a better "match" between predictions from the fluid particle interaction framework and corresponding *three fluid* simulations.

An analysis of the bubble dynamics for both cases showed a very good agreement between three fluid predictions and simulation results from the proposed fluid-particle interaction framework. However, the proportion of small bubbles predicted by the proposed model higher in the bed was found to be greater than the corresponding prediction by the three fluid simulation in both cases. The reason for the discrepancy between the proposed model and three fluid simulations was attributed predominance of a less pronounced bubble coalescence mechanism in the "two fluid" model as compared to the three fluid model. Nonetheless, the mean diameter ratio was found to have no influence on the bubble dynamics. An evaluation of the power of the pressure waves for both cases showed a very good agreement between results obtained from the proposed fluid particle interaction framework and the three-fluid simulation. Here again, the mean diameter ratio was found to have no discernable effect on the results obtained.

In the light of the above, the most significant benefit of the proposed framework would be the potential computational time saving that could be achieved for simulating well mixed binary systems. However an experimental validation will be further required to test the robustness of the model.

Chapter 7

Conclusions and future work

Recent advances in computational software and processors have facilitated the increased use of computers and Computational Fluid Dynamics (CFD) software tools in the numerical solution of complex engineering problems. One such research area where increased computational power and CFD software has facilitated scientific efforts in leaps and bounds is the area of multiphase flow, in particular gas-solid fluidization.

Scientific work featuring the CFD modelling of gas-solid fluidized beds has pervaded literature in the last few years. However, most of the CFD investigations carried out have hitherto been limited to the study of the fluidization behaviour of mono-component gas-solid systems, results of which have aided fundamental understanding and pointed the way to simulating more realistic systems. The problem which was addressed by this work concerns the titanium refining industry where a bubbling fluidized bed is used for extracting titanium from naturally occurring ore. The refining process begins in a fluidized bed with the chlorination of titanium rich rutile ore which is composed of many constituents. There are industrial concerns about the pervasiveness of *dead zones*, within the fluidized bed, which is caused by segregation of the feedstock, as a result of the size and density differences of all the components. The eventual effect of dead zones in the fluid bed is refractory lining erosion, which represents a significant cost of reactor operation. Therefore, it will be of great importance to gain a better understanding of the mixing and segregation phenomena at play within the system.

Hence, the main focus of this research, which was defined in collaboration with Huntsman Tioxide Ltd, was the computer modelling of the dense gas-solid hydrodynamics applied to the fluidization of binary mixtures using a commercial CFD package CFX4.4 code of Ansys Ltd. (formerly AEA Technology) with particular attention placed on industrial materials. To this end, three of the industrial powders used as feedstock for the fluid-bed chlorinator,*i.e.*, slag, natural and synthetic rutile powders were provided by Huntsman Tioxide Ltd for the experimental and CFD studies for this project. The materials all belong to the Geldart Group B classification.

In addressing the problem posed herein, the Eulerian-Eulerian approach was adopted in this thesis, it was chosen based on its suitability for modelling large scale fluidized beds. A review of existing literature revealed two methods for modelling binary systems. The first was characterized by the use of separate momentum equations to cater for each particle species whilst the second makes use of the averaged mixture properties for the formulation of a mixture momentum equation coupled with the use of averaged constitutive relations. Both approaches were investigated in this work, where the former method, was chosen as the principal approach for which the bulk of the numerical investigations were carried out.

The substantiation of using Eulerian-Eulerian approach for modelling the industrial materials provided for this project was addressed by carrying out at first mono-component numerical simulations of the powders. The Granular Kinetic Theory (GKT) model in-built within CFX4.4 was used as a closure for the internal stress associated with the solid phase. This was performed to test the predictive capability of the modelling approach to simulate the dynamics of the industrial powders. Simulation results obtained for bed expansion, bubble size and voidage profiles are compared with dedicated experimental results obtained using a 2D fluid bed experimental rig. This was considered as a first step in verifying the suitability of the modelling approach adopted in this thesis and also a necessary precursor to its application for binary systems.

As part of the investigation of the CFD modelling of the mono-component powders, a comparison was conducted between the GKT model and an alternative approach for which a new

closure suitable for modelling the fluid particle interaction force for mono-component and binary systems was developed based on the fluid bed elasticity concept originally proposed by Wallis (1969).

In developing a new fluid-particle interaction closure model for binary mixtures, this work elucidated the derivation of the Eulerian-Eulerian averaged equations of change for binary mixtures of particles fluidized by means of a Newtonian fluid. Here, an alternative derivation of the averaged equations of motion for binary systems was carried out based on earlier work by Jackson (1997), which to the author's knowledge, has not been performed by any other research group. The intent of the procedure was firstly, to add insight into the meaning of the various terms featuring in the momentum equations found in literature for binary systems, especially the fluid-particle and particle-particle interaction forces and the stress internal to the solid phases and secondly, to clarify the origin of the particle-particle drag force; which requires a closure because of the modelling strategy adopted in this thesis. The development resulted in the proposal of an elastic force closure suitable for the study of the dynamics of binary fluidized systems.

The study of the averaged equations of change for binary mixtures of particles also revealed the true complexity of the internal stress relevant to each solid phase. In the light of the above consideration, The internal stress associated with the solid phase has not been modeled in this work. However, the discretization scheme (SUPERBEE) employed in the numerical solution of the momentum conservation equations used in this work implicitly introduces a *numerical dissipation term* (artificial viscosity), which is purely numerical in origin. This term serves to improve and guarantee the stability of the solution. It was considered that the neglect of the closure for the solid stress might give rise to local over-compaction in some regions of the simulated fluidized bed. To counter this effect, a new numerical algorithm for binary systems was developed based on the algorithm for the *excess solid volume* correction originally proposed by Lettieri et al. (2003) for mono-component systems.

As a first step in verifying the applicability of the new closure developed herein, the mono-component version of the proposed equations of change were examined analytically. Here,

linear stability analysis theory was applied to the proposed equations of change in the face of small fluctuations in the voidage or particle velocity. The effort lead to the development of a new stability criterion for homogenous gas fluidized beds with better predictive capability than the Foscolo & Gibilaro (1984) criterion. Thereafter a validation of the drag force closure relation which has been used in this thesis is carried out, through predictions of bed height and bed voidage as well as through other macroscopic fluidization indicators obtained from CFD simulations of Geldart Group A materials such as FCC catalyst (70 μm). Results were compared with predictions from the Richardson & Zaki (1954a) correlation.

A sensitivity analysis of the closure models describing the *particle-particle drag* force required for the modelling of a binary system described as a *three fluid* system was carried out using Geldart Group B modelling materials e.g. soda glass ballotini having different diameters and same density. Furthermore, a sensitivity analysis on grid and time step resolution was also performed. Results of these analyses enabled the subsequent numerical investigation into the mixing and segregation behaviour of the binary mixture of the industrial materials provided for this project. In this investigation, three different average compositions, corresponding to the average mass fraction of jetsam particles of 0.25, 0.50, 0.75 in the bed were considered, so that the hydrodynamic behavior of three binary mixtures in all was studied.

To conclude, this thesis also investigated the *two fluid* mixture model approach for the simulation of the behaviour of dense gas-solid binary mixtures. This was done by proposing and validating a new general framework for the fluid particle interaction force in a mixture of solid species. The fluid particle interaction framework was defined in a way that considers the presence of both particle species in the mixture, and is analogous to the virial equation of state for binary mixtures (Clifford, 1999). In this study, two different cases were investigated wherein **Case 1)** was based on an industrial mixture previously studied, here an average mass fraction of jetsam particles (slag) of 0.75 in the bed was assumed. **Case 2)** consisted of ballotini particles which are have the same density but different diameters. The mean diameter ratio for **Case 1)** and **Case 2)** used for the investigations was 1.6 and 5 respectively.

The main conclusions from this work are summarized below:

7.1 Mono-component systems

1 Results concerning the numerical and experimental validation of the Eulerian-Eulerian approach for modelling the mono-component behaviour of the industrial powders revealed a good qualitative match between the simulations and experiments for all velocities investigated. In this case, the solid stress tensor was modelled using the Granular Kinetic Theory model available within CFX4.4. Numerical values for bed expansion, obtained from simulations, were found to be in good agreement with experimentally measured values (within 11%) at all the velocities investigated. Experimental bubble data as well as Darton et al. (1977) semi-empirical bubble correlation were used to validate predicted computational results for bubble size. Results obtained showed, for all the industrial powders investigated, that Darton et al. (1977) empirical correlation overpredicts the bubble diameters when compared to experimental and simulated values. The simulated bubbles were also found to be slightly smaller than those observed experimentally. This was attributed to less pronounced bubble growth via coalescence in all the numerical simulations due to the subtle dissimilarity in geometry between the 2D computational domain and the experimental 3D, "thin 2D", domain.

2 The analytical verification of the mono-component equations of change proposed in this thesis was carried out via a linear stability analysis. The linear analysis yielded a stability criterion for gas fluidized beds that gave a better prediction than established criterion (Foscolo & Gibilaro, 1984) for the minimum bubbling voidage in mono-component systems. A good agreement was also found between predictions of the new stability criterion and the experimental data of Xie & Geldart (1995) (error within ± 5%) in the "high" range of mean particle diameters (greater than about 90 μm). However, it was observed that the more the mean particle diameter is reduced the less accurate the predictions of the criterion became (the same holding true also for the criterion by Foscolo & Gibilaro

(1984)). A possible explanation for the poor quality of the theoretical predictions obtained for very low mean particle diameters was attributed to the predominance of the effects of interparticle forces (IPF's), at smaller particle diameters, which are not accounted for in any of the models compared above.

3 The conclusions from the computational study concerning the predictive capability of fluid particle interaction force, for mono-component systems, proposed in this thesis showed a good agreement with predictions obtained from the Richardson & Zaki (1954a) equation. Here, numerical results of the bed voidage were within 1.73% of the predictions of Richardson & Zaki (1954a). Additionally, a comparison between results, for mono-component industrial powders, obtained from the new model and the model which is present within CFX4.4 (GKT theory) showed a good agreement for macroscopic bed properties such as bed height, voidage as well as bubble diameter. Thus, it seemed that the collisional contribution of the internal stress relevant to the solid phase had little impact on the numerical predictions of macroscopic bulk properties of the fluidized bed. However, the numerical dicretization scheme employed in this work , SUPERBEE, might possibly be overwhelming the effects of the collisonal stress (GKT) and the simple pressure model adopted due to the implicit addition of a numerical dissipation term in the numerical algorithm. Further studies might need to be carried out to delineate the effects of the second order discretization scheme on the dynamics of the fluidized system. Nevertheless, results obtained from the new model compared favorably with dedicated experimental data.

7.2 Binary systems

1 The numerical study concerned with the effect of the particle-particle drag on the fluidization behaviour of binary systems showed that the force plays a significant role in the prediction of jetsam mobility within the fluidized bed and should be taken into account when simulating binary systems. Four simulations were carried out using a binary mixture of a modelling material (ballotini); three wherein different constitutive equations for the

particle-particle drag force were used namely Gidaspow et al. (1985), Syamlal (1987b), Bell (2000), and a final one where the force was entirely neglected. The first three case studies yielded similar results in terms of jetsam particle distribution with an almost perfect mixing and a good agreement with the experimental data within the bed. The percent error on the mixing index was found to vary between 9% and 13% with experimental results. In the forth case study, conversely, an overprediction of the jetsam mobility was found with a resulting tendency of such phase to segregate towards the bottom of the bed. This was in clear contrast with the experimental evidence.

2 A disparity in mixing time between computational simulations (4 secs) and experimental measurement (1 min) was observed. A sensitivity study on the influence of the collisional stress on the simulation dynamics demonstrated no effect on the observed disparity in mixing time - this is in agreement with previous observations by other researchers (see Huilin et al., 2003, Huilin & Gidaspow, 2003) who have carried out analogous investigations, using binary systems composed of Geldart Group D particles, while taking into account the collisional solid stress contribution. Thus, the disparity reported might be attributed to the omission of frictional stresses. Nevertheless, an investigation into the bubble dynamics and bulk properties of the binary systems investigated in this thesis did not discriminate between different particle-particle drag force closures and indeed the macroscopic properties appeared to be quite insensitive to the inclusion of the particle-particle drag contribution. For completeness, a sensitivity analysis on the influence of the grid cell size and time step reduction on the simulation dynamics showed a minimal effect on the numerical prediction of mixing and segregation on the materials studied.

3 The experimental validation of the numerical simulations of the mixing and segregation behaviour of a binary mixture of industrial powders supplied for this project (Natural rutile and slag) using the model presented in this thesis showed both qualitatively and quantitatively that the numerical simulations are able to capture the experimentally observed mixing mechanism. Quantitatively, a percent error spanning the range 2.0% - 4.0% for 25% jetsam fraction and 75% jetsam fraction respectively was found for bed

height predictions when computational and experimental results were compared. Furthermore, a range between 5.6% - 7.0% for 25% jetsam and 75% jetsam fraction respectively was found for bed voidage predictions. An investigation into the bubble dynamics and bulk properties of the system showed that the experimental bubble diameter prediction is always larger than the simulated ones, in concurrence with observations from earlier mono-component simulations. In the segregation study carried out, a modest segregation pattern was predicted both numerically and experimentally. The reason for this was attributed to the pervasiveness of solids recirculation and exchange mixing mechanisms over that of segregation.

4 Finally, results obtained with regards to computational time from the new framework for modelling the fluid-particle interaction force in a fully mixed binary mixture using the "two fluid" showed that a potential time saving in the range of $\approx$ 12hrs for a real time simulation of 0.1 secs to a total time saving of 49 days for a real time simulation of 10 secs could be achieved using the fluid-particle interaction framework as compared to a standard three phase approach. A quantitative comparison of numerical predictions of the averaged bulk properties of the bed for both cases revealed on one hand a very good agreement between results from "three phase" model and numerical predictions from the proposed fluid-particle interaction frame work. However, the results also showed that the mean diameter ratio had an influence on simulation predictions from the proposed fluid particle interaction framework. Therein, an increase in the mean diameter ratio resulted in a better "match" between predictions from the fluid particle interaction framework and corresponding *three fluid* simulations.

An analysis of the bubble dynamics for both cases investigated also showed a very good agreement between three fluid predictions and simulation results from the proposed fluid-particle interaction framework. However, the proportion of small bubbles predicted by the proposed model higher in the bed was found to be greater than the corresponding prediction by the three fluid simulation in both cases. The reason for the discrepancy between the proposed model and three fluid simulations was attributed predominance of

a less pronounced bubble coalescence mechanism in the "two fluid" model as compared to the three fluid model. Nonetheless, the mean diameter ratio was found to have no influence on the bubble dynamics. An evaluation of the power of the pressure waves for both cases showed a very good agreement between results obtained from the proposed fluid particle interaction framework and the three-fluid simulation. Here again, the mean diameter ratio was found to have no discernable effect on the results obtained. Thus, the most significant benefit of the proposed fluid particle interaction framework would be the potential computational time saving that could be achieved for simulating well mixed binary systems. However, an experimental validation will be further required to test the robustness of the model.

7.3 Future work

One of the central themes of this work has been to illuminate the mixing and segregation processes that occur in binary gas fluidized beds. To this end, the Eulerian-Eulerian approach was adopted to study binary systems in this thesis. Through the method of local volume averaging of the equations of change for binary systems, carried out in this thesis, a fundamental understanding of the role of the particle-particle drag force on the dynamics of binary gas solid fluidized beds was elucidated.

However, the process of local volume averaging also revealed that the true nature of the internal stresses that define the solid and fluid phases are indeed very complex. For most gas-solid applications, modelling the latter stress in the newtonian form suffices as a description. Nevertheless, due to the fact that high values of particle concentration are encountered in dense gas-solid fluidized beds, the same newtonian form, applicable in the case of fluid phase internal stresses, will not be an adequate depiction for the nature solid stresses in a binary mixture. Although an adhoc approach has been used in this thesis to account for the effect of the solid stress tensor on the fluid dynamics, an investigation into the effect of the use of frictional constitutive closures in the modelling of normal and tangential internal solid

stresses is deemed necessary. It is thought that such a study will shed light on the effect such stresses might play in determining physical quantities like the computational mixing time.

The modelling of binary mixtures in this thesis has been carried out by assuming that the individual components which make up the mixture are monosize in particle distribution, whereas in actual fact each of the components considered has its own unique particle size distribution (PSD). Therefore, it will useful to consider solving the hydrodynamic model developed herein alongside a population balance equation for each solid phase. The population balance could, at first, be formulated such that the individual PSD's do not change with time. The above study could then be possibly extended to a situation where the individual PSD's that make up the mixture evolve due to physical processes like particle attrition. The above task is indeed not easy but nevertheless if accomplished would provide an even more realistic picture of the dynamics of a binary mixture with a particle size distribution.

In this work, the industrial materials supplied have been assumed spherical. However, it is known that particle flow processes involving non-spherical particles can behave very differently than systems involving spherical particles. Therefore, a study into the influence of particle shape on the simulation dynamics of the fluidized bed would be desirable. A first step might be to account for particle shape in the model formulation through use of a non-spherical drag coefficient. Although this might involve the use of a new constitutive model for the fluid particle interaction force. In addition, a longer term objective might be to investigate the effect of particle shape on the internal stresses related to the solid phases.

Lastly, the fluid particle interaction framework proposed in this thesis could potentially save precious computational time into investigations concerning well mixed binary systems. Hence, It is necessary to carry out an experimentally linked validation study to test the robustness of the framework.

Nomenclature

This nomenclature features only the main terms used in this thesis. Terms which have not been listed here can be found at the location where they appear in the thesis.

Roman Symbols

C_f	Co-efficient of friction	
d	Diameter	m
e	Co-efficient of restitution	
E	Elastic modulus	
$\mathbf{g}$	Gravitational constant	m/s^2
p	Pressure,	Pa
g_o	radial distribution function	
$\boldsymbol{u}$	Averaged velocity	m/s
f	Generic force	
V	Volume of fluid	m^3

Greek Symbols

β	Interphase drag constant	kg/m^3s^1
ε	Gas volume fraction	-
γ_Θ	Dissipation of granular energy	$kgm^{-1}s^{-1}$
κ	Bulk viscosity	Pa s
μ	Shear viscosity	Pa s

Φ	Maximum solid packing	
ϕ	Solid volume fraction	-
ρ	Density	kg/m^{-3}
$\mathcal{T}$	Stress tensor	N/m^2
Θ	Granular Temperature	$m^2 s^{-2}$
ζ	Particle-particle drag term	

Superscripts

f	Fluid phase (gas or liquid)	-
max	maximum fraction	
s	Solid Phase	
T	Transpose of a vector	

Subscripts

b	Buoyant force
f	Fluid phase (gas or liquid)
s	Solid Phase

Other Symbols

C_D	Drag Coefficient
$\langle f \rangle$	Averaged fluid-particle interaction force
$\mathscr{F}$	Generic particle phase indicator
Re_p	Particle Reynolds Number

Acronyms

CFD	Computational Fluid Dynamics
DPM	Discrete Particle Model
LBM	Lattice Boltzmann Model
PBM	Particle Bed Model
PSD	Power Spectral Density

Bibliography

ALLEN, M. & TILDESLEY, D. (1990). *Computer Simulations of liquids*. Oxford Science Publications, Oxford, 1st edn.

ANDERSON, J. (1995). *Computational Fluid Dynamics- The basics with applications*. McGraw-Hill.

ANDERSON, T. & JACKSON, R. (1967). A fluid mechanical description of fluidized beds. equations of motion. *Ind. Eng. Chem. Fundam.*, **6**, 527–539.

ARASTOOPOUR, H. (2001). Numerical simulations and experimental analysis of gas/solid flow systems: 1999 fluor-daniel plenary lecture. *Powder Tech.*, **119**, 59–67.

ARASTOOPOUR, H., WANG, C. & WEIL, S. (1982). Particle-particle interaction force in a dilute gas-solid system. *Chem. Eng. Sci.*, **37**, 1379–1384.

ASTARITA, G. (1993). Forces acting on particles in a fluidized bed. *Chem. Eng. Sci.*, **48**, 3438–3440.

AUTON, T., HUNT, J. & PRUD'HOMME, M. (1988). The force exerted on a body in inviscid, unsteady non-uniform, rotational flow. *J. Fluid Mech.*, **197**, 241–257.

BAEYENS, J. & GELDART, D. (1974). An investigation into slugging fluidized beds. *Chem. Eng.Sci*, **29**, 255–265.

BELL, R. (2000). *Numerical Modelling of Multi-Particle Flows in Bubbling Gas -Solid Fluidized Beds*. Ph.D. thesis, Swinburne University of Technology.

BILBAO, R., LEZAUN, J., MENENDEZ, M. & ABANADES, J. (1988). Model of mixing-segregation for straw/sand mixtures in fluidized beds. *Powder Tech*, **56**, 149–155.

BILBAO, R., LEZAUN, J., MENENDEZ, M. & IZQUIERDO, M. (1991). Segration of straw/sand mixtures in fluidized bed in non-steady state. *Powder Tech*, **68**, 31–35.

BIRD, R., STEWART, W. & LIGHTFOOT, E. (1960). *Transport phenomena*. Wiley.

BLAKE, F. (1922). The resistance of packing to fluid flow. *Trans Am Inst Chem Eng*, **14**, 415.

BOEMER, A., H.QI & RENZ, U. (1997). Eulerian simulation of bubble formation at a jet in a two-dimensional fluidized bed. *Int. J Multi. Flow*, **23(5)**, 927–944.

BOKKERS, A. (2005). *Multi-Level Modelling of the Hydrodynamics in Gas Phase Polymerisation Reactors*. Ph.D. thesis, University of Twente.

BOKKERS, G., VAN SINT ANNALAND, M. & KUIPERS, J. (2004). Mixing and segregation in bidisperse gas-solid fluidised bed: a numerical and experimental study. *Powder Tech.*, **140**, 176–186.

BOUILLARD, J., LYCZKOWSKI, R., FOLGA, S., GIDASPOW, D. & BERRY, F. (1989). Hydrodynamics of erosion of haet exchnager tubes in a fluidized bed combustor. *Can.J.Chem.Eng*, **67**, 218.

BURKE, S. & PLUMMER, W. (1928). Gas flow through packed columns. *Ind Eng Chem*, **20**, 1196–1200.

CAMMARATA, L., LETTIERI, P., MICALE, G. & COLEMAN, D. (2003). 2d and 3d cfd simulations of bubbling fluidized beds using eulerian-eulerian models. *IJCRE 1*, **A48**, 1–19.

CAMPBELL, C. (2006). Granular material flows - an overview. *Powder Technol*, **162**, 208–229.

CHAPMAN & COWLING (1970). *The mathematical theory of non-uniform gases.*. Cambridge University Press.

CHEN, Z., GIBILARO, L. & FOSCOLO, P. (1999). Two-dimensional voidage waves in fluidized beds. *Industrial Engineering Chemical Research*, **38**, 610.

CHEN, Z., GIBILARO, L. & JAND, N. (2003). Particle packing constraints in fluid-particle system simulation. *Computers and Chem. Eng*, **27**, 681.

CHEUNG, L., NIENOW, A. & ROWE, P. (1974). Minimum fluidization velocity of a binary mixture of different sized paricles. *Chem.Eng.Sci*, **29**, 1301–1303.

CHIBA, S., CHIBA, T., NIENOW, A. & KOBAYASHI, H. (1979). The minimum fluidisation velocity,bed expansion and pressure drop profile of binary mixtures. *Powder Tech*, **22**, 255–269.

CHIBA, S., CHIBA, T., NIENOW, A. & KOBAYASHI, H. (1980). Fluidized binary mixtures in which the dense component maybe flotsam. *Powder Tech*, **26**, 1–10.

CHRISTIE, I., GANSER, G. & SANZ-SERNA, J. (1991). Numerical solution of a hyperbolic system of conservation laws with source term arising in a fluidized bed model. *J. Comput. Phys.*, **93**, 297–311.

CHURCHILL, S. (1974). *The Interpretation and Use of Rate Data: the rate concept*. Scripta Publishing Co., Washington D.C.

CHURCHILL, S. & USAGI, R. (1972). A general expression for the correlation of rates of transfer and other phenomena. *A.I.Ch.E*, **18**, 1121.

CLIFFORD, T. (1999). *Fundementals of Supercritical fluids*. Oxford Science Publications, Oxford, 1st edn.

CLIFT, R. (1993). An occamist review of fluid bed modelling. *AIChE Symp Series*, **89(296)**, 1–17.

CLIFT, R., SEVILE, J., MOORE, S. & CHAVARIE, C. (1987). Comments on buoyancy in fluidized beds. *Chem. Eng. Sci.*, **42**, 191–194.

COPPER, S. & CORONELLA, C. (2005). Cfd simulations of particle mixing in a binary fluidized bed. *Powder Tech*, **151**, 27–36.

COULOMB, C. (1776). Essai sur une application des règles de maximis et minimis àquelques problèmes de statique, relatifs à l'architecture. *Acad. R. Sci. Mém. Maths Phys. par Divers Savants*, **7**, 343–382.

CUNDALL, P. & STRACK, O. (1979). A discrete numerical model for granular assemblies. *Gèotechnique*, **29**, 47.

CURTIS, J. & VAN WACHEM, B. (2004). Modeling particle -laden flows: A research outlook. *AIChE*, **50**, No 11.

DAHL, S. & HRENYA, C. (2005). Size segregation in gas-solid fluidized beds with continuous size distributions. *Chem. Eng. Sci*, **60**, 6658–6673.

DALLAVALLE (1948). *Micrometrics*. Pitman.

DARTON, R., LANAUZE, R., DAVIDSON, J. & HARRISON, D. (1977). Bubble growth due to coalescence in fluidised beds. *Trans IChemE*, **55**, 274–280.

DAVIDSON, D. (2002). The role of computational fluid dynamics in process industries. *The Bridge*, **32**, 4.

DAVIDSON, J. & HARRISON, D. (1963a). *Fluidised Particles*. Cambridge Press, first edition edn.

DAVIDSON, J. & HARRISON, D. (1963b). *Mathematical modelling of two-phase flow*. Cambridge University Press.

DI FELICE, R. (1988a). *Liquid Fluidisation of Binary Solid Mixtures*. Ph.D. thesis, University of London.

DI FELICE, R. (1988b). *Liquid Fluidization of Binary Solid Mixtures*. Licentiate thesis, University College London, London UK.

DI FELICE, R. (1994). The voidage function for fluid particle interaction systems. *International Journal of Multiphase Flow*, **20**, 153–159.

DING, J. & GIDASPOW, D. (1990). A bubbling fluidization model using kinetic theory of granular flow. *AIChE*, **36**, 523–538.

DREW, D. (1971). Averaged field equations for two phase media. *Stud Appl Math*, **50**, 133–166.

DREW, D. (1983). Mathematical modelling of two-phase flow. *Annual review of fluid mechanics*, **83**, 261–291.

DREW, D. & LAHEY, R. (1993). *Particulate Two-Phase Flow*, chap. 5. Butterworth-Heinemann.

DREW, D. & SEGEL, L. (1971). Averaged field equations for two phase flows. *Stud Appl Math*, **50**, 205–231.

ENWALD, H. & ALMSTEDT, A. (1999). Fluid dynamics of a pressurized fluidized bed: comparison between numerical solutions from two-fluid models and experimental results. *Chem. Eng. Sci.*, **54**, 329–342.

ERGUN, S. (1952). Fluid flow through packed columns. *Chem Eng Progress*, **48**, 89–94.

ERGUN, S. & ORNING, A. (1949). Fluid flow through randomly packed columns and fluidized beds. *Ind. Eng. Chem.*, **41(6)**, 1179.

ETTEHADIEH, B., GIDASPOW, D. & LYCZKOWSKI, R. (1984). Hydrodynamics of fluidization in a semicircular bed with a jet. *AICHE J*, **30**, 529.

FAN, L.S. & ZHU, C. (1998). *Principles of Gas solid Flows*. Cambridge Press University Press, first edition edn.

FEDORS, R. & LANDEL, R. (1979). An emprical method of estimating the void fraction in mixtures of uniform particles of different sizes. *Powder Technology*, **23**, 225–231.

FOSCOLO, P. & GIBILARO, L. (1984). A fully predictive criterion for the transition between particulate and aggregate fluidisation. *Chem. Eng. Sci*, **39**, 1667–1675.

FOSCOLO, P. & GIBILARO, L. (1987). Fluid dynamic stability of fluidised suspensions :the particle bed model. *Chem. Eng. Sci*, **42**, 1489.

FOSCOLO, P., GIBILARO, L. & WALDRAM, S. (1983). A unified model for particulate expansion of fluidised beds and flow in fixed porous media. *Chem. Eng. Sci*, **38**, 1251.

GELDART, D. (1973). Types of gas fluidization. *Powder Tech*, **7**, 285.

GELDART, D. (1986). *Gas Fluidization Technoloy*. John Wiley & sons.

GELDERBLOOM, S., D.GIDASPOW & LYCZKOWSKI, R. (2003). Cfd simulations of bubbling/collapsing fluidized beds for three geldart groups. *AIChE*, **49**, 844–858.

GERA, D., SYAMLAL, M. & O'BRIEN, T. (2004). Hydrodynamics of particle segragation in fluidized beds. *Int. Journal Multi. Flow*, **30**, 419–428.

GIBILARO, L. (2001). *Fluidization-dynamics*. Butterworth-Heineman.

GIBILARO, L. & ROWE, P. (1974). A model for segregating gas fluidized bed. *Chem. Eng. Sci.*, **29**, 1403–1412.

GIBILARO, L., FELICE, R.D., WALDRAM, S. & FOSCOLO, P. (1985). Generalised friction factor and drag coefficient correlations for fluid-particle interactions. *Chem. Eng. Sci*, **40**, 1817.

GIBILARO, L., FELICE, R.D. & WALDRAM, S. (1986). A predictive model for the equilibrium composition and inversion of binary solid liquid fluidized beds. *Chem. Eng. Sci*, **41**, 379–387.

GIDASPOW, D. (1994). *Multiphase flow and fluidization*. Academic Press, San Diego.

GIDASPOW, D. & ETTEHADIEH, B. (1983). Fludization in two dimensional beds with a jet ii-hydrodynamic modelling. *I & EC Fundam*, **22**, 193–201.

GIDASPOW, D., SYAMLAL, M. & Y.SEO (1985). Hydrodynamics of fluidization of single and binary size particles: Supercomputer modelling. In K. Østergarrd & A. SØrensen, eds., *Proceedings of the Fifth Engineering Foundation Conference on Fludization*, vol. 5, 1–8, Engineering Foundation.

GIDASPOW, D., HUILIN, L. & MANGAR, D. (1996). Kinetic theory of multiphase flow and fluidization: Validation and extension to binaries. In *XiXth International Congress of theoretical and applied Mechanics*, 25–31, Kyoto,Japan.

GODARD, K. & RICHARDSON, J. (1968). In *Fluidization*, Instn Chem. Engrs Symp, 126.

GOLDSCHMIDT, M., KUIPERS, J. & VAN SWAIJ, W. (2001). Segregation in dense gas-fluidized beds: validation of multifluid contimuum model with non-intrusive digital image analysis measurements. In 10^{th} *Engineering Foundation Conference on Fluidization*, 795–802, Beijing, China.

GOSSENS, G., DUMONT, G. & SPAEPEN, G. (1971). Fluidization of binary mixtures in the laminar flow region. *Chem. Eng. Prog. Symp. Ser.*, 38–45.

GRACE, J. & SUN, G. (1991). Influence of particle size distribution on performance of fludized bed reactors. *Can. J. Chem Eng*, **69**, 1126–1135.

GUENTHER, C. & SYAMLAL, M. (2001). The effect of numerical diffusion on the simulation of isolated bubbles in gas-solid fluidized beds. *Powder Technology*, 142–154.

GUOGH, P. & ZWARTS, F. (1979). Modelling heterogeneous two-phase reacting flow. *AIAA J*, 17–25.

GWYN, J., MOSER, J. & PARKER, W. (1970). A three phase model for gas-fluidized beds. *Chem. Eng. Prog.Symp. Ser.*, **66**, 19–27.

HL, L., WANG, S., ZHAO, Y., GIDASPOW, D. & DING, J. (2005). Prediction of particle motion in a two dimensional bubbling fluidized bed using discrete hard-sphere model. *Chem. Eng. Sci.*, **60(12)**, 3217–3231.

Ho, T., KIRKPATRICK, M. & HOOPER, J. (1987). Modelling of solids mixing in a coal-limestone fluidzed bed. *AIChE Symp. Ser*, **84**, 42–49.

HOOMANS, B. (1999). *Granular dynamics of gas-solid two-phase flows*. Ph.D. thesis, University of Twente.

HOOMANS, B., J.A.M.KUIPERS, BRIELS, W. & VAN SWAAIJ, W. (1996). Discrete aprticle simulation of bubble and slug formation in a two-dimensional gas fluidized bed : a hard-sphere approach. *Chem. Eng. Sci.*, **51**, 99.

HOWLEY, M. & GLASSER, B. (2002). Hydrodynamics of a uniform liquid-fluidized bed containing a binary mixture of particles. *Chem. Eng. Sci*, **57**, 4209–4226.

HUILIN, L. & GIDASPOW, D. (2003). Hydrodynamics of binary fluidization in a riser: Cfd simulation using two granular temperatures. *Chem. Eng. Sci*, **58**, 3777–3792.

HUILIN, L., YURONG, H. & GIDASPOW, D. (2003). Hydrodynamic modelling of binary mixture in a gas bubbling fluidized bed using the kinetic theory of granular flow. *Chem. Eng. Sci*, **58**, 1197–1205.

IDDIR, H. & ARASTOOPOUR, H. (2005). Modelling of multitype particle flow using the kinetic theory approach. *AIChE Journal*, **51**, 1620.

JACKSON, R. (1963). The mechanics of fluidized beds. i: stability of the state of uniform fluidization. *Trans. Inst. Chem.*, **41**, 12–21.

JACKSON, R. (1997). Locally averaged equations of motion for a mixture of identical spherical particles of a newtonian fluid. *Chem. Eng. Sci*, **52**, 2457–2469.

JACKSON, R. (1998). Erratum. *Chem. Eng. Sci*, **53**, 1955.

JACKSON, R. (2001). *The dynamics of fluid particles*. Cambridge University Press, New York, USA.

JEAN, R. & FAN, F. (1992). On the model equations of gibilaro and foscolo with corrected buoyancy force. *Powder Tech.*, **72**, 201–205.

JENKINS, J. & MANCINI, F. (1989). Kinetic theory for binary mixtures of smooth nearly elastic spheres. *Physics of fluids*, **31**, 2050–2057.

JOHNSON, P. & JACKSON, R. (1987). Frictional-collisional consitutive relations for granular materials with application to plane shearing. *J. Fluid Mech*, **176**, 67–93.

JOHNSSON, F., ZIJERVELD, R., SCHOUTEN, J., VEN DEN BLEEK, C. & LECKNER, B. (2000). Characterization of fluidization regimes by time series analysis of pressure fluctuations. *Int. J. Multi. Flow*, **26**, 663–715.

JOSEPH, D. (1990). Generalization of the foscolo-gibilaro analysis of dynamic waves. *Chem. Eng. Sci.*, **45**, 411–414.

KAFUI, K., THORNTON, C. & ADAMS, M. (2002). Discrete particle-continuum fluid modelling of gas-solid fluidised beds. *Chem. Eng. Sci.*, **57**, 2395–2410.

KOZENY, J. (1927). Über kapillare letiung des wassers im boden. *Sitzungsber Akad Wiss Wien*, **136**, 271.

KUIPERS, J. & VAN SWAAIJ, W. (1997). Application of computational fluid dynamics to chemical reaction engineering. *Review in Chemical Engineering*, **13**, 1–118.

KUIPERS, J., VANDUIN, K., VAN-BECKUM, F. & VAN-SWAAIJ, W. (1993). Computer simulation of the hydrodynamics of a two dimensional gas-fluidized bed. *Computers chem. Engng*, **17**, 839–858.

KUNII, D. & LEVENSPIEL, O. (1989). *Fluidization Engineering*. Butterworth-Heinemann, second edition edn.

LADD, A. (1993). Lattice-boltzmann simulations of particle fluid suspensions. *Journal of Fluid Mechanics*, **271**, 285.

LEBOWITZ, J. (1964). Exact solution of generalised percus-yevick equation for a mixture of hard sphere. *Phys Rev*, 895–899.

LETTIERI, P. (1999). *A study of the influence of temperature on the flow behaviour of solid materials in a gas fluidized bed*. Ph.D. thesis, University College London.

LETTIERI, P. (2002). Fluidization - course notes. Department of Chemical Engineering, University College London.

LETTIERI, P., BRANDANI, S., YATES, J. & NEWTON, D. (2001). A generalization of the foscolo and gibilaro particle bed model to predict the fluid bed stability of some fresh fcc catalysts at elevated temperature. *Chem. Eng.Science*, **56**, 5401–5412.

LETTIERI, P., MICALE, G., CAMMARATA, L. & COLMAN, D. (2002). Computational fluid dyanmic simulations of gas-fluidized beds: a preliminary investi gation of different modelling approaches. In M. Sommerfeld, ed., *Proceedings of the* 10^{th} *Workshop of Two phase flow predictions*, vol. 1, 300–309.

LETTIERI, P., CAMMARATA, L., MICALE, G. & YATES, J. (2003). Cfd simulations of gas fluidized beds using alternative eulerian-eulerian modelling approaches. *IJCRE*, **1**, A5.

LETTIERI, P., SACCONE, G. & CAMMARATA, L. (2004). Predicting the transition from bubbling to slugging fluidization using computational fluid dynamics. *Chem. Eng. Res. Des.*, **82**, 939–944.

LIM, K., ZHU, J. & GRACE, J. (1995). Hydrodynamics of gas-solid fluidization. *Int. J. Multiphase Flow*, **21**, 141–193.

MAKKAWI, Y. & OCONE, R. (2006). A model for gas-solid flow ina horzontal duct witha smooth merge of rapid-intermediate-dense flows. *Chem .Eng. Sci*, **61**, 4271–4281.

MARZOCCHELLA, A., SALATINO, P., DI PASTENA, V. & LIRER, L. (2000). Transient fluidization and segregation of binary mixtures of particles. *AICHE J*, **46**, 2175–2182.

MASSOUDI, M., RAJAGOPAL, K., EKMANN, J. & MATHUR, M. (1992). Remarks on the modeling of fluidized systems. *AIChE Journal*, **38**, 471–472.

MATHIESEN, V., SOLBERG, T. & HJERTAGER, B. (2000a). An experimental and computational study of multiphase flow behaviour in a circulating fluidized bed. *Int. J. Multiphase flow*, 387–419.

MATHIESEN, V., SOLBERG, T. & HJERTAGER, B. (2000b). Predictions of gas/particle flow with an eulerian model including a realistic particle size distribution. *Powder Technol.*, **112**, 34–45.

MAXEY, M. & RILEY, J. (1983). Equations of motion for a small rigid sphere in a nonuniform flow. *Phys Fluids*, **26**, 883–889.

MAZZEI, L. & LETTIERI, P. (2006). A numerical alogarthim for the analysis of the bubble dyanmics in 2d fluidized beds simulated by means of cfd multiphase codes. *IJCRE*, **4**, 1–20.

MAZZEI, L., LETTIERI, P., ELSON, T. & COLEMAN, D. (2006). A reveised mono-dimensional particle bed model for fluidized beds. *Chem. Eng. Sci.*, **61**, 1958–1972.

McKeen, T. & Pugsley, T. (2003). Simulation and experimental validation of a freely bubbling bed of fcc catalyst. *Powder Technol.*, **129**, 139–152.

Nadim, A. & Stone, H. (1991). The motion of small particles and droplets in quadratic flows. *Stud. Appl. Math*, **85**, 53–73.

Nakamura, K. & Capes, C. (1976). Vertical pneumatic conveying of binary particle mixture. In *In Fluidization Technology*, vol. 2, 159–184, Hemisphere Publishing Corp.

Needham, D. & Merkin, J. (1983). The propagation of a voidage disturbance in a uniformly fludized bed. *Journal of fluid Mechanics*, **131**, 427.

Nienow, A. & Chessman, D. (1980). The effect of shape on the mixing and segregation of large particles in gas-fluidized beds of small ones. In *In Fluidization*, vol. 1, 373–380.

Nienow, A. & Chiba, T. (1985). Fluidisation of dissimilar materials. In *Fluidization*, chap. 10, Academic Press London, 2nd edn.

Nienow, A., Rowe, P. & Agbim, T. (1972). The mechanisms by which particles segregate in gas fluidized beds- binary systems of near spherical particles. *Trans Inst Chem Eng*, **50**, 311–319.

Nienow, A., Rowe, P. & Chiba, T. (1978). Mixing and segregation of a small proportion of large particles in gas fluidized beds of considerably smaller ones. *AICHE Sym Series*, **74**, 45–53.

Nienow, A., Naimer, N. & Chiba, T. (1987). Studies of segregation/mixing in fludized beds of different sized particles. *Chem. Eng. Commun.*, **62**, 53–66.

Ocone, R., Sundaresan, S. & Jackson, R. (1993). Gas-particle flow in a duct of arbitrary inclination with particle particle interaction. *AICHE J*, **39**, 1261–1271.

Ouyang, J. & Li, J. (1999). Particle-motion resolved discrete model for simulating gas -solid flu. *Chem. Eng. Sci*, **54**, 2077.

OWOYEMI, O. (2005). *CFD Modelling of Binary Gas Fluidized Beds*. Mphil, University College London.

OWOYEMI, O. & LETTIERI, P. (2006). A hydrodynamic model for the simulation of binary particle systems in gas-fluidized beds. In *Proceedings of the 10th International Conference on Multiphase Flow in Industrial Plant*, vol. 1, 459–470.

OWOYEMI, O., LETTIERI, P. & PLACE, R. (2005). Experimental validation of eulerian-eulerian simulations of rutile industrial powders. *Ind. Eng. Chem. Res.*, 9996–10004.

PAIN, C., MANSOORZADEH, S. & OLIVEIRA, C.D. (2001). A study of bubbling and slugging fluidized beds using the two-fluid granular temperature model. *Int. J. Multiphase flow*, **27**, 527–551.

PANDIT, J., WANG, X. & RHODES, M. (2005). Study of geldart's group a behaviour using discrete element simulation. *Powder Tech.*, **160**, 7–14.

PEIRANO, E., ELLOUME, V. & LECKNER, B. (2001). Two- or three-dimensional simulations of turbulent gas-solid flows applied to fluidization. *Chem. Eng. Sci.*, **56**, 4787–4799.

PIGFORD, R. & BARON, T. (1965). Hydrodyanmic stability of a fluidized bed. *Ind. Eng. Chem. Fundam.*, **4**, 81–87.

PIROG, T. (1998). *Dynamics of destablilization of food emulsions. Measurement and simulation of gravity driven partricle velocities in polydisperse dispersions*. Phd thesis, Purdue University.

RASUL, M., RUDOLPH, V. & CARSKY, M. (1999). Segregation potential in binary gas fluidized beds. *Powder Tech*, **103**, 175–181.

RICHARDSON, J. & ZAKI, W. (1954a). Sedimentation and fluidization. *Trans. Inst. Chem. Eng.*, **32**, 35.

RIETEMA, K. & VAN DEN AKKER, H. (1983). On the momentum equations in dispersed two-phase systems. *Int. J. Multiphase Flow*, **9**, 21.

ROWE, P. (1961). Drag forces in a hydraulic of a fluidized bed, part ii. *Trans. Inst. Chem. Eng.*, **39**, 175.

ROWE, P. (1971). *Fluidization by Davidson, J.F. and Harrison D.*, chap. 4. Academic Press, London, UK.

ROWE, P., NIENOW, A. & AGBIM, A. (1972). A preliminary quantitative study of particle segregation in gas fluidized beds- binary systems of near spherical particles. *Trans. Inst Chem Eng*, **50**, 324–333.

SAFFMAN, P. (1965). The lift on a small sphere ina slow shear flow. *J. Fluid Mech.*, **22**, 385–400.

SAMUELSBERG, A. & HJERTAGER, B. (1996). Computational modeling of gas/particle flow in a riser. *AIChE J.*, **42**, 1536–1546.

SAVAGE, S. (1982). Granular flows down rough inclines - review and extension. In J. Jenikins & M. Satake, eds., *U.S.- Japan Seminar on New Models and Constitutive Relations in the Mechanics of Granular Materials*, 261–282, Elsevier.

SHIH, Y., GIDASPOW, D. & WASAN, D. (1987). Hydrodynamics of sedimentation of multisized particles. *Powder Tech*, **56**.

Soo, S. (1967). *Fluid Dynamics of Multiphase Systems*. Blaisdell Publishing Corp. Waltham, MA.

SRINIVASAN, M. & Doss, E. (1985). Momentum transfer due to particle-particle interaction in dilute gas-solid flows. *Chem. Eng. Sci.*, **40**, 1791–1792.

SUCCI, S. (2001). *The Lattice Boltzmann Equation for Fluid Dynamics and Beyond*. Oxford Science Publications, Oxford, first edition edn.

SUNDARESAN, S. (2000). Modelling the hydrodynamics of multiphase flow reactors: current status and challenges. *AIChE Journal*, **46**, 1102–1105.

SYAMLAL, M. (1985). *Multiphase Hydrodynamics of Gas-Solid Flow*. Ph.D. thesis, Illinois Institute of Technology.

SYAMLAL, M. (1987b). The particle-particle drag term in a multiparticle model of fludization. Topical report, doe/mc/215353-2372, ntis/de87006500, National Technical Information Service, Springfield, VA.

SYAMLAL, M., ROGERS, W. & O'BRIEN, T. (1993). Mfix documentation theory guide. Technical note DOE/METC-94/1004.

TARDOS, G., MCNAMARA, S. & TALU, I. (2003). Slow and intermediate flow of a frictional bulk powder in the coutte geometry. *Powder Tech*, **131**, 23–39.

TOOMEY, R. & JOHNSTONE, H. (1952). *Chemical Engineering Progress*, **48**, 220.

TSUJI, Y., MORIKWA, Y., TANAKA, T., NAKATSUKASA, N. & NAKATANI, N. (1987). Numerical simulation of gas-solid two phase flow in a two-dimensional horizontal channel. *Int. J. Multiphase Flow*, **13**, 671.

TSUJI, Y., KAWAGUCHI, T. & TANAKA, T. (1993). Discrete particle simulation of a two-dimensional fluidized bed. *Powder Tech.*, **77**, 79.

VAN DEEMTER, J. (1961). Mixing and contacting in gas-fluidized beds. *Chem. Eng. Sci.*, **13**, 143–154.

VAN DEN AKKER, H. (1997). On status and merits of computational fluid dynamics. In *W. Nienow, Proceedings of the 4th International Conference on Bioreactor and Bioprocess Fluid Dynamics*, 407–432.

VAN DER HOEF, M., VAN SINT ANNALAND, M. & KUIPERS, J. (2004). Computational fluid dynamics for dense gas-solid fluidized beds: a multi-scale modeling strategy. *Chem. Eng. Sci*, **59**, 5157–5165.

VAN DER SCHAAF, J., SCHOUTEN, J., JOHNSSON, F. & VAN DEN BLEEK, C. (2002). Non-intrusive determination of bubble and slug length scales in fludized beds by decomposition of the power spectral density of pressure time series. *Int. J. Multi. Flow*, **28**, 865–880.

VAN DER SCHAAF, J., VAN OMMEN, J., F.TAKENS, SCHOUTEN, J. & VAN DEN BLEEK, C. (2004). Similarity between chaos analysis and frequency analysis of pressure fluctuations in fluidized beds. *Chem. Eng. Sci.*, **59**, 1829–1840.

VAN WACHEM, B. (2000). *Derivation, Implementation and Validation of Compuer Simulation Models for Gas-Solid Fluidized Beds.* Ph.D. thesis, Delft University of Technology.

VAN WACHEM, B., SCHOUTEN, J., KRISHNA, R. & VAN DEN BLEEK, C. (1998). Eulerian simulations of bubbling behaviour in gas-solid fluidised beds. *Computers Chem. Eng*, **22**, S299–S306.

VAN WACHEM, B., SCHOUTEN, J., VAN DEN BLEEK, C. & R.KRISHNA (1999). Comparative analysis of cfd models of dense gas solid systems. *AIChE*, **47**, 1035.

VAN WACHEM, B., SCHOUTEN, J., KRISHNA, R., VAN DEN BLEEK, C. & SINCLAIR, J. (2001). Cfd modeling of fluidized beds with a bimodal particle mixture. *AIChE J*, **47**, 1291.

VERLOOP, J. & HEERTJES, P. (1970). Shock waves as a criterion for the transition from homogeneous to heterogeneous fluidization. *Chem. Eng. Sci*, **25**, 825.

WALLIS, G. (1969). *One dimensional Two Phase flow.* McGraw Hill.

WEN, C. & YU, Y. (1966). Mechanics of fluidization. *Chemical Engineering Progress Symposium Series*, **62**, 100.

WHITAKER, S. (1973). The transport equations for multiphase systems. *Chem. Eng. Sci.*, 139–147.

WITT, P., PERRY, J. & SCHWARZ, M. (1998). A numerical model for predicting bubble formation in a 3d fludized bed. *Appl. Math. Model*, **22**, 1071–1080.

WU, S. & BAEYENS, J. (1998). Segregation by size difference in gas fluidized beds. *Powder Technology*, 139–150.

XIE, H. & GELDART, D. (1995). Fluidization of fcc powders in the bubble-free regime: Effect of types of gases and temperature. *Powder Tech.*, **82**, 269.

Xu, B. & Yu, A. (1997). Numerical simulation of the gas-solid flow in a fludised bed by combining discrete and particle method with computational fluid dynamics. *Chem. Eng. Sci.*, **52**, 2785–2809.

Yang, W.C. (2003). *Handbook of Fluidization and Fluid particle systems*, chap. 3, 95. Marcel Dekker, New York, USA.

Yates, J., Cheesman, D. & Sergeev, Y. (1994). Experimental observations of voidage distribution around bubbles in a fluidized bed. *Chem. Eng. Sci.*, **49**, 1885–1895.

Ye, M., van der Hoef, M. & Kuipers, J. (2005). The effects of particle and gas properties on the fluidization of geldart a particles. *Chem. Eng. Sci.*, **60(16)**, 4567–4580.

Zamankhan, P. (1995). Kinetic theory of multicomponent dense mixtures of slightly inelastic sphereical particles. *Physical Review E*, **52**, 4877–4891.

Zhang, D. & Prosperetti, A. (1994). Averaged equations for inviscid disperse two phase flows. *J. Fluid. Mech.*, **267**, 185–219.

Zhang, D. & Prosperetti, A. (1997). Momentum and energy equations for disperse two phase flows and their closure for dilute suspensions. *Int. J. Multiphase Flow*, **23**, 425–453.

Zhang, K. & Brandani, S. (2004). A cfd model for fluid dyanmics in gas-fluidized beds. *Chemical Reseacrh in Chinese Universities*, **4**, 483–488.

Zhang, K., Brandani, S. & Bi, J. (2005). Computational fluid dyanmics for dense gas-solid fluidized beds. *Progress in Natural Science*, **15**, 42–52.

Appendix A

Derivation of derivatives used for modelling the binary mixture

A.1 Derivation of fluid averaged position derivatives for a binary mixture

We start with the spatial derivative of the fluid phases. As stated in §4.2, the fluid phase average of a point property is given by

$$\langle \psi(x,t) \rangle^f = \frac{1}{\varepsilon(x,t)} \int_{V_{f\infty}(t)} g(|x-y|)\psi(y,t)\, dV_y \tag{A.1}$$

The spatial derivatives can be expressed as:

$$\frac{\partial}{\partial x_i}\left[\langle\psi(x,t)\rangle^f \varepsilon(x,t)\right] \equiv \frac{\partial}{\partial x_i}\left[\int_{V_{f\infty}(t)} g(|x-y|)\psi(y,t)\,dV_y\right]$$

$$= \int_{V_{f\infty}(t)} \frac{\partial}{\partial x_i}[g(|x-y|)\psi(y,t)]dV_y$$

$$= \int_{V_{f\infty}(t)} \psi(y,t)\frac{\partial}{\partial x_i} g(|x-y|)\,dV_y$$

$$= -\int_{V_{f\infty}(t)} \psi(y,t)\frac{\partial}{\partial y_i} g(|x-y|)\,dV_y$$

$$= -\int_{V_{f\infty}(t)} \frac{\partial}{\partial y_i}[g(|x-y|)\psi(y,t)]dV_y$$

$$+ \int_{V_{f\infty}(t)} g(|x-y|)\frac{\partial}{\partial y_i}\psi(y,t)dV_y \qquad \text{(A.2)}$$

Mathematical manipulation and the application of the fact that (Anderson & Jackson, 1967):

$$\frac{\partial}{\partial x_i} g(|x-y|) = -\frac{\partial}{\partial y_i} g(|x-y|) \qquad \text{(A.3)}$$

Leads to Eq.(A.2). The first term present on the R.H.S of eq.(A.2) can be transformed into a surface integral by the application of divergence theorem thus we have:

$$\int_{V_{f\infty}(t)} \frac{\partial}{\partial y_i}[g(|x-y|)\psi(y,t)]dV_y = \int_{S_{f\infty}(t)} g(|x-y|)\,\psi(y,t)\,n_k(y,t)\,dS_y \qquad \text{(A.4)}$$

where the surface bounding *only* the fluid at time t is given by $S_f(t)$. Also, the surface bounding the the whole system, $S_{f\infty}$ at time t is given by $S_{f\infty}(t) = S_f(t) - S_1(t) - S_2(t)$, where $S_1(t)$ and $S_2(t)$ refer to the surface bounding the fluid-solid inter phase surface of both types of solid particles present in the mixture . Therefore eq.(A.4) can be transformed such

that we have.

$$\int_{S_f(t)} g\,(|x-y|)\,\psi\,(y,t)\,n_k\,(y,t)\,dS_y = \int_{S_{f\infty}(t)} g\,(|x-y|)\,\psi\,(y,t)\,n_k\,(y,t)\,dS_y$$
$$-\sum_{\mathscr{F}_1}\int_{S_1(t)} g\,(|x-y|)\,\psi\,(y,t)\,n_i\,dS - \sum_{\mathscr{F}_2}\int_{S_2(t)} g\,(|x-y|)\,\psi\,(y,t)\,n_k\,(y,t)\,dS_y \tag{A.5}$$

Provided the shortest distance from point x to the surface bounding the whole system $S_{f\infty}$ is considerably larger than the radius over which the weighting function is applied then the first term in eq.(A.5) will be much smaller than the last two terms that follow it. Thus we can rewrite eq.(A.2) as follows:

$$\int_{V_{f\infty}(t)} g\,(|x-y|)\,\frac{\partial}{\partial y_i}\psi\,(y,t)\,dV_y = \frac{\partial}{\partial x_i}\left[\langle\psi\,(x,t)\rangle\,\varepsilon\,(x,t)\right] \tag{A.6}$$
$$-\sum_{\mathscr{F}_1}\int_{S_1(t)} g\,(|x-y|)\,\psi\,(y,t)\,n_k\,(y,t)\,dS_y - \sum_{\mathscr{F}_2}\int_{S_2(t)} g\,(|x-y|)\,\psi\,(y,t)\,n_k\,(y,t)\,dS_y$$

which is the relation shown in eq. (4.5).

A.2 Derivation of fluid averaged time derivatives for a binary mixture

The time derivatives of the averaged quantities can be expressed as follows:

$$\frac{\partial}{\partial t}\left[\int_{V_{f\infty}(t)} g\,(|x-y|)\,\langle\psi\,(x,t)\rangle\right] = \frac{\partial}{\partial t}\left[\int_{V_{f\infty}(t)} g\,(|x-y|)\,\psi\,(y,t)\,dV_y\right] \tag{A.7}$$

Using Leibnitz's rule, the R.H.S of eq. (A.7) can be written as:

$$\int_{V_{f\infty}(t)} \frac{\partial}{\partial t}\left[g\,(|x-y|)\,\psi\,(y,t)\right]dV_y + \int_{sf(t)} \psi\,(y,t)\,g\,(|x-y|)\,u\,(y,t)\cdot n\,(y,t)\,dS_y \tag{A.8}$$

Now the R.H.S.of eq. (A.8) can be approximated using the same procedure described in appendix A.1. Using eqs. (A.7) and (A.8) carrying out the relevant manipulations. Eq. (A.7) can be expressed as:

$$\int_{V_{f\infty}(t)} g(|x-y|)\frac{\partial}{\partial t}\psi(y,t)\,dV_y = \frac{\partial}{\partial t}\left[\int_{V_{f\infty}(t)} g(|x-y|)\langle\psi(x,t)\rangle\right] + \tag{A.9}$$

$$\sum_{\mathcal{F}_1}\int_{S_1(t)} \psi(y,t)\,g(|x-y|)\,u(y,t)\cdot n(y,t)\,dS_y + \sum_{\mathcal{F}_2}\int_{S_2(t)} \psi(y,t)\,g(|x-y|)\,u(y,t)\cdot n(y,t)\,dS_y$$

which is the form shown in eq. (4.6).

A.3 Evaluation of the primary force Differential $\left(\frac{\partial\langle f^{\mathcal{P}_\mathcal{F}}\rangle}{\partial\varepsilon}\right)_{U_o,U_p}$

The evaluation of the $\left(\frac{\partial\langle f^{\mathcal{P}_\mathcal{F}}\rangle}{\partial\varepsilon}\right)_{U_o,U_p}$ function is required to obtain a general expression for the elastic modulus, E_k, shown earlier in eq. (2.28). A mathematical solution to the partial derivative is detailed below. The net force equation is presented here again for convenience:

$$\langle f^{\mathcal{P}_\mathcal{F}}\rangle = \frac{\pi d_k^2}{6}\left[\left(\frac{17.3}{Re_k}\right)^{\alpha} + (0.336)^{\alpha}\right]^{\frac{1}{\alpha}} \rho_f\left(U_o - U_p\right)^2 \varepsilon^{-3.8} - \frac{\pi d_p^3}{6}\left(\rho_p - \rho_f\right) g\varepsilon \tag{A.10}$$

where α is given by:

$$\alpha = 2.55 - 2.1\left[\tanh(20\varepsilon - 8)^{0.33}\right]^3 \tag{A.11}$$

Now let $\left(\frac{17.3}{Re_k}\right) = A$, $0.336 = B$ and

$$K = \frac{\pi d_p^2}{6}\rho_f\left(U_o - U_p\right)^2 \tag{A.12}$$

$$P = \frac{\pi d_p^3}{6}\left(\rho_p - \rho_f\right) \tag{A.13}$$

Substituting the above into eqn. (A.10) we have:

$$\langle f^{\mathcal{P}_\mathcal{F}} \rangle = \underbrace{K\left[A^\alpha + B^\alpha\right]^{\frac{1}{\alpha}} \varepsilon^{-3.8}}_{\langle f^{\mathcal{P}_\mathcal{F}} \rangle_1} + \underbrace{P\varepsilon}_{\langle f^{\mathcal{P}_\mathcal{F}} \rangle_2} \tag{A.14}$$

Now we have:

$$\frac{\partial \langle f^{\mathcal{P}_\mathcal{F}} \rangle}{\partial \varepsilon} = \frac{\partial \langle f^{\mathcal{P}_\mathcal{F}} \rangle_1}{\partial \varepsilon} + \frac{\partial \langle f^{\mathcal{P}_\mathcal{F}} \rangle_2}{\partial \varepsilon} \tag{A.15}$$

We start by the evaluation $\dfrac{\partial \langle f^{\mathcal{P}_\mathcal{F}} \rangle_1}{\partial \varepsilon}$

$$\frac{\partial \langle f^{\mathcal{P}_\mathcal{F}} \rangle_1}{\partial \varepsilon} = -3.8K\varepsilon^{-4.8}\left[A^\alpha + B^\alpha\right]^{\frac{1}{\alpha}} + K\varepsilon^{-3.8}\left\{\frac{\partial\left\{\left[A^\alpha + B^\alpha\right]^{\frac{1}{\alpha}}\right\}}{\partial \varepsilon}\right\} \tag{A.16}$$

Evaluating the function, $\dfrac{\partial\left\{\left[A^\alpha + B^\alpha\right]^{\frac{1}{\alpha}}\right\}}{\partial \varepsilon}$, requires the equation to be broken into parts. Let $\zeta = \left[A^\alpha + B^\alpha\right]^{\frac{1}{\alpha}}$ hence:

$$\frac{\partial \zeta}{\partial \varepsilon} = \frac{\partial \zeta}{\partial \alpha} \cdot \frac{\partial \alpha}{\partial \varepsilon} \tag{A.17}$$

We know from eq. (A.11) that:

$$\alpha = 2.55 - 2.1\left[\tanh\left(20\varepsilon - 8\right)^{0.33}\right]^3 \tag{A.18}$$

Evaluating to obtain the differential function $\dfrac{\partial \alpha}{\partial \varepsilon}$ we obtain the following result:

$$\frac{\partial \alpha}{\partial \varepsilon} = -6.3\left[\tanh\left(20\varepsilon - 8\right)^{0.33}\right] 2 \cdot \sec h^2\left(20\varepsilon - 8\right)^{0.33} \cdot 6.6\left(20\varepsilon - 8\right)^{-0.67} \tag{A.19}$$

We now evaluate the function $\dfrac{\partial \zeta}{\partial \alpha}$ knowing that:

$$\zeta = \left[A^\alpha + B^\alpha\right]^{\frac{1}{\alpha}} \tag{A.20}$$

Taking logs we have:

$$\ln \zeta = \frac{1}{\alpha} \ln\left[A^\alpha + B^\alpha\right] \tag{A.21}$$

We now apply the chain rule to obtain the following equation:

$$\frac{\partial \zeta}{\partial \alpha}\frac{1}{\zeta} = -\frac{1}{\alpha^2}\ln\left[A^\alpha + B^\alpha\right] + \frac{1}{\alpha}\frac{1}{A^\alpha + B^\alpha}\frac{\partial\left\{\left[A^\alpha + B^\alpha\right]\right\}}{\partial \alpha} \tag{A.22}$$

Evaluating the function $\frac{\partial\left\{\left[A^\alpha + B^\alpha\right]\right\}}{\partial \alpha}$ we note the following differentiation rule.

$$\frac{\partial a^u}{\partial x} = a^u \ln a \frac{\partial u}{\partial x} \tag{A.23}$$

Applying eq. (A.23):

$$\frac{\partial\left\{\left[A^\alpha + B^\alpha\right]\right\}}{\partial \alpha} = A^\alpha \ln A + B^\alpha \ln B \tag{A.24}$$

Thus evaluating the function, $\frac{\partial \zeta}{\partial \alpha}$ we have:

$$\frac{\partial \zeta}{\partial \alpha} = \zeta\left\{-\frac{1}{\alpha^2}\ln\left[A^\alpha + B^\alpha\right] + \frac{1}{\alpha}\left[\frac{A^\alpha \ln A + B^\alpha \ln B}{A^\alpha + B^\alpha}\right]\right\} \tag{A.25}$$

Thus $\frac{\partial \zeta}{\partial \varepsilon}$ will be given by:

$$\frac{\partial \zeta}{\partial \varepsilon} = \zeta\left\{-\frac{1}{\alpha^2}\ln\left[A^\alpha + B^\alpha\right] + \frac{1}{\alpha}\left[\frac{A^\alpha \ln A + B^\alpha \ln B}{A^\alpha + B^\alpha}\right]\right\}\times \tag{A.26}$$

$$[0.25cm]\left\{-6.3\left[\tanh(20\varepsilon-8)^{0.33}\right]^2\right\}\times\left\{\sec h^2(20\varepsilon-8)^{0.33}\right\}\times\left\{6.6(20\varepsilon-8)^{-0.67}\right\}$$

We now let:

$$\chi = \left\{-\frac{1}{\alpha^2}\ln\left[A^\alpha + B^\alpha\right] + \frac{1}{\alpha}\left[\frac{A^\alpha \ln A + B^\alpha \ln B}{A^\alpha + B^\alpha}\right]\right\}\times \tag{A.27}$$

$$\left\{-6.3\left[\tanh(20\varepsilon-8)^{0.33}\right]^2\right\}\times\left\{\sec h^2(20\varepsilon-8)^{0.33}\right\}\times\left\{6.6(20\varepsilon-8)^{-0.67}\right\}$$

Thus, $\frac{\partial \zeta}{\partial \varepsilon}$ can be rearranged in a more compact form :

$$\frac{\partial \zeta}{\partial \varepsilon} = \zeta.\chi \tag{A.28}$$

We recall that:

$$\zeta = [A^{\alpha} + B^{\alpha}]^{\frac{1}{\alpha}} \tag{A.29}$$

Leading to:

$$\frac{\partial\left\{[A^{\alpha} + B^{\alpha}]^{\frac{1}{\alpha}}\right\}}{\partial\varepsilon} = \left\{[A^{\alpha} + B^{\alpha}]^{\frac{1}{\alpha}}\right\} \cdot \chi \tag{A.30}$$

Inserting eq. (A.30) in eq. (A.16) we have:

$$\frac{\partial\langle f^{\mathcal{P}_{\mathcal{F}}}\rangle_1}{\partial\varepsilon} = -3.8K\varepsilon^{-4.8}[A^{\alpha} + B^{\alpha}]^{\frac{1}{\alpha}} + K\varepsilon^{-3.8}[A^{\alpha} + B^{\alpha}]^{\frac{1}{\alpha}} \cdot \chi \tag{A.31}$$

Where χ is given by eq. (A.27).The above equation can be re-arranged to give:

$$\boxed{\frac{\partial\langle f^{\mathcal{P}_{\mathcal{F}}}\rangle_1}{\partial\varepsilon} = K\varepsilon^{-3.8}[A^{\alpha} + B^{\alpha}]^{\frac{1}{\alpha}}\left(-3.8\varepsilon^{-1} + \chi\right)} \tag{A.32}$$

Now we evaluate the function $\frac{\partial\langle f^{\mathcal{P}_{\mathcal{F}}}\rangle_2}{\partial\varepsilon}$ from eq. (A.15), we start by:

$$\frac{\partial\langle f^{\mathcal{P}_{\mathcal{F}}}\rangle_2}{\partial\varepsilon} = P \tag{A.33}$$

we obtain the following result upon evaluation:

$$\boxed{\frac{\partial\langle f^{\mathcal{P}_{\mathcal{F}}}\rangle}{\partial\varepsilon} = K\varepsilon^{-3.8}[A^{\alpha} + B^{\alpha}]^{\frac{1}{\alpha}}\left(-3.8\varepsilon^{-1} + \chi\right) - P} \tag{A.34}$$

Re-inserting the appropriate terms we have:

$$\boxed{\frac{\partial\langle f^{\mathcal{P}_{\mathcal{F}}}\rangle}{\partial\varepsilon} = \underbrace{\frac{\pi d_p^2}{6}\rho_f\left(U_o - U_p\right)^2\varepsilon^{-3.8}\left[\left(\frac{17.3}{\mathrm{Re}_p}\right)^{\alpha} + 0.336^{\alpha}\right]^{\frac{1}{\alpha}}}_{\left|\langle f^d\rangle^{\mathcal{F}_k}\right|}\left(-3.8\varepsilon^{-1} + \chi\right) - \frac{\pi d_p^3}{6}\left(\rho_p - \rho_f\right)} \tag{A.35}$$

As we can see the braced term in the equation above represents the drag force on one particle which can be conveniently replaced with the term $\left|\langle f^d\rangle^{\mathcal{F}_k}\right|$ thus we have.

$$\frac{\partial\langle f^{\mathcal{P}_{\mathcal{F}}}\rangle}{\partial\varepsilon} = \left|\langle f^d\rangle^{\mathcal{F}_k}\right|\left(-3.8\varepsilon^{-1} + \chi\right) - \frac{\pi d_p^3}{6}\left(\rho_p - \rho_f\right) \tag{A.36}$$

The drag force expressed per unit volume modifies the above equation into:

$$\frac{\partial\langle f^{\mathcal{P}_\mathcal{F}}\rangle}{\partial\varepsilon} = \frac{\pi d_p^3}{6(1-\varepsilon)}\left|\langle f^d\rangle^{\mathcal{F}_k}\right|\left(-3.8\varepsilon^{-1}+\chi\right) - \frac{\pi d_p^3}{6}\left(\rho_p-\rho_f\right) \tag{A.37}$$

We remember here that:

$$E_k = -\frac{4\cdot(1-\varepsilon)}{\pi\cdot d_k^2}\cdot\left(\frac{\partial\langle f^{\mathcal{P}_\mathcal{F}}\rangle}{\partial\varepsilon}\right)_{U_o,U_p} \tag{A.38}$$

Substituting the eq. (A.37) in eq. (A.38) we have:

$$E = -\frac{4(1-\varepsilon)}{\pi d_p^2}\left\{\frac{\pi d_p^3}{6(1-\varepsilon)}\left|\langle f^d\rangle^{\mathcal{F}_k}\right|\left(-3.8\varepsilon^{-1}+\chi\right) - \frac{\pi d_p^3}{6}\left(\rho_p-\rho_f\right)\right\} \tag{A.39}$$

which can be further reduced to:

$$E = -\frac{2}{3}d_p\left[\left|\langle f^d\rangle^{\mathcal{F}_k}\right|\left(-3.8\varepsilon^{-1}+\chi\right) - (1-\varepsilon)\left(\rho_p-\rho_f\right)g\right] \tag{A.40}$$

Where:

$$\chi = \left\{-\frac{1}{\alpha^2}\ln\left[\left(\frac{17.3}{\mathrm{Re}_p}\right)^\alpha + (0.336)^\alpha\right] + \frac{1}{\alpha}\left[\frac{\left(\frac{17.3}{\mathrm{Re}_p}\right)^\alpha \ln\left(\frac{17.3}{\mathrm{Re}_p}\right) + 0.336^\alpha \ln 0.336}{\left(\frac{17.3}{\mathrm{Re}_p}\right)^\alpha + (0.336)^\alpha}\right]\right\}\times \tag{A.41}$$

$$\left\{-6.3\left[\tanh(20\varepsilon-8)^{0.33}\right]^2\right\}\times\left\{\sec h^2(20\varepsilon-8)^{0.33}\right\}\times\left\{6.6(20\varepsilon-8)^{-0.67}\right\}$$

Where α is given by:

$$\alpha = 2.55 - 2.1\left[\tanh(20\varepsilon-8)^{0.33}\right]^3 \tag{A.42}$$

Appendix B

Gravitational instabilities in Gas fluidized beds

B.1 CFD modelling results

For completeness during the development of this work, I have also used the model developed to study the phenomenon of gravitational instabilities in fluidized beds. The same computational parameters employed in § 5.3.1 were employed for this study. Figures B.1, B.2 and B.3 show snapshots of the transient response of the fluid bed to a fluid flux. It can be seen that the lower part of the bed in all the snapshots during the initial stages (transient period, between 0s - 1.8s) is at a lower density than the upper zone (this is depicted in the figures as the area with a voidage of around 0.6 - 0.7). These pockets of low density are seen to travel unimpeded to the surface of the bed (during the transient period) until the bed attains a final equilibrium condition. This provides an unequivocal support for the phenomenon of *gravitational instabilities*- which are responsible for the longer transient response time in expanding homogenous beds (Gibilaro, 2001).

The effect of gravitational instabilities is further demonstrated in Figures B.4 - B.7. Here, the bed height has been plotted against time for each of the superficial gas velocities investi-

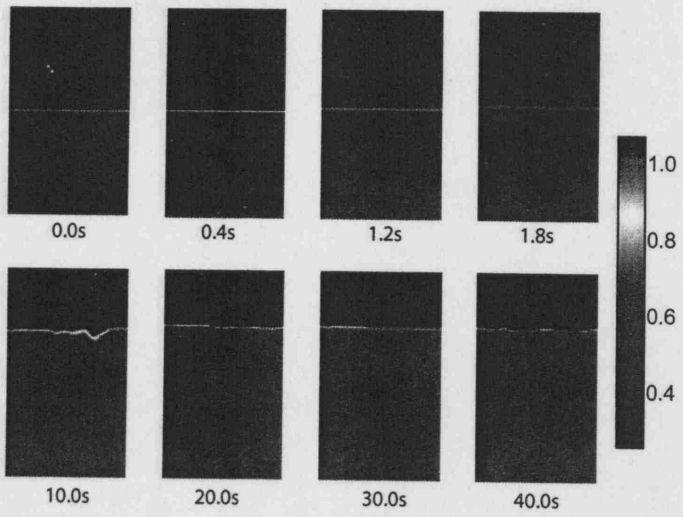

Figure B.1: *Voidage profile showing homogenous expansion of FCC particles at* $U_o = 0.018ms^{-1}$

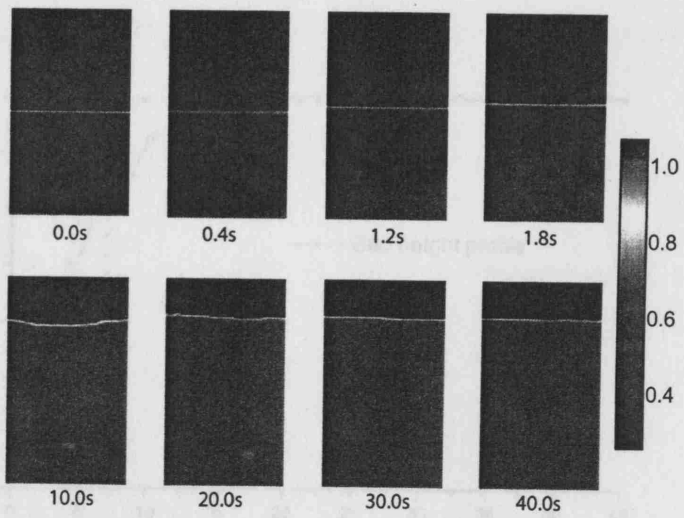

Figure B.2: *Voidage profile showing homogenous expansion of FCC particles at* $U_o = 0.025ms^{-1}$

gated. The red dots in Figure B.4 depict an example of the expected behaviour of the system, from the graph it can be seen that the bed attains the steady state condition much later than predicted (around 12secs in this case).

It is reasonable to conclude that the relationship between the bed height and time during the transient period is *non-linear* in nature and upon closer inspection seems sigmoidal. Using a curve fitting software (Origin ©), the relationship between the bed height and time in an expanding homogenous fluidized bed was found to follow the *Boltzman* function which has

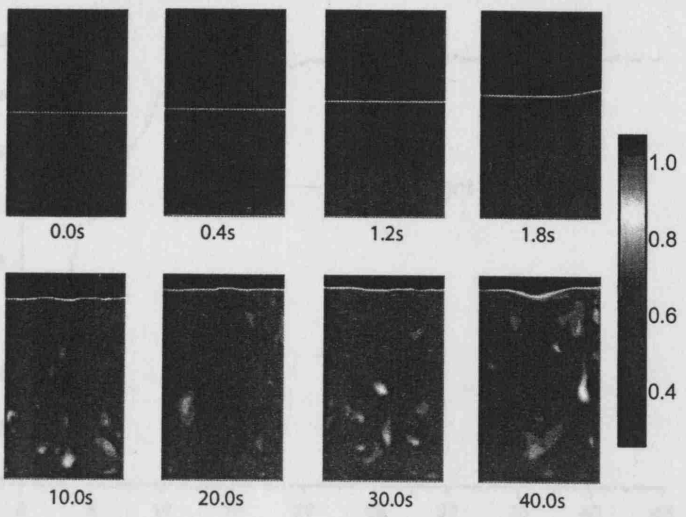

Figure B.3: *Voidage profile showing homogenous expansion of FCC particles at* $U_o = 0.035ms^{-1}$

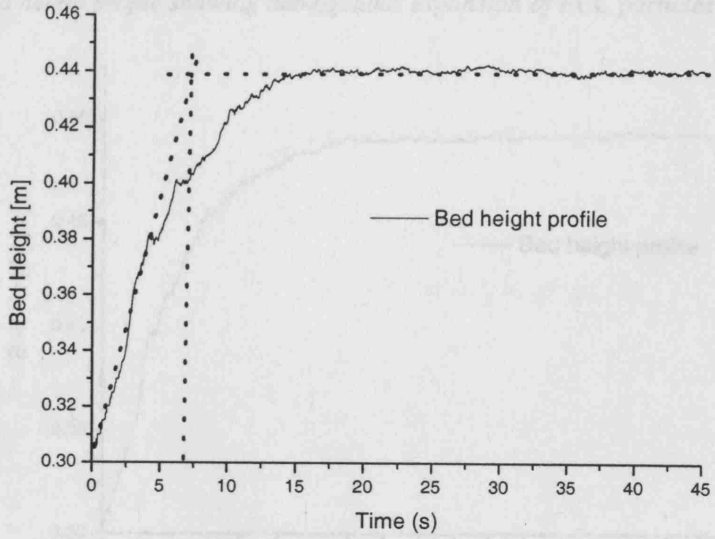

Figure B.4: *Bed height profile showing homogenous expansion of FCC particles at* $U_o = 0.018ms^{-1}$

the following general form:

$$y = \frac{A_1 - A_2}{1 + e^{\frac{x - x_0}{dx}}} + A_2 \tag{B.1}$$

where A_1 and A_2 are empirically fitted numbers, dx refers to the step size in time and x_0 refers to the initial time. An expression based on eq. (B.1) was developed and used in this work for fitting the response curve (Bed height vs time relationship) to changes in fluid flux.

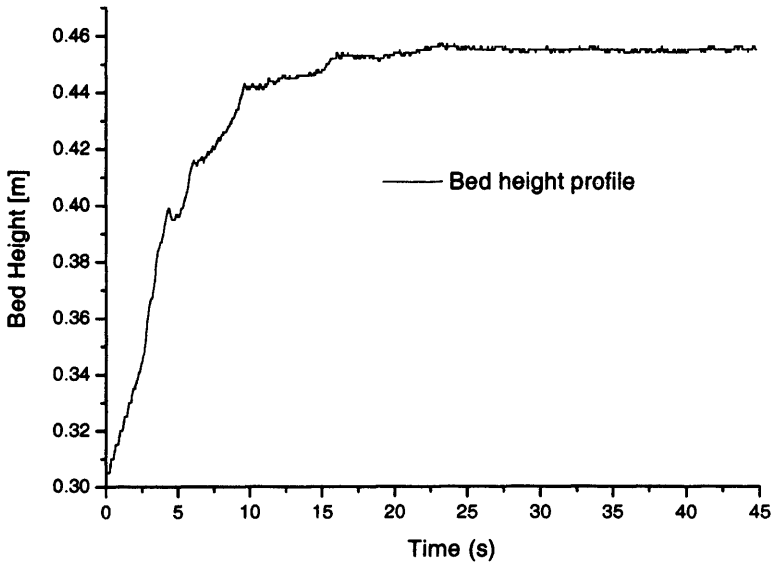

Figure B.5: *Bed height profile showing homogenous expansion of FCC particles at* $U_o = 0.020ms^{-1}$

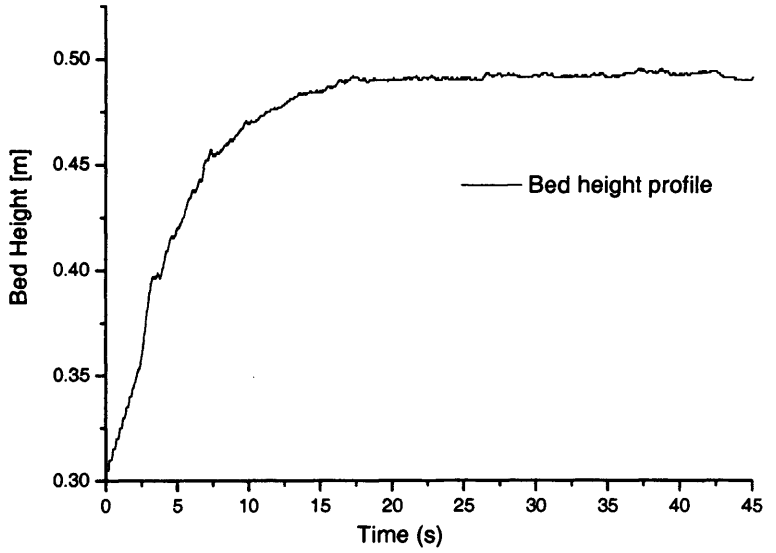

Figure B.6: *Bed height profile showing homogenous expansion of FCC particles at* $U_o = 0.025ms^{-1}$

The expression has the following form:

$$H = \left(0.13329 - H_f\right)\left(1 + e^{\left[\frac{t+0.347}{3.70}\right]}\right)^{-1} + H_f \tag{B.2}$$

where H_f refers to the steady state height and t is the time. Figure B.8 shows the application of the fitting function, eq. (B.2)to results shown earlier in Figure B.4.

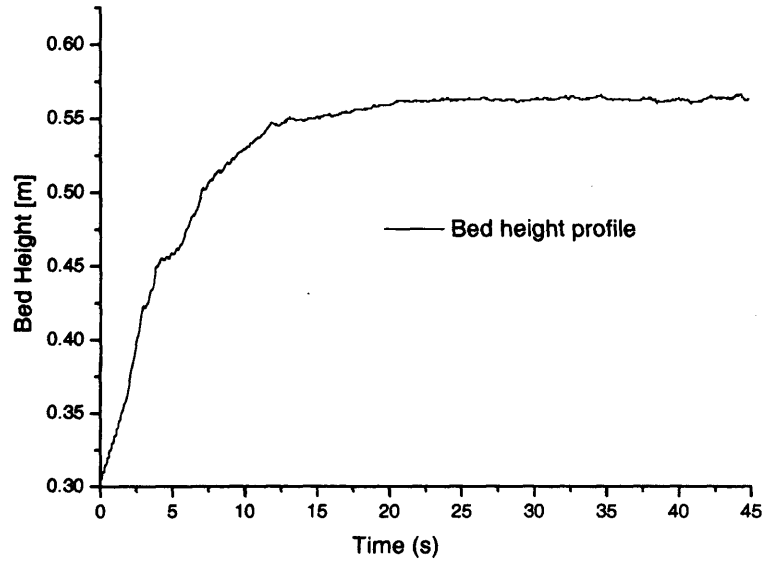

Figure B.7: *Bed height profile showing homogenous expansion of FCC particles at* $U_o = 0.035ms^{-1}$

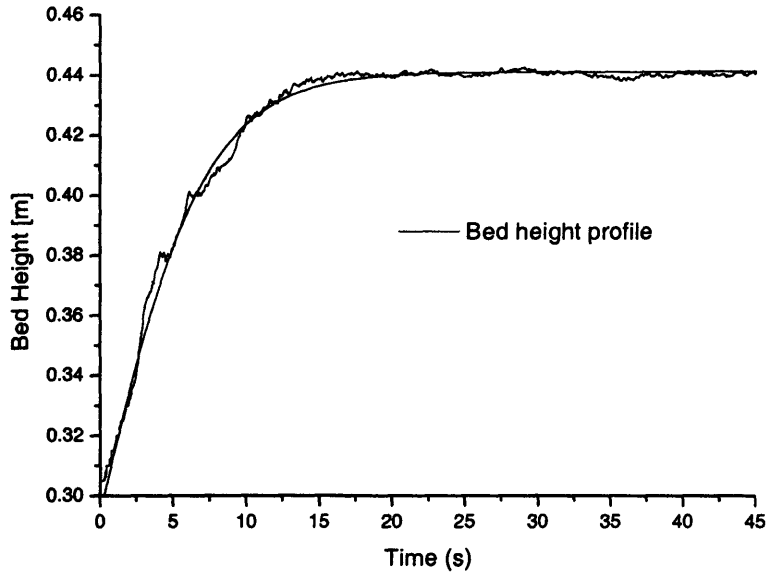

Figure B.8: *Bed height profile showing homogenous expansion of FCC particles at* $U_o = 0.018ms^{-1}$ *fitted using Eq.* (B.2)

It should be noted however that eq. (B.2) has not been generalized for all cases. It is only meant to demonstrate that the response to a fluid flux in an expanding homogenous fluidized bed is *non-linear* and possess a behaviour which can be predicted by function similar to the *boltzmann* equation.

Appendix C

Dynamics of Multi Particle Systems

The presence of many particles in contact with a fluid presents a very different picture from that described in § 2.3.1.1. Exact solutions of the equations of motion are no longer available and the behavior is summarized using empirical correlations. In this section, the dynamics of fixed beds and fluidized beds will be discussed.

C.1 Fixed beds

There have been numerous studies into the flow through packed beds. Most of the theoretical work done to predict pressure drop through fixed beds draw from two main approaches: that of the discrete particle surrounded by fluid and the pipe flow analogy. The latter of the two above mentioned approaches has been more widely employed in describing the functional dependencies between physical parameters. The pipe flow analogy approximates the flow through the packed bed by the flow through a bundle of straight capillaries of equal size. The equations utilized to describe pressure drop in fixed beds under laminar and turbulent conditions respectively, have some theoretical foundations (see,e.g, Bird et al. (1960), Gibilaro (2001)): they have been derived starting from the expressions for pressure drop in a tube

flow (the Hagen-Poisuelle equation)

$$\frac{\Delta P}{L} = 32\frac{\mu v}{D^2} \tag{C.1}$$

where the mean tube velocity is given by, v, the Diameter of the tube is given by ,D, and the viscosity of the fluid is given by μ. D in the Hagen-Poisuelle equation can be replaced by the hydraulic diameter given by

$$d_h = \frac{4 \times \text{void volume}}{\text{internal surface area}} = \frac{2\varepsilon d_p}{3(1-\varepsilon)} \tag{C.2}$$

and v by the interstitial velocity u/ε. Blake (1922) and Kozeny (1927) used the above approach to derive an expression for the pressure drop in a packed bed in the viscous flow regime:

$$\frac{\Delta P}{L} = 150\frac{\mu u}{d_p^2}\frac{(1-\varepsilon)^2}{\varepsilon^3} \tag{C.3}$$

Similarly, for the inertial flow regime Burke & Plummer (1928) applied the same above procedure. In this case the tube flow equation was expressed in terms of the dimensionless *fanning friction* factor.

$$\Delta P = 4f.\left(\frac{L}{D}\right).\left(\frac{\rho_f U^2}{2}\right) \tag{C.4}$$

Making the substitutions for U and D they found:

$$\frac{\Delta P}{L} = 1.75\frac{\rho u^2}{d_p}\frac{(1-\varepsilon)}{\varepsilon^3} \tag{C.5}$$

For the intermediate flow regime Ergun (1952) simply added the two contributions obtaining a very good agreement with experimental data

$$\frac{\Delta P}{L} = 150\frac{\mu u}{d_p^2}\frac{(1-\varepsilon)^2}{\varepsilon^3} + 1.75\frac{\rho u^2}{d_p}\frac{(1-\varepsilon)}{\varepsilon^3} \tag{C.6}$$

Foscolo et al. (1983) modified the Ergun equation and proposed an alternative pressure drop equation in porous media with a single voidage dependency for both the viscous and inertial flow regimes. They introduced two novelties. First they argued that fluid path lengths in

concentrated beds will be significantly greater than the bed length, L, but will approach the bed length as the the void fraction approaches unity. This can be taken into account by means of a tortosity factor, τ, that Foscolo et al. (1983) suggested to be simply given by :

$$\tau(\varepsilon) = \frac{1}{\varepsilon} \tag{C.7}$$

The second innovation was a consequence of a limiting situation which must be described by the model: for bed voidage approaching unity, one would want the force on a particle to approach the unhindered drag force rather than zero and this was achieved simply by adding one to the expression for the force known to apply to single particle in the laminar and turbulent regimes.

All the above modifications gave rise to the following new relationships for pressure drop in a porous media. The equations are reported below

Laminar Regime
$\frac{\Delta P}{L} = 17.3 \frac{\mu(U_o - U_p)}{d_p^2}(1-\varepsilon)\left[\frac{3.33(1-\varepsilon)}{\varepsilon^4} + \frac{1}{\varepsilon}\right]$
Turbulent Regime
$\frac{\Delta P}{L} = 0.336 \frac{\rho_f (U_o - U_p)^2}{d_p}(1-\varepsilon)\left[\frac{3.55(1-\varepsilon)}{\varepsilon^4} + \frac{1}{\varepsilon}\right]$
Here the numerical constants 17.3 and 0.336 were chosen to match the emprical Blake-Kozeny and the Burke-Plummer equations at fixed bed voidage of 0.4. (Foscolo et al., 1983)

(C.8)

They also showed that no numerical error is involved if the previous equations are substituted

by the simpler:

Laminar Regime
$\frac{\Delta P}{L} = 17.3\frac{\mu\left(U_o - U_p\right)}{d_p^2}(1-\varepsilon)\varepsilon^{-4.8}$
Turbulent Regime
$\frac{\Delta P}{L} = 0.336\frac{\rho_f\left(U_o - U_p\right)^2}{d_p}(1-\varepsilon)\varepsilon^{-4.8}$

(C.9)

Figure C.1 shows a plot which compares the above voidage functions over the full operating range. The function $\varepsilon^{-4.8}$ is also shown on the diagram. It can be seen that all three functions are readily interchangeable. Following the same procedure as Ergun (1952), Foscolo et al. (1983) added the two contributions to arrive at an expression for the pressure drop in the intermediate flow regime:

$$\frac{\Delta P}{L} = \frac{\rho_f\left(U_o - U_p\right)^2}{d_p}\left[\frac{17.3}{\mathrm{Re_p}} + 0.336\right](1-\varepsilon)\varepsilon^{-4.8} \tag{C.10}$$

Eqn. (C.10) corresponds numerically exactly to the Ergun equation at $\varepsilon = 0.4$. The proposed equation compared well with published experimental data obtained from high voidage fixed bed of spheres.

C.2 Fluidized beds

The onset of fluidization occurs when the pressure drop balances the total weight of the suspension.

$$\Delta p = Lg\left(\varepsilon\rho + (1-\varepsilon)\rho_p\right) \tag{C.11}$$

Almost all gas fluidized beds operate in the bubbling regime of fluidization however the fluidization of fine powders, at low gas velocities with air, shows a homogeneous expansion region before the appearance of bubbles. The analysis of the characteristics of this homogeneous expansion has been done by adopting the approach of Richardson & Zaki (1954a) for liquid/solid sedimentation and fluidization.

$$\frac{U}{U_t} = \varepsilon^n \tag{C.12}$$

In liquid fluidization n is a function of the diameter of the particle, diameter of the vessel and the terminal Reynolds number, and varies between 4.8 and 2.4 (Geldart, 1986). The above relationship appears to hold for gas solid systems however experimental values of n between 3.84-19.7 has been reported in literature for Geldart Type A powders (see Lettieri et al., 2001, Godard & Richardson, 1968). On the other hand the hypothesis utilized by Foscolo et al. (1983) in deriving their expression for pressure drop in beds of particles did not distinguish between fixed beds and fluidised conditions. Thus the expectation would be that eqn.C.9 and eqn.C.10 would be valid for the fluidised state. The applicability of these equations for fluidized beds, in the laminar and turbulent regime (see eqn.C.9), was

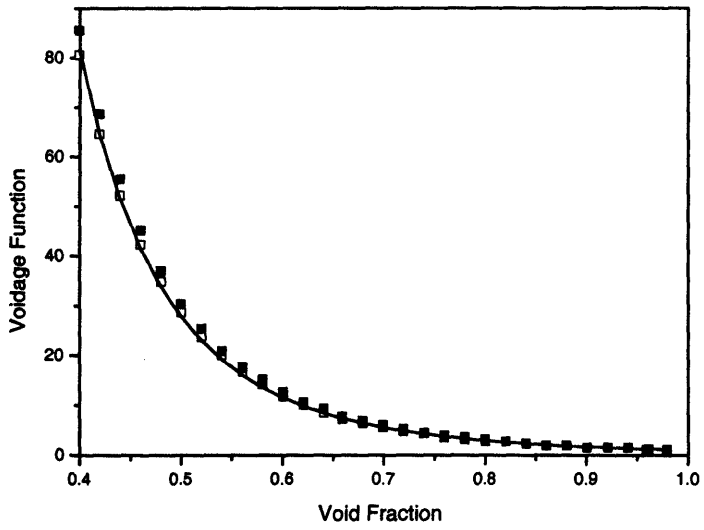

Figure C.1: *"Voidage Functions" : Continuous curve, the adopted form,* $\epsilon^{-4.8}$*; open squares, the viscous regime form,* $3.33(1-\epsilon)/\epsilon^4 + 1/\epsilon$*; solid squares, the inertial regime form,* $3.55(1-\epsilon)/\epsilon^4 + 1/\epsilon$

validated by Di Felice (1988a) in his thesis by the application of a force balance relationship for fluidised beds, which simply states that the piezometric pressure drop through the bed is equal to the buoyant weight of the particles. The verification procedure is reported here for convenience. For laminar case:

$$17.3\frac{\mu\left(U_o - U_p\right)}{d_p^2}(1-\varepsilon)\varepsilon^{-4.8} = (1-\varepsilon)\left(\rho_p - \rho\right)g \tag{C.13}$$

The unhindered terminal velocity of a single particle is the laminar flow regime is given by:

$$U_t = \frac{\left(\rho_p - \rho_f\right)gd_p^2}{18\mu} \tag{C.14}$$

Substituting the eqn.C.14 into eqn.C.13 becomes :

$$\frac{\left(U_o - U_p\right)}{U_t} \approx \varepsilon^{4.8} \tag{C.15}$$

which is very close to the empirical value proposed by Richardson & Zaki (1954a) and widely accepted. The same procedure can be applied to the turbulent regime where the terminal settling velocity of a single particle is given by

$$U_t = \left(\frac{4\left(\rho_p - \rho\right)gd_p}{1.32\rho}\right)^{0.5} \tag{C.16}$$

Equating again the two pressure drops

$$0.336\frac{\rho\left(U_o - U_p\right)^2}{d_p}(1-\varepsilon)\varepsilon^{-4.8} = (1-\varepsilon)\left(\rho_p - \rho\right)g \tag{C.17}$$

leads to:

$$\frac{\left(U_o - U_p\right)}{U_t} \approx \varepsilon^{2.4} \tag{C.18}$$

again in close agreement with the Richardson and Zaki experimental value. For the intermediate flow regime, the same procedure was carried out to verify the voidage velocity relationship. The equation for the intermediate flow regime was derived by Foscolo et al.

(1983) by simply by adding the equations for the viscous and inertial regimes. This procedure is analogous to that which was carried out by Ergun (1952) to derive the pressure drop relationship in all flow regimes for fixed beds.

$$17.3\frac{\mu\left(U_o - U_p\right)}{d_p^2}(1-\varepsilon)\varepsilon^{-4.8} + 0.336\frac{\rho\left(U_o - U_p\right)^2}{d_p}(1-\varepsilon)\varepsilon^{-4.8} = (1-\varepsilon)\left(\rho_p - \rho\right)g \tag{C.19}$$

Foscolo et al. (1983) showed however that the above relationship upon evaluation did not agree with the Richardson-Zaki correlation in the intermediate regime. Di Felice (1988a), in his thesis, addressed this problem by applying a general method devised by Churchill & Usagi (1972) for correlating intermediate conditions. The proposed general form equation is given below:

$$y^{\alpha}(z) = y_0^{\alpha}(z) + y_{\infty}^{\alpha}(z) \tag{C.20}$$

where y represents the friction factor and z the Reynolds number for the particular problem in hand. y_0 and y_∞ are limiting correlations for z approaching 0 or ∞. The exponent α can be evaluated from experimental values. Churchill (1974) showed that using experimental data of pressure drop in fixed beds and utilizing the limiting conditions of viscous and inertial flow, i.e. *Blake-Kozeny and Burke-Plummer*, the data could be well matched using a value of α equal to one, confirming the suggestion of Ergun & Orning (1949), Ergun (1952) of just adding the two contributions. Di Felice (1988a) applied the same method to eqn.C.19 by assuming that the Richardson-Zaki equation summarizes all experimental data and subsequently fitting the values of α with experimental values . The above procedure resulted in the modified equation below:

$$\frac{\Delta P}{L} = \left[\left(\frac{17.3}{\mathrm{Re}_p}\right)^{\alpha} + (0.336)^{\alpha}\right]^{\frac{1}{\alpha}} \frac{\rho\left(U_o - U_p\right)^2}{d_p}(1-\varepsilon)\varepsilon^{-4.8} \tag{C.21}$$

where α is given by

$$\alpha = 2.55 - 2.1\left[\tanh\left(20\varepsilon - 8\right)^{0.33}\right]^3$$

The above equation has been verified extensively with experimental data (see e.g. Gibilaro, 2001, Di Felice, 1988a). For the case of predicting the pressure drop equilibrium relationship for mixture of particles in a fluidised bed Gibilaro et al. (1986) assumed that the coefficient α has the same numerical value as the one obtained for a mono component bed at the same fluid volume fraction and expressed by eqn. C.21. Although the above equation was developed based on a liquid/solid system, it has been successfully used to predict pressure drop equilibrium relationships for binary gas-solid beds (Rasul et al., 1999).

Publications

Owoyemi, O., Lettieri, P., Place, R., (2005). Experimental Validation of Eulerian-Eulerian Simulations of Rutile. Industrial Powders. *Ind Eng Chem Res*, 44, 9996-10004.

Owoyemi, O., Mazzei, L., Lettieri P., (2006). Derivation of the equations of change for binary fluidized suspensions and CFD investigation of different closure relationships for the particle-particle drag force. Submitted to *AICHE J.*.

Lettieri, P., Di Felice, R., Pacciani, R., **Owoyemi, O.**, (2005). CFD modelling of liquid fluidized beds in slugging mode.*Powder Tech.*, 167, 94-103.

Owoyemi, O., Lettieri, P., (2006). A Hydrodynamic Model for the Simulation of Binary Particle Systems in Gas-Fluidized Beds. In *Proceedings of the 10th International Conference on Multiphase Flow in Industrial Plant*, 459-470.

Owoyemi, O., Lettieri, P., (2006). A CFD Study into the influence of the particle-particle darg force on the dynamics of binary gas-solid fluidized beds. In *Proceedings of 12th International Conference on Fluidization*

Owoyemi, O., Lettieri, P., Place, R., (2005). A Mathematical Model for the Simulation of Binary Gas Fluidized Beds. In *Proceedings AIChE 2006 Spring Meeting*, 23-27 April, Orlando Florida.

Owoyemi, O., Lettieri, P., Place, R., (2005). Computational Simulation of Industrial

Powders- A Validation Study. *Proceedings of the Particulate Systems Analysis Conference*, Stratford-upon -Avon, UK.

Owoyemi, O., Cammarata, L., Lettieri, P., Coleman, D., (2005). Analysis of different drag models for the CFD simulations of bubbling gas fluidized beds. In *Proceedings of the 7th World Congress in Chemical Engineering* Glasgow, Scotland, **P45-011**, 548.

Owoyemi, O., Lettieri, P., Place, R., (2005). "CFD modelling of binary mixtures in gas fluidized beds." In *Proceedings AIChE 2005 Annual Meeting*, 30-4 November, Cincinnati.

Owoyemi, O., Lettieri, P., Westwood, M., Place, R., (2004). Computational fluid dynamics modelling of poly-disperse systems. In *Book of Abstracts 6th UK Particle Technology Forum*, 15-16 June, University College London, UK.

Owoyemi, O., Lettieri, P., Place, R., (2004). Towards the CFD modelling of bimodal gas fluidized beds. In *Book of Abstracts CFD in CRE IV*, 19-24 June, Barga, Italy.

Subject Index

Author Index